



**AFRL-AFOSR-VA-TR-2022-0021**

---

**Aerodynamic and Aeroelastic Behavior of Wings in the Presence of Upstream Vortical and Viscous Disturbances**

**Gopalarathnam, Ashok  
NORTH CAROLINA STATE UNIVERSITY  
2601 WOLF VILLAGE WAY  
RALEIGH, NC, 27607  
USA**

---

**11/04/2021  
Final Technical Report**

**DISTRIBUTION A: Distribution approved for public release.**

Air Force Research Laboratory  
Air Force Office of Scientific Research  
Arlington, Virginia 22203  
Air Force Materiel Command

**REPORT DOCUMENTATION PAGE**

Form Approved  
OMB No. 0704-0188

The public reporting burden for this collection of information is estimated to average 1 hour per response, including the time for reviewing instructions, searching existing data sources, gathering and maintaining the data needed, and completing and reviewing the collection of information. Send comments regarding this burden estimate or any other aspect of this collection of information, including suggestions for reducing the burden, to Department of Defense, Washington Headquarters Services, Directorate for Information Operations and Reports (0704-0188), 1215 Jefferson Davis Highway, Suite 1204, Arlington, VA 22202-4302. Respondents should be aware that notwithstanding any other provision of law, no person shall be subject to any penalty for failing to comply with a collection of information if it does not display a currently valid OMB control number.  
**PLEASE DO NOT RETURN YOUR FORM TO THE ABOVE ADDRESS.**

<b>1. REPORT DATE (DD-MM-YYYY)</b> 04-11-2021	<b>2. REPORT TYPE</b> Final	<b>3. DATES COVERED (From - To)</b> 01 Jul 2017 - 30 Jun 2021
--	--------------------------------	--

<b>4. TITLE AND SUBTITLE</b> Aerodynamic and Aeroelastic Behavior of Wings in the Presence of Upstream Vortical and Viscous Disturbances	<b>5a. CONTRACT NUMBER</b>
	<b>5b. GRANT NUMBER</b> FA9550-17-1-0301
	<b>5c. PROGRAM ELEMENT NUMBER</b> 61102F

<b>6. AUTHOR(S)</b> Ashok Gopalarathnam	<b>5d. PROJECT NUMBER</b>
	<b>5e. TASK NUMBER</b>
	<b>5f. WORK UNIT NUMBER</b>

<b>7. PERFORMING ORGANIZATION NAME(S) AND ADDRESS(ES)</b> NORTH CAROLINA STATE UNIVERSITY 2601 WOLF VILLAGE WAY RALEIGH, NC 27607 USA	<b>8. PERFORMING ORGANIZATION REPORT NUMBER</b>
---	---

<b>9. SPONSORING/MONITORING AGENCY NAME(S) AND ADDRESS(ES)</b> AF Office of Scientific Research 875 N. Randolph St. Room 3112 Arlington, VA 22203	<b>10. SPONSOR/MONITOR'S ACRONYM(S)</b> AFRL/AFOSR RTA1
	<b>11. SPONSOR/MONITOR'S REPORT NUMBER(S)</b> AFRL-AFOSR-VA-TR-2022-0021

**12. DISTRIBUTION/AVAILABILITY STATEMENT**  
A Distribution Unlimited: PB Public Release

**13. SUPPLEMENTARY NOTES**

**14. ABSTRACT**  
The objective of the research was to study the effect of upstream flow disturbances on the unsteady aerodynamics and aeroelastic behavior of a downstream wing. A wind-tunnel aeroelastic apparatus, consisting of an elastically-supported airfoil with an optional upstream bluff-body flow-disturbance generator, was developed. The experimental results show that the flow disturbances cause amplitude modulation of an otherwise constant-amplitude limit-cycle oscillation (LCO) of the airfoil. Annihilation of LCO was demonstrated under certain conditions. This is believed to be the first experimental demonstration of the annihilation of an aeroelastic LCO. A new "aeroelastic inverse" algorithm, based on inverting the equations of motion to solve for the lift and moment experienced by an aeroelastic wing, was developed to better understand the LCO modulation. The results show that the pitch-heave mass coupling, which affects the pitch-heave phase difference, controls the amplitude modulation. A new gust generator, that allows for control of the phase of the shed vortices, was designed using computational fluid dynamics. With this gust generator, LCO modulation and annihilation have been demonstrated by open-loop control of the gust-generator oscillation. A low-order prediction method was developed for studying the effects of upstream flow disturbances on the unsteady aerodynamics of a prescribed-motion airfoil. The flow disturbances were seen to modify LEV shedding, the details of which depend on the amplitude and phase of the disturbance relative to the airfoil motion.

**15. SUBJECT TERMS**

<b>16. SECURITY CLASSIFICATION OF:</b>			<b>17. LIMITATION OF ABSTRACT</b>	<b>18. NUMBER OF PAGES</b>	<b>19a. NAME OF RESPONSIBLE PERSON</b> GREGG ABATE
<b>a. REPORT</b>	<b>b. ABSTRACT</b>	<b>c. THIS PAGE</b>			<b>19b. TELEPHONE NUMBER (Include area code)</b>
U	U	U	UU	155	425-1779

Final Report prepared for  
*Air Force Office of Scientific Research*  
on AFOSR Grant # FA9550-17-1-0301

Project Title:  
**Aerodynamic and Aeroelastic Behavior of Wings in the Presence  
of Upstream Vortical and Viscous Disturbances**

Principal Investigators:  
**Ashok Gopalarathnam and Matthew Bryant**  
Department of Mechanical and Aerospace Engineering  
North Carolina State University  
Raleigh, NC 27695

Contributing Post-doctoral Scholars and Graduate Students:  
**Arun Vishnu Suresh Babu, Benjamin Kirschmeier, Zachary Gianikos, Punnag  
Chatterjee, Michael Jenkins, Michael Hughes, Yi Tsung Lee, and Mariah Mook**  
Department of Mechanical and Aerospace Engineering  
North Carolina State University  
Raleigh, NC 27695

Collaborators:  
**Albert Medina and Matthew Rockwood**  
U.S. Air Force Research Laboratory, Air Vehicles Directorate,  
AFRL/RQVA, WPAFB, OH 45433-7333.

Period of Performance:  
**1 July 2017–30 June 2021**

Program Manager:  
**Dr. Gregg Abate**  
Program Officer, Unsteady Aerodynamics & Turbulent Flows  
U.S. Air Force Office of Scientific Research

28 September 2021

# Contents

<b>1</b>	<b>Executive Summary</b>	<b>1</b>
<b>2</b>	<b>Introduction</b>	<b>2</b>
<b>3</b>	<b>Aeroelastic Experimental Setup</b>	<b>5</b>
3.1	Aeroelastic Apparatus Design . . . . .	5
3.2	Upstream Bluff Body . . . . .	7
3.3	Wind Tunnel and Data Collection Methods . . . . .	8
<b>4</b>	<b>Limit Cycle Characterization of an Aeroelastic Wing in a Bluff Body Wake</b>	<b>10</b>
4.1	Chapter Introduction . . . . .	10
4.2	Results and Discussion . . . . .	12
4.2.1	LCO Response with Steady Inflow . . . . .	12
4.2.2	LCO Response with Disturbed Inflow . . . . .	15
4.3	Interim Conclusions . . . . .	26
<b>5</b>	<b>Amplitude Annihilation in Wake-Influenced Aeroelastic Limit-Cycle Oscillations</b>	<b>27</b>
5.1	Chapter Introduction . . . . .	27
5.2	System Characterization and Modeling . . . . .	28
5.2.1	Parameter Estimation . . . . .	28
5.2.2	System Energies . . . . .	31
5.3	Results . . . . .	31
5.3.1	Wing Limit Cycle Oscillation Behavior . . . . .	32
5.4	Analysis and Discussion . . . . .	36
5.4.1	Recurrence Analysis . . . . .	36
5.4.2	Instantaneous Frequency Analysis . . . . .	39

5.4.3	Coupling and Aerodynamic Energy Analysis . . . . .	42
5.5	Interim Conclusions . . . . .	43
<b>6</b>	<b>Aeroelastic Inverse: Estimation of Aerodynamic Loads during Large-Amplitude Limit-Cycle Oscillations</b>	<b>45</b>
6.1	Chapter Introduction . . . . .	45
6.2	Aeroelastic Inverse Method . . . . .	46
6.3	System Identification and Uncertainty Quantification . . . . .	48
6.3.1	Model Selection and Sensitivity Analysis . . . . .	48
6.3.2	Uncertainty Quantification . . . . .	51
6.3.3	Model Calibration . . . . .	51
6.3.4	Aerodynamic Force Prediction and AEI Validation . . . . .	53
6.4	Results and Discussion . . . . .	55
6.4.1	Bifurcation Analysis . . . . .	55
6.4.2	Limit-Cycle Kinematic Analysis . . . . .	57
6.4.3	Limit-Cycle Force Analysis . . . . .	58
6.4.4	Limit-Cycle Power and Energy Analysis . . . . .	60
6.4.5	Coupling Energy Analysis . . . . .	62
6.5	Interim Conclusions . . . . .	63
<b>7</b>	<b>Theoretical and Experimental Investigations of an Unsteady Airfoil Encountering External Flow Disturbances</b>	<b>65</b>
7.1	Chapter Introduction . . . . .	65
7.2	Experimental Setup . . . . .	66
7.2.1	Test geometries . . . . .	67
7.2.2	Flow visualization . . . . .	68
7.2.3	Control of the disturbance phasing . . . . .	68
7.3	Low-Order Aerodynamic Model . . . . .	71
7.3.1	Formulation . . . . .	71
7.3.2	Solution of the flowfield . . . . .	72
7.3.3	Calculation of the unsteady loads . . . . .	74
7.3.4	Low-order model of the oncoming disturbance . . . . .	75
7.3.5	Numerical aspects of the discrete-vortex method . . . . .	77
7.4	Decomposition of the Leading-Edge Suction Parameter (LESP, $\mathcal{L}$ ) . . . . .	78
7.5	Results and Discussion . . . . .	81

7.5.1	Baseline kinematics: pitching airfoil in undisturbed flow . . . . .	81
7.5.2	Pitching airfoil in the presence of disturbance : $\phi = 0^\circ$ . . . . .	83
7.5.3	Pitching airfoil in the presence of disturbance : $\phi = 180^\circ$ . . . . .	91
7.5.4	Effect of the disturbance on the unsteady lift . . . . .	92
7.6	Interim Conclusions . . . . .	95
<b>8</b>	<b>Tailored Bluff Body Motion for Generating Desired Wake Structures</b>	<b>97</b>
8.1	Chapter Introduction . . . . .	97
8.2	Simulation Setup . . . . .	99
8.3	Results and Discussion . . . . .	100
8.4	Interim Conclusions . . . . .	102
<b>9</b>	<b>Design of a Flow Disturbance Generator Based on Oscillating Cylinders With Attached Splitter Plates</b>	<b>105</b>
9.1	Chapter Introduction . . . . .	105
9.2	Materials and Methods . . . . .	106
9.2.1	Bluff Body Sizing . . . . .	106
9.2.2	CFD Simulations . . . . .	107
9.2.3	Bluff Body Construction . . . . .	108
9.2.4	Testing Apparatus . . . . .	109
9.2.5	Test Cases . . . . .	110
9.3	Results and Discussion . . . . .	111
9.3.1	Bluff Body Design Validation . . . . .	111
9.3.2	Aeroelastic Wing LCO Response . . . . .	112
9.4	Interim Conclusions . . . . .	116
<b>10</b>	<b>Summary and Conclusions</b>	<b>120</b>
<b>A</b>	<b>Detailed analysis of the LEV shedding phenomena for <math>\phi = 180^\circ</math></b>	<b>123</b>
<b>B</b>	<b>Parametric study of the interaction phenomena using the low-order model</b>	<b>126</b>
<b>C</b>	<b>List of Publications Resulting from this Effort</b>	<b>130</b>
C.1	Journal articles . . . . .	130
C.2	Conference publications/presentations . . . . .	130
C.3	Ph.D. dissertations . . . . .	131

C.4 M.S. theses . . . . . 131

# List of Figures

3.1	Spring torque measurements with load cell compared to Eqn. 1 . . . . .	6
3.2	CAD model of aeroelastic apparatus . . . . .	6
3.3	Photograph of aeroelastic apparatus shown with bluff body mounted upstream . . .	7
3.4	Schematic of bluff body spatial configuration (wing deflections not to scale) . . . . .	8
4.1	(a) Non-dimensional mean heave amplitude and (b) mean pitch amplitude vs wind-speed for no-bluff-body case. Error bars represent one standard deviation. . . . .	13
4.2	Pitch angle time histories for no-bluff-body case. . . . .	13
4.3	(a) Fundamental LCO frequency for pitch and heave DOF vs windspeed and (b) mean pitch-heave phase difference vs windspeed for no-bluff-body case. . . . .	14
4.4	Pitch angle PSD plotted vs windspeed for no-bluff-body case (PSD magnitude = arbitrary log scale) . . . . .	14
4.5	Pitch angle time histories for $\mathbf{X}_b/\mathbf{D} = 4.3$ case. . . . .	15
4.6	Pitch angle PSD plotted vs windspeed for $\mathbf{X}_b/\mathbf{D} = 4.3$ case (PSD magnitude = arbitrary log scale) . . . . .	16
4.7	Pitch amplitude distributions for (a) no-bluff-body, (b) $\mathbf{X}_b/\mathbf{D} = 6.5$ , (c) $\mathbf{X}_b/\mathbf{D} = 5.6$ , (d) $\mathbf{X}_b/\mathbf{D} = 4.3$ . . . . .	17
4.8	Pitch amplitude CV contours for (a) no-bluff-body, (b) $\mathbf{X}_b/\mathbf{D} = 6.5$ , (c) $\mathbf{X}_b/\mathbf{D} = 5.6$ , (d) $\mathbf{X}_b/\mathbf{D} = 4.3$ . . . . .	18
4.9	Time-frequency content of pitch angle envelope (bottom) with corresponding pitch angle time history (top) for (a) $\mathbf{X}_b/\mathbf{D} = 6.5$ , (b) $\mathbf{X}_b/\mathbf{D} = 5.6$ , and (c) $\mathbf{X}_b/\mathbf{D} = 4.3$ where $f_{shed}/f_{LCO} = 2.8$ . . . . .	19
4.10	Time-frequency content of pitch angle envelope (bottom) with corresponding pitch angle time history (top) for (a) $\mathbf{X}_b/\mathbf{D} = 6.5$ , (b) $\mathbf{X}_b/\mathbf{D} = 5.6$ , and (c) $\mathbf{X}_b/\mathbf{D} = 4.3$ where $f_{shed}/f_{LCO} = 2.9$ . . . . .	20
4.11	Time-frequency content of pitch angle envelope (bottom) with corresponding pitch angle time history (top) for (a) $\mathbf{X}_b/\mathbf{D} = 6.5$ , (b) $\mathbf{X}_b/\mathbf{D} = 5.6$ , and (c) $\mathbf{X}_b/\mathbf{D} = 4.3$ where $f_{shed}/f_{LCO} = 3.1$ . . . . .	20

4.12	Time-frequency content of pitch angle envelope (bottom) with corresponding pitch angle time history (top) for (a) $X_b/D = 6.5$ , (b) $X_b/D = 5.6$ , and (c) $X_b/D = 4.3$ where $f_{shed}/f_{LCO} = 3.25$ . . . . .	21
4.13	Pitch-heave phase portraits for (a) no-bluff-body ( $U_\infty = 10.4m/s$ ) and (b) $X_b/D = 6.5$ , (c) $X_b/D = 5.6$ , and (d) $X_b/D = 4.3$ ( $f_{shed}/f_{LCO} = 2.9$ ). . . . .	22
4.14	$\theta$ (top) and $\phi_{\theta,h}$ (bottom) vs. time for (a) no-bluff-body ( $U_\infty = 10.4m/s$ ) and (b) $X_b/D = 6.5$ , (c) $X_b/D = 5.6$ , and (d) $X_b/D = 4.3$ ( $f_{shed}/f_{LCO} = 2.9$ ). . . . .	23
4.15	Phase portrait of $\theta_A$ vs $\phi_{\theta,h}$ vs. for no-bluff-body ( $U_\infty = 10.4m/s$ ) and $X_b/D = 6.5$ ( $f_{shed}/f_{LCO} = 2.9$ ). . . . .	24
4.16	(a) left: $\phi_{\theta,h}$ and $\bar{P}_{net}$ vs time and (b) right: $\theta_A$ vs time for $X_b/D = 6.5$ , $f_{shed}/f_{LCO} = 2.9$ case. . . . .	25
5.1	Measured pitch restoring moment compared to model . . . . .	29
5.2	Free decay comparison of experiment with model for Config - 1 (a) and Config - 2 (b). . . . .	31
5.3	Pitch time histories for a range of selected wind speeds without the bluff body upstream. . . . .	33
5.4	(a) Pitch amplitude versus wind speed and (b) heave amplitude versus wind speed for wing LCO without the bluff body upstream. . . . .	33
5.5	(a) Frequency spectrum of pitch response for five selected wind speeds without the bluff body present. (b) Frequency spectrum of pitch response with the bluff body present for all wind speeds tested. $x_\theta = 0.078$ for each figure. . . . .	34
5.6	Pitch time histories for a range of selected wind speeds with the bluff body upstream. . . . .	35
5.7	(a) Pitch amplitude versus wind speed and (b) heave amplitude versus wind speed for wing LCO with the bluff body upstream. . . . .	35
5.8	Multiple LCO annihilations at $f_s/f_{LCO} = 2.92$ for $x_\theta = 0.078$ , first two seconds of motion (a) and full time history (b). . . . .	36
5.9	(a) Pitch time history with regions of kinematic similarity to the annihilation event highlighted by blue markers. (b) Pitch time history with regions of kinematic and bluff body force similarity to the annihilation event highlighted by blue markers. $x_\theta = 0.078$ and $f_s/f_{LCO} = 2.98$ for both figures. . . . .	38
5.10	Time histories of multiple annihilation event trials with regions of cross recurrence similarity highlighted with colored markers. $f_s/f_{LCO} = 2.98$ and $x_\theta = 0.078$ . . . . .	39
5.11	Continuous wavelet transforms of the envelope of the pitch time histories for $x_\theta = 0.078$ at (a) $f_s/f_{LCO} = 2.72$ , (b) $f_s/f_{LCO} = 2.98$ , and (c) $f_s/f_{LCO} = 3.21$ . . . . .	40
5.12	(a) Instantaneous frequency and (b) pitch heave frequency ratio versus time for $f_s/f_{LCO} = 2.98$ shown over the full time history. . . . .	41
5.13	(a) Instantaneous frequency and (b) pitch-heave frequency ratio during recoverable decay. . . . .	41
5.14	(a) Instantaneous frequency and (b) pitch-heave frequency ratio during annihilation. . . . .	42

5.15	Coupling energy per cycle and pitch-heave difference versus time for $f_s/f_{LCO} = 2.98$ for the same trial during (a) recoverable amplitude decay and (b) LCO annihilation. Note, $\dots$ represent the 95% credible intervals. . . . .	43
5.16	Aerodynamic energy per cycle and pitch amplitude versus time for $f_s/f_{LCO} = 2.98$ for the same trial during amplitude (a) recoverable decay and (b) LCO annihilation. . . . .	44
6.1	Spring torque measurements with load cell compared to Eqn. 15 . . . . .	49
6.2	Joint densities and marginal posterior histograms for Config - 1 . . . . .	52
6.3	Free decay comparison of experiment and model for (a) Config - 1 and (b) Config - 2. . . . .	53
6.4	Comparison of (a) $C_L$ and (b) $C_M$ from AEI method and AFRL prescribed motion measurements. Reynolds number for this case is 75,600. Note, $\dots$ represent the 95% credible interval for each measurement . . . . .	55
6.5	$E(t)/E_0$ versus time for (a) Config - 1 and (b) Config - 2 for wind speeds tested up to LCO initiation. Pitch and heave response for wind speeds at and below LCO initiation for (c) Config - 1 and (d) Config - 2. . . . .	56
6.6	(a) Heave amplitude, (b) pitch amplitude, and (c) pitch-heave phase difference versus wind speed. Note error bars in amplitude plots represent the deviation in amplitude over the recorded time and not the measurement error. . . . .	57
6.7	Lift coefficient and effective angle of attack versus cycle fraction for (a-c) Config - 1 and (d-f) Config - 2 at three different wind speeds. $A, A'$ represent the maximum and minimum lift while $B, B'$ are when full lift stall occurs ([1]). Note, $\dots$ represent the 95% credible intervals. . . . .	59
6.8	Moment coefficient and effective angle of attack versus cycle fraction for (a-c) Config - 1 and (d-f) Config - 2 at three different wind speeds. $C, C'$ represent the maximum and minimum moment while $D, D'$ are the corresponding moment when full lift stall occurs ([1]). Note, $\dots$ represent the 95% credible intervals. . . . .	60
6.9	a) $C_{L_{max}}$ vs $h/c$ for both mass coupling configurations. b) Dynamic $C_L$ versus $\theta$ compared to thin airfoil theory and static measurements performed by AFRL. c) Dynamic $C_M$ versus $\theta$ compared to static measurements performed by AFRL, measured at the half chord (only Config - 1 shown for clarity). Note, $\dots$ represent the 95% credible intervals. . . . .	60
6.10	Aerodynamic energy for (a) Config - 1 and (b) Config - 2 and aerodynamic efficiency for (c) Config - 1 and (d) Config - 2 versus wind speed. Note, $\dots$ represent the 95% credible intervals. . . . .	61
6.11	Power from aerodynamic lift and heave velocity versus cycle fraction for (a-c) Config - 1 and (d-f) Config -2 at three different wind speeds. Note, $A, A', B, B'$ are the same time stamps from Figure 6.7 and $\dots$ represent the 95% credible intervals. . . . .	62
6.12	Power from aerodynamic moment and pitch velocity versus cycle fraction for (a-c) Config - 1 and (d-f) Config -2 at three different wind speeds. Note, $C, C', D, D'$ are the same time stamps from Figure 6.8 and $\dots$ represent the 95% credible intervals. . . . .	63
6.13	Coupling energy between the degrees of freedom for both configurations. Note, $\dots$ represent the 95% credible intervals. . . . .	64

7.1	Schematic of the experimental setup showing the airfoil subjected to periodic flow disturbances generated by the upstream circular cylinder. . . . .	67
7.2	Experimental setup: direct force measurement and flow visualization using time-resolved particle-image velocimetry. . . . .	68
7.3	Left: Definition of the phase $\phi$ based on the position of the oncoming vortical disturbances relative to the airfoil. Right: Demonstration of the control of $\phi$ . Lift-coefficient histories of a static airfoil at zero incidence for different values of $\phi$ exhibiting a phase shift equal to $\phi$ . . . . .	69
7.4	POD phase plot for cylinder wakes: (Left) static cylinder, (Right) dynamic cylinder.	70
7.5	Phase-averaged vorticity contours of the wake: (Left) static cylinder, (Right) rotating cylinder. . . . .	70
7.6	Illustration of the low-order framework showing the oncoming flow disturbances, the vorticity shed from the airfoil, and the kinematic variables used in the theoretical formulation. Clockwise vorticity is considered positive. . . . .	71
7.7	Discrete-vortex rings introduced into the flowfield at the upstream shedding location forming a vortex street as they convect downstream towards the airfoil location. . .	76
7.8	Static airfoil at 6 degree incidence in the presence of the disturbance: (a) experimentally observed $C_L$ , (b) $C_L$ predicted by LDVM, (c) discrete-vortex plots from LDVM compared with experimental vorticity contours at four time instants in a cycle of lift oscillation. . . . .	77
7.9	LESP map for a symmetric airfoil showing the incremental LESP ( $\mathcal{L}$ ) due to a unit-strength clockwise discrete vortex. . . . .	79
7.10	Distributions of (a) normalwash, (b) bound circulation, (c) chord-parallel velocity, and (d) $\gamma'u'$ induced on the airfoil by a unit-strength clockwise vortex placed at five locations as marked in Fig. 7.9. . . . .	79
7.11	Aerodynamic coefficient histories for the baseline case: (a) Variation with $t^* = tU_{ref}/c$ of $\mathcal{L}$ from LDVM. (b) Lift coefficient predicted by LDVM compared with experimental measurements. . . . .	82
7.12	Comparison between phase-averaged vorticity contours from experiment (top) and discrete-vortex plots from LDVM (bottom) for the baseline case at six time instants.	82
7.13	Phase-averaged vorticity contours from experiment (top) and discrete-vortex plots from LDVM (bottom) at several time instants showing the flowfield evolution of the pitching airfoil in the presence of the disturbances with $\phi = 0^\circ$ . The inset shows the LESP variation from LDVM for $\phi = 0^\circ$ compared with that for the baseline case. . .	84
7.14	FTLE ridges calculated at various time instants for $\phi = 0^\circ$ showing the interruption in LEV shedding. The corresponding discrete-vortex plots from LDVM predictions are also included as insets along with each FTLE image. . . . .	86
7.15	Contribution to $\mathcal{L}$ from each factor governing the LEV shedding dynamics for $\phi = 0^\circ$ .	88
7.16	Total $\mathcal{L}$ history split into contribution from kinematic factors and that from flowfield elements for $\phi = 0^\circ$ for $\phi = 0^\circ$ . . . . .	88

7.17	LESP maps and colorized maps at various time instants highlighting the contribution from individual discrete vortices for $\phi = 0^\circ$ . . . . .	89
7.18	Phase-averaged vorticity contours from experiment (top) and discrete-vortex plots from LDVM (bottom) at several time instants showing the flowfield evolution of the pitching airfoil in the presence of the disturbances with $\phi = 180^\circ$ . The inset shows $\mathcal{L}$ variation from LDVM for $\phi = 180^\circ$ compared with that for the baseline case. . .	91
7.19	Comparison of $C_L$ history from experiment and LDVM for the two values of $\phi$ . The flow images from both the methods are also shown for selected time instants. . . .	93
8.1	The schematic showing tailored vortical disturbances being produced using an actuated cylinder-splitter plate bluff body . . . . .	98
8.2	The figure shows the mesh used in this numerical analysis (a) shows the computational zone partitioned into 3 domains with increasing mesh refinement (b) shows the zoomed in view of the mesh around the bluff body, and (c) shows the enlarged view of the mesh around the sharp corners of the splitter plate. . . . .	99
8.3	The top row of the shows the experimental vorticity plots obtained by Rockwood et. al. [10] for the cases 1, 2 and 3, corresponding to the Strouhal ratios of 0.3, 0.7 and 1 respectively, at their maximum amplitudes of rotation. The bottom row shows the corresponding cases numerically obtained using ANSYS Fluent, showing a very good agreement with the experimental results. . . . .	101
8.4	The series of simulation snapshots are recorded at the maximum amplitude of the bluff body across a range of Strouhal frequency ratios, $St/St_n$ and shows the evolution of the vortices as the actuating frequency is increased. The well-defined vortices observed at lower Strouhal frequency ratios slowly become distorted as the actuation frequency is increased. The snapshots labelled (a) – (i) correspond to cases 4 - 12 in Table 8.2. . . . .	103
8.5	A sample $C_L$ plot for Case 7, shows the variation of the lift coefficient of the bluff body as a function of time. The initial transient effects are observed in the first two seconds of the simulation and are neglected for all analytical purposes . . . . .	104
8.6	The time evolution of the frequency content is plotted for every Strouhal frequency ratio. For each Strouhal ratio, the entire spectrogram is plotted and stitched together to obtain the above figure. The third harmonic of the actuation frequency ( $3f$ ) is co plotted in the above figure to show that a small part of the spectral energy of $C_L$ is also distributed to the third harmonic frequency. . . . .	104
9.1	Proposed bluff body design cross-section. . . . .	108
9.2	Bluff body subassemblies and completed assembly showing splitter plate location and dimensions. . . . .	109
9.3	Bluff body oscillation for an input frequency and amplitude of 4 Hz and $30^\circ$ respectively. . . . .	110
9.4	Streamwise velocity as a function of time for $f_{osc} = 6 Hz$ from CFD. . . . .	112
9.5	Vorticity contours from CFD showing well-defined vortex wakes for oscillation frequencies of (a) 4 Hz, (b) 5 Hz, (c) 6 Hz, (d) 7 Hz and (e) 8 Hz. . . . .	113

9.6	Frequency spectrogram for $f_{osc} = 6 Hz$ , showing an initial peak at $12 Hz$ as expected.	114
9.7	Cross-stream, time-averaged velocity profiles for (a) $4 Hz$ , (b) $5 Hz$ , (c) $6 Hz$ , (d) $7 Hz$ and (e) $8 Hz$ .	115
9.8	Comparison between computational and experimental centerline average velocities.	116
9.9	Bluff body angle, wing pitch angle, and wing heave displacement during forced oscillations at $f_{osc} = 3.9 Hz$ showing non-LCO response of the wing.	117
9.10	Bluff body angle, wing pitch angle, and wing heave displacement during forced oscillations at $f_{osc} = 4.0 Hz$ , showing “beat-like” phenomenon.	118
9.11	Bluff body angle, wing pitch angle, and wing heave displacement after stopping oscillations at $f_{osc} = 4.0 Hz$ , showing: a) excitation of LCOs and b) annihilation of LCOs	119
A.1	Contribution to $\mathcal{L}$ from each factor governing the LEV shedding dynamics for $\phi = 180^\circ$ .	123
A.2	Total $\mathcal{L}$ history split into contribution from kinematic factors and that from flowfield elements for $\phi = 180^\circ$ .	124
A.3	LESP maps and colored maps at various time instants highlighting the contribution from individual discrete vortices for $\phi = 180^\circ$ .	124
B.1	Effect of the value of $\mathcal{L}_{crit}$ on $\mathcal{L}$ and $C_L$ variations for both phases.	127
B.2	Effect of centerline distance on (a) $\mathcal{L}$ and (b) $C_L$ variations for $\phi = 0^\circ$ .	128
B.3	Effect of oncoming vortex strength on (a) $\mathcal{L}$ and (b) $C_L$ variations for $\phi = 0^\circ$ .	129

# Chapter 1

## Executive Summary

The objective of the research was to study the effect of upstream flow disturbances on the unsteady aerodynamics and aeroelastic behavior of a downstream wing. A wind-tunnel aeroelastic apparatus, consisting of an elastically-supported airfoil with an optional upstream bluff-body flow-disturbance generator, was developed. The experimental results show that the flow disturbances cause amplitude modulation of an otherwise constant-amplitude limit-cycle oscillation (LCO) of the airfoil. Annihilation of LCO was demonstrated under certain conditions. This is believed to be the first experimental demonstration of the annihilation of an *aeroelastic* LCO. A new “aeroelastic inverse” algorithm, based on inverting the equations of motion to solve for the lift and moment experienced by an aeroelastic wing, was developed to better understand the LCO modulation. The results show that the pitch-heave mass coupling, which affects the pitch-heave phase difference, controls the amplitude modulation. A new gust generator, that allows for control of the phase of the shed vortices, was designed using computational fluid dynamics. With this gust generator, LCO modulation and annihilation have been demonstrated by open-loop control of the gust-generator oscillation.

A low-order prediction method was developed for studying the effects of upstream flow disturbances on the unsteady aerodynamics of a prescribed-motion airfoil. The flow disturbances were seen to modify LEV shedding, the details of which depend on the amplitude and phase of the disturbance relative to the airfoil motion. These results from the method, which were in excellent agreement with the experimental results from a water-tunnel investigation, show that criticality of suction at the leading edge governs leading-edge vortex shedding even in the presence of flow disturbances. The theoretical effort also led to the development of leading-edge suction maps for visualizing the effect of a vortex in the flow on its capability to suppress or enhance leading-edge vortex shedding from the airfoil, which adds insight into how flow disturbances affect unsteady aerodynamics.

The overall research effort has resulted in four main contributions: (i) experimental demonstration of aeroelastic LCO annihilation using flow disturbances, (ii) a new aeroelastic inverse technique that can be used for estimating forces and moments on an aeroelastic wing, (iii) low-order prediction of flow-disturbance effects and the development of the novel leading-edge suction maps to visualize the effect of vortices on airfoil vortex shedding, and (iv) open-loop control of aeroelastic LCO using a new phase-adjustable gust generator. Taken together, these contributions and the new insights provide substantial improvements in the understanding of flow-disturbance effects on aeroelastic phenomena and unsteady-airfoil aerodynamics. They set the stage for follow-on work including on-demand control of aeroelastic phenomena and novel mitigation strategies for loads due to gust encounters.

# Chapter 2

## Introduction

Unsteady wing-wake interaction research has undergone profound growth in recent years as researchers utilize knowledge of wake impingement to develop new multi-vehicle flight formations, design novel micro-air vehicles [2], and leverage inspirations from biological swimmers and flyers [3]. Examples of such interactions include close formation flight [4], wake-induced flutter [5, 6, 7, 8], aerial refueling [9], and fish schooling dynamics [10]. Although diverse in applications, the fundamental thread through this area of research is the characterization of interactions between unsteady wakes and lifting bodies. Given the ubiquity of wake impingement in real systems, these interactions are pertinent in the characterization of nonlinear aeroelastic systems.

Aeroelasticity has traditionally been a subject dealing with avoidance of hazardous phenomena like divergence, control reversal, and flutter [11, 12] associated with aircraft flight. However, recent research has focused on harnessing the beneficial effects of aeroelasticity. Studies have shown that insects take advantage of aeroelastic interactions between their deformable wings and the surrounding air [13, 14]. Fluid-structure interactions have also been found to be helpful for animal locomotion and swimming [15]. This has inspired researchers in several areas to explore the potential benefits of fluid-structure interactions. For example, the insight gained from the studies on fluid-structure interactions in natural flyers is used for bio-inspired flapping wing MAVs [16, 17, 18]. Passive power generation from fluid-structure interactions is another area which exploits fluid-structure interactions as a source of renewable energy [19]. Bryant and Garcia [20] and Dunnmon et al. [21], for example, present ideas for energy harvesting from nonlinear aeroelastic oscillations.

Nonlinear aeroelastic phenomena remain a topic of considerable interest due to their complex interactions between dynamic systems, structural mechanics, and aerodynamics. Nonlinear interactions can manifest in limit cycle oscillations (LCO) such that the aeroelastic structure oscillates at a bounded amplitude. Significant research efforts have investigated how structural and aerodynamic nonlinearities affect the aeroelastic system response in LCO. For example, the research efforts reported in Refs. [22], [23], [24], [25], [26], [27], [28], and [29], and [30] experimentally investigated stall-influenced LCOs. These experiments demonstrated significant interplay between structural properties and stall phenomena. While the aforementioned and several others studied the aeroelastic response of various systems, one aspect that remains to be explored is modifying the aeroelastic response of a given system. This is important for harnessing the beneficial characteristics of an aeroelastic system and suppressing the harmful ones.

Prior efforts at modifying the fluid-structure interaction behaviors of aeroelastic wings have predominantly focused on changing structural parameters or changing the structure's aerodynamic

characteristics, rather than introducing and exploiting disturbances in the flow field itself. For example, prior research on controlling aeroelastic limit cycles and flutter behavior have used movable control surface flaps [31, 32] or morphing that is aimed at increasing vehicle performance by manipulating structural [33, 34] and aerodynamic characteristics of the wing to better match the vehicle state to the environment and task at hand. The former method has been more commonly investigated because flap control surfaces are well established mechanisms for other aspects of flight control [31]. While mechanically-induced LCO suppression/amplitude death has been the focus of numerous research efforts, aerodynamically-induced LCO suppression/amplitude death has received less attention.

Control of aeroelastic and aerodynamic responses by exploiting upstream disturbances is common in nature. Natural flyers and swimmers are known to take advantage of external flow disturbances to reduce the cost of locomotion [35, 36]. Meanwhile, the interaction of a wing with disturbances raises concerns in several engineering applications. Blade-vortex interactions in helicopters [37], wind turbines [38, 39, 40], and turbomachinery [41] often result in noise, structural, and control issues. Tang and Dowell [42] and Doherty et al. [43] have demonstrated that the post-flutter LCO response can be suppressed or annihilated by the addition of upstream vorticity. Modern pursuits in improving the design and performance of man-made propulsors and energy harvesters demand more consideration of the context of unsteady wings encountering flow disturbances.

While experimental and high-fidelity CFD methods facilitate detailed study of flow phenomena, low-order theoretical models augment these methods by providing an intuitive approach to understanding the flow physics from a fundamental perspective and equipping us with the insight to predict various trends. Moreover, the cost and time considerations in experimental and computational methods pose a problem in employing them for preliminary phases where wide range of parameter sweeps might be necessary. This, along with the inherent limitations of purely-theoretical methods, calls for the development of fast low-order models that are based on theory and augmented with the essential physics. The seminal theoretical modeling works by Wagner [44], Theodorsen [45], Kussner [46], von Kármán and Sears [47], and Sears [48] have proven invaluable to the field of unsteady aerodynamics despite the assumptions of small amplitude motions, planar wakes, and attached flows. The desire for expanded applicability of unsteady potential-flow methods has long motivated inviscid modeling approaches such as those in Refs. [49], [50], and [51] that can perform regardless of amplitude and reduced frequency of motion, and impose no restrictions on the trailing-wake dynamics. Alaminos-Quesada and Fernandez-Feria [52] use potential-flow theory to analyze the effect of the angle of attack on the interaction of a two-dimensional vortex with a flat plate. Wei and Zheng [53] present an approach to explain the formation of leading-edge vortices based on pressure distributions and adverse-pressure-gradient patterns using a simple theoretical model.

Recently, [51] presented a potential-flow-based approach to determine the initiation, growth, and termination of leading-edge vorticity from airfoils engaged in arbitrary unsteady motions based on the critical value of suction at the leading edge. In this phenomenologically augmented method, a single empirical parameter—the critical value of the leading-edge suction parameter (LESP)—unifies all the kinematic factors of the airfoil in determining its LEV shedding characteristics. This concept also eliminates the use of commonly used ad-hoc criteria such as start and stop of LEV shedding based on a local angle of attack or the assumption of continuous shedding, and has a broader scope of application than semi-empirical methods that can only be employed for limited situations. A discrete-vortex implementation of this approach called the LESP-modulated discrete-vortex method (LDVM) has been extensively validated for several case studies by [51].

In this work, we use experimental and computational methods along with theoretical tools based on LDVM and LESP to study the unsteady flow interactions and their effects on the aerodynamics of an airfoil undergoing prescribed and aeroelastic motions in the presence of external disturbances. The development of the model has been informed by the wind-tunnel experiments and numerical simulations at NCSU, and water tunnel experiments at AFRL. The theoretical model complements the experimental and computational analysis and serves as a low-order prediction mechanism. It was derived by augmenting the LDVM framework with a low-order model for the oncoming disturbances using discrete-vortex clusters periodically released into the flowfield, superimposed with a uniform flow. We show that the augmented LDVM model is able to predict intermittent LEV shedding from unsteady airfoils in the presence of external disturbances using the LESP concept and the associated unsteady loads in good agreement with experimental observations. In addition to being a predictive tool, the LDVM also augments the experimental and computational studies by providing a theoretical framework and various graphical approaches to analyze the unsteady flow phenomena from a fundamental perspective and elucidate the role of different factors governing the unsteady flowfield and the loads experienced by the airfoil. We use these tools to identify the roles of external vortical disturbances on suppressing or enhancing the LEV shedding tendency of the airfoil.

This report documents the research effort in understanding the aerodynamic and aeroelastic behaviour of wings in the presence of external flow disturbances and exploring the possibility of using tailored external flow disturbances as a means to modify the behavior of an aeroelastic wing. We use an integrated experimental, computational, and theoretical approach to achieve this objective. The computational and experimental studies performed in this effort not only helped to gain insight into the complex flow and fluid-structure interaction phenomena, but also helped in the development of the low-order theoretical model. The experimental campaign involved both water tunnel and wind-tunnel studies. The water-tunnel experiments were carried out by Medina's team in the U.S. Air Force Research Laboratory's Horizontal Free-Surface Water Tunnel, described in Chapter 7, to study wings undergoing prescribed motions in the presence of external flow disturbances and to visualize flow phenomena. Wind tunnel experiments were conducted by Bryant's group in the North Carolina State University (NCSU) subsonic wind tunnel to study the aeroelastic phenomena (presented in Chapters 3–6). The computational efforts (presented in Chapter 8) and the low-order modeling work (presented in Chapter 7) were carried out by Gopalarathnam's group at NCSU.

## Chapter 3

# Aeroelastic Experimental Setup

This chapter discusses the experimental setup used in Chapters 4 and 5. These experiments were performed in the NCSU Subsonic Wind Tunnel located in HB 103 at NCSU Centennial Campus.

### 3.1 Aeroelastic Apparatus Design

A 2-DOF aeroelastic apparatus was constructed to investigate the effects of wing-wake interaction phenomena (Figure 3.2). The wing is a 3D printed symmetric version of the SD 7003 with a chord length ( $c$ ) of 150 mm and aspect ratio ( $AR$ ) of 4. The 3D printer used is a Stratasys F370 with a nominal resolution of  $\pm 0.400$  mm. The wing was then primed and sanded to reduce the effects of surface roughness. The wing is printed from ABS plastic with two 1/8" diameter aluminum rods as internal spars. The connection between the wing and the upper/lower carriages consists of two 10 mm diameter steel rods. The airfoil is assumed to be rigid with the only significant elastic effects coming from the springs. Heave displacement and pitch angle measurements were taken at both ends of the wing and compared to ensure that there was negligible relative twist or tip deflection along the span of the airfoil. Table 3.1 provides the mass and geometric system properties. These values were obtained via direct measurement except for the center of mass (COM) and moment of inertia (MOI) which were estimated via SolidWorks software.

Based on the results of Visbal and Garmann [54], endplates are attached to the tips of each wing to emulate 2D flow conditions. The endplates extend one chord length forward and aft of the wing section. The pitching axis was located at the mid-chord position for the experiments discussed in this chapter. The aeroelastic system is supported within the wind tunnel test section by an external box structure which acts as a mechanical ground, isolated from the wind tunnel. The wing is supported by upper and lower PBC Linear guide rails and carriages (Figure 3.2). Linear extension springs provide elastic restoring force and moment for both the heave and pitch degrees of freedom. A set of springs are attached to a cable-pulley system to create a restoring moment for the pitch DOF. The heave spring stiffness was measured via a Transducer Techniques LCU-1K on an Instron 4400R tensile testing machine and was found to be constant over the range of the range of heave deflections in the present experiments. Characterization of the effective stiffness in the pitch DOF was obtained via torque and angular position measurements from an ATI Gamma 6 axis load cell and a US Digital encoder, respectively. The restoring moment response of the pitch DOF showed two distinct stiffness regions, labeled A and B in Fig. 3.1. The transition from region

A to B is caused by one side of the pulley losing tension for large deflections, reducing the effective stiffness by half. The pitch stiffness model is given by the following piecewise equation:

$$M_{\theta}(\theta) = \begin{cases} K_{\theta_A} \theta & \text{if } \theta < \theta_T \\ K_{\theta_A} \theta_T + K_{\theta_B} (\theta - \theta_T) & \text{if } \theta \geq \theta_T \end{cases} \quad (1)$$

where  $\theta_T$  is the transition angle between regions A and B. The stiffness parameters  $K_{\theta_A}$  and  $K_{\theta_B}$  were obtained via a first order polynomial least-squares fit of the two respective stiffness regions. Figure 3.1 shows the spring torque responses compared to the pitch stiffness model described in Eq. 1. The piecewise model matches the experimental response well and captures the two stiffness regions: A and B.

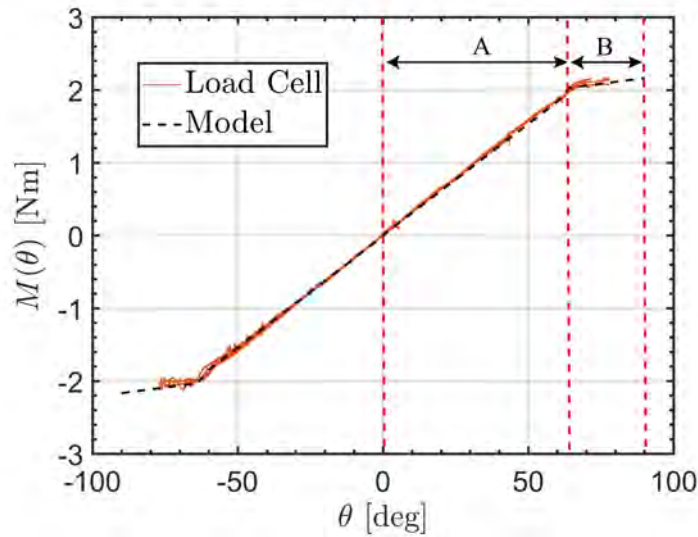


Figure 3.1: Spring torque measurements with load cell compared to Eqn. 1

The stiffness model parameters for the current configuration are listed in Table 3.2 below:

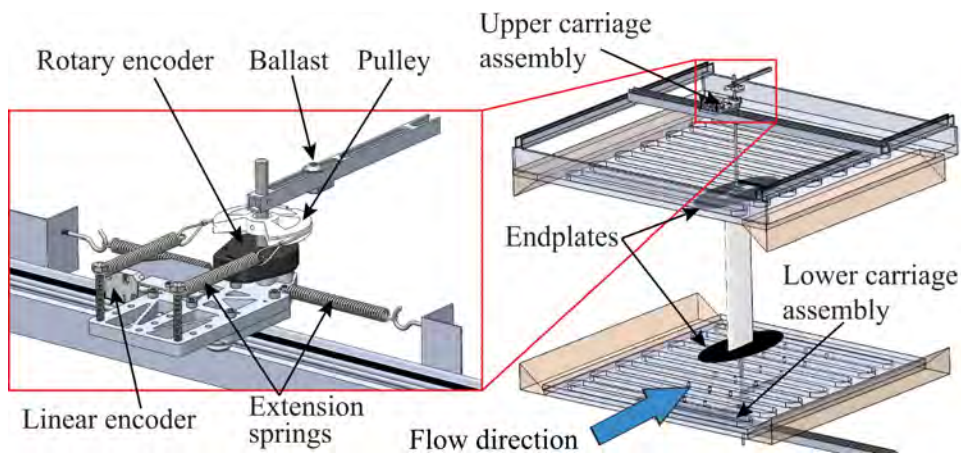


Figure 3.2: CAD model of aeroelastic apparatus

Table 3.1: Mass and dimensional properties

Parameter	Description	Value
$AR$	aspect ratio	4
$c$	chord length [m]	0.15
$I_\theta$	pitching inertia about elastic axis [ $\text{kg} \cdot \text{m}^2$ ]	5.32e-03
$m_T$	mass of all moving parts [kg]	3.27
$m_W$	mass of all rotating parts [kg]	1.61
$x_p$	non-dimensional pitching axis location (chord length fraction from LE)	0.5
$x_\theta$	non-dimensional distance from pitching axis to rotational COM	0.062

Table 3.2: Structural stiffness and damping properties

Parameter	Description	Value
$K_h$ [N/m]	Effective stiffness in heave DOF	$2.17 \times 10^3$
$K_{\theta_A}$ [Nm/rad]	Region A effective pitch stiffness	3.59
$K_{\theta_B}$ [Nm/rad]	Region B effective pitch stiffness	1.80
$\theta_T$ [°]	Pitch Transition angle	62

### 3.2 Upstream Bluff Body

During initial wing-wake interaction experiments an upstream rectangular cylinder was used to create the wake. The streamwise length of the bluff body was 152 mm and the width (D) was 76 mm. Okajima [55] found that the Strouhal number ( $St$ ) for a rectangular cylinder with length to width ratio of 2 is approximately 0.085 for the Reynolds numbers tested herein. This allows for shedding frequencies closer to the natural frequencies of the aeroelastic system than for a circular cylinder where  $St \approx 0.2$ . The bluff body was constructed from laser cut birch plywood and attached to an ATI Gamma 6-axis load cell (not shown) to measure the shedding frequency (Fig. 3.3).

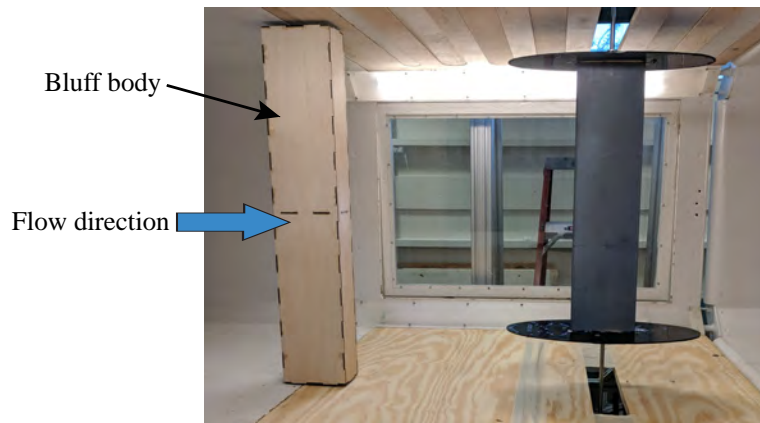


Figure 3.3: Photograph of aeroelastic apparatus shown with bluff body mounted upstream

For the set of experiments outlined in Chapter 4, the bluff body was positioned at three different

locations relative to the wing. A diagram of the test section layout is shown in Fig. 3.4. Table 3.3 defines the three bluff body positions tested. The experiments outlined in Chapter 5 saw the bluff body’s trailing edge placed at 0.49 m ( $X_b/D = 6.4$ ) upstream from the wing leading edge when the wing is at rest.

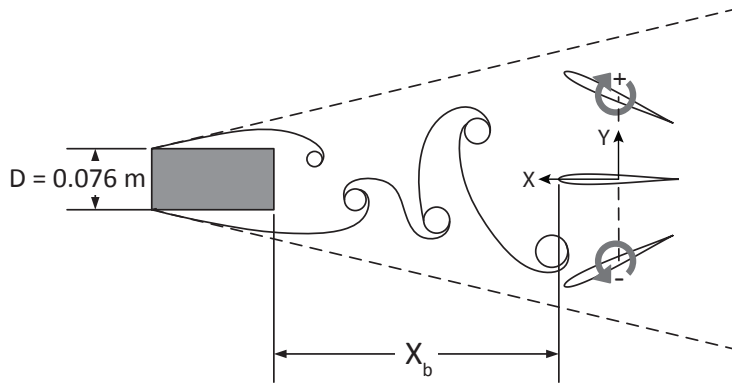


Figure 3.4: Schematic of bluff body spatial configuration (wing deflections not to scale)

Table 3.3: Bluff body spatial configurations

Configuration	$X_b$ [m]	$X_b/D$
1	N/A	N/A
2	0.51	6.5
3	0.43	5.6
4	0.33	4.3

### 3.3 Wind Tunnel and Data Collection Methods

For all experiments outlined in this report pitch and heave kinematics were measured via a National Instruments NI PXIe-6363 I/O module using a LabVIEW based data acquisition system with a nominal sampling rate of 50 kHz. U.S. Digital E6-10000 encoders with 0.07-degree resolution measured the wing’s angular position while Renishaw LM10 magnetic linear encoders with 0.03 mm resolution measured the heave position. Aeroelastic experiments were conducted in the North Carolina State University closed-return subsonic wind tunnel with a 0.81 m x 1.14 m x 1.17 m test section. The freestream velocity for LCO experiments ranged from 6 m/s to 12 m/s, which corresponds to an airfoil chord based Reynolds number range of  $70 \times 10^3$  to  $120 \times 10^3$ . The freestream windspeed ( $U_\infty$ ) was monitored via a dynamic pressure transducer. For each windspeed setting, the wing was given a 45-degree initial deflection unless the wing was already undergoing LCO. If the system returned to equilibrium without sustained oscillation, the dynamic pressure was increased by 4.8 Pa (0.10 lb/ft<sup>2</sup>) and another 45-degree deflection was provided. This process was repeated until a windspeed was reached where an initial deflection resulted in self-sustained

oscillations. From this point on, the windspeed was increased for each test point without disturbing the apparatus. At the start of each LCO test point, the wing was first allowed to oscillate for one minute to avoid measuring transient behavior. Next, the wing position data was recorded for two minutes and the process repeated for increasing dynamic pressures.

## Chapter 4

# Limit Cycle Characterization of an Aeroelastic Wing in a Bluff Body Wake

This chapter presents an experimental investigation aimed at characterizing the kinematics of a pitching-heaving aeroelastic wing placed downstream of a rectangular bluff body. The influence of the bluff body wake on the wing is twofold: a viscous wake which produces a velocity deficit downstream and an oscillating induced velocity field due to periodic vortex shedding. The latter effect is the focus of this chapter, specifically, the interaction between the wake frequency and the wing limit cycle oscillation (LCO) frequency. Wind tunnel experiments showed that the presence of the upstream bluff body causes modulation of the LCO amplitude. The modulation resembles a beat phenomenon, however the modulation frequency is related to the third harmonic of  $f_{LCO}$  rather than the fundamental frequency. The modulation behavior also differs from that of a beat in that the spectral content contains sideband frequencies, characteristic of a multiplication between a carrier wave and a modulation wave rather than a simple sinusoidal superposition. Additionally, the streamwise spacing between the bluff body and the wing significantly influences the wing kinematics, with a closer spacing between the two bodies increasing the intensity of the amplitude modulation. For shedding frequencies sufficiently close to the LCO third harmonic, reducing this streamwise distance was shown to induce an alternation between two distinct modes of amplitude modulation, each with its own intensity and frequency.

### 4.1 Chapter Introduction

While practical aeroelastic structures such as aircraft wings are continuous deformable systems with infinite degrees of freedom, researchers often use simplified lumped-parameter models to gain insight into the underlying physics. This technique was utilized by Song et al. [56] who used a combined physical and computational modeling approach in order to develop an efficient two degree of freedom (2-DOF) flutter onset prediction model. Constraining the degrees of freedom in a model to a canonical form (e.g. pitching and plunging) also allows for easier isolation of nonlinear effects. Nonlinearities arise in real-world systems and are associated with a broader class of responses including LCO. For example, Marsden et al. [57] was able to isolate the effect of free-play, a form of structural nonlinearity, on the aeroelastic response of a pitching-plunging wing

section. Razak et al. [58] used a 2-DOF model instrumented with acceleration and pressure sensors. The data was combined with time-resolved PIV to identify nonlinear aerodynamic effects such as deep stall and their impact on flutter mechanisms and LCO amplitudes. Additionally, Sidlof et al. [59] characterized flow-induced vibration of a NACA 0015 airfoil using surface pressure sensors and synchronized high-speed Schlieren photography. They observed a flutter instability triggered by flow separation in which either damped oscillations or large amplitude dynamic stall flutter occurred depending on the size of the initial deflection.

As discussed above, the characterization of aeroelastic LCO has become an increasingly active area of research, especially in the context of undisturbed freestream conditions [60, 61, 62]. The effect of upstream flow disturbances on the kinematic behavior of wings undergoing LCO, however, has received less attention. In studies of nonlinear aeroelastic systems, researchers found that the wing response dynamics depend heavily on the inflow conditions. Poirel et al. [63] found that longitudinally turbulent inflow can decrease the stability of the system by reducing the flutter speed to a point lower than that for the non-excited case. In addition to reducing the flutter speed, the damping is also diminished for airspeed below the flutter point. In a numerical study of an aeroelastic airfoil with varying inflow, Venkatramani et al. [64] demonstrated intermittency, a phenomenon generally discussed in the context of nonlinear dynamical systems [65, 66]. Intermittency is characterized by an alternation between qualitatively different states, usually in the vicinity of a stability boundary. Venkatramani et al. [64] showed that fluctuations of the flow velocity over large time scales produced an "on-off" intermittency in which the system alternated between states of stability and instability about the flutter point. However, for shorter period velocity fluctuations, the system underwent amplitude-modulated oscillations without fully regaining stability.

The previously mentioned studies [63, 64] have considered effects of either isotropic turbulence or purely longitudinal freestream velocity fluctuations. Although useful conceptualizations, these conditions are rarely encountered outside of wind tunnel experiments or numerical simulations. Several studies in past decades have examined the effect of impinging Kármán vortex streets on downstream airfoils undergoing prescribed motion. These flow structures produce relatively high anisotropy and large-scale unsteadiness and therefore, are analogous to scenarios where the flow is disturbed by an upstream structure. A brief sample of the literature includes several investigations involving an oscillating wing downstream of a bluff body wake. Each of these experiments shared similar non-dimensional parameters to the present study (wing aspect ratio, ratio of bluff body/wing spacing to bluff body diameter ( $X/D$ ), ratio of bluff body diameter to wing chord ( $D/C$ ), and Reynolds number). One such study comes from Chen and Choa [67], who examined the effect of a wake shed from a cylindrical rod upstream of a NACA 0012 airfoil pitching upward at a constant rate and performed measurements of the unsteady forces acting on the airfoil. Chen and Choa [67] reported that the peak suction pressure at the leading edge of the airfoil with the cylinder placed upstream was increased by as much as 50% compared to the undisturbed case and that the peak suction was reached at a larger angle of attack. They attributed this effect to the upstream disturbance acting as a vortex generator that energizes the boundary layer, causing earlier turbulent transition and delayed separation of the dynamic stall vortex (DSV). Merrill and Peet [68] conducted a similar investigation regarding the effect of an impinging wake from a bluff body on the dynamic stall characteristics of a sinusoidally pitching airfoil using direct numerical simulation. They concluded that the impinging wake largely affects the forces and moments acting on the airfoil by altering the formation of vortex structures. For the conditions investigated, Merrill and Peet [68] concluded that dynamic stall for a pitching airfoil occurs later in the pitching cycle when in the presence of a turbulent wake due to the delayed formation and detachment of the DSV. Both of these studies were successful in identifying aerodynamic mechanisms of the impinging wake

structures; however, since the airfoils in both cases underwent prescribed motion, they do not reveal effects on the aeroelastic kinematics and dynamics. Additionally, Derakhshandeh et al. and Lau et al. [5, 8] explored the dynamics of an elastically mounted airfoil undergoing flow-induced vibration due to the wake from an upstream cylinder. Studies of forced vibrations provide valuable insight into the physics of wake-structure interaction; however, they fundamentally differ from the present study, which aims to characterize the effect of an impinging wake on a structure undergoing large amplitude self-excited vibration.

The aim of this chapter is to investigate the kinematic response of an aeroelastic wing system undergoing LCO in the presence of an impinging bluff body wake. This experiment is not designed to directly replicate a specific application, but rather to study fundamental interactions between a lifting body undergoing aeroelastic LCO and periodic freestream disturbances due to a vortical wake. Both the 2-DOF elastically mounted wing and the rectangular bluff body were chosen due to their well understood behaviors as individual test articles. Experiments are first conducted without the presence of an upstream bluff body to establish the baseline case. Then, tests with the bluff body positioned upstream are performed, varying two parameters: the bluff body shedding frequency, which is varied implicitly via the freestream velocity, and the streamwise distance between the bluff body and the wing.

## 4.2 Results and Discussion

### 4.2.1 LCO Response with Steady Inflow

A description of the experimental apparatus used in these experiments can be found in Chapter 3. The LCO response was first characterized without the presence of the upstream bluff body. Figure 4.1(a) and 4.1(b) show the mean LCO amplitude vs windspeed for heave and pitch, respectively. For each DOF, the mean amplitude is defined by taking the mean of the set of upper peaks from the corresponding position signal.

In Figure 4.1, we see that LCO onset occurs at approximately 6 m/s for this configuration. This low onset was prescribed by the selection of appropriate pitch and heave stiffness as well as center of mass location in order to best utilize the wind tunnel facility. That is, the wind-off natural frequency of the pitch and heave DOF were designed to be close together in order to achieve coalescence of the two modal frequencies at a lower windspeed. Note that the LCO onset windspeed does not necessarily correspond to the flutter boundary predicted by a linear analysis. For example, the P-K method with Theodorsen aerodynamics is a robust means of predicting aeroelastic flutter with several simplifying assumptions, however it fails to predict the existence of nonlinear attractors that may exist below the linear flutter boundary. Based on experimental observation, the present system undergoes a subcritical Hopf bifurcation in which LCO can be achieved at windspeeds far below the predicted flutter onset via sufficiently large initial conditions which bring the system from a stable equilibrium, past an unstable limit cycle, and onto a larger, stable limit cycle [69]. This concept was explored by Schwartz et al. [70] who showed that LCO could be triggered below the linear flutter speed either by a sufficiently large perturbation which surpasses the subcritical branch or through a by-pass transition in which an initially small perturbation is amplified in a process known as transient growth. For aeroelastic systems which undergo a supercritical Hopf bifurcation, instabilities often do not exist below the linear stability boundary but LCO may appear above it, resembling classical flutter but with bounded amplitude [71]. In this case, LCO cannot be initiated

below the flutter boundary via large initial perturbation as in the subcritical system.

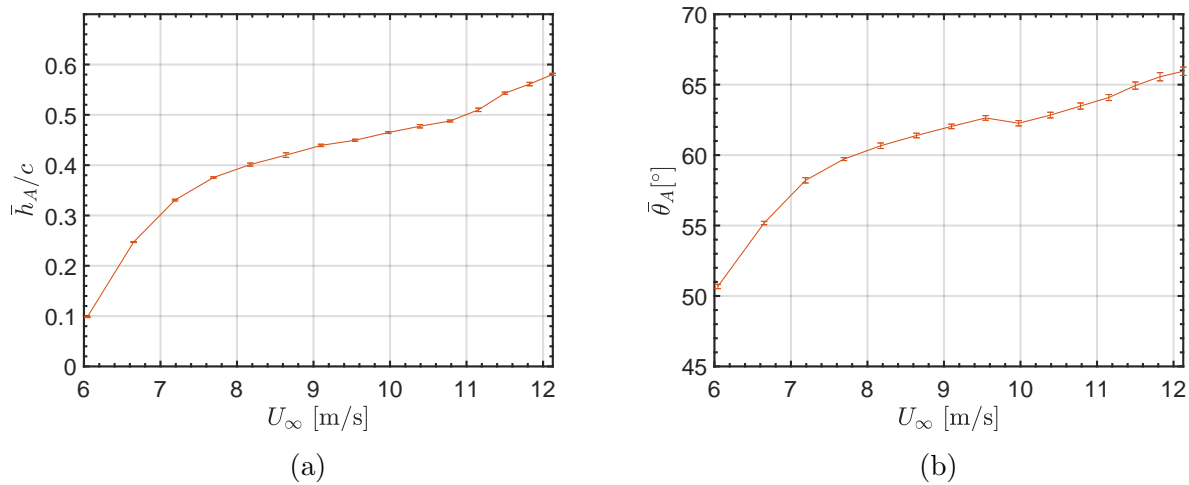


Figure 4.1: (a) Non-dimensional mean heave amplitude and (b) mean pitch amplitude vs windspeed for no-bluff-body case. Error bars represent one standard deviation.

From Figure 4.1, it is seen that the LCO amplitude increases with windspeed with small error bars indicating nearly constant amplitude during each test point. Due to the similarity in the amplitude vs. windspeed trends for the pitch and heave responses, the remainder of the analysis in this chapter will focus primarily on the response of the pitch DOF for brevity. The pitch angle time histories for a set of windspeeds are presented in Figure 4.2. These plots provide a time-domain visualization of the relative uniformity of the LCO amplitude in terms of cycle-to-cycle deviation. Note that the top-left subplot of Figure 4.2 ( $U_\infty = 6.6$  m/s) shows a typical 5 second zoomed-in view for clearer visualization of the LCO waveform.

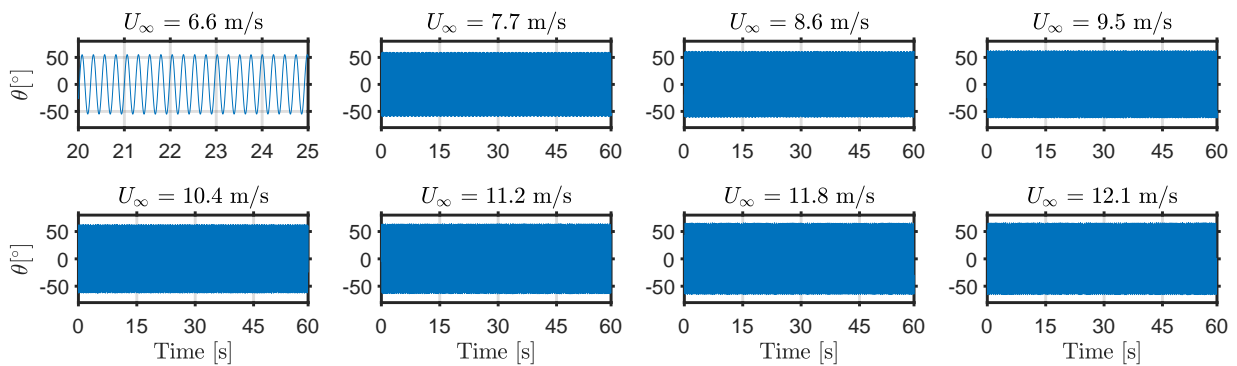


Figure 4.2: Pitch angle time histories for no-bluff-body case.

As shown in Figure 4.3(a), the fundamental LCO frequency is approximately equal to 4 Hz and is invariant with windspeed within 2%. The dominant frequency for each windspeed was determined via FFT with a frequency resolution of  $\Delta f = 1/N\Delta t = 0.017$  Hz where  $N\Delta t$  is the total sampling time of 60 seconds. The frequency curves for the pitch and heave degrees of freedom lie on top of each other which is characteristic of LCO initiated by a modal convergence flutter instability.

The average phase difference between pitch and heave position ( $\bar{\phi}_{\theta,h}$ ) was calculated using cross correlation and is shown in Figure 4.3(b). We see that for this configuration,  $\bar{\phi}_{\theta,h}$  trends from 15 degrees (pitch-leading) to 0 degrees (in-phase).

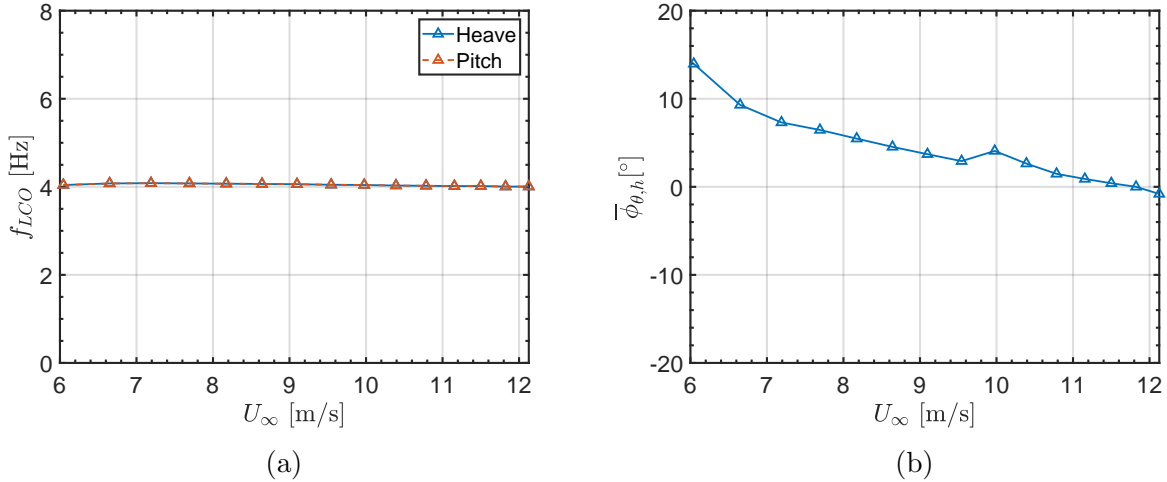


Figure 4.3: (a) Fundamental LCO frequency for pitch and heave DOF vs windspeed and (b) mean pitch-heave phase difference vs windspeed for no-bluff-body case.

Exploring the frequency content of these responses via their power spectral densities (PSD) (Figure 4.4) reveals that in addition to the fundamental frequency peaks, there exist both even and odd superharmonics which are characteristic of nonlinear oscillations. For increasing windspeed, the fundamental frequency of oscillation remains constant.

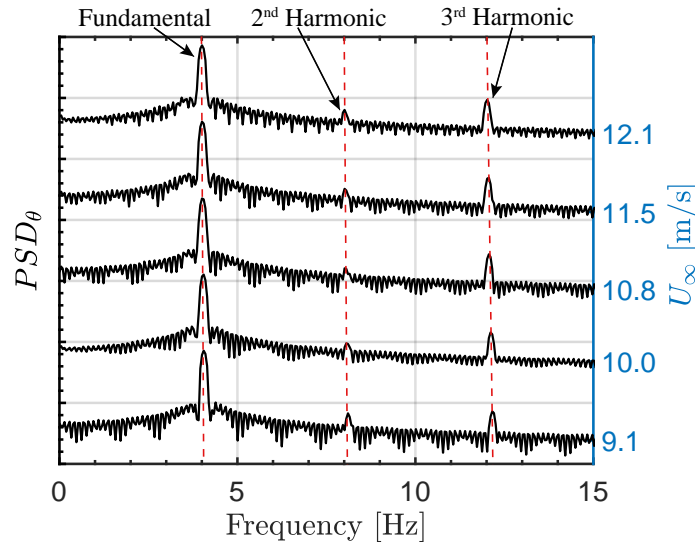


Figure 4.4: Pitch angle PSD plotted vs windspeed for no-bluff-body case (PSD magnitude = arbitrary log scale)

## 4.2.2 LCO Response with Disturbed Inflow

### 4.2.2.1 Amplitude Modulation and LCO Superharmonic Frequency Analysis

The equations of motion for the aeroelastic system are derived in [72]. Here, it is shown that nonlinearities are introduced to the system through the pitch stiffness, nonlinear coupling between the pitch and heave DOF, and the aerodynamics. While the system response in clean inflow conditions showed classical constant-amplitude LCO (Figure 4.2), nonlinearities can result in more complex dynamics when a system is introduced to external disturbances. For example, a 1-DOF linear system exhibits a single resonance when the forcing frequency matches the natural frequency of the system, while in a nonlinear system, subharmonic and superharmonic resonances can exist [73].

For the present system, the bluff body shedding frequency is close to three times the fundamental LCO frequency. In order to investigate the effects of wing-wake frequency interaction, the ratio  $f_{shed}/f_{LCO}$  is defined as the independent variable for each test case. Figure 4.5 presents pitch angle time histories, spanning the range of windspeeds tested, for  $X_b/D = 4.3$ . For windspeeds corresponding to  $f_{shed}/f_{LCO} \leq 2.9$ , the deviation in LCO amplitude is relatively small compared to the mean amplitude. However, as the bluff body shedding frequency migrates closer to  $3f_{LCO}$ , the intensity of the amplitude modulation increases. As the windspeed is increased further, the shedding frequency surpasses  $3f_{LCO}$  and for  $f_{shed}/f_{LCO} > 3.1$ , the modulation intensity diminishes again. This symmetry about  $f_{shed}/f_{LCO} = 3$  indicates that the bluff body shedding frequency, rather than the freestream windspeed, dominates the LCO response in this regime.

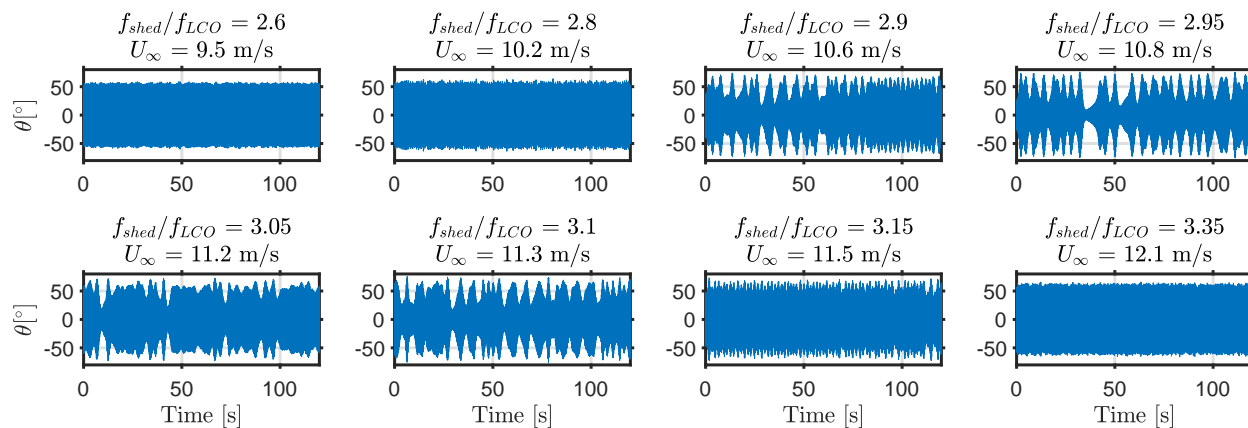


Figure 4.5: Pitch angle time histories for  $X_b/D = 4.3$  case.

The frequency content for a set of responses with the bluff body positioned at  $X_b/D = 4.3$  is provided in Figure 4.6. Similar to the PSDs for the no-bluff-body case in Figure 4.4, the peaks representing the fundamental and superharmonic frequencies are present, however, with the addition of a peak corresponding to the bluff body shedding frequency. The shedding frequency increases linearly from 9.5 Hz to 13.5 Hz with windspeed, following the expected trend for a Strouhal number of 0.085 [55]. The shedding frequency that appears in the PSD also matches the dominant frequency in the PSD of the bluff body load cell data. Additionally, there are two sideband peaks which are symmetric about the fundamental frequency. These sidebands are characteristic of amplitude-

modulated signals and here, the frequency difference between the fundamental frequency and one of the sideband peaks is equal to the modulation frequency.

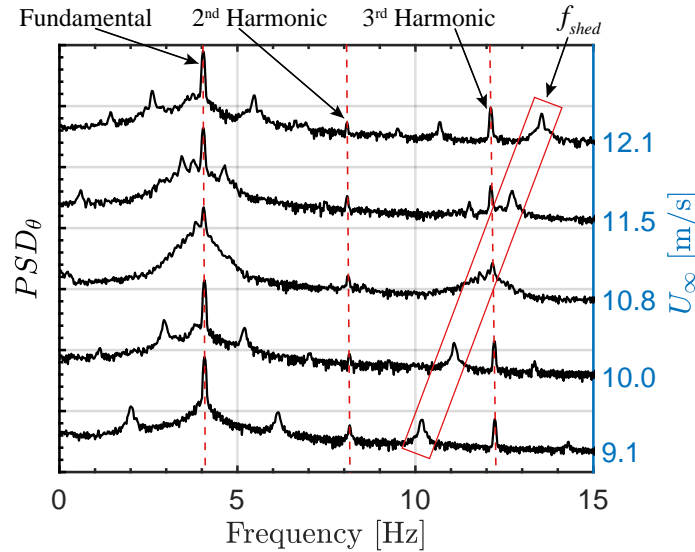


Figure 4.6: Pitch angle PSD plotted vs windspeed for  $X_b/D = 4.3$  case (PSD magnitude = arbitrary log scale)

#### 4.2.2.2 Quantification of LCO Amplitude and Amplitude Modulation Intensity

Figure 4.5 qualitatively illustrates the system's windspeed-dependent (and therefore shedding frequency-dependent) response. To quantify this behavior, Figure 4.7 presents amplitude distribution plots in which the set of peak pitch displacements, i.e. the pitch amplitudes, for each windspeed are overlaid. For the bluff body cases (Figures 4.7(b), 4.7(c), 4.7(d)) there is an additional horizontal axis with the corresponding  $f_{shed}/f_{LCO}$ . Note that the darker shaded regions correspond to a tighter grouping of amplitudes while the lighter regions represent more disperse amplitudes. Figure 4.7(a) shows the no-bluff-body amplitude response in which the pitch amplitude increases with windspeed with tight groupings indicating a constant pitch amplitude. Figure 4.7(b), contains the pitch amplitudes for the case where  $X_b/D = 6.5$ . Here, the trend resembles Figure 4.7(a) for sufficiently low values of  $f_{shed}/f_{LCO}$ ; i.e., the mean amplitude increases with windspeed and the individual cycle amplitudes are tightly grouped. However, this trend is interrupted as the bluff body shedding frequency nears  $3f_{LCO}$ . For values of  $f_{shed}/f_{LCO}$  close to three, the dispersion in pitch amplitude increases significantly. A similar behavior is exhibited by the case shown in Figure 4.7(c) in which  $X_b/D = 5.6$ ; however, here there is a stronger influence from the bluff body, causing the cycle amplitude to drop below 20 degrees at its minimum. Figure 4.7(d), in which the bluff body is in the closest upstream position ( $X_b/D = 4.3$ ), shows a significant disruption in the pitch amplitude trend with cycle amplitudes ranging between approximately 10 and 75 degrees as the systems nears  $f_{shed}/f_{LCO} = 3$ .

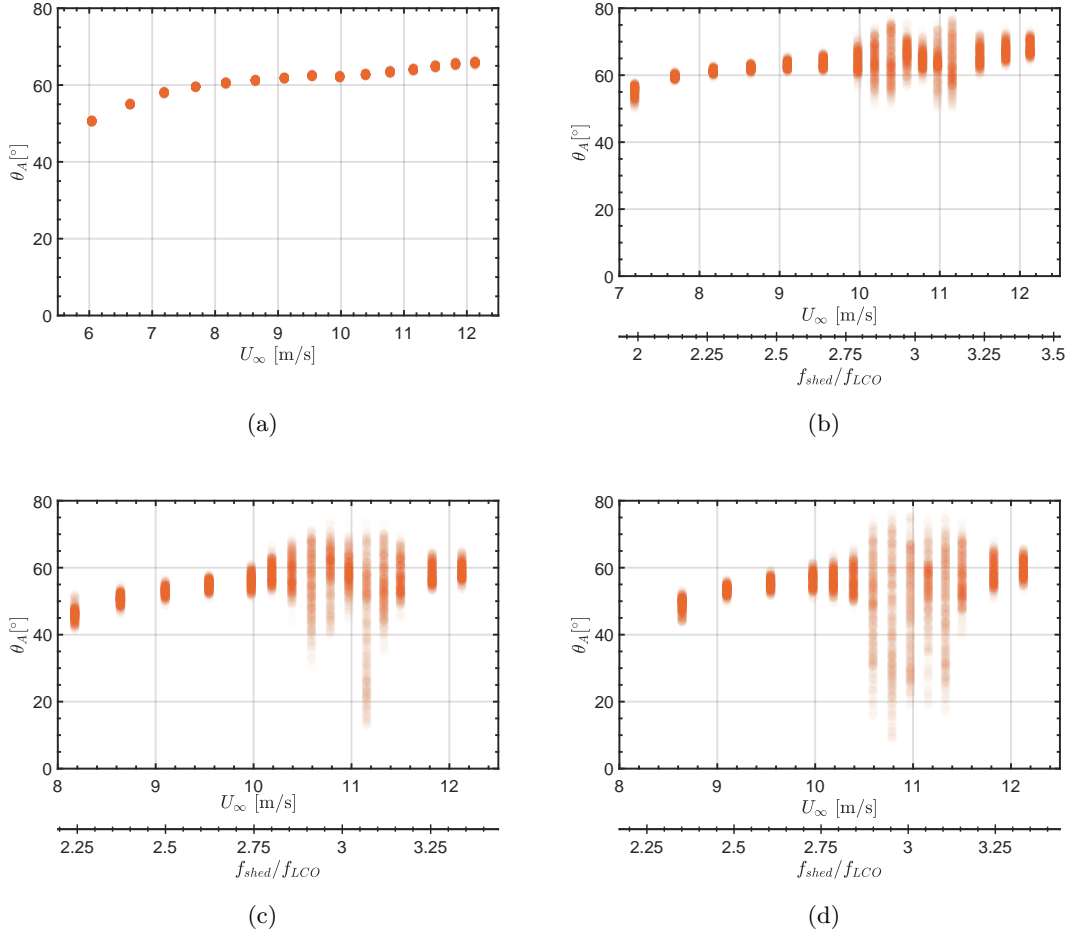


Figure 4.7: Pitch amplitude distributions for (a) no-bluff-body, (b)  $X_b/D = 6.5$ , (c)  $X_b/D = 5.6$ , (d)  $X_b/D = 4.3$ .

In Figure 4.8, the amplitude modulation intensity is quantified via the coefficient of variation (CV) or the standard deviation of amplitude divided by the mean. The CV serves as a measure of dispersion in LCO amplitude or how heavily the amplitude is modulated at a given point in time. The local mean and standard deviation were obtained by dividing the time history into 10 second windows and interpolating to produce the contours seen in Figure 4.8. Figure 4.8(a) shows a uniformly small CV across the time and windspeed domains on the order  $1 \times 10^{-3}$ , reflecting a non-modulated, steady LCO. For the bluff body cases, for windspeeds in which  $f_{shed}/f_{LCO}$  was not close to an integer value, the LCO exhibited a relatively small degree of amplitude modulation, similar to the no-bluff-body case. However, as  $f_{shed}$  approaches and passes through the third harmonic of  $f_{LCO}$ , the system exhibits a drastic change in behavior. The system returns to a relatively low modulation intensity for  $f_{shed}/f_{LCO} \geq 3.2$ , demonstrating the frequency-dominated nature of the phenomenon. This effect is reflected in Figure 4.8(b) which shows two distinct bands of increased modulation intensity on either side of the  $f_{shed}/f_{LCO} = 3$  line. These regions of increased CV correspond directly to the regions of increased pitch amplitude dispersion from Figure 4.7(b). Similar behavior is exhibited in Figures 4.8(c) and 4.8(d), however with increased modulation intensity for decreased  $X_b/D$ . The global maximum CV increased 300% between Figures 4.8(b)

and 4.8(c) and 530% between Figures 4.8(b) and 4.8(d). Additionally, as the distance  $X_b/D$  decreases, the modulation intensity becomes more time-dependent in the  $f_{shed}/f_{LCO} \approx 3$  regime.

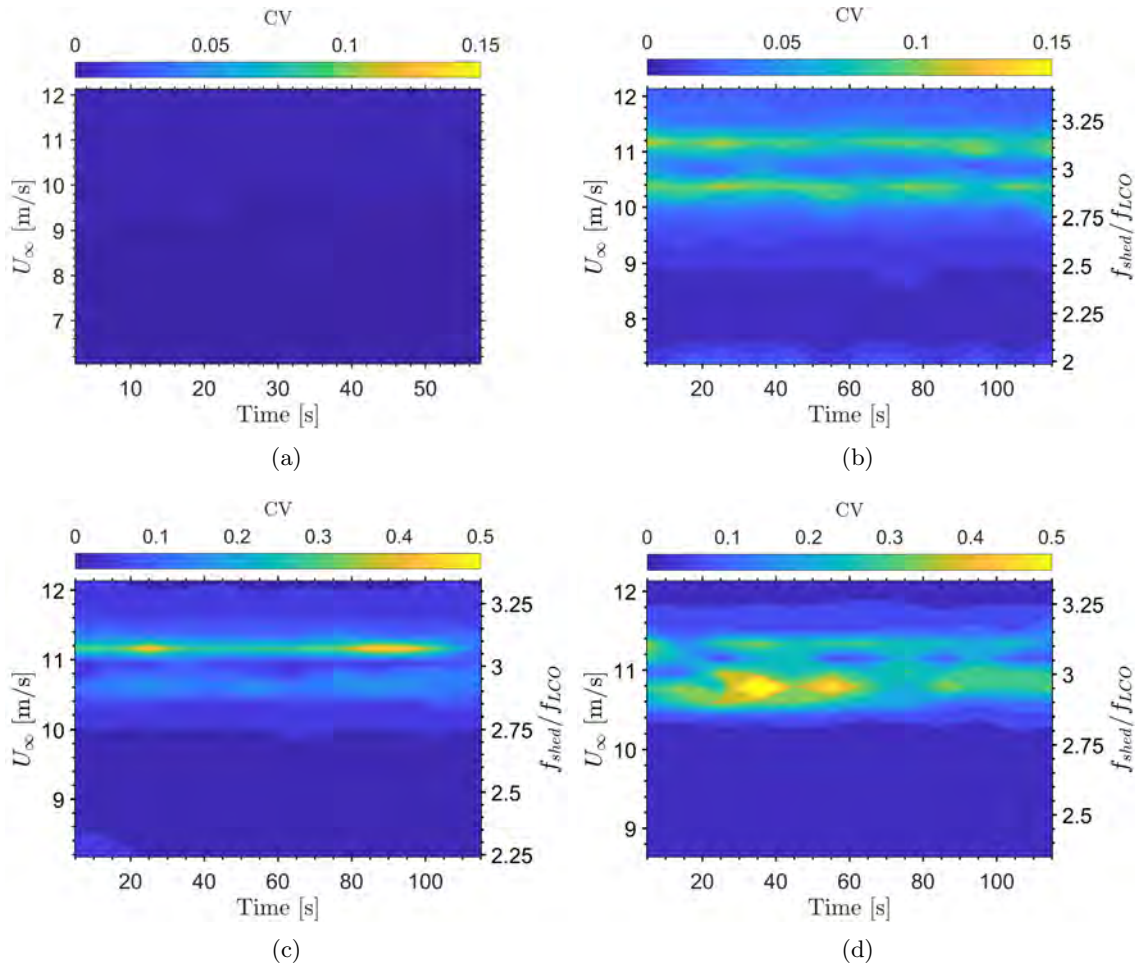


Figure 4.8: Pitch amplitude CV contours for (a) no-bluff-body, (b)  $X_b/D = 6.5$ , (c)  $X_b/D = 5.6$ , (d)  $X_b/D = 4.3$ .

#### 4.2.2.3 Time-frequency Analysis of LCO Modulation

Further characterization of the LCO amplitude modulation was performed via a time-frequency wavelet analysis of the LCO envelope. The envelope is defined as a spline interpolation over the positive peaks of the LCO signal. The continuous wavelet transform (CWT) of the LCO envelope is shown as a series of scalograms which illustrate the evolution of the modulation frequency over time.

Figure 4.9 contains the CWTs and time histories corresponding to  $f_{shed}/f_{LCO} = 2.8$  for the three bluff body positions (a)  $X_b/D = 6.5$ , (b)  $X_b/D = 5.6$ , (c)  $X_b/D = 4.3$ . In this regime, where  $f_{shed}/f_{LCO}$  is sufficiently far from an integer value, the distance  $X_b/D$  has little influence on neither the modulation intensity nor the modulation frequency. The intensity of the modulation for the three bluff body positions is uniform with respect to time and the dominant modulation frequency is approximately 0.9 Hz. By examining the PSD of the pitch angle time history for  $X_b/D = 4.3$

(Figure 4.6), we see that the LCO third harmonic frequency is 12.2 Hz and the shedding frequency is equal to 11.3 Hz. The difference between these two frequencies ( $f_{shed} - 3f_{LCO}$ ) is equal to the modulation frequency found in Figure 4.9(c), indicating behavior analogous to a beat phenomenon except that the interaction is with a harmonic frequency rather than the fundamental. Extending the same analysis to the other configurations (Figures 4.9(a) and 4.9(b)), the modulating frequency is equal to  $f_{shed} - 3f_{LCO}$  in both cases.

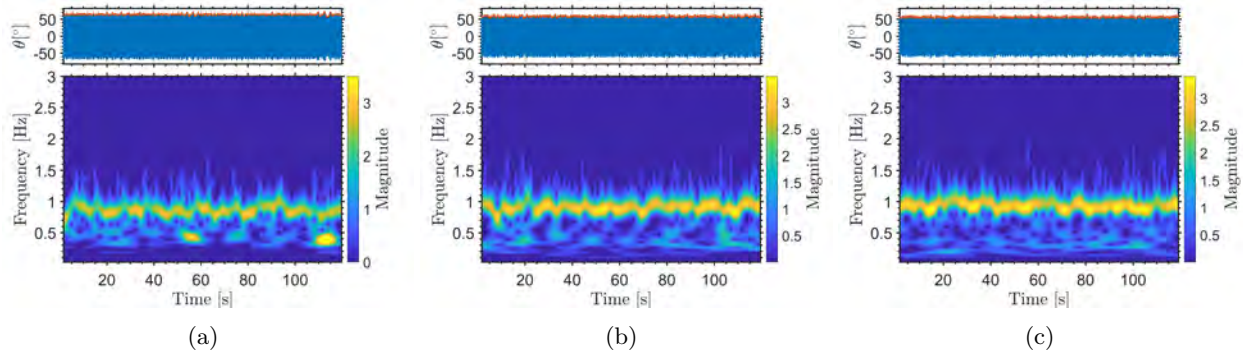


Figure 4.9: Time-frequency content of pitch angle envelope (bottom) with corresponding pitch angle time history (top) for (a)  $X_b/D = 6.5$ , (b)  $X_b/D = 5.6$ , and (c)  $X_b/D = 4.3$  where  $f_{shed}/f_{LCO} = 2.8$ .

Figure 4.10 contains envelope CWTs and pitch angle time history plots for  $f_{shed}/f_{LCO} = 2.9$ . Figure 4.10(a) shows an amplitude modulation that is relatively uniform in intensity and frequency with a dominant modulation frequency equal to  $f_{shed} - 3f_{LCO}$ . Compared to Figure 4.9(a), the modulation is lower in frequency due to the smaller difference between  $3f_{LCO}$  and  $f_{shed}$ . When the bluff body is moved to  $X_b/D = 5.6$  (Figure 4.10(b)),  $f_{shed} - 3f_{LCO}$  is still present in the envelope CWT, however it is no longer the only modulation frequency. In this case, the LCO response alternates between two modulation modes, represented by the two dominant modulation frequencies seen in the envelope CWT. Further evidence of this is provided by Figure 4.10(c) in which  $X_b/D = 4.3$  and the two modes are even more pronounced. Among the two distinct modulation modes present, the first is a low frequency mode that persists during the first 60 seconds of the trial and causes a relatively intense modulation of the LCO amplitude. The second is a higher frequency mode representing  $f_{shed} - 3f_{LCO}$  which dominates between  $t = 80$  sec. and  $t = 120$  sec. and produces a less intense modulation. Figure 4.10(c) also shows transient period between the two modes ( $t = 60$  sec. to  $t = 80$  sec.) in which neither frequency dominates entirely.

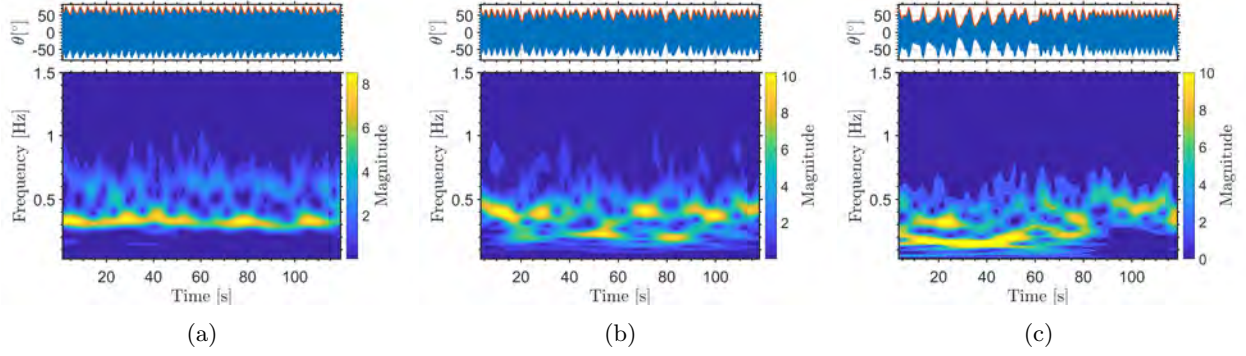


Figure 4.10: Time-frequency content of pitch angle envelope (bottom) with corresponding pitch angle time history (top) for (a)  $X_b/D = 6.5$ , (b)  $X_b/D = 5.6$ , and (c)  $X_b/D = 4.3$  where  $f_{shed}/f_{LCO} = 2.9$ .

The pitch angle time histories and envelope CWTs for  $f_{shed}/f_{LCO} = 3.1$  are shown in Figure 4.11. Here, the system exhibits responses similar to the case in Figure 4.10 where  $f_{shed}/f_{LCO} = 2.9$ . The amplitude modulation is uniform in frequency and intensity for  $X_b/D = 6.5$  with a dominant modulation frequency equal to  $f_{shed} - 3f_{LCO}$  (Figure 4.11(a)). For the case of  $X_b/D = 5.6$ , the modulation becomes less uniform, with lower frequency content appearing sporadically throughout the time history (Figure 4.11(b)). For the case of  $X_b/D = 4.3$ , the low frequency modulation dominates the signal along with the  $f_{shed} - 3f_{LCO}$  (Figure 4.11(c)). Referencing Figure 4.7(d), it is clear that the cause of the large amplitude dispersion corresponds due to the lower frequency mode. Comparing Figure 4.11(c) to Figure 4.10(c), the switching between the two primary modulation modes does not occur over a consistent period, as evidenced by a more rapid alternation between modes seen in Figure 4.11(c).

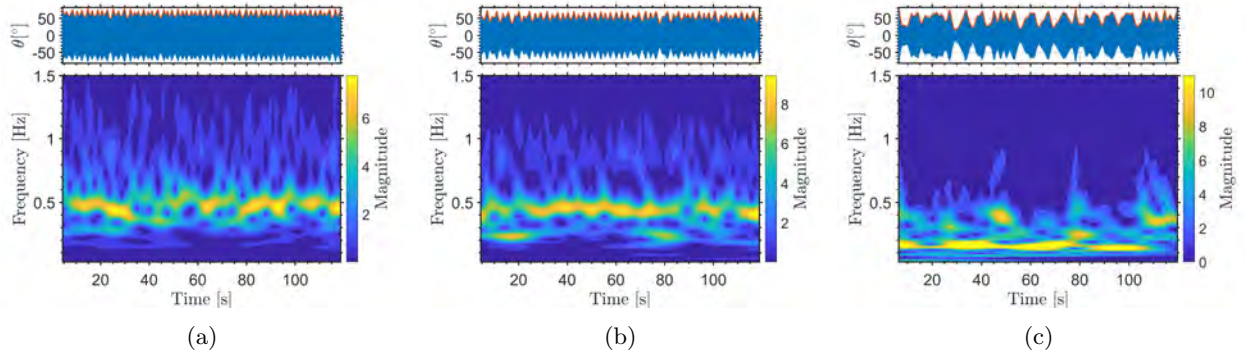


Figure 4.11: Time-frequency content of pitch angle envelope (bottom) with corresponding pitch angle time history (top) for (a)  $X_b/D = 6.5$ , (b)  $X_b/D = 5.6$ , and (c)  $X_b/D = 4.3$  where  $f_{shed}/f_{LCO} = 3.1$ .

As discussed previously, the amplitude CV decreases as  $f_{shed}$  increases sufficiently past  $3f_{LCO}$ , demonstrating that the order of magnitude of the intensity of modulation is symmetric about  $3f_{LCO}$ . Figure 4.12 shows how this symmetry is also reflected in the frequency of the modulation. Figures 4.9 and 4.12 both show a low intensity modulation with a dominant modulation frequency equal to  $f_{shed} - 3f_{LCO}$ , that is invariant with respect to bluff body position.

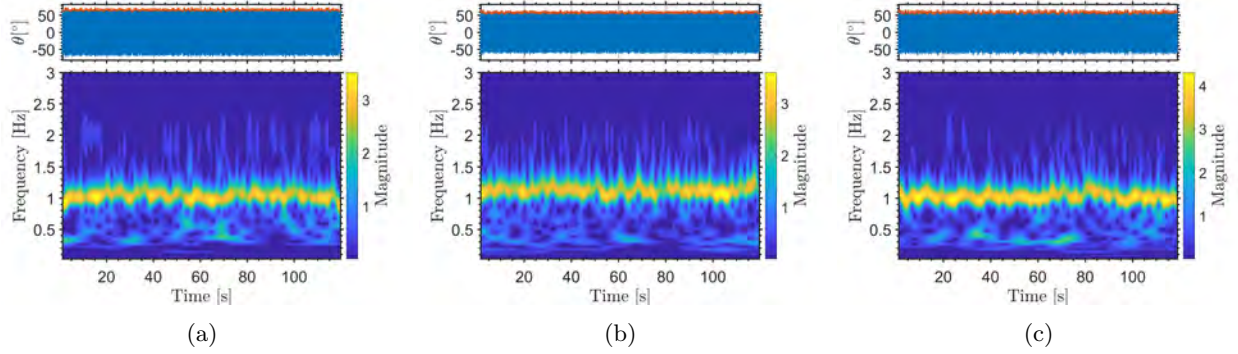


Figure 4.12: Time-frequency content of pitch angle envelope (bottom) with corresponding pitch angle time history (top) for (a)  $X_b/D = 6.5$ , (b)  $X_b/D = 5.6$ , and (c)  $X_b/D = 4.3$  where  $f_{shed}/f_{LCO} = 3.25$ .

#### 4.2.2.4 Instantaneous Phase and Aeroelastic Energy Analysis

The efficiency of aeroelastic systems is often discussed in literature in the context of energy harvesting and bio-inspired vehicle locomotion. Several studies that have examined the efficiency of pitch-heave aeroelastic systems have concluded that the phase angle difference between the two degrees of freedom is an important parameter for predicting efficiency. Anderson et al. [74] conducted an experiment in which the propulsive efficiency of an airfoil undergoing prescribed motion was determined as a function of the phase angle between heave and pitch. They found the optimal phase angle for propulsion to be about 75 degrees since this condition produces favorable timing of the leading edge vortex (LEV) shedding, facilitating the formation of a thrust-producing reverse Kármán street. Similarly, McKinney and DeLaurier [75] found that a phase angle of about 90 degrees is optimally efficient for power extraction in a pitching-heaving aeroelastic system. Here, efficiency is defined as the ratio of the total power extracted to the total power available in the oncoming flow passing through the swept area normal to the mean wind vector. Later, Kinsey and Dumas [76] showed that LEV shedding is an important mechanism by which favorable synchronization is achieved between the lift force and the heaving velocity, thus controlling the power input to the system.

In order to examine the influence of the bluff body in this context, we begin by performing a phase plane analysis of the LCO. Figure 4.13 contains the pitch-heave displacement phase portraits for (a) no-bluff-body ( $U_\infty = 10.4m/s$ ) and (b)  $X_b/D = 6.5$ , (c)  $X_b/D = 5.6$ , and (d)  $X_b/D = 4.3$  for similar windspeed ( $f_{shed}/f_{LCO} = 2.9$ ). In Figure 4.13(a), the no-bluff-body motion trajectory maintains little deviation from the closed orbit defined by the thin ellipse. This is in contrast to the trajectories for the three bluff body cases (Figures 4.13(b), 4.13(c), 4.13(d)) in which the paths overlap and fill a large portion of the phase space.

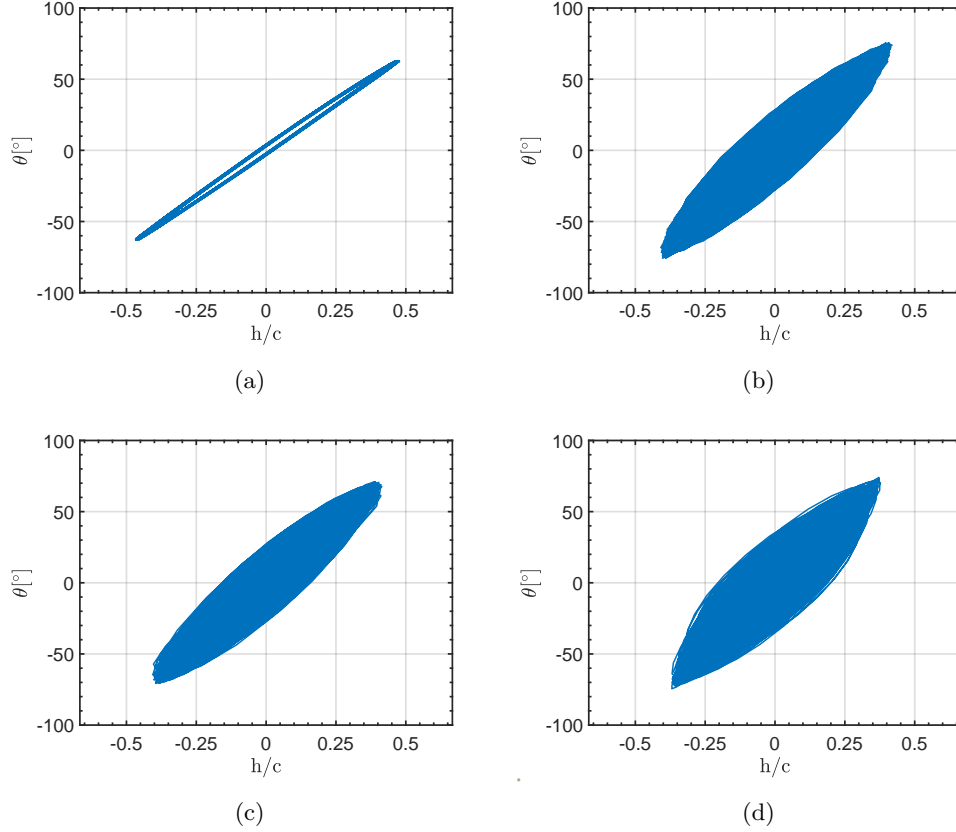


Figure 4.13: Pitch-heave phase portraits for (a) no-bluff-body ( $U_\infty = 10.4\text{m/s}$ ) and (b)  $X_b/D = 6.5$ , (c)  $X_b/D = 5.6$ , and (d)  $X_b/D = 4.3$  ( $f_{shed}/f_{LCO} = 2.9$ ).

Since the phase portraits shown in Figure 4.13 contain the entire time history of the LCO, it is difficult to gain a detailed understanding of how the phase space trajectory evolves with time. To determine the phase angle difference as a function of time, the instantaneous pitch-heave phase difference,  $\phi_{\theta,h}$ , was calculated as a function of time via the discrete-time analytic signal which is a complex-valued function comprised of the real-valued LCO signal and its Hilbert transform. The algorithm used for computing the analytic signal of a discrete function is described by Marple [77]. The form of the analytic signal is:

$$z(t) = z_r(t) + iz_i(t) = x(t) + HT[x(t)] \quad (1)$$

where  $z_r(t)$  is the real component of  $z(t)$ ,  $z_i(t)$  is the imaginary component of  $z(t)$ ,  $x(t)$  is the original signal and  $HT[\cdot]$  is the Hilbert transform operation. Next, the instantaneous phase angle is computed as follows:

$$\phi(t) = \arctan \frac{z_i(t)}{z_r(t)} \quad (2)$$

where  $\phi(t)$  is the instantaneous phase angle. For this system, the instantaneous phase difference between pitch and heave is calculated as the difference  $\phi_{\theta,h} = \phi(t)_{pitch} - \phi(t)_{heave}$ .

Figure 4.14 shows  $\phi_{\theta,h}$  for the same four configurations displayed in Figure 4.13. Figure 4.14(a) demonstrates that the instantaneous phase difference  $\phi_{\theta,h}$  is constant within 1.5 degrees in the

absence of an upstream bluff body. Figures 4.14(b), 4.14(c), and 4.14(d) show significant modulation of  $\phi_{\theta,h}$  that occurs as the wing oscillates through the bluff body wake. The modulation of  $\phi_{\theta,h}$  creates a path through the phase space that is time-dependent when the bluff body is upstream. This is qualitatively reflected by the phase portraits in Figure 4.13. Note that the frequency of the  $\phi_{\theta,h}$  modulation is dependent on the bluff body spatial configuration. For the case where  $X_b/D = 6.5$  (Figure 4.14(b)), the phase difference oscillates at a frequency equal to  $f_{shed} - 3f_{LCO}$  for all time shown. For both the  $X_b/D = 5.6$  and  $X_b/D = 4.3$ , (Figures 4.14(c) and 4.14(d), respectively) the frequency of phase modulation is not uniform with time. Comparing the frequency of the phase modulation in both cases to their respective amplitude modulation frequencies (Figures 4.10(b)) and 4.10(c)), we find that they are equal. Also, note that the time periods of intense  $\phi_{\theta,h}$  modulation ( $t = 0$  sec to  $t = 60$  sec) seen in Figure 4.14(d) correspond directly to the time periods of intense amplitude modulation seen in Figure 4.10(c). Conversely, the time period of low intensity phase modulation ( $t = 80$  sec to  $t = 120$  sec) corresponds to the period of low intensity amplitude modulation, indicating a correlation between the magnitude of the phase difference  $\phi_{\theta,h}$  and the LCO amplitude.

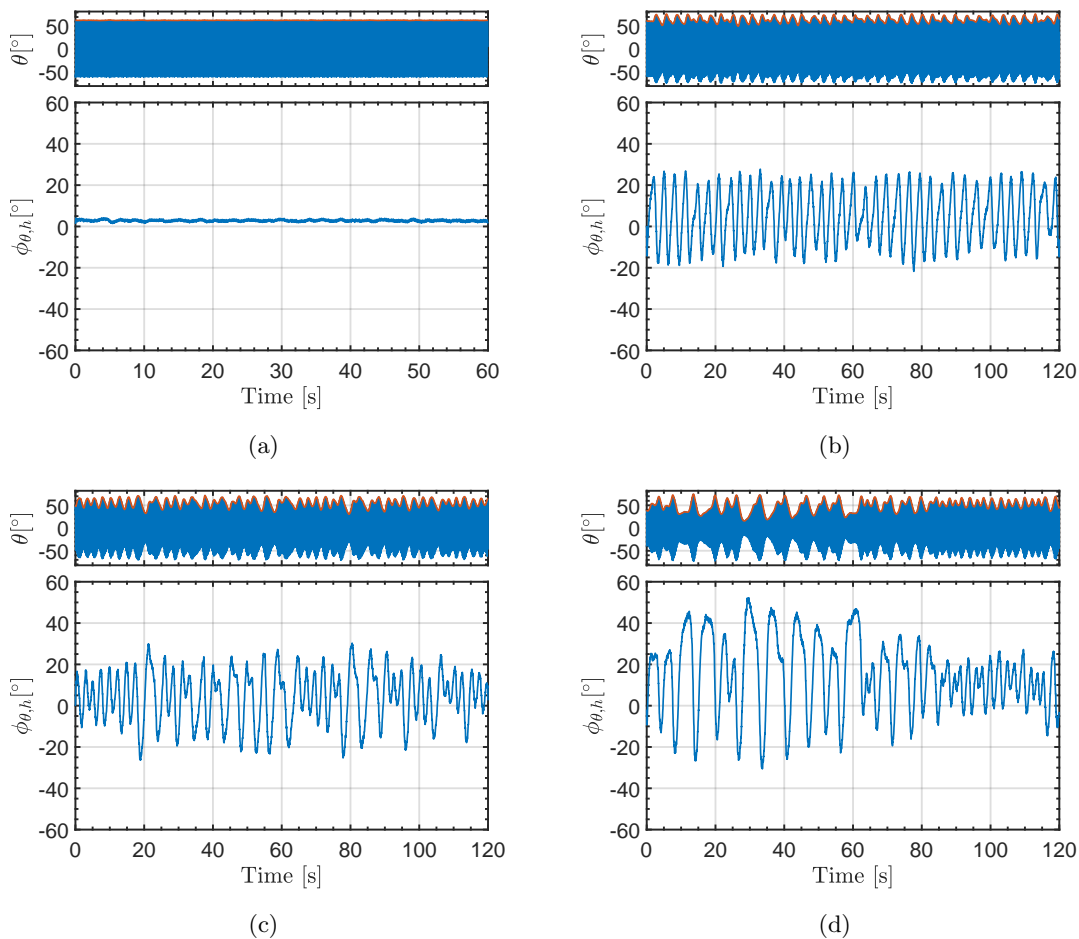


Figure 4.14:  $\theta$  (top) and  $\phi_{\theta,h}$  (bottom) vs. time for (a) no-bluff-body ( $U_\infty = 10.4m/s$ ) and (b)  $X_b/D = 6.5$ , (c)  $X_b/D = 5.6$ , and (d)  $X_b/D = 4.3$  ( $f_{shed}/f_{LCO} = 2.9$ ).

A phase portrait is shown in Figure 4.15, depicting the phase relationship between  $\phi_{\theta,h}$  and the

LCO amplitude. The orange trajectory represents the no-bluff-body configuration from Figure 4.14(a) and shows that there is an insignificant change in either  $\phi_{\theta,h}$  or the pitch amplitude ( $\theta_A$ ) with time. The blue curve represents the  $X_b/D = 6.5$  case from Figure 4.14(b) and shows a strong correlation between  $\phi_{\theta,h}$  and  $\theta_A$ . The phase portrait maintains an elliptical shape, with the arrow indicating the direction of time. When read in the counterclockwise direction, this plot shows that  $\phi_{\theta,h}$  leads  $\theta_A$  by approximately 90 degrees.

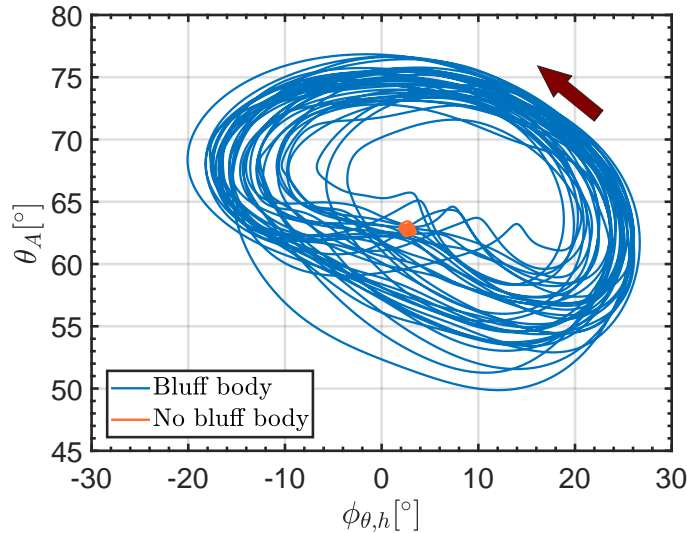


Figure 4.15: Phase portrait of  $\theta_A$  vs  $\phi_{\theta,h}$  vs. for no-bluff-body ( $U_\infty = 10.4m/s$ ) and  $X_b/D = 6.5$  ( $f_{shed}/f_{LCO} = 2.9$ ).

The previously mentioned studies [74, 75, 76] focused primarily on the wing efficiency for the purposes of exploiting the dynamics to extract power from the structure. However, since the aeroelastic system in the present study is not designed for energy harvesting, any net power into the structure manifests as a change in the kinematics. For the case of a constant amplitude aeroelastic LCO, the net aerodynamic work is balanced by the losses due to structural forces over a given cycle. Thus, it follows that the average net power over a cycle is equal to zero. This differs from the conditions in which the average net power over a cycle is either positive or negative, where the amplitude will grow or decay, respectively. For the present system, the available power is considered to be constant for a fixed freestream windspeed and the bluff body alters the distribution of kinetic energy in the flowfield. Therefore, any net power into the structure must be due to a change in aeroelastic efficiency. We define the total mechanical energy of the aeroelastic system,  $E$ , as the sum of the kinetic and potential energy,  $T + U$ . From this definition, the net work done on the structure ( $W_{net}$ ) includes contributions from the aerodynamics ( $W_A$ ) and the structural damping ( $W_D$ ) and is defined as:

$$W_{net} = W_A - W_D = T + U - E_0 \quad (3)$$

where  $E_0$  is the initial energy of the wing at the  $t = 0$  reference point for the aerodynamic and damping work. This definition can be expanded by incorporating the definitions for  $T$  and  $U$  for

this system, previously derived by Kirschmeier et al. [72]:

$$W_{net} = \frac{1}{2}m_T\dot{h}^2 + \frac{1}{2}I_\theta\dot{\theta}^2 - m_Wbx_\theta\dot{h}\dot{\theta}\cos\theta + \frac{1}{2}K_h h^2 + \int_0^\theta M_\theta(\theta)d\theta - E_0 \quad (4)$$

where  $M_\theta(\theta)$  is the function defining the pitch nonlinearity. Next, the net instantaneous power is calculated as the numerical time derivative of work via a central difference scheme:

$$P_{net}(t_i) \approx \frac{W_{net}(t_i + \Delta t) - W_{net}(t_i - \Delta t)}{2\Delta t} \quad (5)$$

where  $\Delta t$  is the sampling period. Since we are interested in power on the time scale of the amplitude modulation rather than the intracycle power, the mean power over a cycle ( $\bar{P}_{net}$ ) is calculated by applying a central moving average to the instantaneous power:

$$\bar{P}_{net}(t_i) = \frac{1}{N} \sum_{j=-\frac{1}{2}(N-1)}^{\frac{1}{2}(N-1)} P_{net}(t_{i+j}) \quad (6)$$

where  $N$  is size of the sliding window which is set to cover a single wing cycle period (0.25 sec via PSD) and  $t_i$  is the  $i^{th}$  data point.

Figure 4.16(a) shows  $\phi_{\theta,h}$  and  $\bar{P}_{net}$  as functions of time for the  $X_b/D = 6.5$ ,  $f_{shed}/f_{LCO} = 2.9$  case. We see that  $\bar{P}_{net}$  oscillates at the same frequency as both  $\phi_{\theta,h}$  and the LCO amplitude. Also,  $\phi_{\theta,h}$  and  $\bar{P}_{net}$  are in phase with each other; i.e., maximum  $\phi_{\theta,h}$  corresponds to maximum  $\bar{P}_{net}$ . Note that this is in contrast to Figure 4.15 where  $\phi_{\theta,h}$  leads  $\theta_A$  by approximately 90 degrees. This result makes sense when we consider that  $\bar{P}_{net}$  is the time derivative of the average total energy,  $\bar{E}$ . That is, maximum and minimum  $\phi_{\theta,h}$  correspond to the maximum rates of amplitude increase and decrease, respectively, as seen in (Figure 4.16(b)).

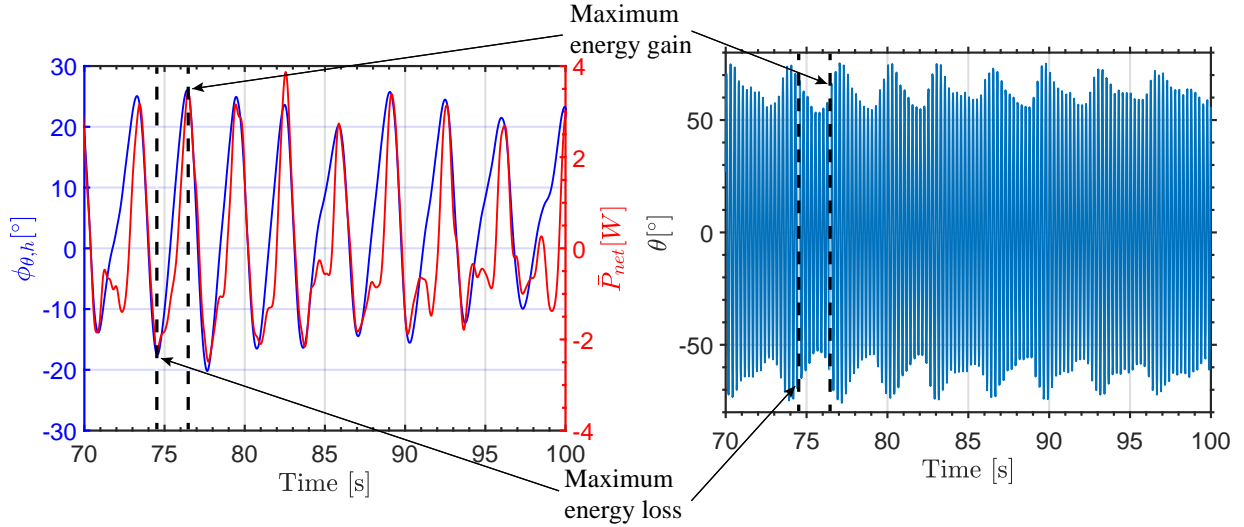


Figure 4.16: (a) left:  $\phi_{\theta,h}$  and  $\bar{P}_{net}$  vs time and (b) right:  $\theta_A$  vs time for  $X_b/D = 6.5$ ,  $f_{shed}/f_{LCO} = 2.9$  case.

### 4.3 Interim Conclusions

The aim of this research is to elucidate the complex interactions between a nonlinear aeroelastic wing and an oscillating wake shed from an upstream bluff body. The main conclusions stem from the characterization of LCO amplitude modulation and can be summarized as follows:

1. The cases in which the bluff body was present showed amplitude-modulated responses in both the pitch and heave degrees of freedom. The intensity of this modulation, defined by the coefficient of variation of the amplitude, increases sharply as the difference between the LCO third harmonic and the bluff body shedding frequency decreases. It is possible that similar interaction exists for shedding frequency regimes near integer multiples other than three, thus indicating the potential for future work in further exploration of the system dynamics.
2. The streamwise distance between the bluff body and the wing influenced the intensity of the modulation. For a given shedding frequency to LCO frequency ratio, a shorter distance between the wing and the bluff body resulted in greater deviations in amplitude and increased the variation of the modulation intensity itself with time. The greater influence from the bluff body at closer distances is attributed to increased strength of the impinging wake vortices.
3. The modulation frequency was equal to  $f_{shed} - 3f_{LCO}$  for the  $X_b/D = 6.5$  case for all frequency ratios  $f_{shed}/f_{LCO}$ . This was true for all bluff body spatial configurations when  $f_{shed}/f_{LCO} \leq 2.8$  or  $f_{shed}/f_{LCO} \geq 3.2$ . However, when  $2.8 \leq f_{shed}/f_{LCO} \leq 3.2$ , decreasing  $X_b/D$  was shown to cause intermittent alternation between two modulation modes, each with distinct characteristic intensity and frequency.
4. The mechanism of amplitude modulation was revealed through instantaneous phase and energy analysis. The presence of the bluff body alters the dynamics such that instantaneous pitch-heave phase difference modulates with time. This phase difference manifests as an effective change in the aeroelastic efficiency of the wing. That is, for a limit cycle to maintain constant amplitude, the phase difference between pitch and heave must be such that the average power over a cycle is zero. When the bluff body alters this phase difference, the balance of power into and out of the structure over a cycle is disrupted, resulting in either amplitude growth or decay.

## Chapter 5

# Amplitude Annihilation in Wake-Influenced Aeroelastic Limit-Cycle Oscillations

This chapter investigates the dynamics of a pitching and heaving aeroelastic wing undergoing large amplitude limit cycle oscillations influenced by a vortical wake from an upstream rectangular cylinder bluff body. The results show that under certain conditions, the limit cycle is annihilated. The conditions in which annihilation occurs is dependent on the limit cycle frequency, bluff body shedding frequency, and the magnitude of the mass coupling in the system. The low mass coupling configuration shows that vortical disturbances on the wing causes minor amplitude modulation until the shedding frequency is within a critical distance of the third harmonic of the limit cycle oscillation frequency. Within this band, the amplitude modulations grow such that the pitch amplitude varies by up to  $10^\circ$ . When the mass coupling is increased and when the shedding frequency is within a critical distance of the third harmonic, the limit cycle is annihilated and the system returns to equilibrium. The annihilation phenomena is caused by the addition of strong aerodynamic coupling between the vortex wake and the wing, influencing the limit-cycle kinematics such that the limit cycle returns to the equilibrium position. The chapter discusses both the kinematic and aerodynamic behavior of wake-influenced aeroelastic limit cycle annihilation.

### 5.1 Chapter Introduction

Researchers have been investigating aeroelastic phenomena of elastically restrained airfoils and deformable wings for the past century. While initially concerned with linear stability analysis to determine the onset of the flutter instability, contemporary aeroelastic research efforts focus heavily on nonlinear aeroelastic phenomena. Nonlinear aeroelastic research has included investigations of dynamic stall [78], nonlinear structural effects such as freeplay [79] or hardening stiffness [80], and limit cycle oscillations [81, 82, 61, 7] (LCOs). Recent experimental investigations of aeroelastic airfoil and wing LCOs have highlighted the influence of unsteady aerodynamic phenomena on LCO kinematics and stability. Such experimental works have demonstrated asymmetric bifurcation [83, 58], boundary-layer separation induced LCOs [84, 61, 85, 86], compressible deep dynamic stall [59], and dynamic stall driven large amplitude heaving and pitching LCOs [87, 88, 7].

Since LCOs can cause structural damage and reduce aircraft performance, numerous researchers have investigated ways to mitigate LCO motion. One such way to mitigate the LCO response is through the use of nonlinear energy sinks [89, 90, 91]. To date, nonlinear energy sinks applied to aeroelastic systems have taken the form of nonlinear mass-spring-dampers. These devices are attached to the wing to capture and dissipate energy that would have gone to either the pitch or heave degree of freedom. Lee et al. [89] used a nonlinear energy sink that coupled to the heave degree of freedom and dissipated aerodynamic energy entering the structure. Lee et al.[89] demonstrated that for a given wind speed, as the coupling strength of the nonlinear energy sink increased, a stable fixed point emerged and the limit cycle disappeared. The results of Lee et al. [89] represent one of the first experimental applications of nonlinear amplitude death phenomena to aeroelastic LCO suppression.

Broadly, amplitude death is the emergence of a stable fixed point from a limit cycle and cessation of oscillations in systems of two or more coupled nonlinear oscillators [92, 93]. Research into amplitude death has investigated how different coupling mechanisms lead to the suppression of LCOs. Amplitude death mechanisms relevant to aeroelastic LCO suppression include dynamic coupling, velocity coupling, and nonlinear coupling [94]. The energy sink of Lee et al. [89] can be classified as an example of dynamic coupling, wherein dynamic coupling refers to the addition of a nonlinear oscillator to the system. In this case, the system oscillators are the wing heave and pitch degrees of freedom, and the added dynamic oscillator is a passive, nonlinear, mechanical device attached to the heave degree of freedom.

The current chapter investigates a system undergoing large amplitude LCOs in a sub-critical Hopf bifurcation regime. Based on the importance of coupling in the amplitude death literature and previous research [95, 72], we hypothesize that increasing the mass coupling can lead to the spontaneous cessation of LCOs when the oscillating aeroelastic system is influenced by upstream vortical disturbances near a superharmonic of the LCO frequency. We refer to this return to an equilibrium from a limit cycle as limit cycle annihilation. This chapter presents the time history, amplitude, and frequency characteristics of LCO annihilation before employing various signal analysis techniques to investigate the routes for amplitude decay, recovery and LCO annihilation.

## 5.2 System Characterization and Modeling

### 5.2.1 Parameter Estimation

**5.2.1.0.1** The system is characterized using Markov Chain Monte Carlo (MCMC) Bayesian inferencing to estimate the stiffness, damping, and coupling parameters of the aeroelastic model. This approach allows us to propagate parameter uncertainties through the model response to use in aeroelastic inverse (AEI) methods [96, 72]. An AEI method is used to compute the aerodynamic energy into the structure and determine how the energy is distributed throughout the structure. The AEI method is applied by solving Eqn. 1 and 2 for  $C_L$  and  $C_M$ , where all the state variables  $\vec{X} = \{h, \dot{h}, \ddot{h}, \theta, \dot{\theta}, \ddot{\theta}\}$ , are experimental measurements and all parameter values are estimated through Bayesian inference or measured. A smooth curve of the position signals was fitted to reduce the effects of noise while taking derivatives. Following the work of Epps[97] and Truscott and Epps[98], a smoothing spline, using MATLAB's `spaps` command, is fit to the heave and pitch signal such that the error and roughness of the spline are minimized. Additionally, a low pass filter is applied to the heave and pitch accelerations 1 Hz below 3 times the fundamental limit cycle oscillation frequency.

Validation of the this method can be found in Kirschmeier et al. [72]. The equations of motion of the aeroelastic system are:

$$m_{total}\ddot{h} + m_w b x_\theta \dot{\theta}^2 \sin(\theta) - m_w b x_\theta \ddot{\theta} \cos(\theta) + k_h h + c_h \dot{h} + F_f \text{sgn}(\dot{h}) = C_L \frac{1}{2} \rho U_\infty^2 c S \quad (1)$$

$$I_\theta \ddot{\theta} - m_w b x_\theta \cos(\theta) \ddot{h} + M_{k_\theta}(\theta) + c_\theta \dot{\theta} + M_f \text{sgn}(\dot{\theta}) = C_M \frac{1}{2} \rho U_\infty^2 c^2 S \quad (2)$$

Where the  $(\dot{\phantom{x}})$  notation is used for time derivatives. Additionally, load cell force and torque measurements of the heave springs and pitch spring pulley system were used to characterize the force and moment versus displacement behaviour of the elastic elements. Tensile test measurements using an Instron 4400R found the heave stiffness to remain linear over the displacements observed in LCO. Based on load cell measurements of the spring pulley system, Fig. 5.1, a piecewise pitch stiffness exists at high pitch deflection angles,  $\theta > 60^\circ$ . Additionally, pitch-only free decay experiments found a softening stiffness to occur when  $\theta < 6^\circ$ . The pitch spring moment model is given as

$$M_{k_\theta}(\theta) = \begin{cases} K_{\theta_L}(\theta)\theta & \text{if } |\theta| < \theta_{P_1} \\ \text{where } K_{\theta_L}(\theta) = C_1\theta^{2\beta} + C_2\theta^\beta + C_3 & \\ K_{\theta_H}(\theta_{T_1} + (\theta - \theta_{P_1})) & \text{if } \theta_{P_1} \leq |\theta| < \theta_{P_2} \\ K_{\theta_S}(\theta_{T_2} + (\theta - \theta_{P_2})) & \text{if } \theta_{P_2} \leq |\theta| \\ \text{where } K_{\theta_S} = K_{\theta_L}(\theta_{P_1})/2 & \end{cases} \quad (3)$$

where  $K_{\theta_L}$ ,  $K_{\theta_H}$  and  $K_{\theta_S}$  are the spring constants for the three different regions and  $\theta_{P_{1,2}}$ ,  $\theta_{T_{1,2}}$  are the geometric transition angles and modified transition angles to ensure a continuous moment when the stiffness changes. The modified transition angles are defined as

$$\theta_{T_1} = \frac{K_{\theta_L}(\theta_{P_1})\theta_{P_1}}{K_{\theta_H}}, \quad \theta_{T_2} = \frac{K_{\theta_H}(\theta_{T_1} + \theta_{P_2} - \theta_{P_1})}{K_{\theta_S}}; \quad (4)$$

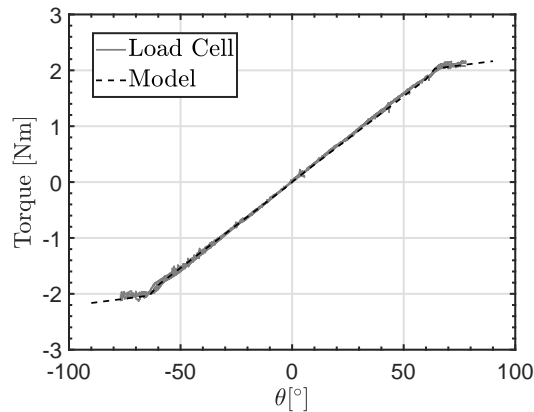


Figure 5.1: Measured pitch restoring moment compared to model

**5.2.1.0.2** Structural parameters not estimated through Bayesian inferencing include  $m_{total}, m_\theta, I_\theta, C_1, C_2, \theta_{P_1}$ , and  $\theta_{P_2}$ . These parameters were measured and estimated through weight scales,

CAD software, free decay experiments, and torque measurements; their values are listed in Table 5.1. Structural parameter estimates for  $\{k_h, x_\theta, c_h, c_\theta, \beta, C_3, F_f, M_f\}$  were determined using Markov Chain Monte Carlo simulations in MATLAB using the Delayed Rejection Adaptive Metropolis (DRAM) algorithm ([99, 100]). The DRAM algorithm estimates the distributions of the parameters based on experimental free decay data by using the sum of squares error between the measurement and the simulation as a likelihood. Figure 5.2 shows the maximum a posteriori (MAP) estimate along with the data and credible intervals to ensure model accuracy. The MAP estimate is given by the parameter combination that corresponds to the highest density of the parameter distributions. This value is closely related to the maximum likelihood estimator (MLE), that minimizes the sum-of-squares error ([101]). The 95% credible intervals are constructed by sampling from the parameter chains and computing the corresponding model response. The MAP estimates and 95% credible intervals for the structural parameters are listed in Table 5.2. The results demonstrate that the model captures the structural response and shows the estimates of the parameters are valid. These parameter estimates will be used in the AEI method to calculate the coupling and aerodynamic energy per cycle.

Table 5.1: Structural parameter values.

Parameter	Description	Config - 1	Config - 2
$m_{total}$	Total mass all moving parts (kg)	3.268	
$m_w$	Mass of all rotating parts (kg)	1.609	
$I_\theta$	Pitching inertia about elastic axis ( $\text{kg} \cdot \text{m}^2$ )	5.32e-03	5.77e-03
$c$	Chord length (m)	0.15	
$S$	Span length (m)	0.6	
$C_1$	Pitch stiffness coefficient ( $\text{kg} \cdot \text{m}^2$ )	6.86e-04	7.44e-04
$C_2$	Pitch stiffness coefficient ( $\text{kg} \cdot \text{m}^2$ )	4.87e-02	1.05e-01
$\theta_{P_1}$	Transition angles for $k_\theta$ ( $^\circ$ )	60	
$\theta_{P_2}$	Transition angles for $k_\theta$ ( $^\circ$ )	64	
$K_{\theta H}$	Pitch stiffness at high deflection angles (Nm/rad)	5.92	

Table 5.2: MAP estimates and credible intervals for Bayesian parameter estimation of Config - 1 and Config - 2.

Parameter	MAP	Config - 1	MAP	Config - 2
		95% Credible Interval		95% Credible Interval
$c_h$ [Ns/m]	1.73e+00	[1.13e+00, 2.19e+00]	1.56e+00	[0.99e+00, 1.58e+00]
$c_p$ [Nm s/rad]	3.36e-03	[2.75e-03, 3.93e-03]	3.62e-03	[3.047e-03, 3.70e-03]
$F_f$ [N]	1.02e+00	[9.29e-01, 1.28e+00]	0.82e+00	[0.73e+00, 0.96e+00]
$M_f$ [Nm]	8.19e-03	[6.32e-03, 1.02e-02]	7.62e-03	[7.22e-03, 8.72e-02]
$x_\theta$	6.21e-02	[6.04e-02, 6.34e-02]	7.82e-02	[7.61e-02, 8.07e-02]
$k_h$ [N/m]	2.17e+03	[2.16e+03, 2.17e+06]	2.21e+03	[2.21e+03, 2.22e+03]
$c_3$ [Nm/rad]	3.47e+00	[3.45e+00, 3.49e+00]	3.52e+00	[3.52e+00, 3.53e+00]
$\beta$	-4.39e-01	[-4.82e-01, -3.94e-01]	-4.83e-01	[-4.96e-01, -4.57e-01]

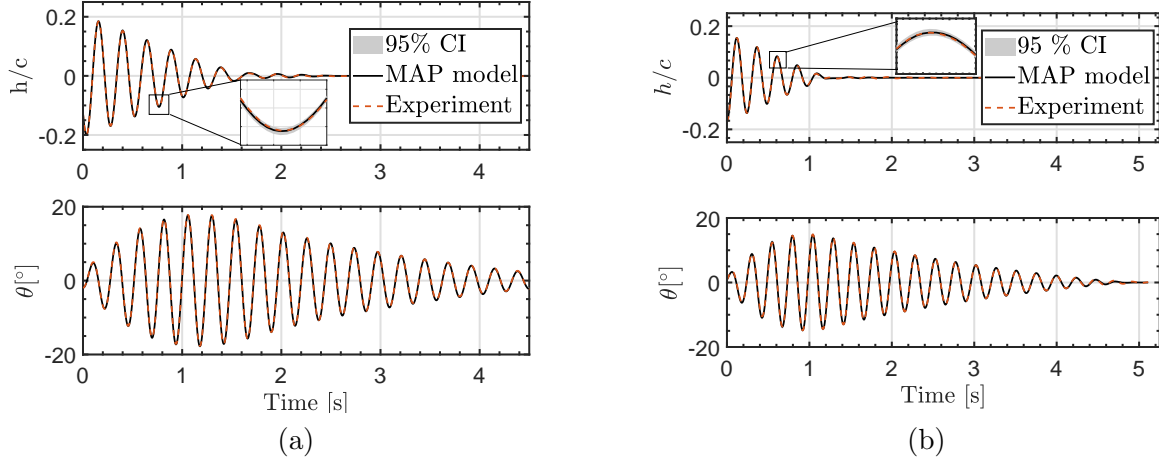


Figure 5.2: Free decay comparison of experiment with model for Config - 1 (a) and Config - 2 (b).

## 5.2.2 System Energies

The system energy transfer from the flow into the structure is developed following Bendiksen [102] to examine how the aerodynamic energy and coupling energy transfer between the two degrees of freedom affect the aeroelastic system. The aerodynamic power is calculated by evaluating the flow of energy into the aeroelastic structure:

$$P_L = C_L \frac{1}{2} \rho U^2 c S \dot{h}, \quad P_M = C_M \frac{1}{2} \rho U^2 c^2 S \dot{\theta} \quad (5)$$

**5.2.2.0.1**  $P_L, P_M$  are positive when energy is being added to the structure, and negative when the aerodynamic forces are dissipating energy from the structure. The aerodynamic energy input or dissipated per cycle is found by integrating the power flow over a cycle.

$$E_L = \int_0^T P_L dt, \quad E_M = \int_0^T P_M dt \quad (6)$$

**5.2.2.0.2** Additionally, the coupling energy transfer per cycle is found by multiplying the mass coupling terms in Eqn. 1 by  $\dot{h}$  and Eqn. 2 by  $\dot{\theta}$ , respectively and integrating over an oscillation cycle. The coupling energy provides insights into the distribution of aerodynamic energy throughout the structure. The coupling energy per cycle for each degree of freedom is given by:

$$E_{x_{\theta}, h} = \int_0^T (m_w b x_{\theta} \ddot{\theta} \cos \theta - m_w b x_{\theta} \dot{\theta}^2 \sin(\theta)) \dot{h} dt, \quad E_{x_{\theta}, \theta} = \int_0^T m_w b x_{\theta} \ddot{h} \cos(\theta) \dot{\theta} dt \quad (7)$$

## 5.3 Results

A description of the experimental apparatus used in this work can be found in Chapter 3. The experimental procedure begins with determining the LCO initiation wind speed. Starting at the minimum wind tunnel speed, the wing is given an initial pitch angle displacement of  $40^\circ$  and then released to determine if a limit cycle exists at that wind speed. The wind speed is increased and

the process is repeated until an LCO is established. The initiation of limit cycles given a large disturbance is characteristic of a sub critical Hopf bifurcation wherein a limit cycle exists around a stable fixed point or equilibrium. The sub-critical Hopf bifurcation is characterized by requiring a minimum energy input into the aeroelastic system such that a limit cycle forms. Initial conditions below this energy threshold result in the system returning to the equilibrium position whereas initial conditions above this energy threshold result in limit cycles. It should be noted that the minimum initial condition needed to initiate limit cycle oscillations decreases as the wind speed is increased. At 11.2 m/s the smallest initial condition need is  $15^\circ$ . For this airfoil, this angle is above the static stall angle[72], and indicative of the influence of stall on the limit cycle initiation. Further analysis of the pre-LCO behavior of the system can be found in Kirschmeier et al. [72]. Once a limit cycle is established, the motion history is recorded for one minute for cases without the bluff body upstream and up to three minutes for cases with the bluff body present. In cases where amplitude annihilation occurred, numerous different initial angle displacements were tested to evaluate the sensitivity of the system response to the given initial condition.

### 5.3.1 Wing Limit Cycle Oscillation Behavior

The entire pitch time histories of the no-bluff-body LCOs for both configurations at selected wind speeds are shown in Fig. 5.3. An enlarged view of the time history showing a few cycles is shown in the first time history of Fig. 5.3. The entire time history is shown to contrast the amplitude response of Config -1 with Config - 2 as well as contrast the no-bluff body and bluff body response. Figure 5.4a-b shows the pitch and heave amplitudes for both configurations when the bluff body is not present. The amplitude plots are generated by plotting a semitransparent marker for the maximum of each cycle over the full time history. Therefore, a darker region represents a higher number of cycles at that LCO amplitude while a lighter region represents a lower number of cycles at that LCO amplitude. For Config - 1, the LCO amplitude at a given wind speed remains constant over the measured time history, however, small, transient amplitude modulations exist for Config - 2. These transient amplitude modulations are represented as a light marker region surrounding a high cluster of markers in Fig. 5.4a-b for the no-bluff-body cases. For Config - 1, the no-bluff-body pitch and heave amplitudes range from  $58$  to  $66^\circ$  and  $h/c=0.3-0.6$ , respectively. Whereas the no-bluff-body pitch and heave amplitudes for Config - 2 range from  $40$  to  $58^\circ$  and  $h/c=0.1$  to  $0.33$ , respectively. Additionally, slightly higher wind speeds are required for LCOs to appear for Config - 2 as compared to Config - 1. The relationship between the mass coupling and the LCO amplitude is discussed further in Kirschmeier et al. [72] and is the result of changing the pitch-heave phase difference such that the distribution of energy between the two degrees of freedom is altered and the efficiency of the aerodynamic power transfer is reduced for higher mass coupling across all wind speeds.

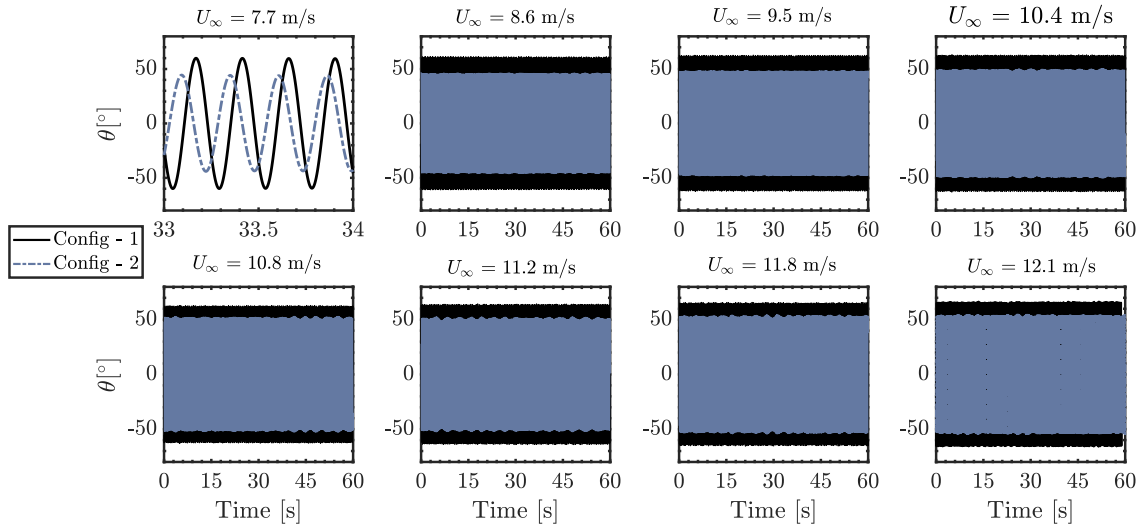


Figure 5.3: Pitch time histories for a range of selected wind speeds without the bluff body upstream.

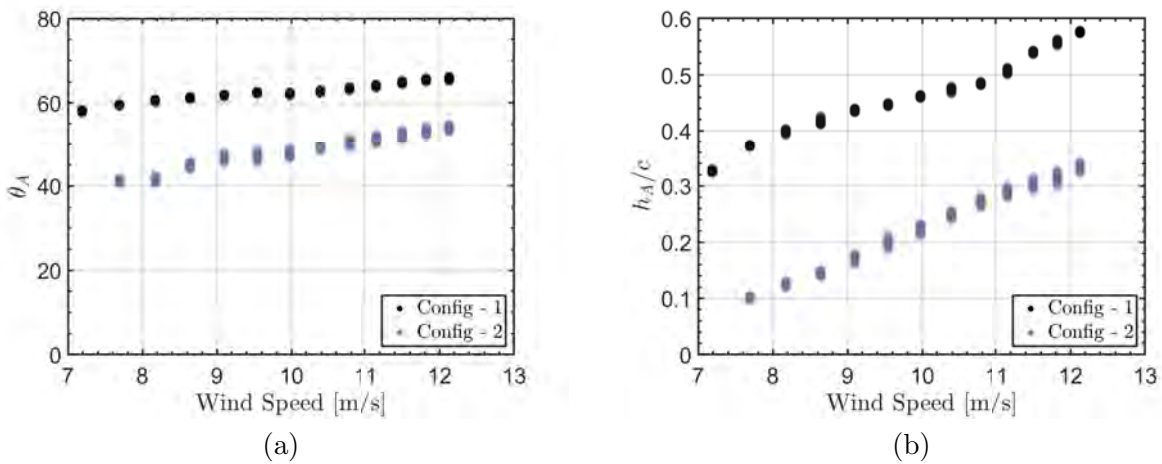


Figure 5.4: (a) Pitch amplitude versus wind speed and (b) heave amplitude versus wind speed for wing LCO without the bluff body upstream.

**5.3.1.0.1** For each of the configurations, a fast Fourier transform of the pitch signal is used to determine the mean frequency[103] components when the bluff body is not present. Figure 5.5 shows the spectral analysis for  $x_\theta = 0.078$ , however both configurations show similar trends. The frequency spectrum is dominated by the fundamental LCO frequency, at 4 Hz, and lower amplitude super harmonics of the structure, with odd harmonics showing a stronger influence. The 4 Hz LCO frequency is the convergence of the pitch and heave natural frequencies.

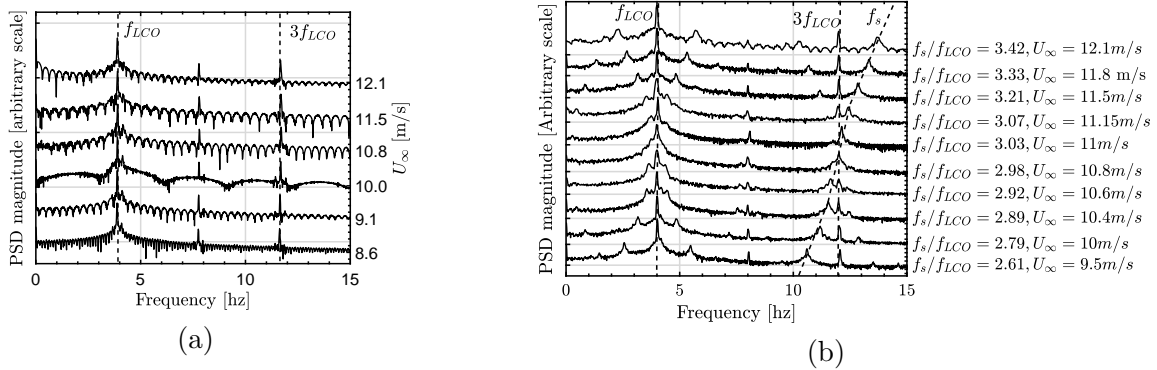


Figure 5.5: (a) Frequency spectrum of pitch response for five selected wind speeds without the bluff body present. (b) Frequency spectrum of pitch response with the bluff body present for all wind speeds tested.  $x_\theta = 0.078$  for each figure.

The introduction of an upstream bluff body influences the aeroelastic LCO of the downstream wing. A fast Fourier transform of the pitch signal, Fig. 5.5b, shows the presence of the bluff body introduces not only frequency content at the shedding frequency, but additional side band frequencies around the LCO frequency. The difference between the side-band frequencies and the LCO frequency is determined by the difference between the shedding frequency and  $3f_{LCO}$ . The presence of side band frequencies in the spectral content is characteristic of amplitude modulated signals. At the lowest wind speed tested with the bluff body, the shedding frequency is below the LCO third harmonic. The shedding frequency passes through the third harmonic of the LCO and then moves past it as the wind speed is increased. Figure 5.6 shows the amplitude modulated pitch time histories for both mass coupling configurations. The time histories for Config - 1 show an amplitude modulated response for all wind speeds tested, however, the LCO is stable and does not annihilate. For Config - 2, amplitude modulation exists for all wind speeds, however for a certain range of wind speeds and consequently bluff body shedding frequencies, the limit cycle is annihilated. When the LCOs are annihilated, the pitch and heave amplitudes reduce to negligible deflections that are due to harmonic forcing from the bluff body shedding. The instances of LCO annihilation occur when the bluff body vortex shedding frequency to LCO oscillation frequency is within  $2.9 < f_s/f_{LCO} < 3.08$ , and when the side band modulation frequencies are within 0.3Hz of the mean LCO frequency. Above  $U_\infty = 11.2$ m/s, stable limit cycles return and no LCO annihilation is found. Additionally, only one of the multiple time histories during LCO annihilation is shown in Fig. 5.6. While  $f_s/f_{LCO}$  of 2.98 and 3.02 show the longest oscillation time, other experiments performed at the same frequency ratio show much smaller time to LCO annihilation. Furthermore, during the time histories exhibiting LCO annihilation there exists a high amplitude modulation mode, where the pitch amplitude varies by up to  $30^\circ$  over a  $5 \sim 10$  second period and a low amplitude modulation mode where the pitch amplitude varies up to  $15^\circ$ .

Figure 5.7a-b shows all the pitch and heave cycle amplitudes over the full time history of each configuration at each wind speed tested. The results show that placing a bluff body upstream of the wing does not alter the LCO initiation speed when  $x_\theta = 0.062$ , however there is a 1.7 m/s increase in the LCO initiation speed when  $x_\theta = 0.078$ . Since stable oscillations exist at wind speeds less than the LCO annihilation region, the shift in LCO initiation speed caused by the increased mass coupling does not account for LCO annihilation. Additionally, both configurations show significant amplitude modulation occurs once the shedding frequency is within a critical distance

of the third harmonic of the LCO. Since both configurations only show large amplitude modulation at a specific wind speed and ratio of bluff body shedding frequency to mean LCO frequency, we conclude that the mean flow velocity deficit due to the bluff body does not describe the amplitude annihilation phenomena.

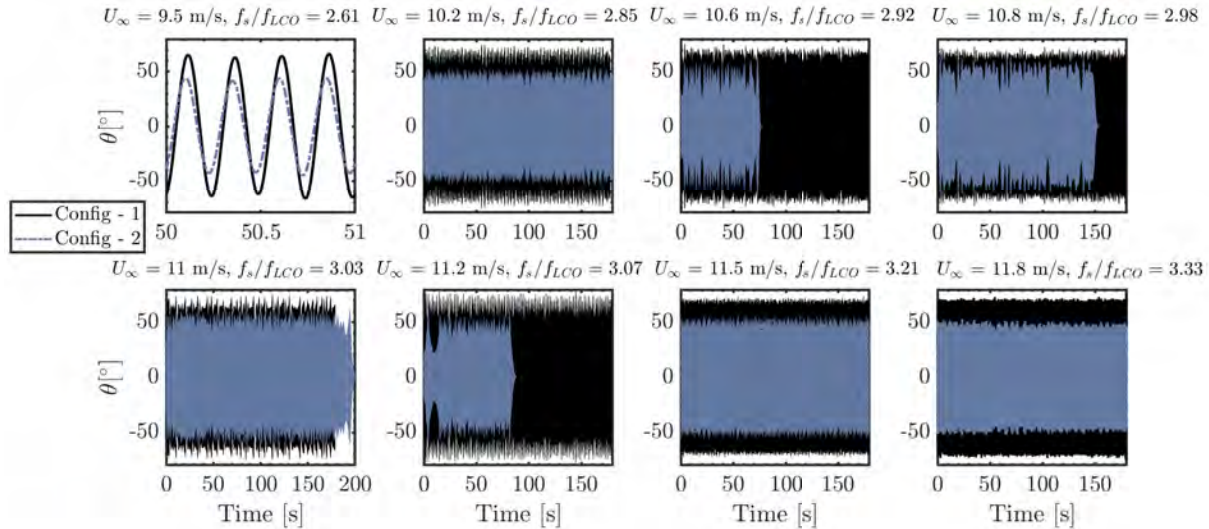


Figure 5.6: Pitch time histories for a range of selected wind speeds with the bluff body upstream.

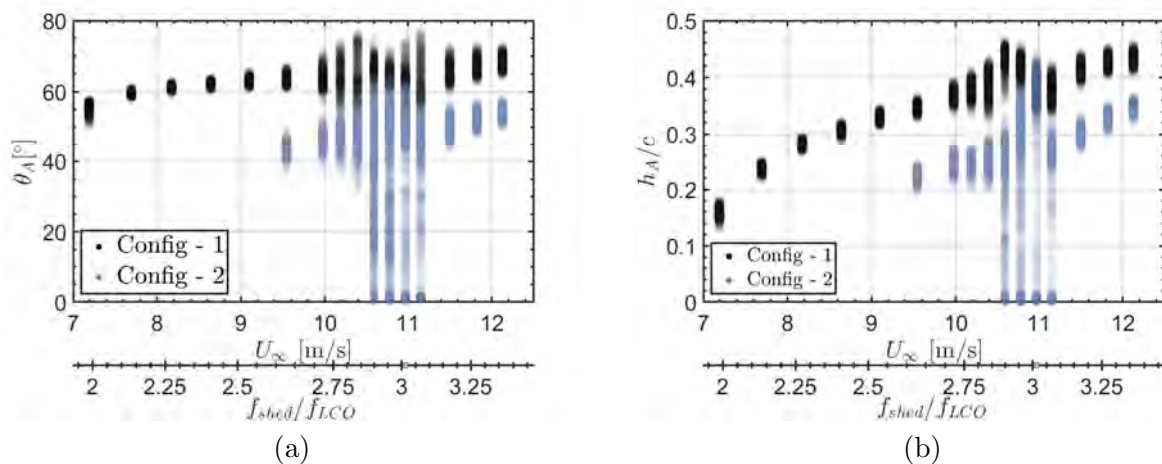


Figure 5.7: (a) Pitch amplitude versus wind speed and (b) heave amplitude versus wind speed for wing LCO with the bluff body upstream.

**5.3.1.0.2** At each wind speed where LCO annihilation occurred, multiple initial conditions were tested to understand the sensitivity of LCO annihilation to the starting conditions. Figure 5.8 shows multiple time histories for  $f_s/f_{LCO} = 2.91$ . The results demonstrate that LCO annihilation does not depend on the initial conditions, with amplitude annihilation present in all trials. Therefore, the initial energy input into the structure only influences whether or not the system grows to the LCO before returning to the equilibrium position. Additionally, the time to LCO annihilation does not have an apparent pattern or correlation to the initial condition amplitude. The initial condition

near  $\theta = 20^\circ$  oscillated for 70 seconds while for the two initial conditions near  $\theta = 40^\circ$ , one oscillated for approximately 10 seconds and the other 30 seconds. It is hypothesized, and discussed further in Section 5.4.1, that LCO annihilation requires a specific phase relationship between the bluff body shedding and the wing kinematics. Furthermore, the switching between the low amplitude modulation mode and the large amplitude modulation mode does not appear to have a specific time scale associated with it, suggesting a chaotic nature. Moreover, the path to LCO annihilation does not have to occur with a direct transition to the equilibrium position. Certain time histories show that LCO annihilation occurs over a longer period of time, with a large amplitude drop occurring within 5 seconds followed by 5 seconds of oscillations with a pitch amplitude around  $15^\circ$ , Trial 2 of Fig. 5.8. The oscillations near  $15^\circ$  are just below the minimum energy needed to sustain LCOs.

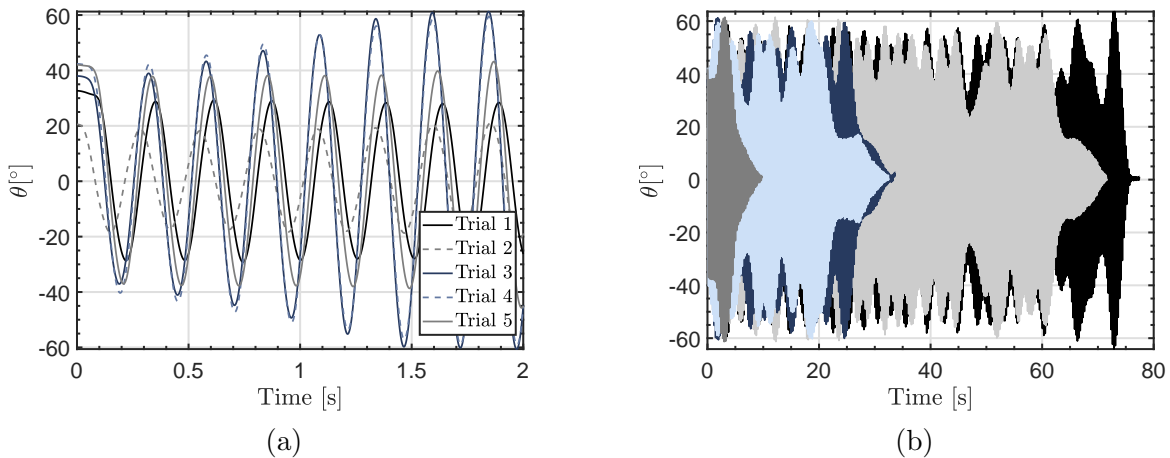


Figure 5.8: Multiple LCO annihilations at  $f_s/f_{LCO} = 2.92$  for  $x_\theta = 0.078$ , first two seconds of motion (a) and full time history (b).

## 5.4 Analysis and Discussion

**5.4.0.0.1** The emergence of LCO annihilation in the system requires further investigation of the underlying phenomenon. It will be shown that the route to LCO cessation depends on the emergence of a different frequency dominated LCO and a unique kinematic-bluff body vortex shedding phase wherein there is a region of wing kinematics and bluff body shed vortex-wing interaction that results in the annihilation.

### 5.4.1 Recurrence Analysis

The time histories during which LCO annihilation occurs show multiple amplitude decay and recovery intervals before LCO annihilation occurs. A recurrence analysis is used to investigate whether the LCO annihilation event is kinematically unique or if there is a unique combination of kinematic states and bluff body vortex shedding states. Recurrence analysis has been applied in recent years as a way to analyze how often a signal returns to a location within a phase space[104]. Recurrence analysis is based on a Euclidean distance formula that finds the distance between a current point in the phase space and another point in the phase space and then assigns a 1 or 0 to that combination of time instances depending on a threshold level set[104]. While there are several

ways to calculate the distance threshold, we set the threshold to either be 5,10, or 20 times the measurement error associated with the specific variable. We relax the threshold to 20 times the measurement error to ensure the comparisons are not too restrictive. The kinematic recurrence calculation is given by

$$R_{i,j}(\epsilon) = \Theta(\epsilon^{\vec{x}} - \|\vec{x}_i - \vec{x}_j\|), \quad i = 1, \dots, N, j = 1, \dots, M \quad (8)$$

where  $\|\cdot\|$  is a norm,  $\epsilon$  is the threshold,  $i, j$  are instances in time of  $\vec{x}$ , where in our system  $\vec{x} = \{h, \dot{h}, \theta, \dot{\theta}\}$ , and  $R_{i,j}$  is the recurrence matrix. The signals and errors are normalized by the maximum values of the state in the given signal. The normalization is done to account for the order of magnitude differences between the position and velocity terms as well as the difference in magnitudes between the heave and pitch states. Additionally, a kinematic and bluff body force joint recurrence is used to investigate the hypothesis that a unique combination of kinematic and bluff body shedding states results in LCO annihilation. The kinematic and bluff body force joint recurrence is defined as

$$JR_{i,j}^{\vec{x},\vec{z}} = \Theta(\epsilon^{\vec{x}} - \|\vec{x}_i - \vec{x}_j\|)\Theta(\epsilon^{\vec{z}} - \|\vec{z}_i - \vec{z}_j\|), \quad i = 1, \dots, N, j = 1, \dots, M \quad (9)$$

Where  $\vec{z}$  is the bluff body force and its derivative, as measured by the load cell. A kinematic and bluff body force joint recurrence is used instead of a traditional recurrence calculation as in Eqn. 8, because grouping the bluff body force signal into  $\vec{x}$  results in false recurrence values due to the fact that the dominant frequency of the force signal is a higher frequency than the LCO frequency. Additionally,  $\vec{z}$  is defined using the force signal and its derivative to remove false recurrences associated with sinusoidal signals. In simple sinusoidal signals, recurrence analysis will calculate that values on either side of a peak or trough are the same, however, one side is going towards the peak or trough while the other side is moving away from that peak or trough. Therefore, a rate dependence is required in the recurrence analysis to differentiate the direction of motion through the phase space. Furthermore, a multi-trial cross recurrence analysis was performed to analyze how kinematically similar the LCO annihilation events are between multiple trials at the same wind speed. The multi-trial cross recurrence is used to evaluate whether there is a kinematic trigger such that LCO annihilation occurs. The cross recurrence is defined as

$$CR_{i,j}^{\vec{x},\vec{y}} = \Theta(\epsilon^{\vec{x}} - \|\vec{x}_i - \vec{y}_j\|), \quad i = 1, \dots, N, j = 1, \dots, M \quad (10)$$

where  $\vec{y}$  are the same states as  $\vec{x}$  but from a different trial time series. The nondimensionalization procedure is different than that used for the recurrence calculation. Since there is no guarantee that the maximum values of  $\vec{x}$  and  $\vec{y}$  are the same, the maximum values of  $\vec{x}$  are used to normalize  $\vec{x}$  and nondimensionalize  $\vec{y}$ , keeping the same magnitude scale relationships between the two signals. Unfortunately, recurrence analysis is memory intensive since  $R_{i,j}$  is usually defined as an NxN matrix where N is the number of data points in the time series. This is mitigated in two ways; by limiting the evaluation window such that each recurrence matrix only encapsulates 1.5 seconds of data, and by only evaluating the recurrence of the last 12 seconds of data with the rest of the signal. The last 12 seconds of data covers a few seconds before the annihilation starts through the entirety of LCO annihilation event. This analysis is done for both the kinematic recurrence and the kinematic and bluff body joint recurrence analysis. In the multi-trial cross recurrence analysis, only the LCO annihilation events are compared to each other and the signals are still divided into 1.5 seconds to maintain efficient computation.

**5.4.1.0.1** Figure 5.9a shows the pitch time history overlaid with blue markers highlighting samples with similarity to the annihilation event (red dashed box) via kinematic recurrence analysis.

The results show that even though there are multiple instances of large amplitude modulation in the signal, only one region has noticeable kinematic similarity with the LCO annihilation event. The similarity with only a small portion of one of the handful of large amplitude recoverable decay regions demonstrates that the majority of the recoverable decay regions take on a different kinematic path compared to LCO annihilation. Additionally, since amplitude decay can take a similar path to LCO annihilation, other factors must exist such that LCO annihilation occurs. The kinematic similarity between recoverable decay and annihilation is present in the other trials, with few if any of the decay regions of signals showing similarity to the LCO annihilation region. The specific kinematic differences will be further discussed in Section 5.4.2 while the factors separating recoverable decay and annihilation are found in the joint recurrence.

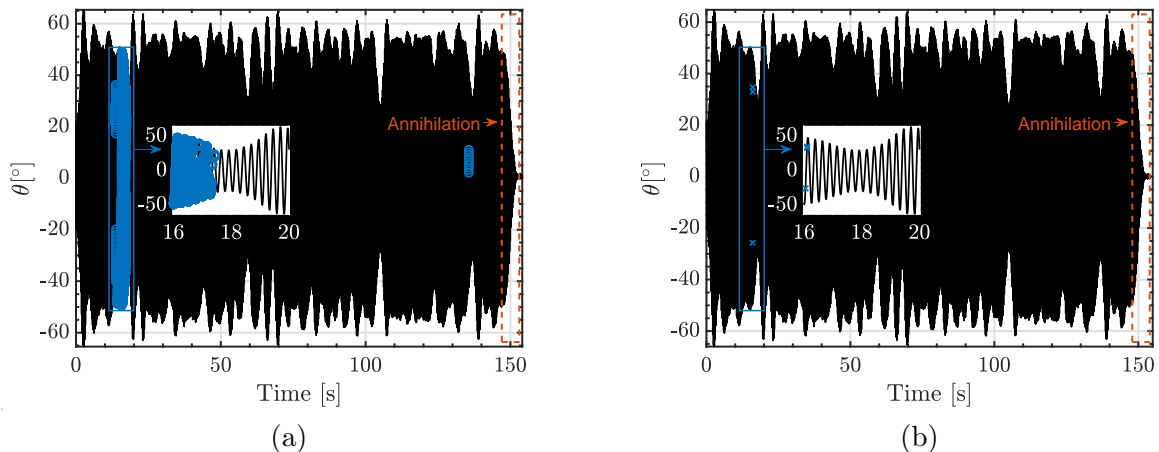


Figure 5.9: (a) Pitch time history with regions of kinematic similarity to the annihilation event highlighted by blue markers. (b) Pitch time history with regions of kinematic and bluff body force similarity to the annihilation event highlighted by blue markers.  $x_\theta = 0.078$  and  $f_s/f_{LCO} = 2.98$  for both figures.

**5.4.1.0.2** Besides kinematic factors, the influence of the bluff body on LCO annihilation is captured in the kinematic and bluff body joint recurrence analysis. The kinematic and bluff body joint recurrence analysis, shows that there are only 3 instances in time, Fig. 5.9b, for any of the tolerance values chosen, in which the bluff body force signal and the kinematics of the LCO annihilation are similar to other parts of the signal. The bluff body force signal is used as an analog for the formation and shedding of vortices from the bluff body. Therefore, the reduction in similarity of the decay region with the annihilation region aligns with the hypothesis that LCO annihilation is caused by a unique combination of bluff body vortex and kinematic states which drives the system to equilibrium.

**5.4.1.0.3** Figure 5.10 shows the regions of similarities on the time histories from the multi-trial cross recurrence between three LCO annihilation regions at  $f_s/f_{LCO} = 2.98$ . As shown, there is high degree of similarity between two LCO annihilation cases,  $CR^{1,2}$ , where the superscripts refer to the trial number. The similarity region of  $CR^{1,2}$  goes from the maximum pitch amplitude right before annihilation until the pitch amplitudes are around  $10^\circ$ , then the signals are dissimilar until the pitch amplitude are less than  $5^\circ$ . The similarity implies that both trials follow similar kinematic paths to LCO annihilation. However, there is little similarity in the LCO annihilation regions as

demonstrated by  $CR^{1,3}$  and  $CR^{2,3}$ , with the only similarity coming before the annihilation event and for oscillations near the equilibrium position. Therefore, there is not a unique kinematic threshold that results in LCO annihilation but rather a phase space of kinematic relationships that must exist for LCO annihilation. The annihilation phase space represents a region of attraction for the oscillator that will annihilate the oscillations given proper kinematic and bluff body vortex interactions. As will be shown, the annihilation phase space for kinematics is governed by the LCO frequency and pitch-heave phase difference.

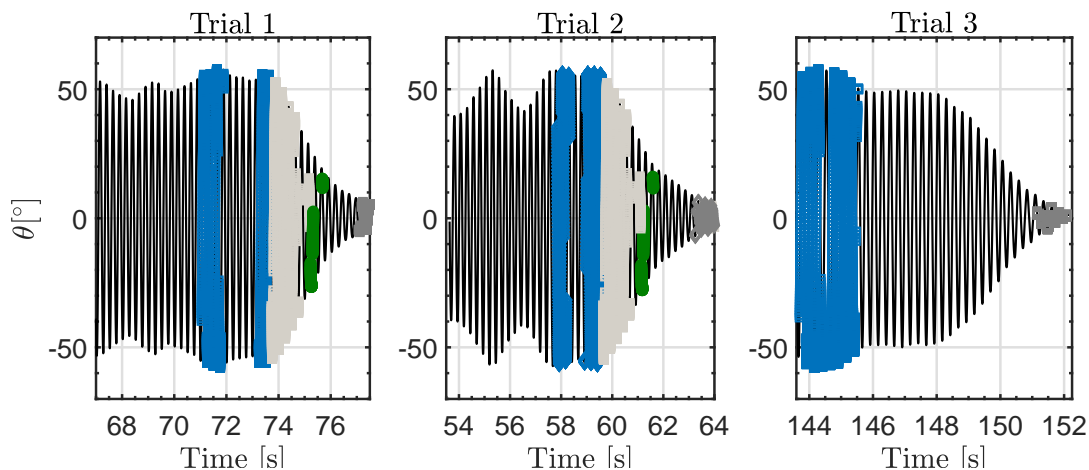


Figure 5.10: Time histories of multiple annihilation event trials with regions of cross recurrence similarity highlighted with colored markers.  $f_s/f_{LCO} = 2.98$  and  $x_\theta = 0.078$

#### 5.4.2 Instantaneous Frequency Analysis

A continuous wavelet transform and a Hilbert transform are used to gather instantaneous frequency and phase information from the amplitude envelope and the LCO signal, respectively. The continuous wavelet transform of the envelope of the pitch signal is used to study the frequency interactions that govern the amplitude modulation, while the Hilbert transform of the heave and pitch time histories will be used to analyze instantaneous frequencies and phase differences. The MATLAB CWT command is used to calculate the continuous wavelet transform. Figure 5.11 shows that when  $f_s/f_{LCO} < 2.9$  and  $f_s/f_{LCO} > 3.1$ , the amplitude modulation frequencies are dominated by the difference between the third harmonic and the bluff body vortex shedding frequency. However, when  $2.9 < f_s/f_{LCO} < 3.1$ , the modulation content includes durations dominated by the third harmonic and the bluff body vortex shedding frequency and durations dominated by a secondary mode of oscillation. The secondary mode of oscillation corresponds to the large amplitude modulation mentioned in Section 5.3. The wavelet transform reveals that the secondary mode can present itself when  $f_s/f_{LCO} < 2.9$  and  $3.1 < f_s/f_{LCO}$ , however the magnitude of such interaction is significantly lower and results only in a small amplitude change.

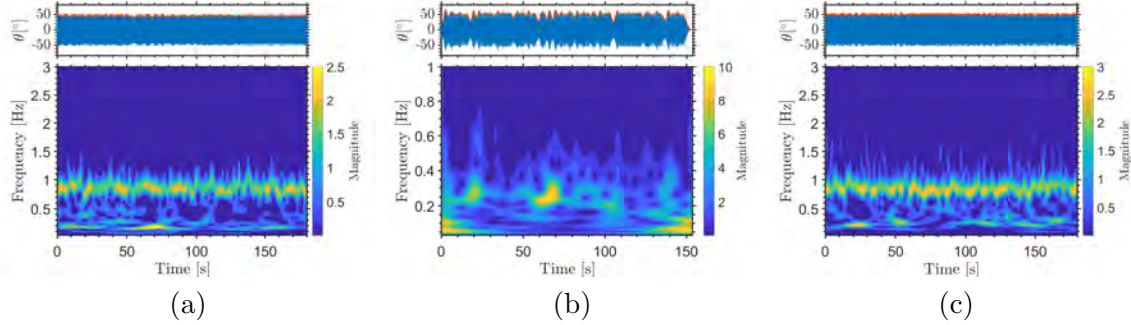


Figure 5.11: Continuous wavelet transforms of the envelope of the pitch time histories for  $x_\theta = 0.078$  at (a)  $f_s/f_{LCO} = 2.72$ , (b)  $f_s/f_{LCO} = 2.98$ , and (c)  $f_s/f_{LCO} = 3.21$ .

**5.4.2.0.1** Instantaneous frequency of each degree of freedom,  $f_{h,LCO}$ ,  $f_{\theta,LCO}$ , and frequency ratio,  $f_{h,LCO}/f_{\theta,LCO}$ , are computed by applying the Hilbert transform to each position signal. The instantaneous frequencies are passed through a moving mean window, whose window size is 4 Hz, to understand the global frequency change as opposed to the intra-cycle frequency change. Figure 5.12a shows the LCO frequency of the each degree of freedom over the entire time history for  $f_s/f_{LCO} = 2.98$ . During each of the recoverable amplitude decay intervals and the annihilation event, both  $f_{h,LCO}$  and  $f_{\theta,LCO}$  drop from 4 Hz to 3.8 Hz. This reduction in frequency is the secondary mode of oscillation. Examining the intervals of amplitude decay and recovery shown in Fig. 5.13a,  $f_{h,LCO}$  and  $f_{\theta,LCO}$  reduce to 3.8 Hz near the amplitude trough and then recover back to the 4 Hz frequency dominated LCO. During LCO annihilation, Fig. 5.14a shows that  $f_{h,LCO}$  and  $f_{\theta,LCO}$  converge towards a 3.8 Hz frequency LCO and the frequency does not recover to the 4 Hz frequency dominated LCO.

Figure 5.12b shows the frequency ratio of pitch to heave frequency at  $f_s/f_{LCO} = 2.98, U_\infty = 10.8m/s$ . The frequency ratio when  $f_s/f_{LCO} = 3.42$  is also plotted to show the nominal variations caused by the bluff body when annihilation does not occur. The nominal variations are used to classify the frequency spread caused by the bluff body and represent a  $\pm 1\%$  frequency variation. Outside of this region, the pitch-heave modal convergence begins to break down causing the heave and pitch degrees of freedom to oscillate at dissimilar frequencies. Figure 5.13b shows that the amplitude decay and recovery regions incur greater than 1% mismatches in the pitch-heave frequency ratio. The noticeable mismatches in the pitch-heave frequency ratio occur just before the trough of the recoverable amplitude decay interval and during the amplitude recovery portion. Combined with the joint recurrence, the noticeable mismatches in frequency ratio before and at the amplitude trough of the recoverable amplitude decay region indicate that amplitude recovery occurs because the interactions with the bluff body wake cause the system to escape the 3.8 Hz frequency dominated LCO. By breaking the convergence to the 3.8 Hz frequency dominated LCO the system is able to escape and return to the 4 Hz frequency dominated LCO. Conversely, Fig. 5.14b shows that the pitch-heave frequencies during LCO annihilation remain locked-on. The frequency lock-on highlights why the recurrence analysis in Fig. 5.9a shows few amplitude decay regions matching with the LCO annihilation region. Therefore, the LCO annihilation requires that the aeroelastic frequencies converge to a 3.8 Hz frequency LCO and remain converged to this frequency throughout the amplitude decay.

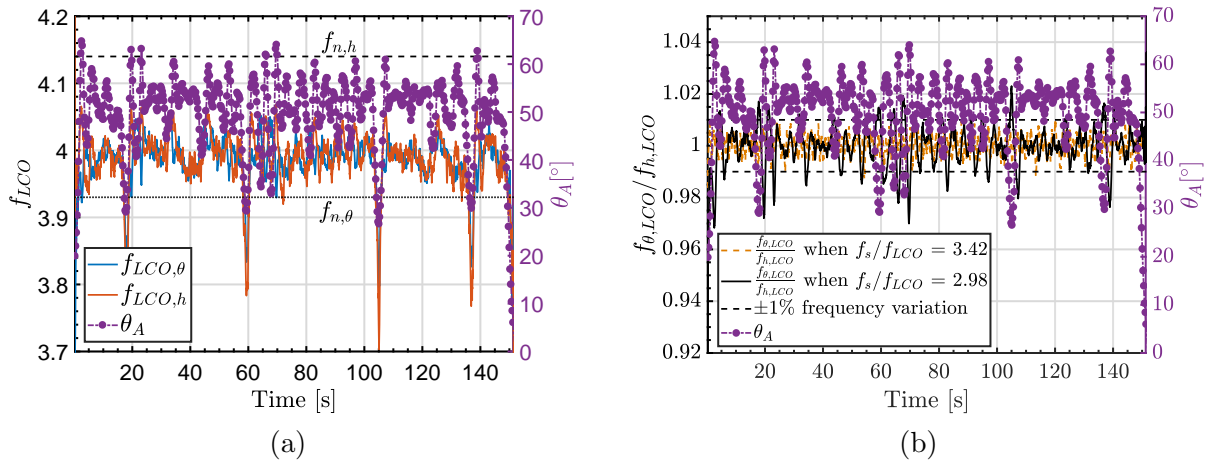


Figure 5.12: (a) Instantaneous frequency and (b) pitch heave frequency ratio versus time for  $f_s/f_{LCO} = 2.98$  shown over the full time history.

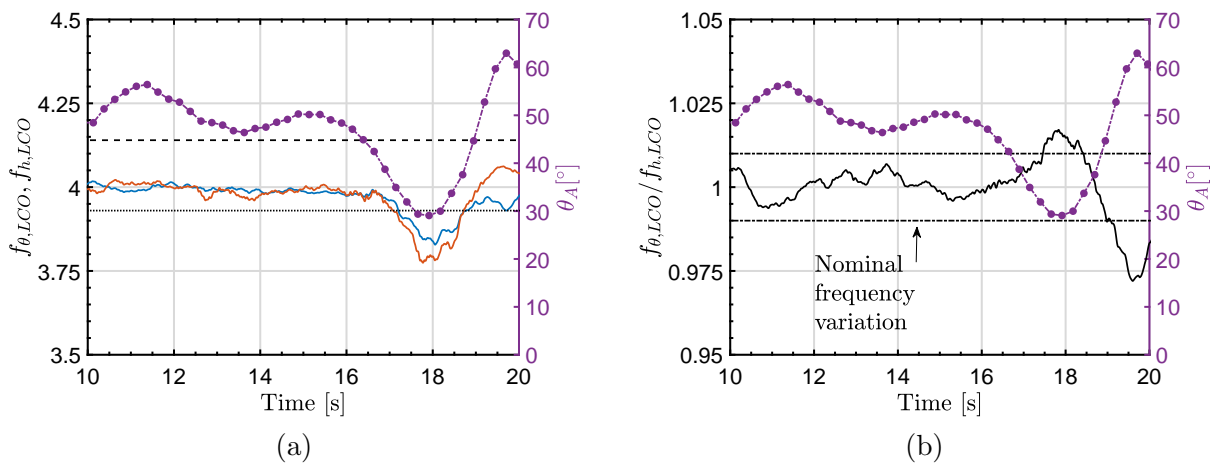


Figure 5.13: (a) Instantaneous frequency and (b) pitch-heave frequency ratio during recoverable decay.

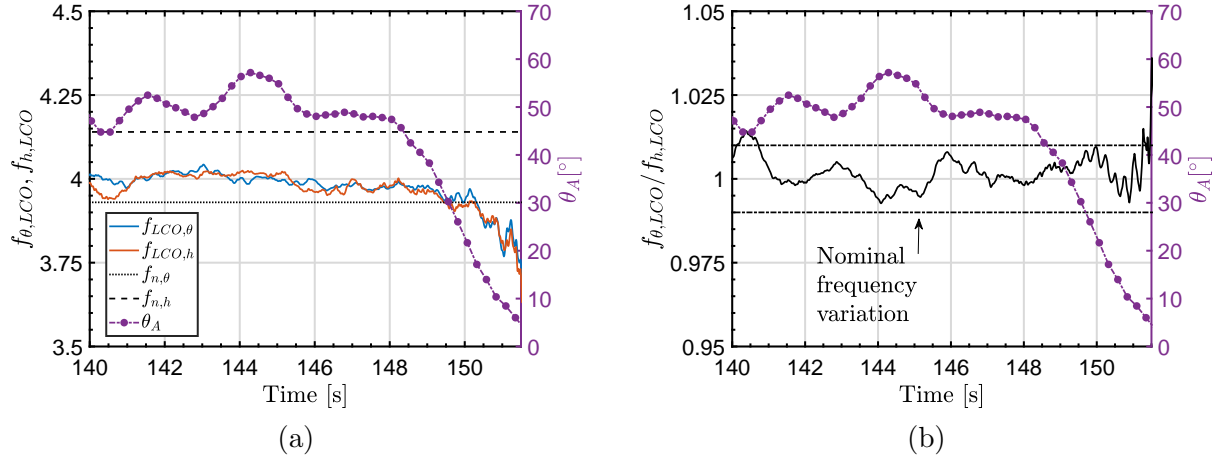


Figure 5.14: (a) Instantaneous frequency and (b) pitch-heave frequency ratio during annihilation.

### 5.4.3 Coupling and Aerodynamic Energy Analysis

The aeroelastic inverse method[72] is employed to study the evolution of the cycle-to-cycle coupling (Eqn. 7) and aerodynamic energy (Eqn 6) over the full time history. The cycle-to-cycle coupling energy is tracked over the full time history to determine how the energy is flowing between the two degrees of freedom (Fig. 5.15). Before amplitude decay occurs,  $E_{x_{\theta,h}}$  is positive, indicating energy is being transferred from the pitch degree of freedom into the heave degree of freedom. During recoverable amplitude decay,  $E_{x_{\theta,h}}$  remains positive until the trough of the amplitude decay interval. During amplitude recovery,  $E_{x_{\theta,h}}$  is negative, therefore, energy from the heave degree of freedom is being transferred into the pitch degree of freedom. The pitch-heave phase difference switching sign, going from a heave-leading motion (negative  $\phi_{\theta,h}$ ) to a pitch-leading motion (positive  $\phi_{\theta,h}$ ), causes the direction of the coupling energy to change. Additionally, as shown in Gianikos et al. [95],  $\phi_{\theta,h}$  is correlated to the power flow into the structure, with greater positive  $\phi_{\theta,h}$  leading to amplitude growth and more negative  $\phi_{\theta,h}$  leading to amplitude decay. Therefore, the kinematic requirements for LCO recovery are positive  $\phi_{\theta,h}$  and energy flow from the heave degree of freedom to the pitch degree of freedom. At the start of the LCO annihilation event,  $E_{x_{\theta,h}}$  is positive, however at a smaller energy transfer per cycle than during the recoverable decays. Additionally,  $E_{x_{\theta,h}}$  becomes negative during the LCO annihilation event, however the energy transfer is not sufficient to break the frequency convergence and grow the pitch amplitude. Furthermore, at the start of the annihilation event,  $\phi_{\theta,h}$  is a small negative value, thus, a large negative  $\phi_{\theta,h}$  is not an indicator of LCO annihilation. Therefore, additional kinematic differences that arise in amplitude annihilation as opposed to recoverable amplitude decay are due to the evolution in pitch-heave difference.

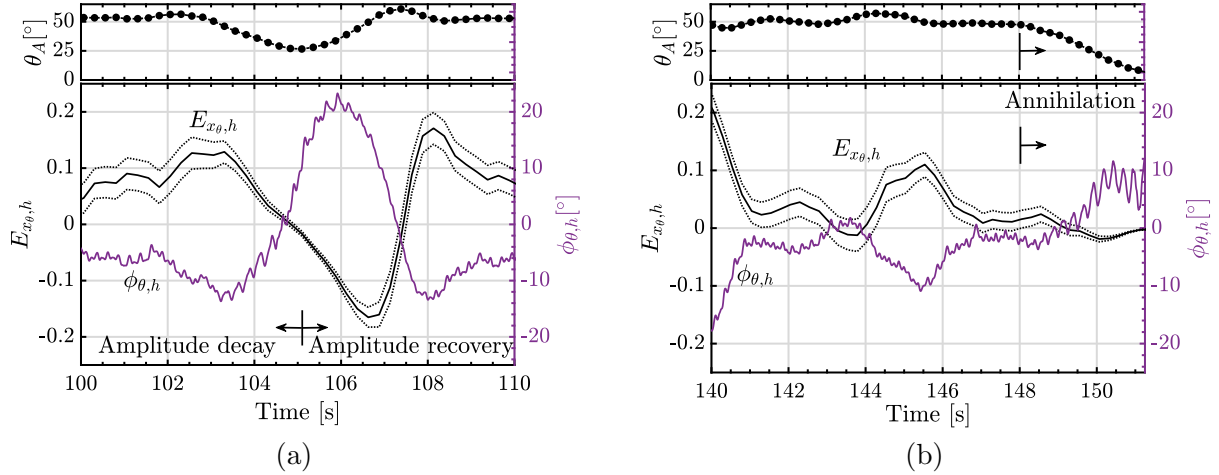


Figure 5.15: Coupling energy per cycle and pitch-heave difference versus time for  $f_s/f_{LCO} = 2.98$  for the same trial during (a) recoverable amplitude decay and (b) LCO annihilation. Note,  $\dots$  represent the 95% credible intervals.

Figure 5.16 shows the aerodynamic energy into the heave and pitch degrees of freedom during a region of amplitude decay and during LCO annihilation for the same trial. The amplitude decay region is characterized by  $E_L$  becoming negative, which indicates the aerodynamics are dissipating energy from the structure. However, during this time,  $E_M$  remains positive. Results from other recoverable amplitude decay regions show similar effects where  $E_L$  reduces to near zero or becomes negative while  $E_M$  reduces to near zero but remains positive. However, the LCO annihilation event, Fig. 5.16b, is always characterized by  $E_M$  becoming negative while  $E_L$  is either positive or negative but near zero. Additionally, from multiple trials at  $f_s/f_{LCO} = 2.98$ , the minimum pitch amplitude needed to initiate LCOs is approximately  $20^\circ$ . Therefore, the time when  $E_M$  becomes dissipative occurs a few cycles before  $\theta_A$  drops below  $20^\circ$ . Combining with the joint recurrence analysis,  $E_M$  becoming negative occurs because the bluff body wake causes adverse aerodynamic interactions. Therefore, a loss of aerodynamic energy in the heave and pitch degrees of freedom combined with pitch energy transferring to the heave degree of freedom results in a precipitous decline of system energy and eventual amplitude cessation.

## 5.5 Interim Conclusions

The work presented here investigated aerodynamically annihilated aeroelastic limit cycle oscillations due to superharmonic interactions. The aerodynamic limit cycle annihilation phenomenon is caused by the presence of upstream vortical disturbances on the wing. The results show that limit-cycle annihilation depends on the magnitude of the mass coupling and the proximity of the bluff body shedding frequency to the third harmonic of the primary limit-cycle oscillation frequency. Given these conditions, the large amplitude limit cycle oscillation returns to its equilibrium position. Instantaneous frequency analysis through the wavelet and Hilbert transforms shows that large amplitude modulations are caused by the excitation and convergence of the limit cycle to a different limit-cycle frequency that results in large energy dissipation from the structure. Therefore, the kinematic requirements for limit-cycle annihilation are the convergence of the aeroelastic frequencies onto a different limit cycle frequency and a small negative pitch-heave phase difference.

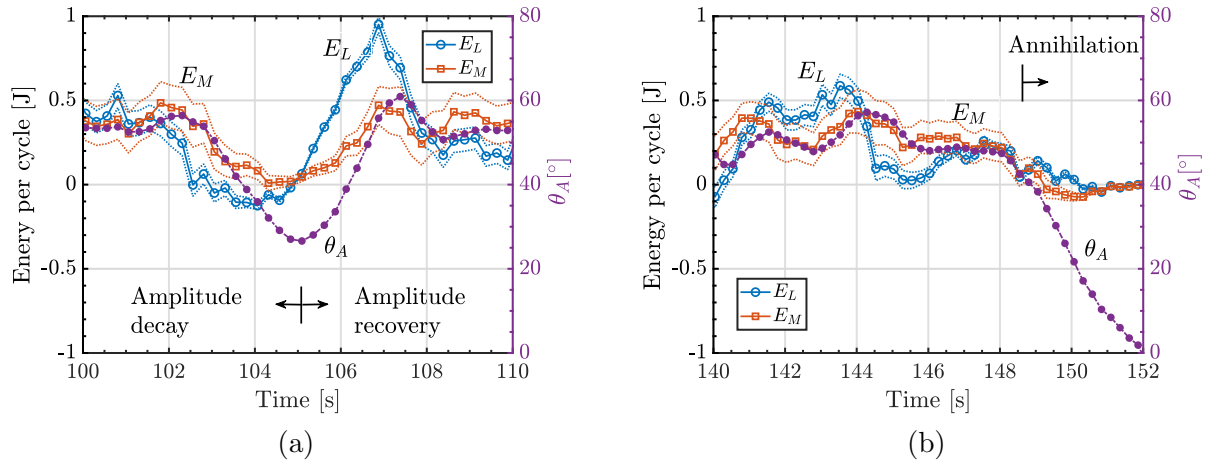


Figure 5.16: Aerodynamic energy per cycle and pitch amplitude versus time for  $f_s/f_{LCO} = 2.98$  for the same trial during amplitude (a) recoverable decay and (b) LCO annihilation.

Combined with the results from the kinematic and bluff body joint recurrence, the results suggest that a disruption in unsteady flow features over the wing result in limit cycle annihilation. These results present unique aerodynamic interactions between vortex wakes and aeroelastic limit cycle oscillations and provide insight that can benefit engineers designing aeroelastic systems in vortex-dominated flows.

## Chapter 6

# Aeroelastic Inverse: Estimation of Aerodynamic Loads during Large-Amplitude Limit-Cycle Oscillations

This chapter presents an algorithm to compute the aerodynamic forces and moments of an aeroelastic wing undergoing large amplitude heave and pitch limit cycle oscillations. The technique is based on inverting the equations of motion to solve for the lift and moment experienced by the wing. Bayesian inferencing is used to estimate the structural parameters of the system and generate credible intervals on the lift and moment calculations. The inversion technique is applied to study the affect of mass coupling on limit cycle oscillation amplitude. Examining the force, power, and energy of the system, the reasons for amplitude growth with wind speed can be determined. The results demonstrate that the influence of mass coupling on the pitch-heave difference is the driving factor in amplitude variation. The pitch-heave phase difference not only controls how much aerodynamic energy is transferred into the system but also how the aerodynamic energy is distributed between the degrees of freedom.

### 6.1 Chapter Introduction

While researchers such as [105] measured forces using piezoelectric force balances and [22] measured forces using piezoresistive pressure transducers, both technologies implementation in aeroelastic experiments is not widespread. Although there are applications of direct force measurement in hydroelastic systems, such as [106], the Reynolds number of such experiments is typically lower than the desired Reynolds number of aeroelastic testing. Limited use of direct force measurement or pressure transducers is due to challenges developing models of the inertial and stiffness contributions in the piezoelectric force balances, or potentially prohibitive wing geometry in the case of the pressure transducers. Alternatively, a few researchers have explored inverting the dynamic equations to solve for the lift and moment based on kinematic measurements, called the aeroelastic inverse (AEI) method. [107, 108, 27, 109], [110], and [111] have each applied AEI methods to their systems. As an example of the efficacy of the AEI method, [107] demonstrated that the nonlinear

moment associated with transitional Reynolds number aeroelastic LCOs is caused by laminar separation bubbles. We expand off AEI principles from previous researchers by combining uncertainty quantification techniques into the AEI method to build credible intervals on the aerodynamic force and moment of a two degree-of-freedom wing undergoing large amplitude LCOs influenced by stall phenomena.

The AEI method presented here incorporates statistical uncertainties from position, velocity, acceleration, and system parameter estimates directly into the inverse calculations for aerodynamic lift and moment during large amplitude heave and pitch motions. The stiffness, damping, friction, and mass coupling parameters in the aeroelastic system are estimated using the Delayed Rejection Adaptive Metropolis (DRAM) algorithm [99], as part of a Markov Chain Monte Carlo (MCMC) simulation. The parameter estimates from the DRAM algorithm represent a distribution of acceptable parameter values. The AEI method is validated against measured lift and moment from aeroelastic motion profiles prescribed in the Air Force Research Lab (AFRL) water tunnel at Wright-Patterson Air Force Base. The utility of the AEI method is demonstrated by investigating the affects of pitch-heave mass coupling on stall, power flow, and the motion kinematics in large amplitude pitch-heave LCOs. The power and force analysis demonstrate that the correlation between heave and pitch amplitude and pitch-heave phase difference is not causal. Additionally, the results demonstrate how pitch-heave phase difference not only controls the aerodynamic energy transfer but also the distribution of aerodynamic energy between the heave and pitch degrees of freedom. It is found that the distribution of aerodynamic energy is crucial in understanding how the LCO amplitude varies with wind speed. Furthermore, it is found that increased mass coupling does not equate to more energy transfer between the degrees of freedom.

## 6.2 Aeroelastic Inverse Method

The aeroelastic apparatus discussed in Chapter 3 and shown in Figure 3.2, is modeled as a coupled two degree-of-freedom mass-spring-damper system. The aeroelastic equations of motion derived previously in [112] are reproduced in Eqns. (1) and (2),

$$m_{total}\ddot{h} + m_w b x_\theta \dot{\theta}^2 \sin(\theta) - m_w b x_\theta \ddot{\theta} \cos(\theta) + k_h h + c_h \dot{h} + F_f \text{sign}(\dot{h}) = C_L \frac{1}{2} \rho U_\infty^2 c S \quad (1)$$

$$I_\theta \ddot{\theta} - m_w b x_\theta \cos(\theta) \ddot{h} + k_\theta(\theta) \theta + c_\theta \dot{\theta} + M_f \text{sign}(\dot{\theta}) = C_M \frac{1}{2} \rho U_\infty^2 c^2 S \quad (2)$$

Where the  $(\dot{\quad})$  notation is used for time derivatives.  $m_{total}$  is the sum of  $m_h$  and  $m_w$ ,  $m_h$  is the mass of all translating but non-rotating components (e.g. the carriages),  $m_w$  is the mass of all rotating parts.  $I_\theta$  is the moment of inertia about the elastic axis.  $x_\theta$  is the distance between the elastic axis and center of mass of rotating parts, nondimensionalized by half chord,  $b$ , and with positive defined towards trailing edge.  $k_h$  and  $k_\theta$  are the effective stiffnesses in the heave and pitch DOF, respectively.  $c_h$  and  $c_\theta$  are the viscous damping coefficients for the heave and pitch DOF, respectively.  $F_f$  and  $M_f$  are the force and moment due to kinetic friction for the pitch and heave DOF, respectively. Finally,  $C_L$  is the aerodynamic force coefficient in the heave direction,  $C_M$  is the aerodynamic moment coefficient,  $\rho$  is the air density, and  $U_\infty$  is the freestream wind speed. The AEI method is applied by solving Eqn. 1 and 2 for  $C_L$  and  $C_M$ , where all the state variables  $\vec{X} = \{h, \dot{h}, \ddot{h}, \theta, \dot{\theta}, \ddot{\theta}\}$ , are experimental measurements. This results in

$$C_L = \frac{2}{\rho U_\infty^2 c S} \left[ m_{total} \ddot{h} + m_w b x_\theta \dot{\theta}^2 \sin(\theta) - m_w b x_\theta \ddot{\theta} \cos(\theta) + k_h h + c_h \dot{h} + F_f \text{sign}(\dot{h}) \right] \quad (3)$$

$$C_M = \frac{2}{\rho U_\infty^2 c^2 S} \left[ I_\theta \ddot{\theta} - m_w b x_\theta \cos(\theta) \ddot{h} + k_\theta(\theta) \theta + c_\theta \dot{\theta} + M_f \text{sign}(\dot{\theta}) \right] \quad (4)$$

Parameter estimation is done using data from free decay experiments. Experiments with and without the wing attached were performed to determine if there was significant aerodynamic interaction during the free decays. The results found negligible aerodynamic interaction, thus, for free decay, (1) and (2) reduce to

$$m_{total} \ddot{h} + m_w b x_\theta \dot{\theta}^2 \sin(\theta) - m_w b x_\theta \ddot{\theta} \cos(\theta) + k_h h + c_h \dot{h} + F_f \text{sign}(\dot{h}) = 0 \quad (5)$$

$$I_\theta \ddot{\theta} - m_w b x_\theta \cos(\theta) \ddot{h} + k_\theta(\theta) \theta + c_\theta \dot{\theta} + M_f \text{sign}(\dot{\theta}) = 0 \quad (6)$$

and can be used to determine the unknown parameters in the system. We next develop expressions for the system energy transfer from the flow into the structure.

We formulate the system energies following ([113]) to examine how aerodynamic energy, power, and energy transfer between the two degrees of freedom affect the LCO amplitude. The kinetic energy of the system is given by

$$KE = \frac{1}{2} m_h (\bar{\vec{v}}_{cm/o} \cdot \bar{\vec{v}}_{cm/o}) + \frac{1}{2} m_w (\bar{\vec{v}}_{cm/o} \cdot \bar{\vec{v}}_{cm/o}) + \frac{1}{2} I_{cm} \dot{\theta}^2 \quad (7)$$

where  $\bar{\vec{v}}_{cm/o}$  is the velocity of the center of mass relative to the inertial frame, and  $I_{cm}$  is the inertia about the center of mass of the wing. The velocity of the wing center of mass,  $\bar{\vec{v}}_{cm/o}$ , can be found by differentiating the position of the center of mass,  $\bar{\vec{x}}$ ,

$$\bar{\vec{x}} = -b x_\theta \cos \theta \hat{i} + h - b x_\theta \sin \theta \hat{j}, \quad \bar{\vec{v}}_{cm/o} = \dot{\theta} b x_\theta \sin \theta \hat{i} + \dot{h} - \dot{\theta} b x_\theta \cos \theta \hat{j} \quad (8)$$

Combining Eqns. 7-8 the total kinetic energy is

$$KE = \frac{1}{2} m_{total} \dot{h}^2 - m_{wing} b x_\theta \cos(\theta) \dot{\theta} \dot{h} + \frac{1}{2} m_{total} I_\theta \dot{\theta}^2 \quad (9)$$

The first and last terms represent the kinetic energy in the heave and pitch degrees of freedom, respectively. The middle term is the kinetic energy due to the coupling between the two degrees of freedom. The potential energy is found by integrating the restoring forces in the heave and pitch degrees of freedom,

$$U = \int_0^h k_h h dh + \int_0^\theta M_{k_\theta}(\theta) d\theta \quad (10)$$

Evaluating the flow of energy into the aeroelastic structure from the aerodynamic forces, the aerodynamic power is given by

$$P_L = C_L \frac{1}{2} \rho U^2 c S \dot{h}, \quad P_M = C_M \frac{1}{2} \rho U^2 c^2 S \dot{\theta} \quad (11)$$

where  $P_L, P_M$  are positive when energy is being added to the structure, and negative when the aerodynamic forces are dissipating energy from the structure. Integrating the power flow over a cycle gives the aerodynamic energy input or dissipated per cycle.

$$E_L = \int_0^T P_L dt, \quad E_M = \int_0^T P_M dt \quad (12)$$

Where  $T$  is the oscillation period. Since wind speed is an independent variable in the experiment used to control the kinetic energy of the flow,  $E_L$  and  $E_M$  are translated to a cycle-average aerodynamic efficiency, following a similar definition from [114]. The aerodynamic efficiency is,

$$\eta_{L,M} = \frac{E_{L,M}}{(1/2)T\rho U_\infty^3 dS} \quad (13)$$

where  $d$  is the largest peak to peak excursion of any point on the wing. Additionally, the coupling energy transfer is found by multiplying the mass coupling terms in Eqn. 1 and Eqn. 2 by  $\dot{h}$  and  $\dot{\theta}$ , respectively. The coupling energy provides insights into the distribution of aerodynamic energy throughout the structure. The coupling energy per cycle for each degree of freedom is given by:

$$E_{x_{\theta,h}} = \int_0^T (m_w b x_{\theta} \ddot{\theta} \cos \theta - m_w b x_{\theta} \dot{\theta}^2 \sin(\theta)) \dot{h} dt, \quad E_{x_{\theta,\theta}} = \int_0^T m_w b x_{\theta} \ddot{h} \cos(\theta) \dot{\theta} dt \quad (14)$$

## 6.3 System Identification and Uncertainty Quantification

There are numerous techniques used to estimate the structural parameters in a typical aeroelastic system. [107], and [27] estimated damping parameters using log decrement methods. [27] modified existing log decrement methods to account for both friction and viscous damping. [111] employed a hybrid force measurement and used an equivalent energy principle to identify nonlinear parameters. [24] implemented a modified unifying least squares method ([115]) to estimate viscous damping coefficients. However, maximum-likelihood methods only provide a point estimate, whereas a Bayesian framework produces inferred parameter distributions which accounts for measurement and modeling errors, providing more information about parameter uncertainties. [116] used MCMC Bayesian inferencing to estimate the stiffness and damping parameters of their system. MCMC methods construct Markov chains whose stationary distribution is the posterior distribution. Evaluating realizations of the converged Markov chains will sample the posterior parameter distributions conditioned on observed measurements ([117]). However, the evaluation of the normalization constant in MCMC typically requires high-dimensional integration realized through quadrature techniques or Markov Chain Monte Carlo methods and therefore it is computationally intensive to apply Bayes Theorem to complex models. [116]’s approach is well suited to our coupled free decay model because it easily incorporates the system nonlinearities, gives credible intervals on the estimated parameters, and allows us to propagate the uncertainties through to the model response. Our approach couples MCMC Bayesian inverse methods with load cell measurements to determine the form and values of the structural parameters. Those values are then implemented to estimate the aerodynamic force and moment coefficients during limit cycle oscillations.

### 6.3.1 Model Selection and Sensitivity Analysis

A model of the structural stiffness and damping is required before MCMC parameter estimation can occur. A series of load cell and free decay measurements were used to develop a model of the

system. The heave stiffness was measured via tensile testing of the heave springs using an Instron 4400R machine, while an ATI Gamma six axis load cell was used to measure the moment generated by the pitch spring and pulley arrangement. As demonstrated in Figure 6.1, the restoring moment measurements capture a piece-wise nonlinearity when the pitch angle is high enough such that the springs on one side of the pulley lose tension. Additionally, during pitch-only and coupled free decay tests where the initial deflection angle did not go into the piece-wise stiffness regime, a shift in the decay frequency at low pitch angles was observed. An exponential softening model was incorporated into the piecewise stiffness model to increase the accuracy of the numerical simulations, over a constant stiffness model, by capturing this experimentally observed phenomenon. A feature of the softening exponential model, is that it incorporates a negative exponent such that the terms lose influence as the pitch angle is increased, with little to no influence on the pitch stiffness when  $\theta > 6^\circ$ . The pitch spring moment equation is

$$M_{k_\theta}(\theta) = \begin{cases} K_{\theta_L}(\theta)\theta & \text{if } |\theta| < \theta_{P_1} \\ \text{where } K_{\theta_L}(\theta) = C_1\theta^{2\beta} + C_2\theta^\beta + C_3 & \\ K_{\theta_H}(\theta_{T_1} + (\theta - \theta_{P_1})) & \text{if } \theta_{P_1} \leq |\theta| < \theta_{P_2} \\ K_{\theta_S}(\theta_{T_2} + (\theta - \theta_{P_2})) & \text{if } \theta_{P_2} \leq |\theta| \\ \text{where } K_{\theta_S} = K_{\theta_L}(\theta_{P_1})/2 & \end{cases} \quad (15)$$

where  $K_{\theta_L}$ ,  $K_{\theta_H}$  and  $K_{\theta_S}$  are the spring constants for the three different regions and  $\theta_{P_{1,2}}$ ,  $\theta_{T_{1,2}}$  are the geometric transition angles and modified transition angles to ensure a continuous moment when the stiffness changes. The modified transition angles are defined as

$$\theta_{T_1} = \frac{K_{\theta_L}(\theta_{P_1})\theta_{P_1}}{K_{\theta_H}}, \quad \theta_{T_2} = \frac{K_{\theta_H}(\theta_{T_1} + \theta_{P_2} - \theta_{P_1})}{K_{\theta_S}}; \quad (16)$$

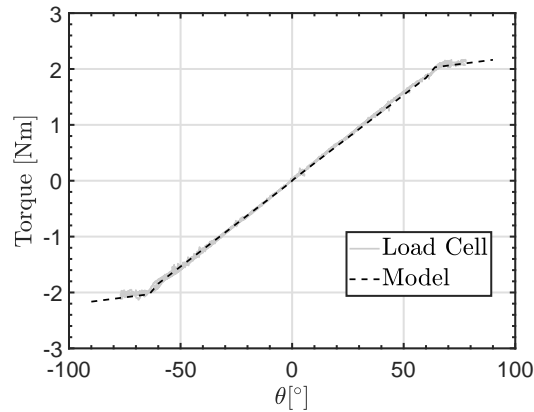


Figure 6.1: Spring torque measurements with load cell compared to Eqn. 15

Based on the envelope of the free decay response, friction along with viscous damping dissipate energy from the system. Therefore, the form of the stiffness and dissipation elements have been determined and are incorporated into Eqn 1-6. The unknown structural parameters in our model are the set  $q = \{k_h, C_1, C_2, C_3, \beta, c_h, c_p, F_f, M_f, x_\theta\}$ . However, from Eqn. (15), the contributions from  $\{C_1, C_2, \beta\}$  cannot be individually distinguished through a Bayesian framework. As a result,

the parameter subset selection (PSS) algorithm described in [118, 119] is used to evaluate the relative importance of the parameters  $\{C_1, C_2, \beta\}$  and determine which parameter to retain. The PSS method is based on a quasi-global gradient analysis evaluating the effect of small perturbations in parameters,  $q$ , on the overall model response. A scaled gradient method is employed to account for the differences that may arise in parameter scales. The PSS method builds a sensitivity matrix of the form

$$R = \begin{bmatrix} \frac{\partial Q_I}{\partial q_1}(t_1; q^*) & \cdots & \frac{\partial Q_I}{\partial q_p}(t_1; q^*) \\ \vdots & & \vdots \\ \frac{\partial Q_I}{\partial q_1}(t_N; q^*) & \cdots & \frac{\partial Q_I}{\partial q_p}(t_N; q^*) \end{bmatrix}, \quad (17)$$

Where  $Q_I$  is a quantity of interest, specifically  $h(t)$ ,  $\theta(t)$ ;  $q^*$  represents a nominal set of parameter values. The PSS algorithm compares the the eigenvalues of the Fisher Information matrix ( $R^T R$ ) with respect to a specific threshold to determine parameter significance. The results from the PSS algorithm are shown in Table 6.1. The algorithm is a sifting process that removes the parameter most aligned with the least informative eigenvector. After a parameter is removed, the eigenvalues and eigenvectors are recomputed and the sifting process repeated until no eigenvalue is below the threshold. The parameter  $\beta$  should be retained for Bayesian inferencing based on the results of the PSS algorithm, so our reduced parameter set is

$$q = \{k_h, C_3, \beta, c_h, c_p, F_f, M_f, x_\theta\} \quad (18)$$

Table 6.1: Results from Parameter Subset Selection Algorithm with the quasi-global sensitivity matrix to determine least influential parameters of  $M(\theta)$ .

Iteration	$ \lambda_1 $	Eigenvector $\Delta\theta_1$ with corresponding parameters		
		$C_1$	$C_2$	$\beta$
1	1.7e-03	9.99e-01	-4.66e-02	-2.94e-02
2	6.1e-02	—	-9.12e-01	-4.11e-01
3	1.00	—	—	1.00
Result: $C_1, C_2$ are less influential than $\beta$ .				

The values of the structural parameters  $m_{total}$ ,  $m_w$ ,  $I_\theta$ ,  $\theta_P$  are fixed for Bayesian inferencing, with values provided in Table 6.2.

Table 6.2: Fixed structural parameter values.

Parameter	Description	Config - 1	Config - 2
$m_{total}$	Total mass all moving parts (kg)	3.268	
$m_w$	Mass of all rotating parts (kg)	1.609	
$I_\theta$	Pitching inertia about elastic axis ( $\text{kg} \cdot \text{m}^2$ )	5.32e-03	6.16e-03
$c$	Chord length (m)	0.15	
$S$	Span length (m)	0.6	
$\theta_{P_1}$	Transition angles for $k_\theta$ ( $^\circ$ )	60	
$\theta_{P_2}$	Transition angles for $k_\theta$ ( $^\circ$ )	64	
$C_1$	Pitch stiffness coefficient (Nm/rad)	6.86e-04	7.90e-04
$C_2$	Pitch stiffness coefficient (Nm/rad)	9.74e-02	1.13e-01

### 6.3.2 Uncertainty Quantification

A Bayesian inference framework is implemented to estimate the parameters and quantify their uncertainty for both mass coupling configurations. Utilizing a Bayesian framework serves two purposes: (1) to construct marginal densities for the parameter set  $q$  in Eqn. 18 and (2) to assess parameter identifiability and correlation. In Bayesian inverse problems, parameters are considered to be random variables whose densities incorporate information obtained through acquired measurements ([120]). The solution to this inverse problem is to find the posterior density  $\mathcal{P}(q|D(t))$  whose marginal densities of  $q$  reflect the distribution of parameters based on the measured observations. From Bayes' relation we observe

$$\mathcal{P}(q|D(t)) = \frac{\mathcal{P}(D(t)|q)\mathcal{P}_0(q)}{\mathcal{P}(D(t))} = \frac{\mathcal{P}(D(t)|q)\mathcal{P}_0(q)}{\int_{\mathbb{R}^p} \mathcal{P}(D(t)|q)\mathcal{P}_0(q) dq} \quad (19)$$

where  $\mathcal{P}(D(t)|q)$  is the likelihood function. The prior function  $\mathcal{P}_0(q)$  encodes information known *a priori* about the parameters  $q$ . The denominator is a normalization term that ensures the probability distribution integrates to unity. The statistical model employed is assumed to have identically and independently distributed (i.i.d.) errors,  $\varepsilon_i$

$$D_i(t) = f_i(q) + \varepsilon_i, i = 1, \dots, n \quad (20)$$

This is an additive noise model, where the data observed,  $D_i = \{h(t), \theta(t)\}$ , is assumed to be generated from the parameter-dependent model,  $f_i(q)$ , (Eqns. 5, 6). The likelihood function utilized is the sum-of-squares likelihood, which has the form.

$$\mathcal{P}(D(t)|q) = \frac{1}{(2\pi\sigma^2)^{N/2}} \exp\left(\frac{-\sum_{i=1}^N [D_i(t) - f(q_i)]^2}{2\sigma^2}\right) \quad (21)$$

where  $\sigma^2$  is the variance estimate and  $N$  is the number of data points. Structural parameter estimates are determined in MATLAB using the Delayed Rejection Adaptive Metropolis (DRAM) MCMC algorithm ([99, 100]). DRAM extends the traditional Metropolis-Hastings algorithm by combining two ideas, delayed rejection and an adaptive covariance. The delayed rejection step considers second or higher order steps after rejected candidates allowing for local adaptation in the Markov chain and increased candidate acceptance requiring fewer model evaluations to converge. The Adaptive Metropolis updates the proposed distribution by updating the covariance matrix using the past chain, which helps the chain to mix more quickly.

### 6.3.3 Model Calibration

Initial estimates of  $k_h$  are found from tensile test measurements, while the other initial parameter estimates are found using MATLAB's `fmincon.m` routine. Initial estimates are only provided to speed up the convergence of the model calibration. A non-informative uniform prior parameter distribution is employed with physical constraints, e.g. positive damping. Marginal densities are constructed with a kernel density estimate algorithm after the chains have converged to the fixed posterior distribution. Figure 6.2 presents joint densities and marginal posterior histograms. The parameters that have correlation are chosen for representation in Figure 6.2a-c, while the other

two parameters are shown in Figure 6.2d. The marginal posterior densities show each of the parameters apart from the heave friction are unimodal and symmetric. The pairwise correlations demonstrate that correlation exists between damping and friction parameters, as well as the pitch spring moment parameters. In this case, Bayesian parameter inference is useful over traditional least-squares optimization schemes because correlated parameters represent local minimums. No correlations are single-valued however, supporting the conclusion that all the parameters were identifiable given the free decay data.

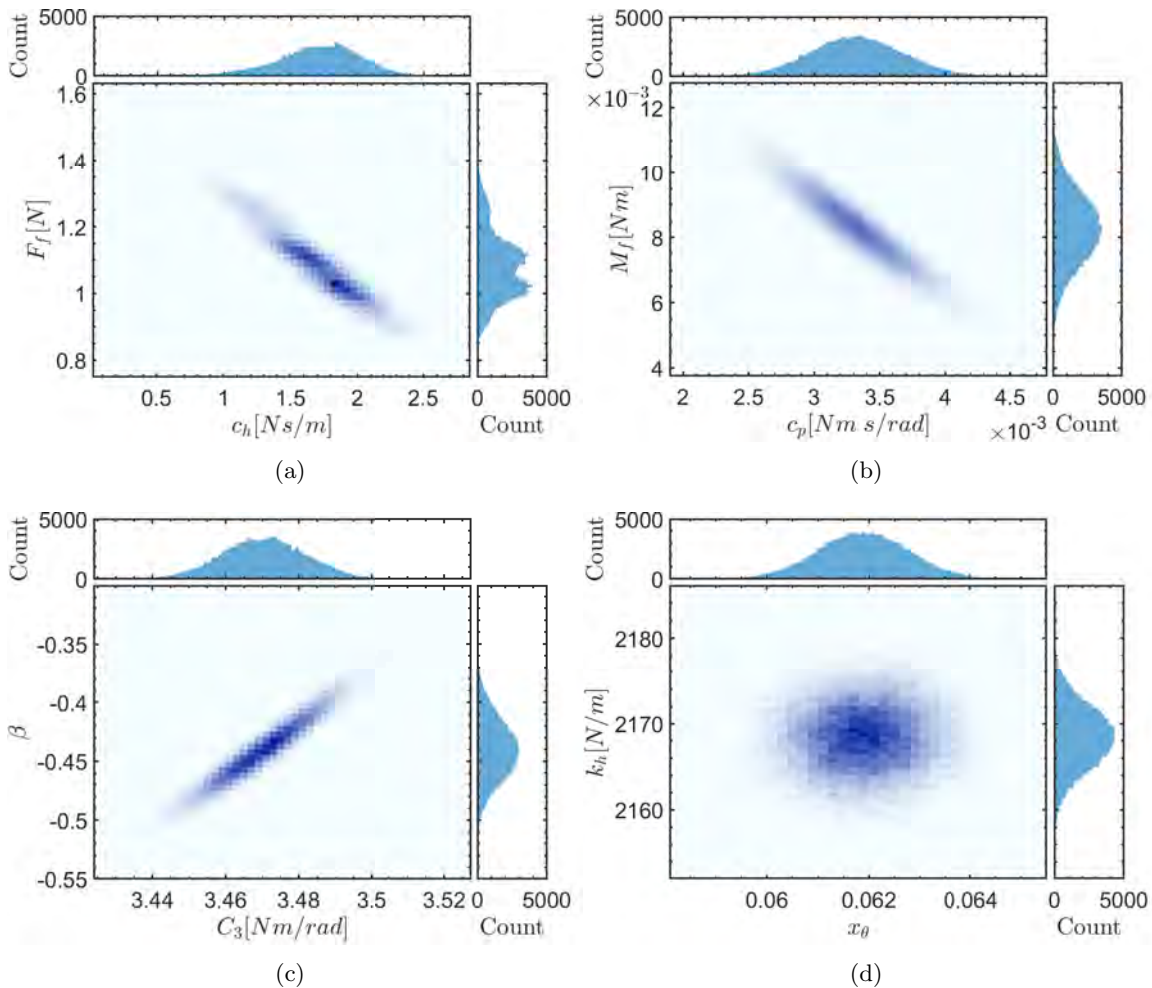


Figure 6.2: Joint densities and marginal posterior histograms for Config - 1

Figure 6.3 shows the predicted system responses using the maximum a posteriori (MAP) parameter estimate and prediction intervals (PI), along with the experimental data to illustrate the accuracy of the resulting system dynamics. The MAP estimate is given by the parameter combination that corresponds to the maximum of the posterior distribution (maximum of main diagonal elements in Figure 6.2). This value is closely related to the maximum likelihood estimator (MLE) that maximizes the likelihood or, equivalently, minimizes the sum-of-squares error. The prediction intervals are constructed by sampling from the MCMC parameter chains, incorporating measurement uncertainty, and computing the corresponding model response. The results demonstrate that the model captures the structural response and shows the estimates of the parameters are valid.

Table 6.3: MAP estimates and credible intervals for the Config - 1 and Config - 2.

Parameter	Config - 1		Config - 2	
	MAP	95% Credible Interval	MAP	95% Credible Interval
$c_h$ [Ns/m]	1.73e+00	[1.13e+00, 2.19e+00]	2.08e+00	[1.54e+00, 2.66e+00]
$c_p$ [Nm s/rad]	3.36e-03	[2.75e-03, 3.93e-03]	3.77e-03	[3.045e-03, 4.91e-03]
$F_f$ [N]	1.02e+00	[9.29e-01, 1.28e+00]	1.77e+00	[1.56e+00, 1.90e+00]
$M_f$ [Nm]	8.19e-03	[6.32e-03, 1.02e-02]	9.56e-03	[6.43e-03, 1.16e-02]
$x_\theta$	6.21e-02	[6.04e-02, 6.34e-02]	9.44e-02	[9.09e-02, 9.84e-02]
$k_h$ [N/m]	2.17e+03	[2.16e+03, 2.17e+06]	2.18e+03	[2.17e+03, 2.19e+03]
$C_3$ [Nm/rad]	3.47e+00	[3.45e+00, 3.49e+00]	3.65e+00	[3.62e+00, 3.69e+00]
$\beta$	-4.39e-01	[-4.82e-01, -3.94e-01]	-4.11e-01	[-4.59e-01, -3.32e-01]

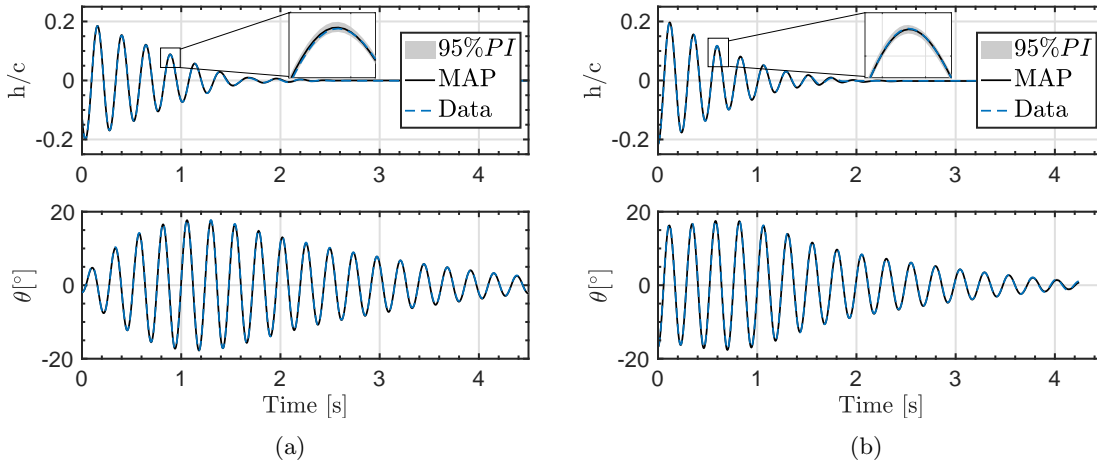


Figure 6.3: Free decay comparison of experiment and model for (a) Config - 1 and (b) Config - 2.

### 6.3.4 Aerodynamic Force Prediction and AEI Validation

After finding the parameter distributions, the next step in this AEI method is to compute velocity and acceleration from the heave and pitch position data. The heave and pitch position signals include measurement uncertainty as well uncertainty caused by any flexibility in the rod. The measurements between the each of the heave and pitch encoders is used to define the error bound due to any flexibility. The inclusion of this error metric resulted in an increase of  $\pm 0.1C_{L_{max}}$  versus not including the error metric at the highest wind speeds tested and was negligible at lower wind speeds. The results from this analysis demonstrate that the wing acts like a rigid 2 DOF oscillator over the range of wind speeds tested. The next step is to fit a smooth curve to the signals to reduce the effects of noise while taking derivatives. Following the work of [121] and [98], a smoothing spline, using MATLAB's `spaps` command, is fit to the heave and pitch signal such that the error and roughness of the spline are minimized. The formulation proposed by [121] and [98] defines the tolerance value for use in the `spaps` command and results in smooth velocity and acceleration derivatives. For each heave and pitch measurement point, 1000 data points are generated based on the uncertainty in the heave and pitch signals. One thousand splines are fit to the heave and pitch position by randomly sampling from the data points generated to account for error induced

by curve fitting. This procedure will quantify the uncertainties in velocity and acceleration from fitting splines to the position data. Additionally, a low pass filter is applied to the heave and pitch accelerations 1 Hz below 3 times the fundamental limit cycle oscillation frequency. This low pass filter is chosen based on the comparisons done with AFRL's measured force data (Figure 6.4). The effect of the low-pass filter is similar to the cut off frequency used in Poirel and Yuan (2008)[107] for their inversion technique.

Eqns. 3-4 are used to solve  $C_L$  and  $C_M$  once the position, velocity, and acceleration signals have been processed and the parameter distributions and correlations found. The lift and moment are calculated by randomly sampling the parameter distributions,  $q$ , for a given  $\vec{X}$ . This process is repeated for every realization of  $\vec{X}$  to sufficiently sample the entire parameter space and build credible intervals on  $C_L$  and  $C_M$ . The one thousand different numerical computations are then phase-averaged to get the nominal lift and moment per oscillation cycle. The phase averaging begins when the pitch angle is at a maximum and ends when the pitch angle reaches the next maximum. The credible intervals of the phase-averaged  $C_L$  and  $C_M$  include the uncertainty in the measurement system, parameter distributions, and any cycle to cycle deviation. The phase-averaging is given by

$$C_L = \frac{1}{N} \sum_{k=1}^N C_{Lk}(t), \quad C_M = \frac{1}{N} \sum_{k=1}^N C_{Mk}(t) \quad (22)$$

where  $k$  corresponds to the  $k^{th}$  oscillation cycle and  $N$  is the number of oscillations over the recorded signal.

The efficacy of the AEI method was determined by comparing  $C_L$  and  $C_M$  estimates to direct force measurements from re-created LCO kinematics in AFRL's free surface water tunnel. In the water tunnel experiments, LCO pitch-heave time histories are played back on the actuated pitch-heave apparatus in the water tunnel as prescribed motion trajectories. The water tunnel is a horizontal free surface water tunnel with a 4:1 contraction and a 0.46x0.61m test section. The wing position is controlled via three H2W Technologies linear motors that are driven by AMC DigiFlex servo drives controlled by a Galil DMC 4040 four channel card. Hydrodynamic forces were measured by an ATI NANO-25 IP68 six component force/torque balance. More details about AFRL's experimental apparatus can be found in [122, 123, 124]. Only a small number of LCO experiments were used due to the Reynolds number and amplitude limitations of the water tunnel. Reynolds and Strouhal numbers for these LCO cases were 70,700-77,600 and 0.082-0.074 respectively. The heave and pitch signals from an LCO were phase-averaged to generate one nominal LCO cycle for recreation in AFRL's water tunnel. The nominal heave and pitch cycle is repeated 70 times in the water tunnel to generate sufficient  $C_L$ ,  $C_M$ , and  $C_D$  time histories for phase averaging ([125]). Figure 6.4 shows that good agreement in  $C_L$  and  $C_M$  exist between the inverse method and the prescribed motion experiments. Note that Figure 6.4 plots only the  $t/T$  range when the geometric effective angle of attack ( $\alpha_{eff}$ ), defined at the leading edge, is positive. In particular we consider the leading edge effective angle of attack based on the work of [126], who demonstrated a criticality of leading edge velocity with leading edge vortex formation. Inconsistent matching in  $C_L$  and  $C_M$  exists for negative  $\alpha_{eff}$  ( $t/T = 0.3$  and  $0.8$ ). In this time range, flow interference due to the actuator push rods in the AFRL apparatus are known to affect the vortex development over the wing when the effective angle of attack is negative. The force and moment matching between the two systems demonstrate that the AEI method captures the dominant flow physics of the aeroelastic LCO.

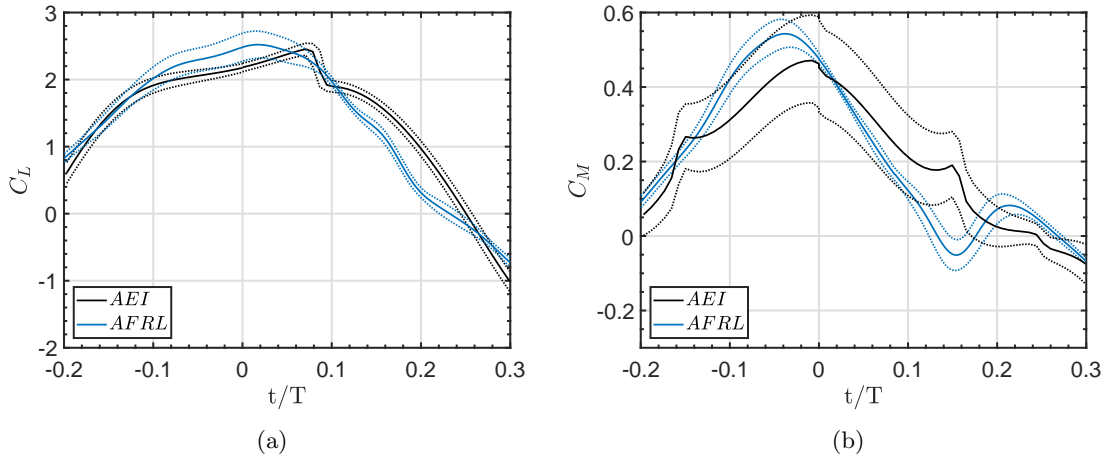


Figure 6.4: Comparison of (a)  $C_L$  and (b)  $C_M$  from AEI method and AFRL prescribed motion measurements. Reynolds number for this case is 75,600. Note,  $\dots$  represent the 95% credible interval for each measurement

## 6.4 Results and Discussion

### 6.4.1 Bifurcation Analysis

A series of experiments was performed below the LCO initiation wind speed to characterize the nature of the bifurcation. In each test, the wind speed was set to a prescribed value and the wing was released from rest with a  $40^\circ$  initial pitch angle. In subsequent tests, the wind speed was increased and the process repeated until a sustained limit cycle was observed. Time histories of the pitch and heave responses and energy of the system,  $E(t) = U(t) + KE(t)$ , over the initial potential energy input,  $E_0$ , are shown in Figure 6.5. The pitch and heave time histories of both mass coupling configurations before the onset of LCOs indicate that the pitch degree of freedom is lightly damped. At low wind speeds the heave degree of freedom is more heavily damped and shows little response; however, once the wind speed approaches the LCO onset, the aerodynamic coupling between pitch angle and lift force begins to increase the heave motion. Compared to Config - 1, the increased mass coupling in Config - 2 delays the wind speed at which LCOs formed to 6.9 m/s and the resultant LCO amplitude at LCO initiation decreased from  $\theta_A = 50^\circ$  to  $\theta_A = 46^\circ$  and  $h_A/c = 0.08$  to  $h_A/c = 0.05$ . The time histories of the energy ratio,  $E(t)/E_0$ , are useful in understanding the nature of the bifurcation. Regardless of the configuration, the wing exhibits a by-pass transition ([127]) without any evidence of transient growth effects ([128]) wherein  $E(t)/E_0 < 1$  for all stable wind speeds. A by-pass transition means that the instability is highly dependent on the initial amplitude, and is characteristic of a sub-critical hopf-bifurcation, wherein a limit cycle exists around a stable fixed point. It is hypothesized that because the initial amplitude given is well above the static stall angle, the stall features are a necessary condition for the wing to start oscillating in this sub-critical hopf-bifurcation regime.

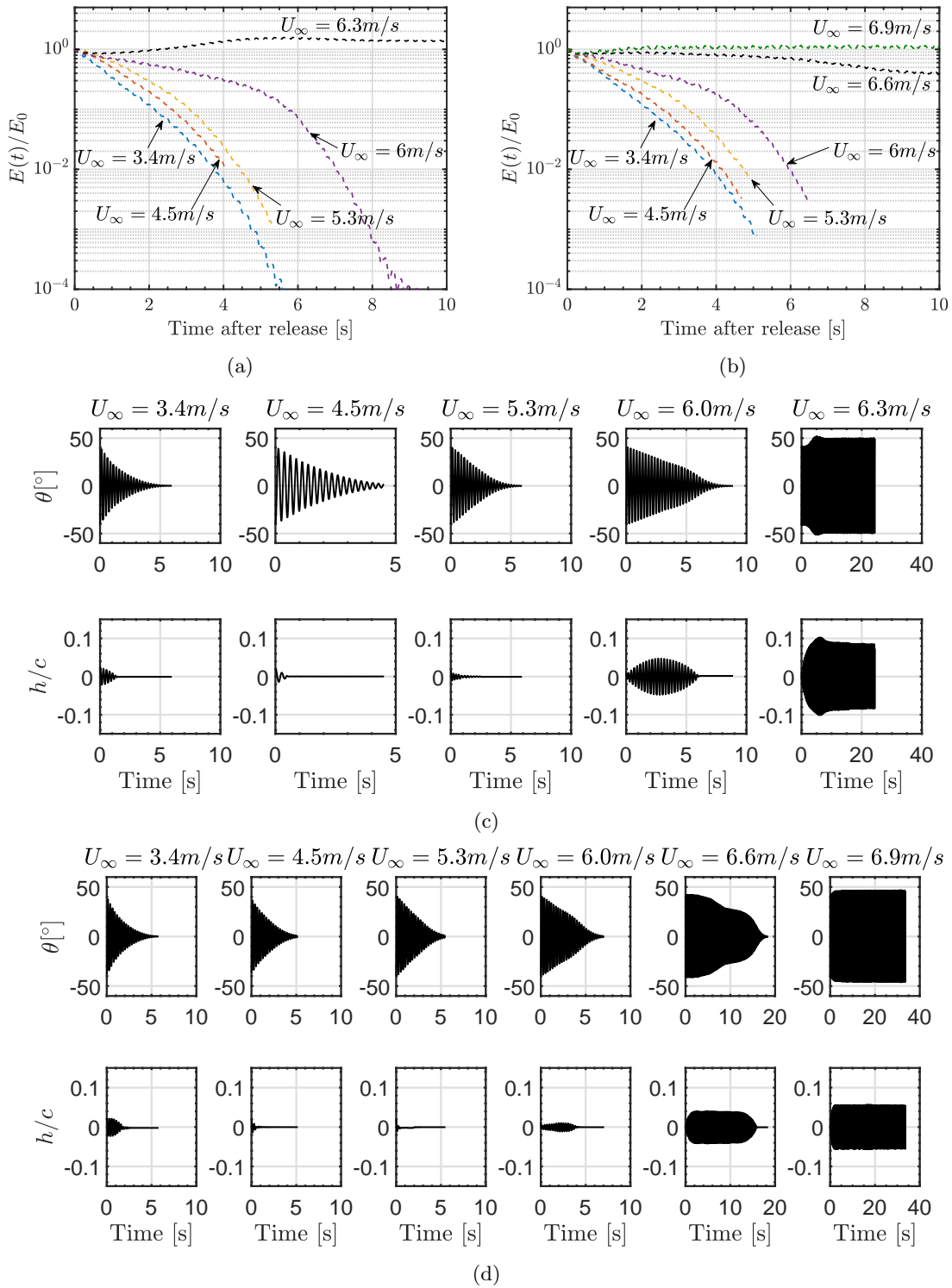


Figure 6.5:  $E(t)/E_0$  versus time for (a) Config - 1 and (b) Config - 2 for wind speeds tested up to LCO initiation. Pitch and heave response for wind speeds at and below LCO initiation for (c) Config - 1 and (d) Config - 2.

## 6.4.2 Limit-Cycle Kinematic Analysis

Beyond the bifurcation wind speed, the wing was left to oscillate for several minutes to allow the system to reach a constant amplitude LCO. The LCO motion history was then recorded for one minute at each wind speed tested. Figure 6.6 plots the mean heave amplitude, pitch amplitude, and pitch-heave phase difference as functions of free stream speed. The results show large LCO amplitudes with heave and pitch amplitudes up to  $0.52c$  and  $65^\circ$ , respectively, in Config - 1 and  $0.24c$  and  $59^\circ$  in Config - 2. In Config - 1, the heave and pitch motions undergo rapid amplitude increase with incident wind speed until the piecewise nonlinearity is reached,  $|\theta| > \theta_{p1}$ , depicted when  $\frac{\partial \bar{h}_A}{\partial U_\infty}$  and  $\frac{\partial \bar{\theta}_A}{\partial U_\infty}$  change abruptly at approximately  $7.5 \text{ m/s}$  wind speed. The deviations in amplitude over the recorded time are negligible and demonstrate an unmodulated LCO. Config - 1's LCO frequency reduces from  $4.03 \text{ Hz}$  to  $4.00 \text{ Hz}$  as wind speed is increased to  $12.1 \text{ m/s}$ , while Figure 6.6c shows that the phase difference between the pitch and heave degrees of freedom,  $\phi_{\theta,h}$ , starts at  $20^\circ$  and decreases as the wind speed increases.  $\phi_{\theta,h}$  is defined positive when pitch is leading the heave degree of freedom and negative when heave is leading pitch. In Config - 2, the heave and pitch amplitudes steadily rise as the wind speed increases, however, the pitch motions did not reach the piecewise pitch stiffness transition regime, i.e.  $|\theta| < \theta_{p1}$ , over the wind speed range tested. Comparing Config - 2 to Config - 1, the maximum heave amplitude is 2.3 times less than Config - 1. Meanwhile,  $\phi_{\theta,h}$  starts at  $0^\circ$  and decreases to  $-20^\circ$ , showing a similar trend with wind speed of Config - 1. The larger mass coupling/inertia in Config - 2 results in the LCO frequency dropping to  $3.89 \text{ Hz}$ , which further reduces to  $3.80 \text{ Hz}$  at the highest wind speed tested.

These results show that increasing the mass coupling decreases both the heave and pitch amplitudes and LCO frequency. Furthermore, the decrease in phase angle with wind speed is correlated with larger amplitude heave and pitch motions. In contrast, [24] performed a similar parameter variation and found that increased mass coupling resulted in larger heave and pitch amplitudes, while also having a strong influence on the initial phase difference between the two degrees of freedom. The contradictory trends between mass coupling and amplitude demonstrate the difficulties in drawing causal relationships from kinematic results about the mechanisms for amplitude growth. Therefore, we propose that causality can be revealed by examining the aerodynamic forces and the energy transfer into and out of the structure.

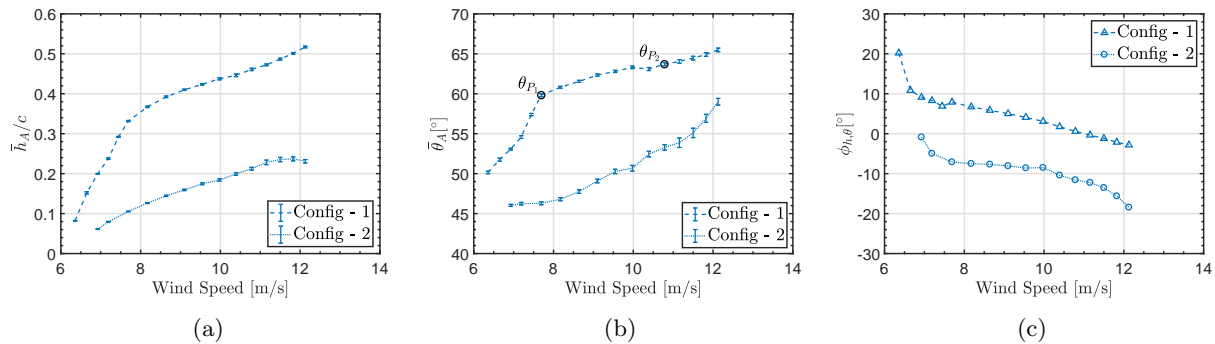


Figure 6.6: (a) Heave amplitude, (b) pitch amplitude, and (c) pitch-heave phase difference versus wind speed. Note error bars in amplitude plots represent the deviation in amplitude over the recorded time and not the measurement error.

### 6.4.3 Limit-Cycle Force Analysis

Figures 6.7-6.8 show the aerodynamic forces and moments for each configuration at 7.2, 10.0, and 12.1  $m/s$ . The aerodynamic forces and moments reach a maximum value before the maximum heave, pitch, and geometric effective angle of attack calculated at the leading edge. After  $C_L$  and  $C_M$  reach a maximum, the lift and moment decrease and reach a local minimum when heave and pitch reversal occur and  $\alpha_{eff}$  reaches a maximum. This loss of lift and moment is indicative of stalled conditions over the wing. The stalled regions highlighted in Figures 6.7-6.8 are based on the definitions from [1] and denote lift stall to when the boundary layer begins to reattach. Shortly after, the flow is in an attached flow state, illustrated by the fact that  $\partial C_L/\partial\theta$  and  $\partial C_M/\partial\theta$  match static measurements taken by AFRL (Figure 6.9b). The entire stall and recovery process occurs between  $t/T = 0.35 - 0.65$  and  $t/T = 0.85 - 1, 0.0 - 0.15$ . Additionally, altering the mass coupling does not change  $\partial C_L/\partial\theta$  or  $\partial C_M/\partial\theta$  during the attached flow regions of the time cycle because these regions are dependent on the airfoil geometry and not the wing kinematics.

Figures 6.7-6.8 also demonstrate that  $C_L$  and  $C_M$  follow a similar phase-averaged profile regardless of wind speed. The cycle fraction when maximum lift occurs changes by 5% from  $U_\infty = 7.2 m/s$  to  $U_\infty = 12.1 m/s$  for Config - 1 and Config - 2. Furthermore, the cycle fraction difference between  $C_L$  max, points  $A, A'$ , and full stall ([1]), points  $B, B'$  are similar between Config - 1 and Config - 2. Additionally, the cycle fraction difference between  $C_M$  max, points  $C, C'$ , and the corresponding moment at full stall, points  $D, D'$  are also similar between Config - 1 and Config - 2. Interestingly, maximum  $C_L$  and  $C_M$  are inversely proportional to kinematic amplitude (Figure 6.9a), with Config - 2 having larger maximum  $C_L$ , and significantly lower heave amplitude. As a result, a force-only analysis does not fully illustrate the underlying aeroelastic mechanism for LCO amplitude growth. Thus, a power and energy analysis is required to elucidate causal mechanisms for LCO amplitude.

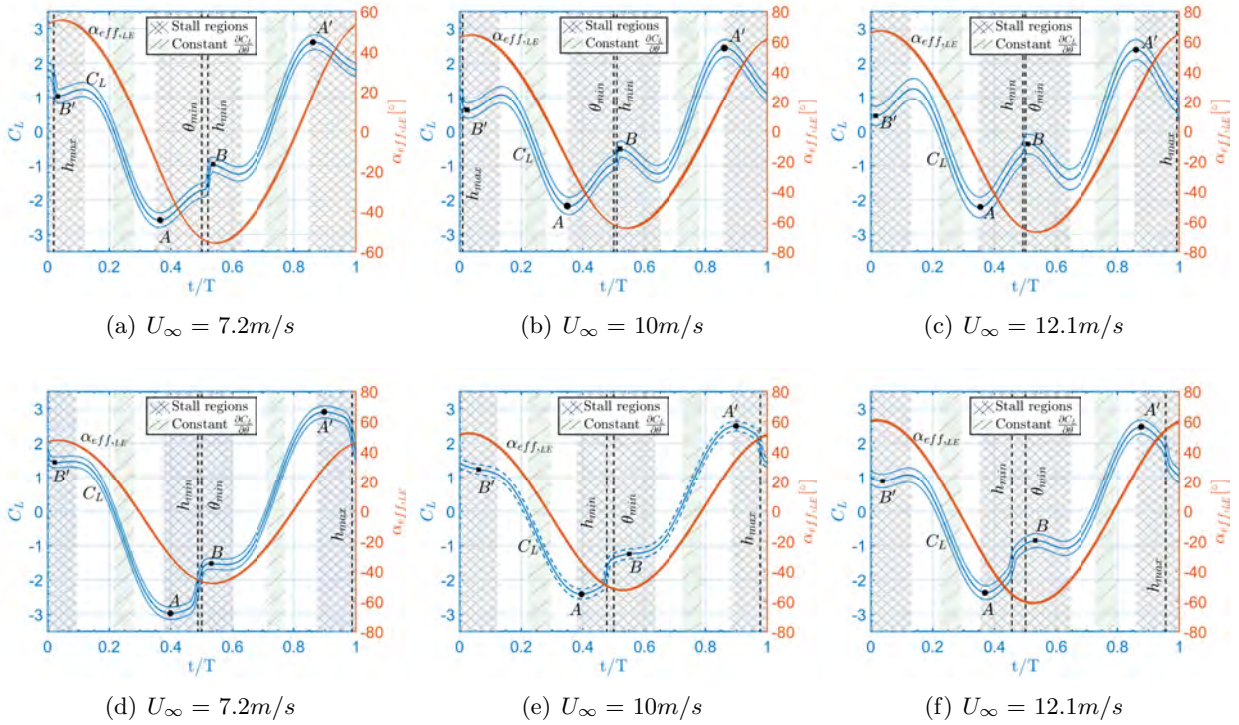


Figure 6.7: Lift coefficient and effective angle of attack versus cycle fraction for (a-c) Config - 1 and (d-f) Config - 2 at three different wind speeds.  $A, A'$  represent the maximum and minimum lift while  $B, B'$  are when full lift stall occurs ([1]). Note,  $\dots$  represent the 95% credible intervals.

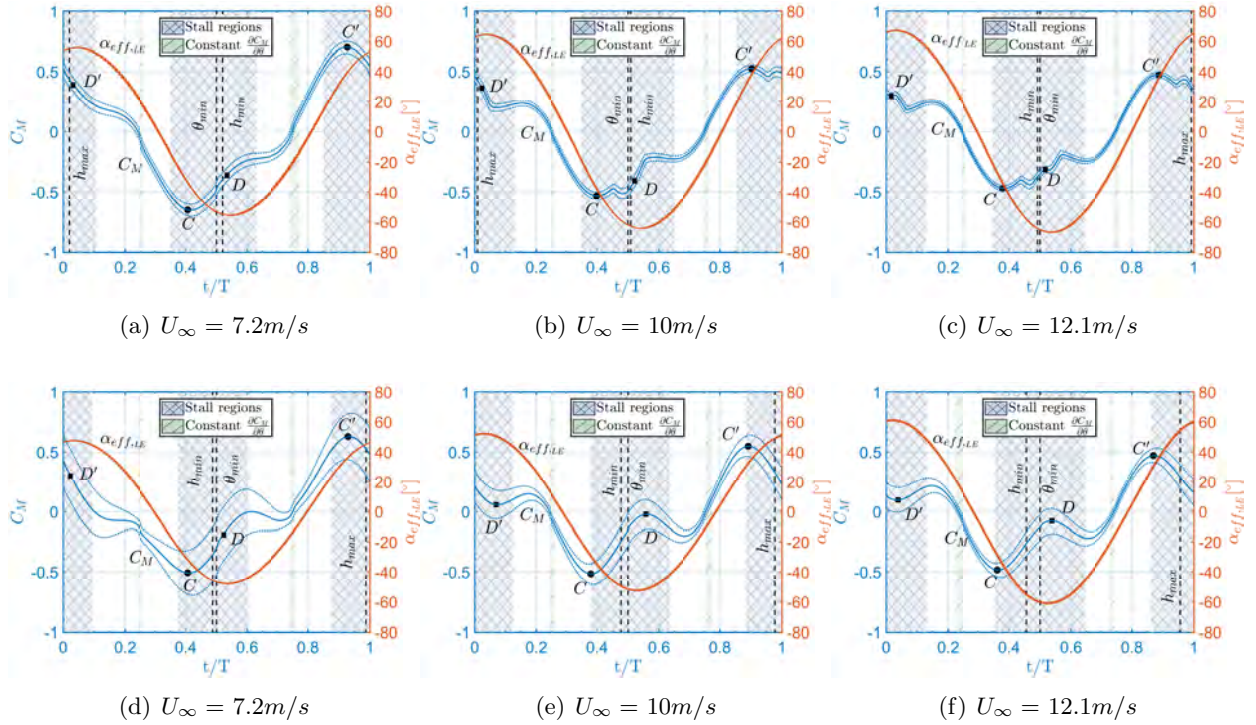


Figure 6.8: Moment coefficient and effective angle of attack versus cycle fraction for (a-c) Config - 1 and (d-f) Config - 2 at three different wind speeds.  $C, C'$  represent the maximum and minimum moment while  $D, D'$  are the corresponding moment when full lift stall occurs ([1]). Note,  $\dots$  represent the 95% credible intervals.

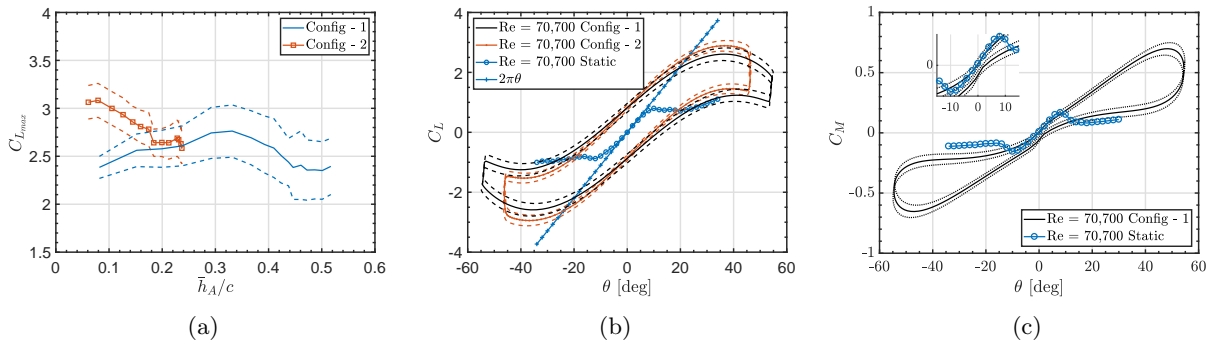


Figure 6.9: a)  $C_{L,max}$  vs  $h/c$  for both mass coupling configurations. b) Dynamic  $C_L$  versus  $\theta$  compared to thin airfoil theory and static measurements performed by AFRL. c) Dynamic  $C_M$  versus  $\theta$  compared to static measurements performed by AFRL, measured at the half chord (only Config - 1 shown for clarity). Note,  $\dots$  represent the 95% credible intervals.

#### 6.4.4 Limit-Cycle Power and Energy Analysis

The input aerodynamic energy per cycle due to lift and moment,  $E_L$  and  $E_M$ , respectively, (Figure 6.10a-b), and the power flow into the structure from the aerodynamics,  $P_L$  and  $P_M$  (Figures 6.11-

6.12), demonstrate how energy is distributed throughout the system. Figure 6.10a-b shows that  $E_L$  and  $E_M$  are positive for each wind speed tested, thus the aerodynamics are sustaining both the heave and pitch degrees of freedom. Positive energy flow into both degrees of freedom is not a necessary requirement because the mass coupling allows energy to transfer between the two degrees of freedom. The lift aerodynamic energy for Config - 1,  $E_{LConfig-1}$ , is up to twice as much as the aerodynamic moment energy in Config - 1 and the aerodynamic lift and moment energy of Config - 2. However, in Config - 2,  $E_{LConfig-2}$  is less than  $E_{MConfig-2}$  for all wind speeds tested (Figure 6.10a-b). The larger  $E_{LConfig-1}$  compared to  $E_{LConfig-2}$  is associated with increased aerodynamic efficiency (Figure 6.10c-d). The aerodynamic power analysis will elucidate the causes of increased aerodynamic efficiency.

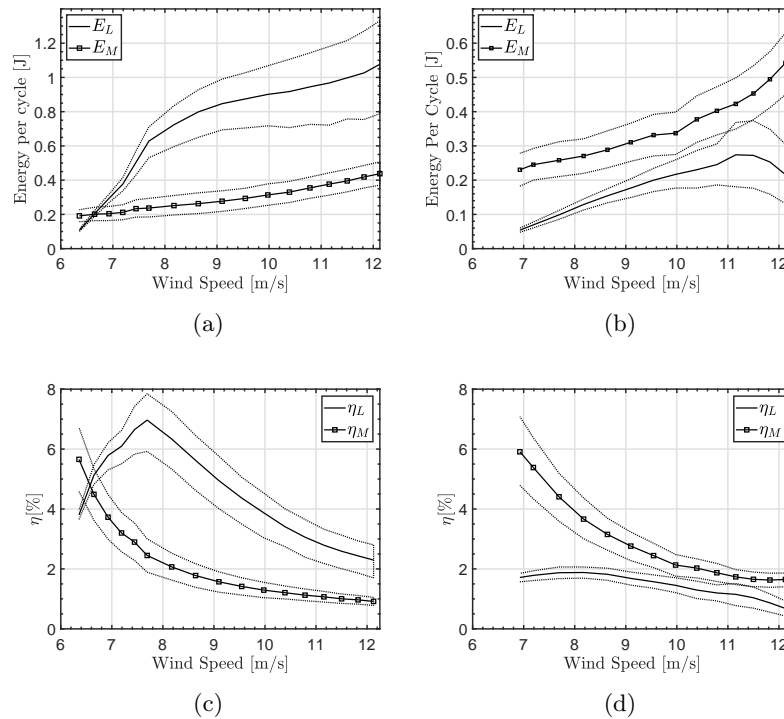


Figure 6.10: Aerodynamic energy for (a) Config - 1 and (b) Config - 2 and aerodynamic efficiency for (c) Config - 1 and (d) Config - 2 versus wind speed. Note,  $\dots$  represent the 95% credible intervals.

The cycle fractions where  $P_L$  and  $P_M$  are positive, regardless of mass coupling, correlate to constant  $\partial C_L/\partial\theta$  and  $\partial C_M/\partial\theta$  and until just after maximum lift and moment (Figures 6.11-6.12). Positive  $P_L$  and  $P_M$  after lift and moment maximum indicate that aerodynamic energy is still added to the structure during the stall regions. Aerodynamic energy dissipation, i.e. negative  $P_L$  and  $P_M$ , starts near the local minima of  $C_L, C_m$ , point B,B',D,D' in Figures 6.7 -6.8, and lasts until the flow reattaches over the wing. Furthermore, the time difference between peak  $P_L$  and peak heave velocity is significantly greater in Config - 2 than in Config - 1 (Figure 6.11), making Config - 2 less efficient. Additionally, the difference in  $P_L$  between the two configurations arises because  $\phi_{\theta,h}$  modulates the timing of the lift force with the heave motion. As  $\phi_{\theta,h}$  decreases, the heave position moves more in phase with maximum  $C_L$ , i.e. lift force is moving out of phase with heave velocity, indicating a decrease in efficient power transfer (Figure 6.7). Consequently, since the cycle fractions of maximum

$C_L$  and  $C_M$  are nearly constant (i.e. changing by only 5%), varying  $\phi_{\theta,h}$  affects how efficiently the motion kinematics capture the kinetic energy in the flow. The efficiency-phase relationship found here has been demonstrated by previous researchers for prescribed motion ([129]), and aeroelastic motion ([27]), with pitch-heave phase differences closer to  $90^\circ$  being more efficient. Conversely, since  $P_M$ ,  $E_M$ , and  $\eta_{E_M}$  are similar for each of the mass coupling configurations, a different energy transfer mechanism causes the differences in pitch amplitude.

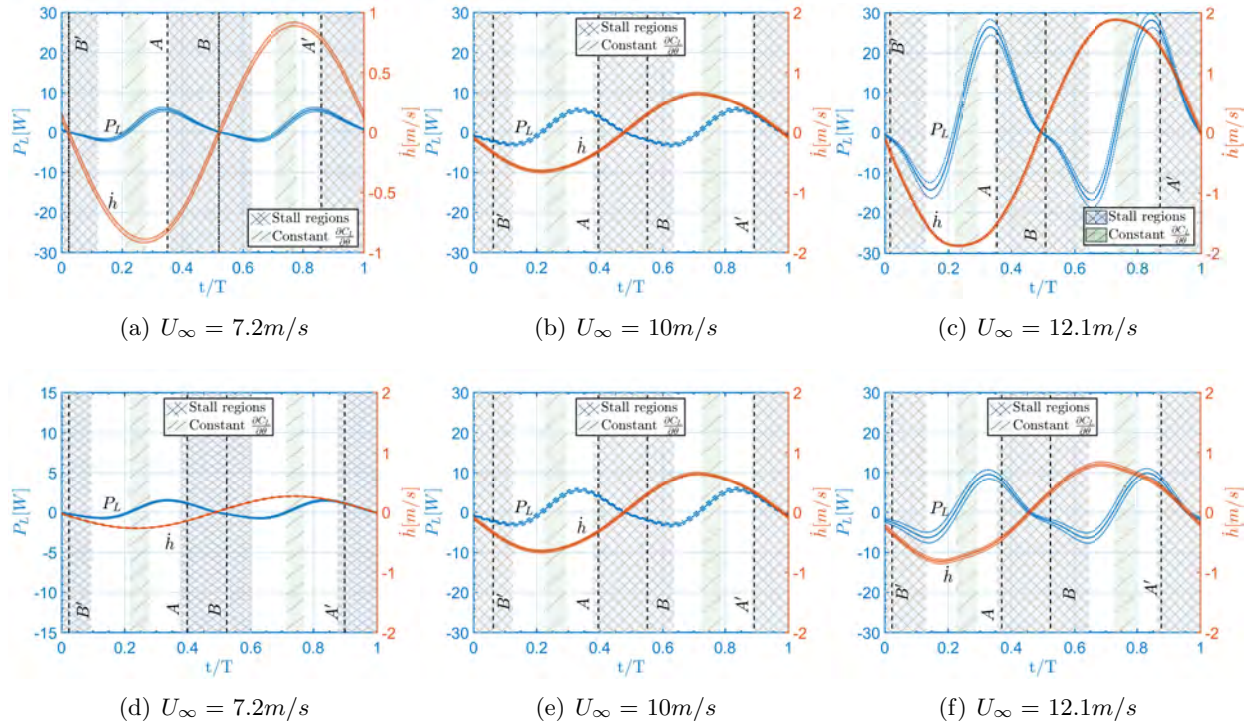


Figure 6.11: Power from aerodynamic lift and heave velocity versus cycle fraction for (a-c) Config - 1 and (d-f) Config - 2 at three different wind speeds. Note,  $A, A', B, B'$  are the same time stamps from Figure 6.7 and  $\cdots$  represent the 95% credible intervals.

### 6.4.5 Coupling Energy Analysis

The coupling energy plays a significant role in determining LCO amplitude kinematics. Positive  $E_{x_{\theta,h}}$  results in energy transfer from the pitch degree of freedom to the heave degree of freedom and vice-versa for positive  $E_{x_{\theta,\theta}}$ . Figure 6.13 shows that in Config - 1, energy passed to the structure through through the aerodynamic lift is transferred into the pitch degree of freedom for wind speeds up to  $U_\infty = 11 \text{ m/s}$ . On the contrary, in Config - 2, the heave degree of freedom accepts energy from the pitch degree of freedom for all wind speeds tested. At the highest wind speed tested, the heave degree of freedom receives nearly 40% of its total energy input from the coupling energy. Consequently, the differences in pitch amplitude between configurations occurs because the coupling energy in Config - 1 grows the pitch amplitude, whereas in Config - 2 it limits the pitch amplitude. Additionally, increasing the coupling between the two degrees of freedom does not equate to larger energy transfer between the two degrees freedom, as Figure 6.13 shows  $E_{x_{\theta}}$  Config - 2 is less than  $E_{x_{\theta}}$  Config - 1 for half of the wind speeds tested. Therefore,  $E_{x_{\theta}}$  is more sensitive to changes in  $\phi_{\theta,h}$ . The direction of the coupling flow is governed by  $\phi_{\theta,h}$ , therefore, modulating  $\phi_{\theta,h}$  strongly

effects the resultant LCO kinematics. Additionally in Config - 2, the heave amplitude saturates at high wind speeds (Figure 6.6a) because the coupling energy does not compensate for the inefficient capture of energy from the lift force. It is hypothesized that a similar amplitude saturation would occur in Config - 1 at higher wind speeds as  $\phi_{\theta,h}$  continues to decrease for that configuration. Moreover, the correlational relationship between increasing amplitude and decreasing  $\phi_{\theta,h}$  is not causal because  $\phi_{\theta,h}$  limits the growth in the pitch degree of freedom. Furthermore,  $\phi_{\theta,h}$  is crucial in influencing the LCO amplitude because it not only controls the efficiency of the aerodynamic energy capture but also how the aerodynamic energy is distributed throughout the system.

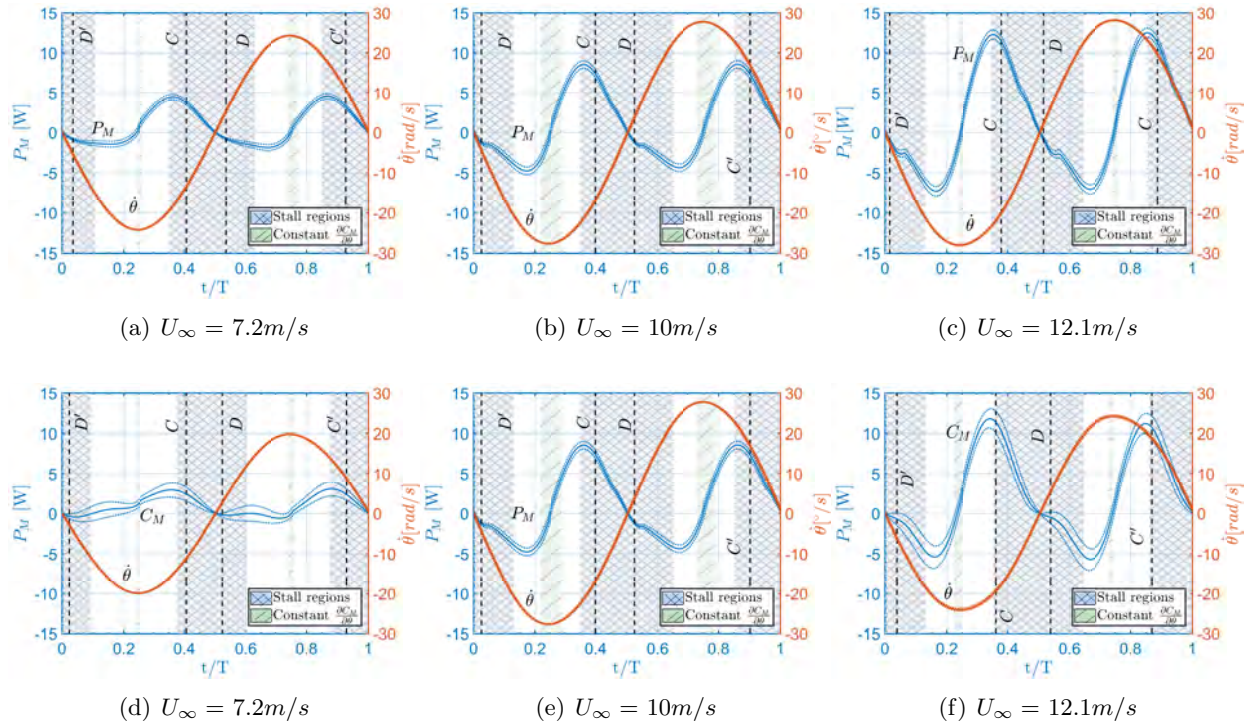
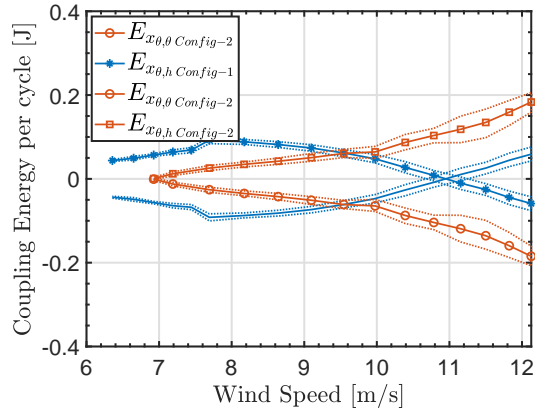


Figure 6.12: Power from aerodynamic moment and pitch velocity versus cycle fraction for (a-c) Config - 1 and (d-f) Config - 2 at three different wind speeds. Note,  $C, C', D, D'$  are the same time stamps from Figure 6.8 and  $\dots$  represent the 95% credible intervals.

## 6.5 Interim Conclusions

The aerodynamics of an aeroelastic wing undergoing stall-influenced limit cycle oscillations are investigated by inverting the equations of motion to solve for the aerodynamic lift and moment. The inverse method utilizes Markov Chain Monte Carlo simulations to estimate the stiffness, damping, friction, and mass coupling parameters of the system. The parameter distributions are propagated through the inverse method to generate credible intervals on the measured lift, moment, power, and energy. The aeroelastic inverse method is validated against prescribed motion experiments from the AFRL water tunnel with matched Reynolds number and Strouhal number scaled kinematics. After validation, a study of how mass coupling alters large amplitude limit cycle oscillations is conducted by examining the aerodynamic forces and energy transfer mechanisms. It is found that



(a)

Figure 6.13: Coupling energy between the degrees of freedom for both configurations. Note, ... represent the 95% credible intervals.

the mass coupling alters the phase angle between the heave and pitch degrees of freedom. This is important because the pitch-heave phase angle controls the aerodynamic efficiency. Additionally, the pitch-heave phase angle also directs how the aerodynamic energy is distributed throughout the structure by varying the influence of the coupling energy. Therefore, the pitch-heave phase difference is shown as a mechanism for controlling the amplitude growth in aeroelastic limit cycle oscillations.

## Chapter 7

# Theoretical and Experimental Investigations of an Unsteady Airfoil Encountering External Flow Disturbances

In this chapter, experimental and theoretical investigations are conducted on an unsteady airfoil encountering flow disturbances generated by an external source. Particular focus is placed on the effect of the encounter on the leading-edge vortex (LEV) shedding characteristics of the airfoil. The complex flow interactions are observed qualitatively in water-tunnel experiments using particle-image velocimetry (PIV) and analyzed in detail using finite-time Lyapunov exponent (FTLE) techniques. A low-order model informed by experiments is developed to predict the unsteady flow phenomena and associated loads experienced by the airfoil. Some graphical tools based on inviscid theory are also presented to gain insight into the role of various factors affecting the airfoil-disturbance interaction phenomena.

### 7.1 Chapter Introduction

The effect of flow interactions manifests in the performance measures such as propulsive efficiency, thrust, or lift. [130] show that lift of an airfoil in the wake of a circular cylinder adopts the shedding frequency of the cylinder. Fish have been observed to capture energy from an oncoming vortex street through Kármán gaiting [131]. Detailed investigations on Kármán gaiting reveal that fish optimize the efficiency of energy extraction by altering the phase difference between their motion and the oncoming vortex street [132, 133, 134]. For a flapping foil encountering a vortex street, a strong dependence exists between the efficiency of the foil and the phase difference between the foil oscillation and the arrival of incident vortices [135, 10]. The thrust of propulsive foils [136, 137] and the energy harvesting potential of flapping-foil energy harvesters [53, 138] can be enhanced significantly depending on the interaction mode. The interaction mode is often classified as constructive or destructive [139] based on its effect on the performance measure under consideration. Multi-wing systems present another arena for studying such interactions where one wing encounters the disturbances generated by another one. Substantial enhancement in thrust

[140] and energy harvesting potential [141] compared to single-wing case resulting from constructive wing-wake interaction has been observed in such arrangements.

Interesting fluid-dynamic phenomena like dynamic stall and LEV formation are often encountered in airfoils and wings performing unsteady motion. The formation and dynamics of LEV on unsteady wings has been extensively studied [142, 50, 51] and is well known to be responsible for lift augmentation in flapping flight [143, 144, 145]. While early works like that of [146] have reported the observations of LEV shedding characteristics of airfoils being altered by external flow disturbances, recent research efforts using high-fidelity numerical studies and advanced experimental techniques have attempted to take a detailed look into the mechanisms governing the interaction phenomena. In an experimental study on a tandem wing configuration, [147] observed that vortex-induced separation can lead to the formation of an LEV on the downstream wing, and associated the cause with the upwash generated at the leading edge by the vortices shed from the upstream wing. A numerical study by [53] reveals that the susceptibility to LEV formation or suppression of an unsteady airfoil in the presence of an oncoming vortex street can be correlated to the pattern of pressure distributions and adverse pressure gradients arising from the interactions.

In this chapter, we use experimental methods and theoretical tools based on LDVM and LESP to study the unsteady flow interactions and their effects on the lift of an airfoil undergoing high-amplitude pitching motions in the presence of oncoming disturbances. The periodic disturbances are systematically generated in the experiments as a von Kármán street using a sinusoidally rotating circular cylinder placed upstream of the airfoil. The complex flow interactions are observed qualitatively using particle-image velocimetry (PIV) and analyzed in detail using finite-time Lyapunov exponent (FTLE) techniques. The experimental setup used for this study is described in 7.2. With the confidence gained from the previous success of the LDVM method and the LESP concept, the LDVM framework is extended in 7.3 to obtain a low-order model that incorporates the effects of the encounter of an unsteady airfoil with external flow disturbances. The disturbance model is initially informed by results from experiments on a static airfoil and is then used for predictions of unsteady airfoils. Some theoretical tools based on LESP are derived in 7.4. These tools are used hand-in-hand with experimental results in 7.5 to gain insight into the effect of the disturbances on the LEV shedding characteristics and associated loads of the airfoil. Finally, the conclusions are discussed in 7.6.

## 7.2 Experimental Setup

The effect of external flow disturbances on the aerodynamic loading and vortex shedding characteristics of an unsteady airfoil is examined experimentally under the influence of disturbances generated systematically using an upstream circular cylinder. The cylinder-airfoil arrangement is illustrated in figure 7.1. The experiments are performed in the US Air Force Research Laboratory's horizontal free-surface water tunnel. The tunnel has 4:1 contraction and a 46 cm wide by 61 cm high test section with an operational speed range of 3–105 cm/s and  $u$ -component turbulence intensity of 0.4% at 5–40 cm/s. The tunnel is outfitted with a three degree of freedom motion rig, consisting of a triplet of H2W linear motors, driven by AMC DigiFlex servo-drives controlled by a Galil DMC 4040 4-channel card, with user-selected proportional/integral/derivative (PID) constants for each channel. This allows for the pitching, plunging, and surging of test articles. Direct force measurement is conducted via an ATI NANO-25 IP68 six-component force balance. Measurements are sampled at a rate of 1kHz and treated with a Chebyshev 2 low-pass filter with

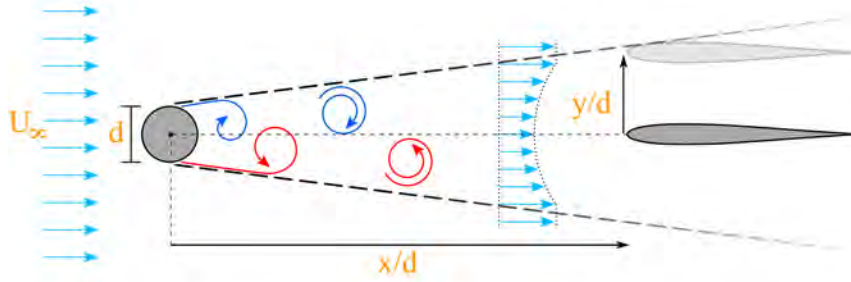


Figure 7.1: Schematic of the experimental setup showing the airfoil subjected to periodic flow disturbances generated by the upstream circular cylinder.

a cut-off frequency of 16Hz. All the force measurements are ensemble-averaged over 10 runs.

### 7.2.1 Test geometries

In this study, a symmetric version of the SD7003 airfoil is chosen for the wing geometry so as to eliminate the effects of camber and isolate the effects of the flow disturbances on the aerodynamics of the airfoil. The symmetric airfoil is derived from the SD7003 airfoil by a modification of the airfoil profile to a zero-camber configuration while preserving the airfoil thickness distribution along the chord. This approach maintains the leading-edge curvature of the airfoil, thus nominally maintaining the Reynolds-number-specific critical-LESP value (and thus the LEV-shedding characteristics, as explained later in 7.5.1) previously determined by [51] for the SD7003 airfoil. The wing model used in the experiments is fabricated from plastic (VeroWhite) through additive manufacturing and is reinforced with a spanwise carbon-fiber rod insert. The wing chord length of the model is  $c = 10.16$  cm.

The cylinder has a diameter,  $d$ , of 2.54 cm and aspect ratio,  $L/d$ , of 18. The axis of the cylinder is oriented normal to the tunnel walls, parallel to the wing leading edge. Both the wing and the cylinder span the width of the test section to produce a nominally two-dimensional flow field. Experiments were conducted at a freestream speed of  $U_\infty = 29.6$  cm/s, corresponding to a diameter-based Reynolds number of  $Re_d = 7500$  and a chord-based Reynolds number of  $Re_c = 3 \times 10^4$ . The wing has a minor gap of  $\sim 0.5$  mm existing at the wing-wall interface at both ends of its span. The cylinder is supported at the tunnel walls via low-profile vertical plate inserts.

The cylinder generates a periodic disturbance to be encountered by the downstream wing in the form of a von Kármán vortex street with a natural shedding frequency,  $f$ , corresponding to a Strouhal number of  $St = fd/U_\infty = 0.2$ . With a chord-to-diameter ratio of  $c/d = 4$ , the resulting street of vortices is comparable in size to leading-edge vortices of the wing in dynamic stall. The wing is positioned downstream of the cylinder at a distance of  $x/d = 8$ , measured from the cylinder center to the wing leading edge. This spacing is selected to ensure that the presence of the wing does not alter the natural shedding dynamics of the cylinder. The setup allows for various vertical positions of the wing relative to the cylinder centerline. In this paper, we focus on the cases where the airfoil performs pitching motions about a pivot point that coincides with the centerline of  $y/d = 0$ .

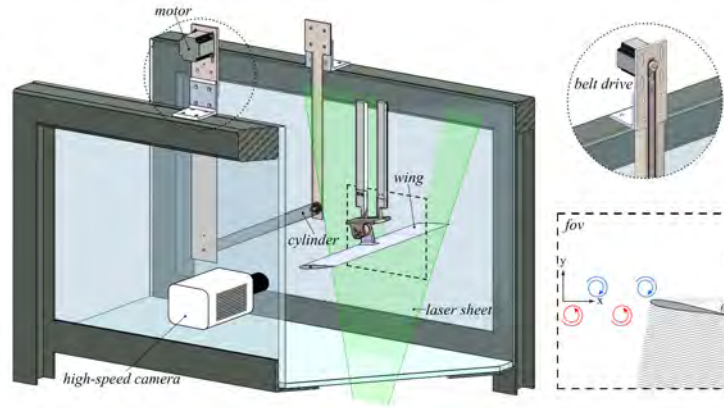


Figure 7.2: Experimental setup: direct force measurement and flow visualization using time-resolved particle-image velocimetry.

### 7.2.2 Flow visualization

Two-dimensional time-resolved particle-image velocimetry (PIV) measurements were performed using the experimental setup illustrated in figure 7.2. The water tunnel was seeded with polyamide particles of  $60\mu\text{m}$ -diameter (LaVision,  $\text{SG}=1.03$ ) and illumination was provided by an Nd:YLF laser sheet (Photonics Industries DM50-527,  $50\text{mJ}/\text{pulse}$ ,  $10\text{kHz}$  max) oriented in the streamwise direction and positioned at the three-quarter span of the wing. Images were recorded by high-speed camera (PCO Dimax S4, 4MP, 1279 fps at max resolution). The velocity vectors were calculated using Fluere version 1.3. Two passes of interrogation areas, with initial and final sizes of  $64\text{ px}^2$  and  $32\text{ px}^2$ , respectively, were used to determine the particle displacements from single-frame images sampled at 350 Hz. An interrogation area overlap of 50% was used. The resultant vector fields contained  $123 \times 123$  vectors with a resolution of  $(x/d, y/d) = (0.074, 0.074)$ . Instantaneous vector fields were phase-averaged using snapshot proper orthogonal decomposition (POD) [148] for the cylinder-only cases. For the studies of the airfoil in the cylinder wake, the PIV data was ensemble-averaged over consecutive runs of the experiment. A programmed trigger was used to ensure that all the runs were synchronized.

### 7.2.3 Control of the disturbance phasing

The focus of this work is the effect of the upstream disturbances generated by the cylinder on the dynamic wing positioned downstream. Critical to this effort is the capability to control the phase of the proximal vortical disturbances relative to the wing's kinematic commencement. Previous works [149, 150, 151] have shown that phase control of the periodic wake can be achieved by rotational oscillation of the cylinder about its axis. To this end, a timing belt was integrated flush into one of the vertical plates to provide rotary motion to the cylinder about its respective axial coordinate via a stepper motor, as illustrated in figure 7.2. The cylinder is driven in a sinusoidal angular profile of rotational amplitude  $45^\circ$  and at the natural shedding frequency of the cylinder corresponding to a Strouhal number of  $St = 0.2$ .

The commanded cylinder rotation,  $\psi_c$ , is given by:

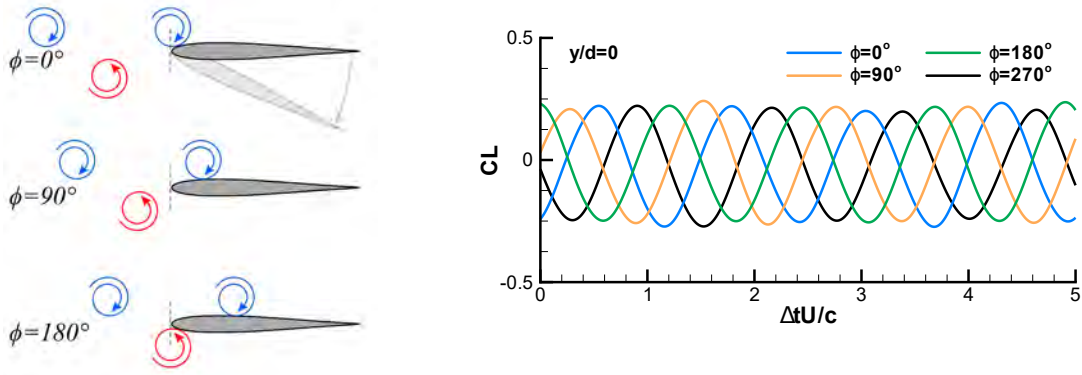


Figure 7.3: Left: Definition of the phase  $\phi$  based on the position of the oncoming vortical disturbances relative to the airfoil. Right: Demonstration of the control of  $\phi$ . Lift-coefficient histories of a static airfoil at zero incidence for different values of  $\phi$  exhibiting a phase shift equal to  $\phi$ .

$$\psi_c(t) = \psi_{c,max} \sin(\omega t + \Theta) \quad (1)$$

in which the cylinder-oscillation phase,  $\Theta$ , is set to achieve a desired relative position of the oncoming vortices with respect to the wing leading edge at a particular instant in time. The result is a commanded phase,  $\phi$ , of the vortical disturbance with respect to the wing's position and kinematic timing. The phasing convention, illustrated in figure 7.3, corresponds to the relative position of the vortical disturbances with respect to the wing leading edge.

For a static wing,  $\phi = 0^\circ$  is defined as the case when a clockwise vortex is coincident with the streamwise location of the leading edge at a reference point in time. The case where a counter-clockwise vortex is encountered by the leading edge at the same time corresponds to  $\phi = 180^\circ$ . Figure 7.3 also demonstrates the effective phase control enabled by active shedding of the rotating cylinder for a static airfoil placed in the flow centerline at  $y/d = 0$  at zero incidence. For this configuration, the von Kármán street emanating from the cylinder is bisected by the wing. Lift histories for various values of  $\phi$ , 90 degrees apart, showcase a phase differential of 90-degree increments as intended. For a dynamic wing,  $\phi$  is similarly defined based on the location of the vortices at the start of the wing's prescribed kinematic profile. Different disturbance configurations (corresponding to different values of  $\phi$ ) can be achieved at the initiation of motion by changing the cylinder-rotation phase  $\Theta$ . This leads to different interaction modes between the wing and the oncoming disturbances, as visualized and discussed in detail later in 7.5.

Another benefit of using the rotating cylinder is that the rotating cylinder preserves the spatial layout of the wake shed by a static cylinder but reduces spurious cycle-to-cycle variation in the shedding pattern. In cylinder wakes the two most energetic modes are associated with the von Kármán vortices, and when their respective temporal coefficients, denoted by  $a_1$  and  $a_2$ , are normalized by their energy and plotted against each other, they produce a phase plot, an example of which is shown in figure 7.4(a) for the static cylinder and in figure 7.4(b) for the rotating cylinder. Using figure 7.4(a) for the discussion, each point in this figure corresponds to a velocity field at one instant in time. From this figure, a phase angle can easily be determined for each velocity field as  $\beta = \tan^{-1}(a_{2,normalized}/a_{1,normalized})$ . In this study the phase plot was divided equally into 36 bins, each 10 degrees wide. A total of 4000 velocity fields were used, which encompassed 55 periods of von Kármán vortex shedding. Each velocity field was placed in the corresponding bin

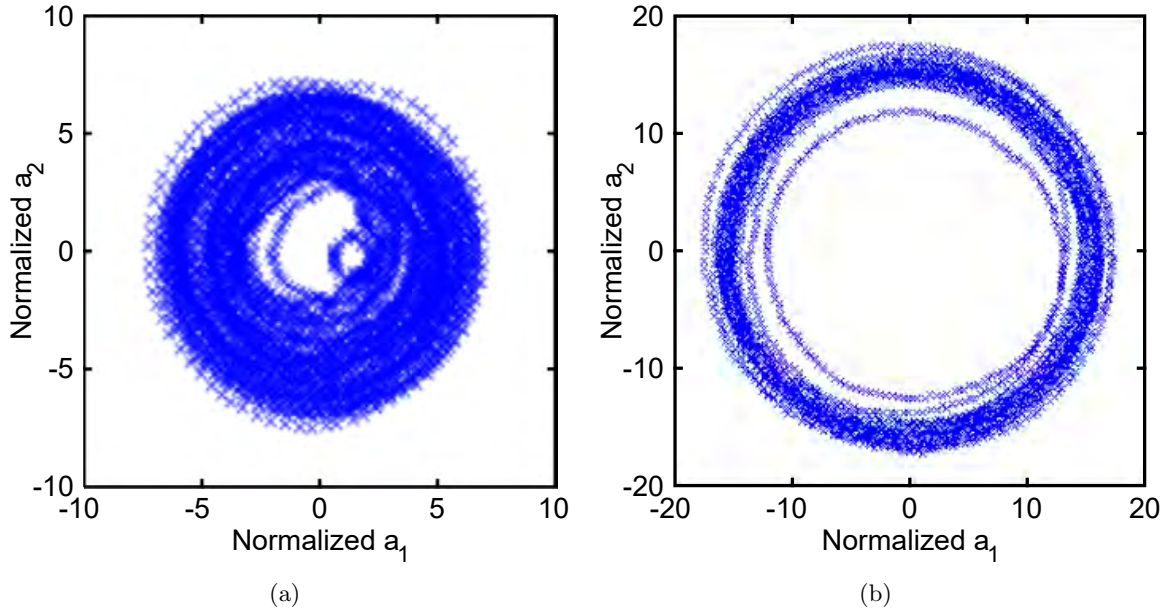


Figure 7.4: POD phase plot for cylinder wakes: (Left) static cylinder, (Right) dynamic cylinder.

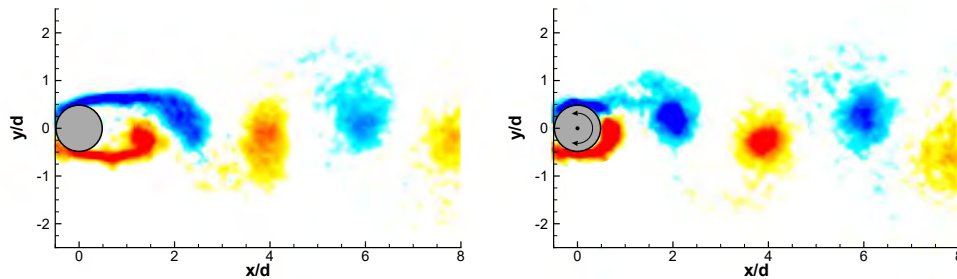


Figure 7.5: Phase-averaged vorticity contours of the wake: (Left) static cylinder, (Right) rotating cylinder.

based on its phase angle, and then all velocity fields within each bin were averaged together to form phase-averaged velocity fields. Phase-averaging mitigates some of the random errors derived from the PIV velocity-vector calculation. Comparison between static-cylinder and rotating-cylinder POD phase plots of figure 7.4 reveals significant reduction in hysteresis for the rotating cylinder. This observation translates to a reduction in cycle-to-cycle fluctuations in vortical shedding for the rotating cylinder.

Figure 7.5 showcases the typical wake structure behind the rotating cylinder in contrast to the static cylinder. Note that the rotating cylinder also provides for greater vorticity concentration for a given vortical element of the vortex street. This characteristic helps to ensure that a given vortical element maintains coherency downstream at the point of wing interaction.

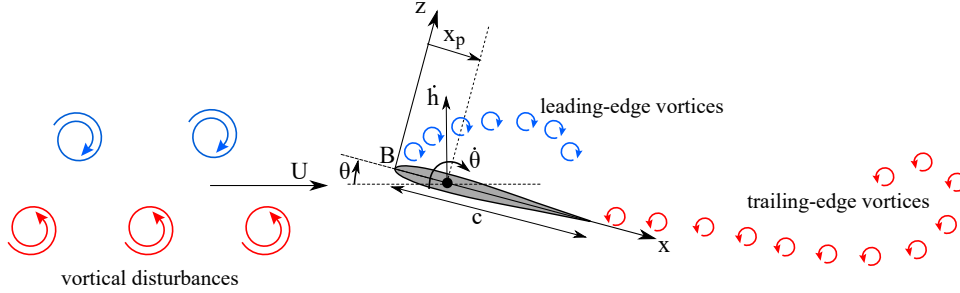


Figure 7.6: Illustration of the low-order framework showing the oncoming flow disturbances, the vorticity shed from the airfoil, and the kinematic variables used in the theoretical formulation. Clockwise vorticity is considered positive.

## 7.3 Low-Order Aerodynamic Model

The low-order modeling methodology builds upon the LESP-modulated discrete-vortex method (LDVM) developed in previous research by [51] for unsteady airfoils with intermittent LEV shedding. LDVM distills the determination of the initiation and termination of LEV shedding in unsteady airfoils to a single empirical parameter, the leading-edge suction parameter (LESP). The backbone of this potential-flow based discrete-vortex method is a large-angle unsteady thin-airfoil theory phenomenologically augmented using CFD or experimental information. The discrete-vortex implementation is realized as a time-stepping approach outlined by [152] in which the wake vorticity is modeled using discrete vortices. In the current work, the LESP concept is extended to an airfoil undergoing arbitrary unsteady motion in the presence of upstream flow disturbances generated by an external source. The essential elements of LDVM theory are briefly outlined and the theoretical background of the current approach is presented below.

### 7.3.1 Formulation

The schematic representation in figure 7.6 shows an airfoil of chord  $c$  undergoing arbitrary pitching and heaving kinematics in the presence of an upstream disturbance. The kinematic state of the airfoil is defined by the pitch angle  $\theta$ , the heave position  $h$ , and the respective velocities  $\dot{\theta}$  and  $\dot{h}$ . The pivot point, located at a distance  $x_p$  aft of the leading edge, denotes the centre of rotation of the airfoil. Also shown is a body-fixed frame  $Bxz$ , with the origin coinciding with the leading edge of the airfoil and the  $x$  and  $z$  axes extending in the chord-wise and chord-normal directions, respectively. The upstream disturbance is modeled using a vortical component resembling a von Kármán street superimposed on a mean component referred to here as the “uniform-flow speed,” denoted by  $U$ . Note that this uniform-flow speed,  $U$ , may be different from the freestream speed of  $U_\infty$  for modeling purposes to account for a velocity deficit when the airfoil is in the wake of the cylinder. The combined flow induces fluctuations in the flow velocity and the flow angle experienced by the airfoil. The wake of the airfoil consists of discrete LEVs and trailing-edge vortices (TEVs) shed from either edges of the airfoil in the previous time steps.

The solution seeks a velocity potential,  $\Phi$ , that satisfies the incompressible continuity equation

$$\nabla^2 \Phi = 0 \quad (2)$$

subject to the time-dependent zero-normal-flow boundary condition,

$$(\nabla\vec{\Phi} + \vec{V}_{kin}) \cdot \hat{n} = 0, \quad (3)$$

where  $\vec{V}_{kin}$  is the relative fluid velocity experienced by the airfoil due to the airfoil kinematics (pitch and heave), and  $\hat{n}$  is the unit normal to the local camberline of the airfoil. The velocity potential,  $\Phi$ , consists of the unknown bound potential,  $\Phi_B$ , the uniform-flow potential  $\Phi_U$ , the potential due to the vortical disturbances,  $\Phi_D$ , and the wake potential potential,  $\Phi_W$ , which in turn can be broken down into the velocity potential due to the discrete LEVs and TEVs.

$$\Phi = \Phi_B + \Phi_U + \Phi_D + \Phi_W = \Phi_B + \Phi_U + \Phi_D + \Phi_{LEV} + \Phi_{TEV} \quad (4)$$

The velocity potential,  $\Phi_D$ , due to the vortical component of the upstream disturbance, is a superposition of the potentials of two infinite rows of alternating-sign vortices of strength  $\Gamma_k$ , resembling a von Kármán street. Using the boundary condition (3), the unknown bound potential can be expressed in terms of the known airfoil kinematics and the free vorticity (comprising upstream vortical disturbances, LEVs, and TEVs) as:

$$\frac{\partial\Phi_B}{\partial z} = -\vec{V}_{kin} \cdot \hat{n} - \frac{\partial}{\partial z}(\Phi_U + \Phi_D + \Phi_{LEV} + \Phi_{TEV}) \quad (5)$$

We now introduce the term downwash, denoted by  $W$ , as the component of the induced velocity opposite to the normal direction, i.e., along the  $-\hat{n}$  direction, due to uniform flow, kinematics, upstream vortical disturbances, LEVs, and TEVs. We see that, to satisfy the zero-normal-flow boundary condition along the airfoil chord,  $\partial\Phi_B(x)/\partial z$  should be equal to  $W(x)$  everywhere along the chord:

$$W(x, t) = \frac{\partial\Phi_B}{\partial z} = \frac{\partial\eta}{\partial x}(U \cos\theta + \dot{h} \sin\theta + u_{ind}) - U \sin\theta - \dot{\theta}(x - x_p) + \dot{h} \cos\theta - w_{ind}, \quad (6)$$

where  $\eta(x)$  is the camberline shape of the airfoil, assumed to be small in comparison to the chord length, and  $u_{ind}(x)$  and  $w_{ind}(x)$  are the chordwise and normal components (along positive  $x$  and  $z$  axes), respectively, of the velocity induced by all the free vortices along the airfoil chord:

$$u_{ind}(x) = \frac{\partial\Phi_{LEV}}{\partial x} + \frac{\partial\Phi_{TEV}}{\partial x} + \frac{\partial\Phi_D}{\partial x} \quad (7)$$

$$w_{ind}(x) = \frac{\partial\Phi_{LEV}}{\partial z} + \frac{\partial\Phi_{TEV}}{\partial z} + \frac{\partial\Phi_D}{\partial z} \quad (8)$$

### 7.3.2 Solution of the flowfield

Using the Glauert transformation,  $x = \frac{c}{2}(1 - \cos\nu)$ , the chordwise distribution of the bound vortex-sheet strength,  $\gamma(x, t)$ , which is positive for clockwise direction, can be written in terms of  $\nu$  as:

$$\gamma(\nu, t) = 2U_{ref} \left[ A_0(t) \frac{1 + \cos\nu}{\sin\nu} + \sum_{n=1}^{\infty} A_n(t) \sin(n\nu) \right], \quad (9)$$

where  $U_{ref}$  is the reference velocity used as a scaling parameter, the choice of which is arbitrary. This transformation boils down the solution of the flowfield to obtaining the time-dependent Fourier

coefficients,  $A_n(t)$ , from the instantaneous downwash,  $W(x, t)$ :

$$A_0(t) = -\frac{1}{\pi} \int_0^\pi \frac{W(x, t)}{U_{ref}} d\nu \quad (10)$$

$$A_n(t) = \frac{2}{\pi} \int_0^\pi \frac{W(x, t)}{U_{ref}} \cos(n\nu) d\nu, \quad n \geq 1 \quad (11)$$

The bound circulation can then be obtained by integrating  $\gamma$  as:

$$\Gamma_B(t) = \int_0^c \gamma(x) d\nu = \pi c U_{ref} [A_0(t) + \frac{A_1(t)}{2}] \quad (12)$$

In the time-stepping implementation, the wake vorticity shed from the airfoil edges are represented using discrete vortices. A newly shed vortex is placed at one-third distance between the shedding edge and the previous vortex shed from that edge. The strength of the latest-shed vortices need to be determined to obtain  $W$ . At every time step a discrete TEV is released, the strength of which is obtained in accordance with Kelvin condition. At the  $j^{th}$  time step:

$$\pi c U_{ref} [A_0(t) + \frac{A_1(t)}{2}] + \Gamma_{TEV}^j = \Gamma_B^{j-1}, \quad (13)$$

where  $\Gamma_{TEV}^j$  is the unknown strength of the latest TEV and  $\Gamma_B^{j-1}$  is the bound circulation of the airfoil at the previous time step. After some manipulation, we get:

$$\Gamma_{TEV}^j = \frac{\Gamma_B^{j-1} + c \int_0^\pi W^0 (1 - \cos \nu) d\nu}{1 - c \int_0^\pi W'_{TEV} (1 - \cos \nu) d\nu}, \quad (14)$$

where  $W'_{TEV}(x)$  is the downwash distribution induced by a unit-strength discrete vortex placed at the location of the latest TEV and  $W^0$  is the downwash due to all the other discrete vortices present in the flowfield as well as the kinematic state of the airfoil. [51] presented a criterion to predict the initiation and termination of LEV shedding based on the maximum allowable value of suction that can be supported at the leading edge. The nondimensional measure of the chord-parallel leading-edge suction force, called the leading-edge suction parameter (LESP, denoted by  $\mathcal{L}$  henceforth), was shown to be associated with the leading Fourier-coefficient  $A_0$ :

$$\mathcal{L}(t) = A_0(t) \quad (15)$$

In LDVM, discrete LEVs are shed when  $\mathcal{L}$  exceeds a critical value denoted by  $\mathcal{L}_{crit}$ . The value of  $\mathcal{L}_{crit}$  for a given airfoil is largely independent of motion kinematics at a given  $Re$ . Once the value of  $\mathcal{L}_{crit}$  for a given airfoil at a given  $Re$  is determined using experimental or CFD data, LDVM can predict the LEV shedding characteristics of that geometry for any arbitrary motion kinematics at that  $Re$ . The strengths of the LEVs are determined so as to maintain the  $\mathcal{L}$  at  $\mathcal{L}_{crit}$ . Hence, when LEV shedding is active, the strengths of the LEV and TEV shed at every time step have to be determined to satisfy the Kelvin condition as well as to maintain  $\mathcal{L}$  at  $\mathcal{L}_{crit}$ . This leads to a simultaneous two-variable problem in the form

$$[A] \begin{Bmatrix} \Gamma_{TEV} \\ \Gamma_{LEV} \end{Bmatrix} = \{B\} \quad (16)$$

where,

$$[A] = \begin{bmatrix} 1 - c \int_0^\pi W'_{TEV}(1 - \cos \nu) d\nu & 1 - c \int_0^\pi W'_{LEV}(1 - \cos \nu) d\nu \\ \int_0^\pi W'_{TEV} d\nu & \int_0^\pi W'_{LEV} d\nu \end{bmatrix} \quad (17)$$

and

$$\{B\} = \begin{Bmatrix} \Gamma_B^{j-1} + c \int_0^\pi W^0(1 - \cos \nu) d\nu \\ -\pi U_{ref} \mathcal{L}_{crit} - \int_0^\pi W^0 d\nu \end{Bmatrix} \quad (18)$$

where  $W'_{LEV}(x)$  is the downwash distribution induced by a unit-strength discrete vortex placed at the location of the latest-shed LEV. As noted by [153], this approach eliminates the Newton-iteration procedure suggested by [152] and implemented previously by [51], and easily extends to multiple lifting-surfaces. Once the strengths of the latest discrete vortices are determined, the solution of the flowfield can be completed by computing the Fourier coefficients and subsequently obtaining the bound-vortex distribution that satisfies the zero-normal-flow boundary condition.

We note that the recent work by [154] has proposed an updated definition for the LESP to take into account the effect of pitch rate on the reference velocity,  $U_{ref}$ . Their work considered the critical LESP at the initiation of LEV formation for pitching airfoils with a range of pivot points from leading edge to trailing edge, a range of non-dimensional pitch rates from  $K = 0.005$  to  $0.6$ , and two Reynolds numbers of  $30,000$  and  $3$  million. It was shown that, while the updated definition of LESP significantly improved the collapse of the critical LESP values for all cases at the higher Reynolds number, there was little to no improvement between the original and updated LESP definitions in the critical LESP values at LEV initiation at the lower Reynolds number, especially for the low-pitch-rate cases. Because the current work considers a low-Reynolds-number and low-pitch-rate motion, in this work we use the original definition of LESP in which  $U_{ref}$  is set to a constant value of the freestream velocity,  $U_\infty$ .

### 7.3.3 Calculation of the unsteady loads

The pressure distribution over the airfoil is given by the unsteady Bernoulli equation:

$$\Delta p(x) = \rho \left[ \left( U \cos \theta + \dot{h} \sin \theta + u_{ind}(x) \right) \gamma(x) + \frac{\partial}{\partial t} \int_{x'=0}^x \gamma(x') dx' + \dot{\Gamma}_{lev} \right] \quad (19)$$

The last term in (19) explicitly takes into account the effect of circulation production due to LEV shedding on the unsteady loads of the airfoil [155]. The forces and moment on the airfoil are calculated by the integration of the pressure distribution over the chord. The normal force per unit span of the airfoil can be obtained in terms of the Fourier coefficients using (9) as:

$$F_N = \rho \pi c U_{ref} \left[ \left( U \cos \theta + \dot{h} \sin \theta \right) \left( A_0(t) + \frac{1}{2} A_1(t) \right) + c \left( \frac{3}{4} \dot{A}_0(t) + \frac{1}{4} \dot{A}_1(t) + \frac{1}{8} \dot{A}_2(t) \right) \right] \\ + \rho \int_0^c u_{ind}(x) \gamma(x, t) dx + \rho c \dot{\Gamma}_{lev} \quad (20)$$

and the suction force per unit span of the airfoil is given by,

$$F_S = \rho \pi c U_{ref}^2 A_0^2 \quad (21)$$

The normal and suction force coefficients  $C_N$  and  $C_S$  can be obtained through nondimensionalization of the forces using the quantity  $\frac{1}{2}\rho U_{ref}^2 c$ . The lift and drag coefficients can then be evaluated as:

$$C_L = C_N \cos \theta + C_S \sin \theta \quad (22)$$

$$C_D = C_N \sin \theta - C_S \cos \theta \quad (23)$$

The detailed derivation of these expressions is given by [51] and [155].

### 7.3.4 Low-order model of the oncoming disturbance

The oncoming vortical disturbance is modeled in LDVM as clusters of discrete vortices with alternating sense as shown in figure 7.7. The clusters are introduced into the flowfield at a shedding location  $15c$  upstream of the airfoil to minimize any sudden disturbances to the flowfield. The experimentally observed vortex-shedding frequency  $f$  is expressed in terms of the diameter-based Strouhal number,  $St = fd/U_\infty = 0.2$ . This corresponds to a chord-based nondimensional shedding interval of  $T^* = c/(0.8U_\infty)$ . In LDVM, two clusters of opposite strength are simultaneously released at this shedding interval (instead of releasing one cluster at every  $0.5T^*$ ) to maintain zero net circulation in the flow domain. Based on the suggestion by [51], a nondimensional time step of  $\delta t^* = \delta t U_\infty / c = 0.014$  is used in LDVM. Thus, a pair of clusters with opposite strength is introduced at every 89 nondimensional time steps in LDVM. Each cluster is initially introduced in the form of a circular ring containing 50 equally-spaced discrete vortices. One cluster is released at the shedding location while the other one is released at  $0.5UT^*$  downstream of the shedding location to account for convection. From the PIV data of the rotating-cylinder wake, the distance from the wake centerline to the center of a given vortex at  $x/d = 8$  in figure 7.5 was measured to be  $y/d = 0.6$  using the Galilean invariant  $\Gamma_2$  criterion of [156]. Based on this information, the clusters are introduced with a vertical offset of  $1.2d$  between their centers. The predictions of the model is in best agreement with experimental observations when using more than 30 vortices per cluster. Meanwhile, using more than 50 vortices is not seen to change the low-order predictions and also results in large computation times. Using 30 to 50 vortices per cluster is recommended to strike a balance between capturing the flow-interaction phenomena accurately and doing so with reasonable computational expense. The diameter of the rings was set to  $0.6d$ . The evolution of the vortex street is not seen to be sensitive to this parameter. Other initial configurations such as a random distribution of vortices in a circular area are also seen to result in von Kármán streets similar to those produced with the ring shape for the initial configuration.

Once released into the flow domain, the clusters convect downstream with the uniform-flow speed  $U$  and under mutual influence. As they move downstream, the rings deform to form patches and stabilize into two rows of alternating-sign vortex clusters, representing a von Kármán street. The vertical separation between the centroids of the two rows is not seen to vary much during the downstream convection. The airfoil is held static for a duration of  $t^* = 5$  after the first cluster reaches the leading edge. This allows the airfoil-vortex-street interactions to reach a steady state before data collection. For unsteady simulations, the pitch motion is initiated when the centroid of a cluster aligns with the airfoil leading edge.

The aggregate strength of a vortex cluster in LDVM and the uniform-flow speed  $U$  experienced by the airfoil are estimated based on the experimentally-observed lift fluctuations of a static airfoil placed in the cylinder wake. For this portion of the experimental study, the static airfoil is placed

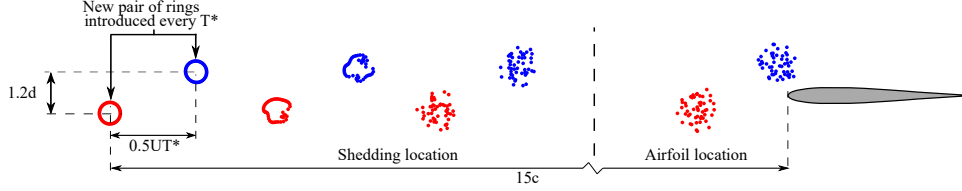


Figure 7.7: Discrete-vortex rings introduced into the flowfield at the upstream shedding location forming a vortex street as they convect downstream towards the airfoil location.

at a pitch angle of  $\theta = 6^\circ$  in the wake of the cylinder at a streamwise position of  $x/d = 8$  aft of the longitudinal axis of the cylinder and at a centerline vertical position. In the absence of any oncoming disturbance, a lift coefficient of 0.59 is observed (blue line in figure 7.8 (a)). Under the influence of the vortical and velocity-deficit effects of the disturbances generated by the cylinder, the airfoil exhibits a fluctuating lift history with a reduction in mean lift. Previous studies have reported a reduction in mean lift when a static wing is placed at pre-stall angles near the centerline of a bluff-body wake [157, 158]. Ten typical cycles of lift oscillations are shown using the black curve in figure 7.8 (a)). The average peak-to-peak amplitude of  $C_L$  fluctuations is 0.52 and the mean  $C_L$  is 0.39 (red line), corresponding to a 35% decrease in mean  $C_L$ . In LDVM, the velocity components induced by the vortex clusters cause the airfoil to experience velocity- and flow-angle fluctuations and thus result in  $C_L$  oscillations of the static airfoil. The amplitude of the oscillations is seen to be largely determined by the strength of the vortex clusters, while the mean of the lift fluctuations are primarily dependent on the uniform-flow speed. Through an error minimization study, a value of  $\Gamma/(cU_\infty) = 0.3$  of the nondimensional strength of the vortex clusters and an uniform-flow speed  $0.85U_\infty$  were found to result in  $C_L$  oscillations with similar amplitude and percentage reduction in mean. The lift history predicted by the low-order model for the airfoil at  $\theta = 6^\circ$  and located at the centerline is shown in figure 7.8(b). Figure 7.8(b) shows a 35% reduction in mean  $C_L$  (from 0.66 to 0.43) and a lift amplitude of 0.55 using these values in the LDVM simulations. In previous work [159], we presented the studies on an airfoil positioned outside the von Kármán street at an offset location of  $y/d = -1.5$ . The low-order model of the vortex street with the same value of nondimensional strength and  $U = 0.92U_\infty$  was obtained using the same approach and the predicted flow interaction phenomena were in good agreement with experimental results. All the studies presented in this paper are for the airfoil positioned at the centerline, and hence the value of 0.3 for the nondimensional strength of the vortex clusters and a value of  $0.85U_\infty$  for the uniform-flow speed are used in all the LDVM simulations presented in Section 7.5.

Vorticity-contour images from experiment and discrete-vortex plots from LDVM corresponding to four instants of time during a lift-oscillation cycle are presented in figure 7.8(c). The discrete-vortex plots show the clockwise (CW) vortices in blue and counter-clockwise vortices (CCW) in red. The flow images can be used to infer the association between the lift fluctuations and the spatio-temporal features of the oncoming disturbance. From figure 7.8(c), a local lift peak can be associated with the presence of a CW vortex near the midchord on the upper surface and a CCW vortex near the leading edge on the lower surface ( $t = mT + 0.5$ , where  $m$  is an integer to denote the start of a period in the lift oscillation). It is known from the vortex-force-map study of [160] that a CW vortical structure on the upper surface of the airfoil is lift enhancing while it is in the vicinity of the leading edge and becomes lift reducing as the vortex convects downstream towards the trailing edge. A CCW structure convecting downstream below the airfoil has a similar effect on lift. Thus, the lift peak occurs when the airfoil experiences the best combined lift enhancement due to the positions of both vortical structures. From an effective-angle-of-attack perspective, a CW

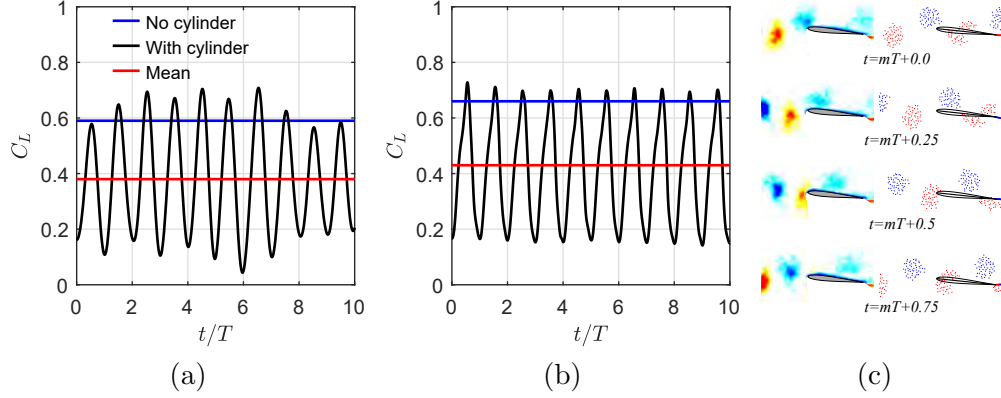


Figure 7.8: Static airfoil at 6 degree incidence in the presence of the disturbance: (a) experimentally observed  $C_L$ , (b)  $C_L$  predicted by LDVM, (c) discrete-vortex plots from LDVM compared with experimental vorticity contours at four time instants in a cycle of lift oscillation.

vortex located above the airfoil induces maximum upwash at the leading edge and thus the largest effective angle of attack when it is slightly downstream of the leading edge. Also, a CCW vortex convecting downstream on the bottom surface of the airfoil induces the largest upwash when it is slightly upstream of the leading edge. The lift-peak configuration thus corresponds to the situation where the net upwash induced by the two vortex structures is maximized resulting in the largest effective angle of attack. Based on similar arguments, a local valley in lift can be associated with the presence of an approaching CW vortex at the leading edge on the upper surface ( $t = mT + 0.0$ ).

### 7.3.5 Numerical aspects of the discrete-vortex method

The discrete vortices are represented as vortex blobs using the vortex-core model proposed by [161], which is a close approximation of the Lamb-Oseen vortex. The components of velocity induced at a point  $(x, z)$  by the  $j^{th}$  discrete vortex are given by,

$$u = \frac{-\Gamma_j}{2\pi} \frac{z_j - z}{\sqrt{[(x_j - x)^2 + (z_j - z)^2]^2 + r_{core}^4}} \quad (24)$$

$$w = \frac{\Gamma_j}{2\pi} \frac{x_j - x}{\sqrt{[(x_j - x)^2 + (z_j - z)^2]^2 + r_{core}^4}} \quad (25)$$

A core radius  $r_{core}$  of  $0.02c$  is used, which is approximately 1.3 times the average spacing between vortices according to the suggestion by [162]. The discrete vortices are convected using the total velocity induced at their respective locations by the uniform-flow speed, the bound vorticity, and the other discrete vortices in the flowfield. Thus, the current discrete-vortex approach simulates the wake rollup in the flowfield and accommodates non-planar wakes.

## 7.4 Decomposition of the Leading-Edge Suction Parameter (LESP, $\mathcal{L}$ )

An advantage of the current low-order modeling approach is that it helps us to segregate the contributions from different sources on the aerodynamics of the airfoil, and to comprehend the relative importance of each factor. A closer look at (6) reveals that the total downwash  $W$  can be interpreted as the contributions from different sources:

$$W = W_\theta + W_{\dot{\theta}} + W_{\dot{h}} + W_{LEV} + W_{TEV} + W_D \quad (26)$$

Here,  $W_\theta = \frac{\partial \eta}{\partial x} U \cos \theta - U \sin \theta$ ,  $W_{\dot{\theta}} = -\dot{\theta}(x - x_p)$ , and  $W_{\dot{h}} = \frac{\partial \eta}{\partial x} \dot{h} \sin \theta + \dot{h} \cos \theta$  are the components due to the kinematic state of the airfoil.  $W_{LEV}$ ,  $W_{TEV}$ , and  $W_D$  are the contributions from the LEVs, TEVs and the vortical disturbances, respectively, and can be expressed in the form:  $W_{[\ ]} = \frac{\partial \eta}{\partial x} \left( \frac{\partial \Phi_{[\ ]}}{\partial x} \right) - \frac{\partial \Phi_{[\ ]}}{\partial z}$ .

This idea allows us to obtain a detailed look into the flow features of the airfoil and associate various phenomena with their respective causes. We mainly attempt to expand on the LESP concept, previously derived by [51] for an unsteady airfoil in a uniform freestream, to account for the presence of the oncoming flow disturbances and use it as a theoretical tool to predict and analyze the modifications to the LEV shedding characteristics of the airfoil. Eqn. (26) enables us to perform a decomposition of LESP,  $\mathcal{L}$ , into components due to various sources:

$$\begin{aligned} \mathcal{L} = A_0(t) &= -\frac{1}{\pi U_{ref}} \int_0^\pi (W_\theta + W_{\dot{\theta}} + W_{\dot{h}} + W_{LEV} + W_{TEV} + W_D) d\nu \\ &= A_0^\theta + A_0^{\dot{\theta}} + A_0^{\dot{h}} + A_0^{LEV} + A_0^{TEV} + A_0^D \\ &= \mathcal{L}_\theta + \mathcal{L}_{\dot{\theta}} + \mathcal{L}_{\dot{h}} + \mathcal{L}_{LEV} + \mathcal{L}_{TEV} + \mathcal{L}_D \end{aligned} \quad (27)$$

This decomposition of  $\mathcal{L}$  can be used to elucidate how the role of various kinematic and flowfield elements evolve over time. Of particular interest is the contribution to  $\mathcal{L}$  from a given discrete vortex in the flow field located at  $(x_i, z_i)$  in the body coordinates, which can be obtained by integrating the corresponding downwash induced by the vortex.

$$\mathcal{L}^i(t) = -\frac{1}{\pi} \int_0^\pi \frac{W^i(x, t)}{U_{ref}} d\nu \quad (28)$$

$$= \frac{1}{\pi} \int_0^\pi \frac{\Gamma^i \left[ (x_i - x) + \frac{\partial \eta}{\partial x} (z_i - z) \right]}{2\pi U_{ref} \sqrt{((x_i - x)^2 + (z_i - \eta)^2)^2 + r_{core}^4}} d\nu \quad (29)$$

In the above equations,  $i$  may refer to any kind of discrete vortex in the flow field: LEVs or TEVs shed from the airfoil, or the external vortices. Further,

$$\mathcal{L}^i(t) = \frac{\Gamma^i}{c U_{ref}} \frac{1}{2\pi^2} \int_0^\pi \frac{\left[ (\tilde{x}_i - \tilde{x}) + \frac{\partial \tilde{\eta}}{\partial \tilde{x}} (\tilde{z}_i - \tilde{z}) \right]}{\sqrt{((\tilde{x}_i - \tilde{x})^2 + (\tilde{z}_i - \tilde{\eta})^2)^2 + \tilde{r}_{core}^4}} d\nu = \bar{\Gamma}^i f^i \quad (30)$$

where,  $\tilde{\cdot}$  denotes normalization using the airfoil chord  $c$ , and  $\bar{\Gamma}^i = \Gamma^i / (c U_{ref})$  is the nondimensional strength of the discrete vortex. The function  $f^i$  depends only on the location of the vortex relative to the airfoil and can be interpreted as  $\mathcal{L}$  due to a discrete vortex of unit strength located at  $(x_i/c, z_i/c)$ . Thus, the above equation can be re-written in the form:

$$\mathcal{L}^i(t) = \bar{\Gamma}^i \hat{\mathcal{L}}^i(t) \quad (31)$$

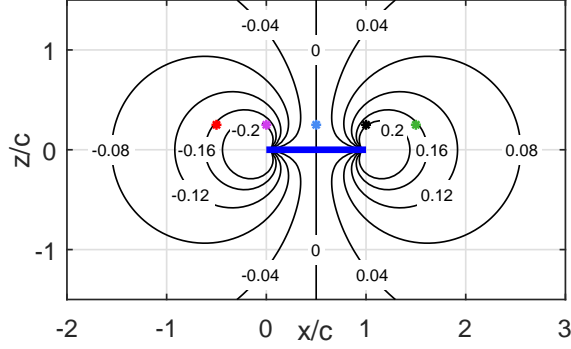


Figure 7.9: LESP map for a symmetric airfoil showing the incremental LESP ( $\mathcal{L}$ ) due to a unit-strength clockwise discrete vortex.

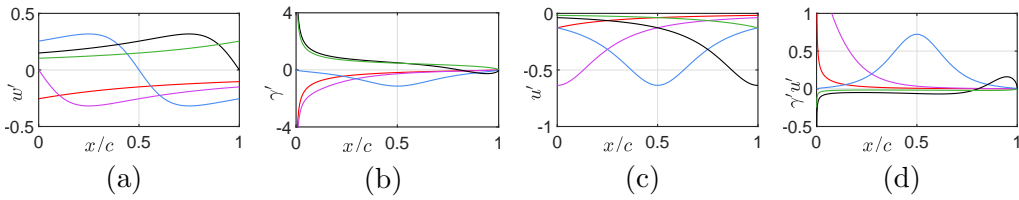


Figure 7.10: Distributions of (a) normalwash, (b) bound circulation, (c) chord-parallel velocity, and (d)  $\gamma' u'$  induced on the airfoil by a unit-strength clockwise vortex placed at five locations as marked in Fig. 7.9.

This expression splits  $\mathcal{L}$  into a strength factor and a distance factor. The contours of constant  $\hat{\mathcal{L}}^i$  enable the visualization of the contribution to  $\mathcal{L}$  due to the position of a unit-strength discrete vortex relative to the airfoil, and is henceforth referred to as the LESP map. The LESP map for a symmetric geometry is shown in figure 7.9. A unit-strength clockwise vortex located anywhere along an isoline causes an incremental  $\mathcal{L}$  equal to the value  $\hat{\mathcal{L}}^i$  of the contour line. Five different vortex locations are marked on the LESP map using ‘\*’ markers of various colors, and the corresponding normalwash ( $w'$ , positive for upwash) distributions on the airfoil are plotted using the respective colors in figure 7.10(a). For a given  $x/c$ , the normalwash distributions will be identical for two vortices located symmetrically ( $\pm z$ ) about the chord line. Thus,  $\mathcal{L}$ , which is the integral of the normalwash along the chord, will be the same for the two vortices, making the LESP map symmetric about the chord line. Also, the normalwash distribution due to a vortex located to the left of the mid-chord location is negative (downward), and that due to a vortex located to the right of the mid-chord location is positive (upward). Thus,  $\mathcal{L}$  will be negative for all clockwise vortices located to the left of the mid-chord location, and will be positive for the ones located to the right of the mid-chord location. When the horizontal position of the vortex is at mid-chord location, the normalwash will have equal negative and positive distributions along the chord (blue line in figure 7.10(a)), and will integrate to zero (thus leading to a zero  $\mathcal{L} = A_0$ ). This is true for any  $z/c$  value. Thus, the zero-contour line on the LESP map is a vertical line passing through the mid-chord location. It can also be seen from figure 7.9 that the magnitude of  $\mathcal{L}$  induced by a vortex increases for locations close to the LE or TE due to the relatively large magnitude of the velocity induced by the vortex on the airfoil surface.

It is worth discussing some interesting insights here. Plotted in figures 7.10(b) through 7.10(d) are the chordwise distributions of the bound-circulation ( $\gamma'$ ), the chord-parallel velocity ( $u'$ ), and the quantity  $\gamma' u'$  induced on the airfoil by a unit-strength clockwise vortex placed at the five locations,

indicated using the respective colors. From figure 7.10(b), we can see that the  $\gamma'$  distribution due to a vortex at the mid-chord location (blue curve) is purely negative (counter-clockwise). Also, from figure 7.10(c), if a clockwise vortex is situated above the mid-chord location,  $u'(x)$  due to that vortex will be negative (towards the left), leading to a positive distribution of the quantity  $\gamma'(x)u'(x)$  in figure 7.10(d). This results in a positive value of the integral term,  $\int_0^c u'(x)\gamma'(x)dx$ , in (20) and thus a positive (upward) contribution to the normal force. This observation is consistent with that of [163] who derived an exact expression for the lift of a flat plate in the presence of a vortex located at the midchord. (It is to be noted that the total normal force due to the vortex will also include the first term of (20),  $\rho U \Gamma_B$ , which is not discussed here.) If the vortex is located at the same  $z/c$  below the airfoil, the normalwash and  $\gamma'$  distributions will remain the same; however  $u'$  will change sign (now the vortex will induce a chord-parallel velocity towards the right), leading to a negative (downward) normal force contribution. Also, as the vortex above the airfoil moves to the right of the midchord,  $\gamma'$  will start becoming mostly positive (while the direction of  $u'$  remains the same), resulting in a decrease in the force. For example, we can see that  $\gamma'(x)$  due to a clockwise vortex above the trailing edge (black curve) is largely positive, and is hence force reducing. This is also in agreement with previous observations like those of [160].

A number of recent research efforts have presented similar graphical approaches to analyze the contribution of vortices in the flowfield to the unsteady loads on a body. [160, 164] introduced the idea of vortex-force-line (VFL) maps to identify the contribution of a point vortex in the flowfield to the normal force on a flat plate. Based on the location of a vortex on the force map and its direction of motion, the effect of the vortex can be easily identified as force production or force deterioration. [165] generalized this idea to obtain lift and drag maps for general airfoils. More recently, [166] proposed the concept of vortex-moment maps for two dimensional bodies of arbitrary shape to analyze the contribution to the pitching moment from a given vortex in the flowfield. In another recent work, a three dimensional extension of the force-map approach was used by [167] to gain insight into the effect of vortical structures on the unsteady force of a delta wing.

The LESP map in the current work is similar to the vortex force line (VFL) maps introduced by [160, 164] in that it also uses precomputed maps to identify the contribution of a vortex to some aerodynamic quantity of an airfoil. However, but for this similarity, the LESP map is fundamentally different from the VFL maps. While the VFL maps are intended to identify the contribution of the vortex to the force on the airfoil, the LESP map provides information about the role of a discrete vortex in promoting or suppressing the LEV shedding tendency of the airfoil. In addition, the LESP due to a vortex depends only on the position of the vortex whereas the force due to a vortex depends on both its position and its velocity. Thus, the LESP map requires only the vortex-position information while the force map requires the vortex-position information along with the streamline information.

In this work, we use the LESP map as a graphical tool to identify the incremental contribution from a discrete vortex in the flowfield to the LESP ( $\mathcal{L}$ ), the criticality of which governs the LEV shedding phenomena. The LESP map can be thought of as a stationary field attached to the airfoil in the body frame of reference. To evaluate the contribution to  $\mathcal{L}$  due to the vortices in the flowfield, the vortex distribution has to be overlaid on the LESP map, and the strength of each vortex must be multiplied by the contour value from the location of the vortex on the LESP map. Repeating this procedure over consecutive instants in time will give us a picture of what happens to the  $\mathcal{L}$  contributions from the vortices as they move around in the flowfield. The LESP map will also help us to identify the dominant contributors to  $\mathcal{L}$  from among all the vortices in the flowfield at any given time instant. The demonstration of the application of the LESP map will be presented in

## 7.5 Results and Discussion

In this section, the effect of the relative phase between the disturbances and the pitching motion of the airfoil on its LEV shedding process and the associated lift is presented. The baseline motion sequence considered is a 0–25–0 degree pitch-up–hold–return maneuver following the  $C^\infty$ -smoothing ramp function presented by [50] :

$$G(t) = \ln \left[ \frac{\cosh(a(t-t_1)U_{ref}/c) \cosh(a(t-t_4)U_{ref}/c)}{\cosh(a(t-t_2)U_{ref}/c) \cosh(a(t-t_3)U_{ref}/c)} \right] \quad (32)$$

$$\theta(t) = \theta_A G(t) / G_{\max} \quad (33)$$

where  $\theta_A$  is the maximum pitch angle ( $= 25^\circ$ ),  $a$  is the smoothing parameter ( $= 11$ ),  $U_{ref}$  the reference velocity,  $c$  the chord length, and  $G_{\max}$  is taken over the interval of interest such that  $\theta = \theta_A$  is achieved when  $G$  reaches its maximum. The kinematic history is plotted in figure 7.11. The airfoil motion achieves a non-dimensional pitch rate of  $K = \dot{\theta}c/(2U_\infty) = 0.11$  for the non-smoothed kinematic profile. The constant  $t_1$  is the time from the reference 0 to the initiation of the ramp,  $t_2 = t_1 + \theta_A/2K$ ,  $t_3 = t_2 + \pi\theta_A/4K$ , and  $t_4 = t_3 + \theta_A/2K$ . The pitch axis is coincident with the airfoil leading edge.

The desired phase,  $\phi$ , between the vortical disturbances and the airfoil is achieved by modulating the initiation of the pitch-up motion relative to the arrival of the vortex clusters at the airfoil leading edge. Results for two values of  $\phi$  are presented, namely  $\phi = 0^\circ$  and  $\phi = 180^\circ$ . Discussions of the flowfield evolution for the two values of  $\phi$  are presented in §7.5.2 and §7.5.3, respectively. The effect of  $\phi$  on the unsteady lift of the airfoil is presented for both values of  $\phi$  in §7.5.4.

### 7.5.1 Baseline kinematics: pitching airfoil in undisturbed flow

We first establish the baseline behavior of the airfoil executing the pitching kinematics in the absence of any disturbances in this subsection. These results also serve to present some background on the application of the LESP concept for completeness, as well as to perform a quick validation of LDVM for the symmetric SD7003 airfoil. [51] reported  $\mathcal{L}_{crit} = 0.18$  for the SD70003 airfoil at  $Re_c = 30,000$ . Since the leading-edge radius remains unaffected by the removal of camber, the  $\mathcal{L}_{crit}$  for the symmetric SD7003 can be expected to be the same as that of the SD70003 airfoil.

The aerodynamic-coefficient histories of the airfoil predicted by LDVM are compared with experimental results in figure 7.11. The coefficients are plotted against the nondimensional (convective) time,  $t^* = tU_{ref}/c$ . Flow snapshots from LDVM and experiment are presented in figure 7.12 for six time instants. In the LDVM images, CW discrete vortices are colored blue while the CCW ones are colored red. At  $t^* = 0.0$ , the airfoil is oriented parallel to the freestream with  $\theta = 0^\circ$ . As the airfoil proceeds to pitch upward,  $\mathcal{L}$ , shown in figure 7.11(a), increases and reaches the critical value at  $t^* = 1.9$ , indicating the initiation of LEV shedding. The discrete-vortex plot from LDVM at  $t^* = 2.0$  shows a few discrete LEVs shed since LEV initiation while the corresponding experimental PIV image shows some CW vorticity starting to accumulate near the leading edge. The value of  $\mathcal{L}$  is maintained at the critical value for the remainder of the pitch-up phase as well as during the

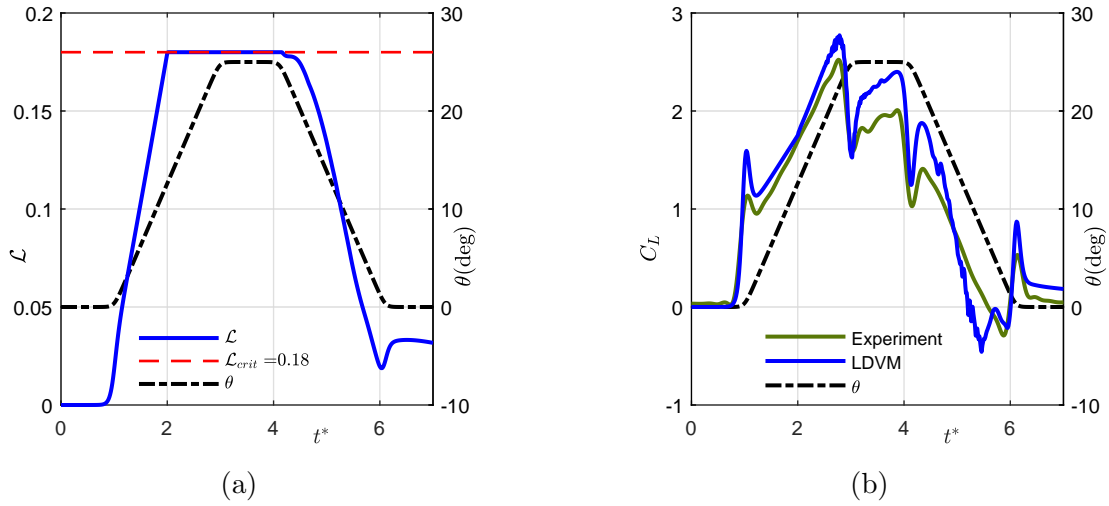


Figure 7.11: Aerodynamic coefficient histories for the baseline case: (a) Variation with  $t^* = tU_{ref}/c$  of  $\mathcal{L}$  from LDVM. (b) Lift coefficient predicted by LDVM compared with experimental measurements.

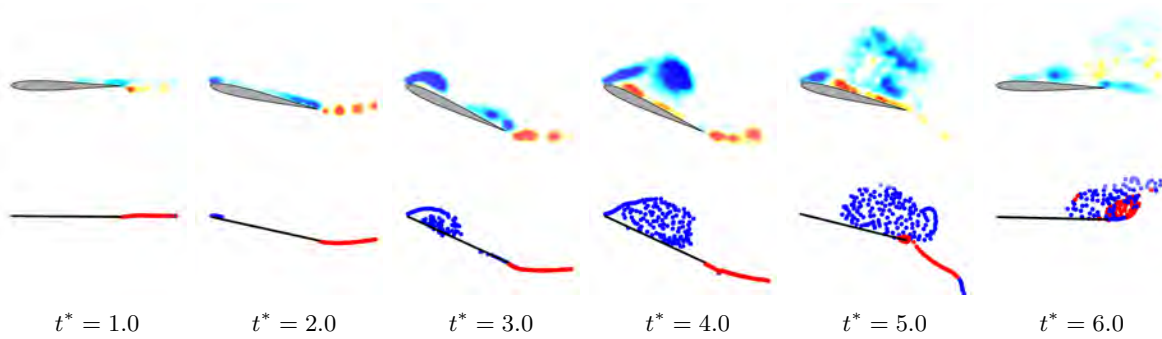


Figure 7.12: Comparison between phase-averaged vorticity contours from experiment (top) and discrete-vortex plots from LDVM (bottom) for the baseline case at six time instants.

hold phase, resulting in continuous release of discrete LEVs from the leading edge of the airfoil. The flow images at  $t^* = 3.0$  and  $t^* = 4.0$  from both LDVM and experiment show a shear layer rollup that eventually leads to the formation of a large LEV structure dominating the suction side of the airfoil. The drop of  $\mathcal{L}$  from  $\mathcal{L}_{crit}$  at  $t^* = 4.2$  in figure 7.11(b) at the start of the return phase marks the termination of LEV shedding in LDVM. Following this termination, the LEV structure detaches from the leading edge and is seen to be convecting downstream in the flow images at  $t^* = 5.0$  and  $t^* = 6.0$  while the airfoil returns towards its initial orientation.

The unsteady lift history for this case predicted by LDVM is compared with the experimental measurements in figure 7.11(a). Given the initial orientation, as the airfoil proceeds to pitch upward, non-circulatory loading contributes predominantly to the lift. This aids in the rise of an inertial spike in lift shortly after  $t^* = 1.0$ . Thereafter, lift continues a steady climb owing to the increase in bound circulation with increase in pitch angle. At the completion of the pitch-up phase, the wing experiences a second inertial spike near  $t^* = 3.0$  that acts to reduce lift. The concurrent formation of an LEV on the airfoil then causes the subsequent rise in lift during the hold-phase of motion. The termination of LEV shedding from the airfoil occurs shortly after the pitch-down

phase begins. During the return phase, the airfoil is seen to experience a steady decline of lift. Also visible are two inertial spikes corresponding to the start and end of the pitch-down motion.

Thus, LDVM predictions of the flowfield as well as the associated lift are seen to be in good agreement with experimental results and we proceed to use  $\mathcal{L}_{crit} = 0.18$  for all the LDVM predictions presented herein.

### 7.5.2 Pitching airfoil in the presence of disturbance : $\phi = 0^\circ$

The LESP variation predicted by LDVM for the airfoil under the influence of the disturbances with  $\phi = 0^\circ$  is shown in figure 7.13 using the blue curve. The LESP history for the baseline case (black curve) in the absence of any external flow disturbance is also included for highlighting the effect of the disturbances on the LESP. Snapshots of the flowfield evolution stemming from the interactions of the pitching airfoil and the oncoming disturbances are also presented using phase-averaged vorticity contours from experiment and discrete-vortex plots from LDVM. To differentiate the oncoming vortex clusters from the discrete vortices shed by the airfoil, the CW vortices shed from the airfoil are colored green and the CCW vortices are colored magenta. For the oncoming vortex clusters, blue dots represent CW clusters and red dots represent CCW clusters.

The flow images at the initiation of motion,  $t^* = 1.0$ , shows a CW vortex positioned above the leading edge that is devoid of any discernible vortex formation. The shear layer remains attached to the zero-incidence airfoil, indicating that the interactions with the disturbance are insufficient to induce leading-edge shear-layer rollup on the airfoil. The airfoil pitches up between  $t^* = 1.0$  and  $t^* = 3.0$  while interacting with the oncoming vortices. The LESP variation shows a generally increasing trend during the pitch-up phase of the motion and reaches the critical value at  $t^* = 2.3$ , marking the initiation of LEV shedding. The PIV image at  $t^* = 2.5$  shows an accumulation of CW vorticity about the leading edge. Meanwhile, LDVM predicts a nascent leading-edge vortex with the introduction of discrete vortices released at the leading edge. It is also clear from the LESP history that the effect of the disturbance is to delay the initiation of LEV shedding compared to the baseline case.

During the hold phase at  $t^* = 3.0$ , the LEV has matured considerably in experiment, though has not yet detached from the feeding shear layer. This is captured in the low-order results with a prominent large-scale vortical structure residing above the midchord, tethered to the leading edge. The LESP shows a dip from the critical value between  $t^* = 3.01$  and  $t^* = 3.37$ , resulting in a brief interruption of LEV shedding in LDVM. LEV shedding resumes when the LESP reaches the critical value again at  $t^* = 3.38$ . This is in contrast to the baseline case where the LESP remains at the critical value during the hold phase, indicating uninterrupted vortex shedding. The new series of discrete LEVs is seen to emanate in the discrete-vortex plots at  $t^* = 3.5$  while the previous cluster of LEVs has detached and started convecting downstream. Two distinct patches of leading-edge vorticity are apparent in the corresponding PIV image, corroborating the LEV interruption phenomenon predicted by LDVM. The second LEV structure is seen to develop near the leading edge in the flow images at  $t^* = 4.0$  while the first LEV structure continues to convect further downstream.

The LDVM predicts the termination of LEV shedding during the downstroke at  $t^* = 4.15$  when  $\mathcal{L}$  drops below the critical value and continues to drop overall thereafter. The presence of the disturbances results in a slightly early termination of LEV shedding compared to the baseline case. The experimental flow image at  $t^* = 4.5$  shows the second LEV structure detached from

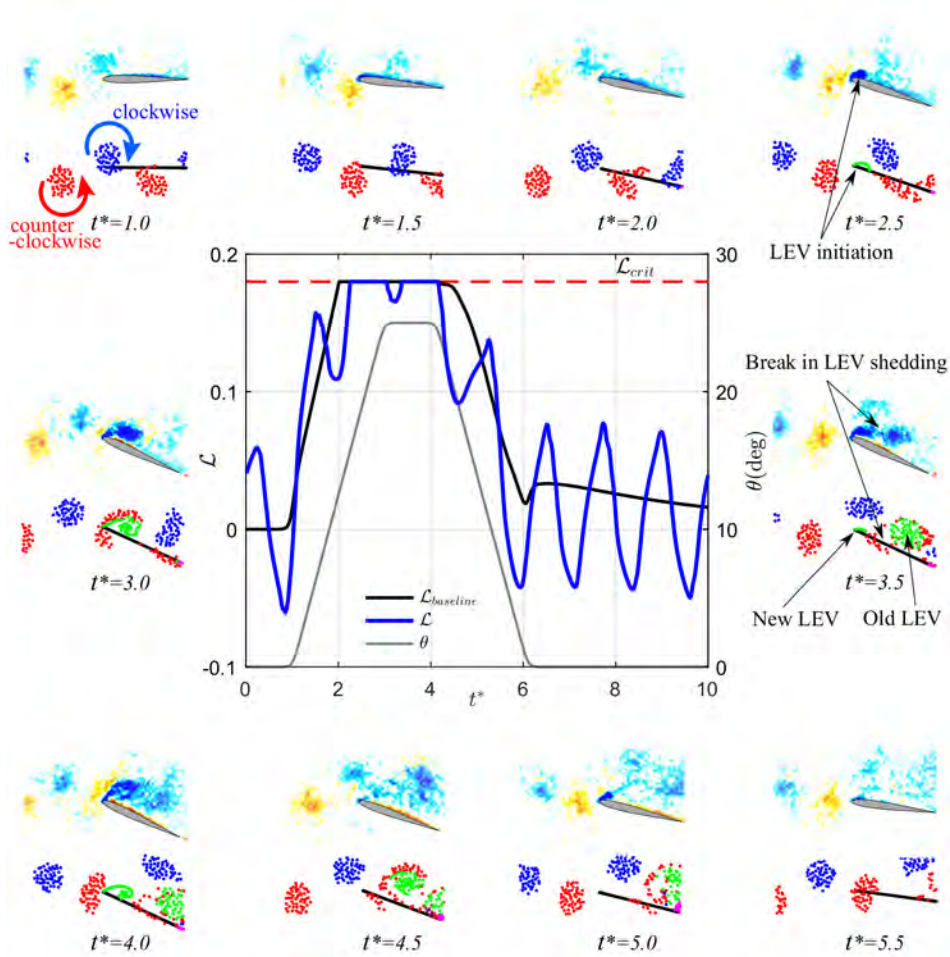


Figure 7.13: Phase-averaged vorticity contours from experiment (top) and discrete-vortex plots from LDVM (bottom) at several time instants showing the flowfield evolution of the pitching airfoil in the presence of the disturbances with  $\phi = 0^\circ$ . The inset shows the LESP variation from LDVM for  $\phi = 0^\circ$  compared with that for the baseline case.

the leading-edge free-shear layer. The LDVM also reflects this event with the display of a large amalgamated volume of CW LEVs severed from the leading edge and convecting downstream over the trailing edge. The flow images at later time instants depict the convection of the remnants of the free-shear layer along the airfoil surface while the airfoil returns to its initial orientation.

### 7.5.2.1 Finite-time Lyapunov exponent analysis of the flowfield evolution using experimental data

One of the important contributions of this work is the observation of a break in LEV shedding from the airfoil due to the effect of the oncoming vortex street. While the LEV interruption phenomenon is apparent in the vorticity images of Figure 7.13, an objective approach is necessary to obtain conclusive evidence for its occurrence. In the absence of any surface signatures using other information like pressure or shear force data, the finite-time Lyapunov exponent (FTLE) [168] analysis using the velocity data provides an excellent means to confirm the interruption of LEV shedding. Using the FTLE approach, we can track the boundaries of the different vortical structures to confirm that the two LEV structures labeled ‘New LEV’ and ‘Old LEV’ in Figure 7.13 contain materially-distinct regions of fluid and that they form due to an interruption in the LEV shedding rather than from a splitting of the primary LEV structure. For this reason, an FTLE analysis was conducted using the PIV velocity data to explore if the results support the more qualitative observation of the interruption in LEV shedding in the vorticity images.

FTLE ridges along with the  $Q$  criterion [169] calculated using experimentally collected velocity fields are used in this analysis. While the  $Q$  criterion visualizes the vortex cores, FTLE provides the additional ability to objectively visualize the transport boundaries around the vortices and provides additional insight into the vortex dynamics, such as entrainment. The FTLE calculation yields negative-time FTLE ridges (nFTLE) and positive-time FTLE ridges (pFTLE), and their movement in time can be tracked to locate transport boundaries that separate dynamically distinct regions of an unsteady flowfield. The FTLE approach has been applied, for example, to delineate the boundary between a vortex and the freestream flow [168], to locate the wake breakdown behind pitching plates [170], and to identify the shedding time of vortices from circular cylinders [171]. Additional information on the calculation of  $Q$  and FTLE can be found in the authors’ previous works [171, 172].

FTLE fields are calculated from PIV data using a trajectory grid five times finer than the velocity grid. If trajectories are integrated for less than 3.5 convective times, the ridges appear slightly blurry, and not well defined. Once an integration time of 3.5 convective times is reached, further integration has minimal effect on the results. Therefore, an integration time of 3.5 convective times is used. During the trajectory integration process, every other velocity field is used, effectively reducing the temporal resolution to 100 Hz. Trajectories that leave the available domain during the integration process are advected at the freestream velocity. Trajectories that erroneously enter the airfoil are displaced to a location just outside the airfoil.

FTLE ridges are calculated in figure 7.14 for select instances of the leading-edge vortex shedding cycle. The images contain contours of the  $Q$  criterion (grayscale contours), negative-time FTLE ridges (nFTLE, red), and positive-time FTLE ridges (pFTLE, blue). The airfoil is shown in green. Also included with each FTLE image is the flow field predicted by LDVM at the corresponding time instant. Figure 7.14(a) shows a set of blue pFTLE ridges atop the airfoil that run along the leading edge at  $t^* = 2.0$ . This pattern corresponds to a flow state prior to the initiation of any LEV formation, early within the pitch-up phase of motion. The pFTLE ridges of figure 7.14(b) are now

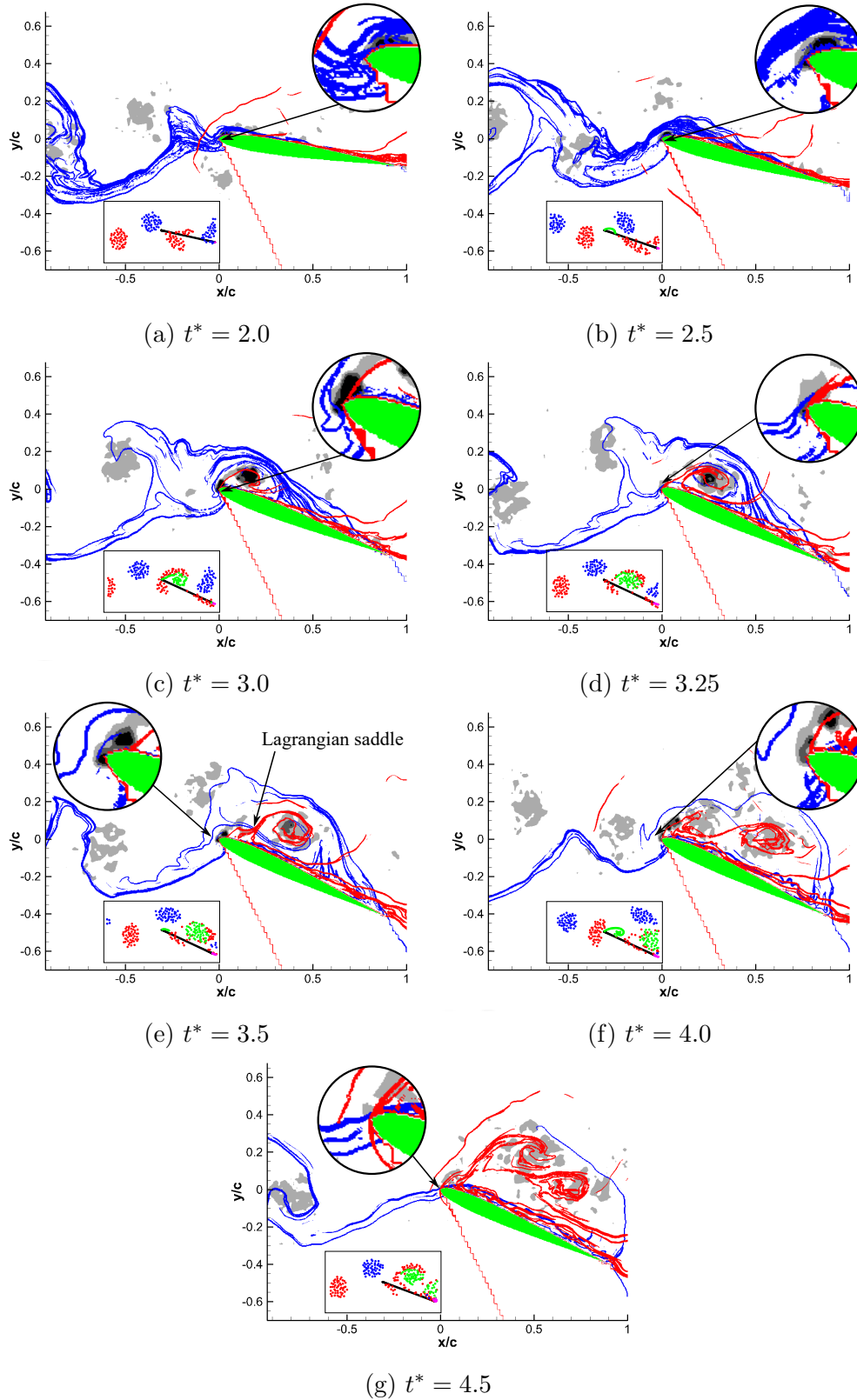


Figure 7.14: FTLE ridges calculated at various time instants for  $\phi = 0^\circ$  showing the interruption in LEV shedding. The corresponding discrete-vortex plots from LDVM predictions are also included as insets along with each FTLE image.

removed from the airfoil surface, outlining a semicircular region of vorticity rollup, as the LEV has begun to form. Figure 7.14(c) shows an advanced stage of LEV maturity. While the shear-feeding layer remains uninterrupted, the blue pFTLE ridge that envelops the LEV is seen to intersect the airfoil surface at two points near the leading edge. A disruption of LEV shedding is showcased in figure 7.14(d) where the pFTLE ridge is observed adjacent to the leading-edge surface. In such an instance the close proximity would amount to interruption and separation of the LEV. Shedding resumes in figure 7.14(e) with the relocation of the pFTLE ridge away from the leading edge, giving way to an incipient secondary LEV. It can be noticed that there is a clear indication in the FTLE ridges that the original LEV is distinct from the secondary LEV that is developing. There is a Lagrangian saddle separating the two LEVs, identified by the intersection of red and blue ridges, indicating that the two vortices contain materially distinct regions of the fluid. Figure 7.14(f) shows the maturing of the secondary LEV structure and a pFTLE ridge intersecting the wing near the leading edge. Finally the LEV production is ceased in figure 7.14(g) as the airfoil is engaged in pitch-down motion. As with previous disruptions to the shear-feeding layer the pFTLE ridge is again observed adjacent to the airfoil, following its contours. Comparison with modeled results in the respective inset image reveals that the various flow phenomena are accurately captured by the low-order model.

### 7.5.2.2 Theoretical analysis of the LEV shedding phenomena

The low-order framework equips us with various tools to analyze the effect of different factors governing the LEV shedding phenomenon. The decomposition of the LESP according to Eqn. (27), shown in figure 7.15, provides an insight into the relative contribution to the LESP from all the sources. Figure 7.16 gives us another perspective by grouping these contributions into kinematic and flowfield factors. The LESP-map approach helps us further decompose the orange curve in figure 7.16 and visualize the contributions from each of the flowfield elements, i.e, from the discrete LEVs and TEVs shed from the airfoil, and the oncoming vortex clusters. Displayed in figure 7.17 are the discrete vortices from LDVM at various time instants, superimposed on an LESP-map overlay. Also presented, corresponding to each LESP-map image, is a colorized image where the discrete-vortex locations are represented using dots colored according to the magnitude and sign of their individual contributions to the LESP. Discrete vortices with positive contribution to the LESP are colored blue and the ones with negative contribution are colored red. The scale used for the colorized images is also shown at the bottom of figure 7.17. Thus, the cumulative sum of the values of all the points in the colorized map at a given instant of time in figure 7.17 is same as the value of the orange curve in figure 7.16 for the corresponding time instant. Note that even though this sum is to be taken over the entire flow domain, the dominant effect is due to the vortices present in the vicinity of the airfoil.

As the oncoming vortex clusters pass by the airfoil, they result in an oscillating  $\mathcal{L}_D$  contribution about a zero mean as can be seen in figure 7.15. The contribution from the pitch-angle variation of the airfoil,  $\mathcal{L}_\theta$ , follows the same pattern as the kinematic history of the airfoil: it increases in the positive direction as the airfoil pitches up, levels off during the hold phase, and drops back to zero as the airfoil returns to the initial orientation of  $\theta = 0^\circ$ . The pitch-rate contribution,  $\mathcal{L}_{\dot{\theta}}$ , is active only during the pitch-up and return phases and has a sign dependent on the direction of pitching.

At  $t^* = 1.0$ , the LESP map shows two CW vortex clusters (marked A and C) positioned at either edges of the airfoil on the top surface. These two clusters have the same sense; but being located on either side of the zero line of the LESP map, their role in the leading-edge suction can be expected

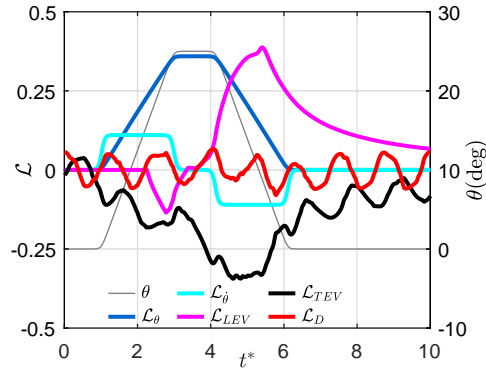


Figure 7.15: Contribution to  $\mathcal{L}$  from each factor governing the LEV shedding dynamics for  $\phi = 0^\circ$ .

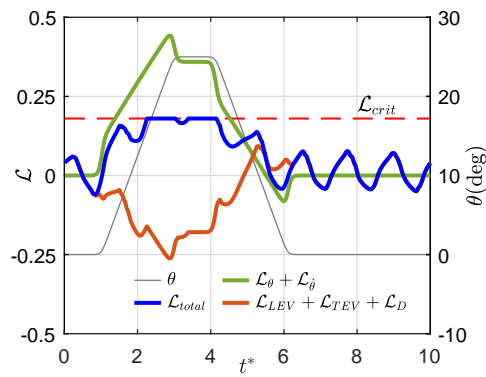


Figure 7.16: Total  $\mathcal{L}$  history split into contribution from kinematic factors and that from flowfield elements for  $\phi = 0^\circ$  for  $\phi = 0^\circ$ .

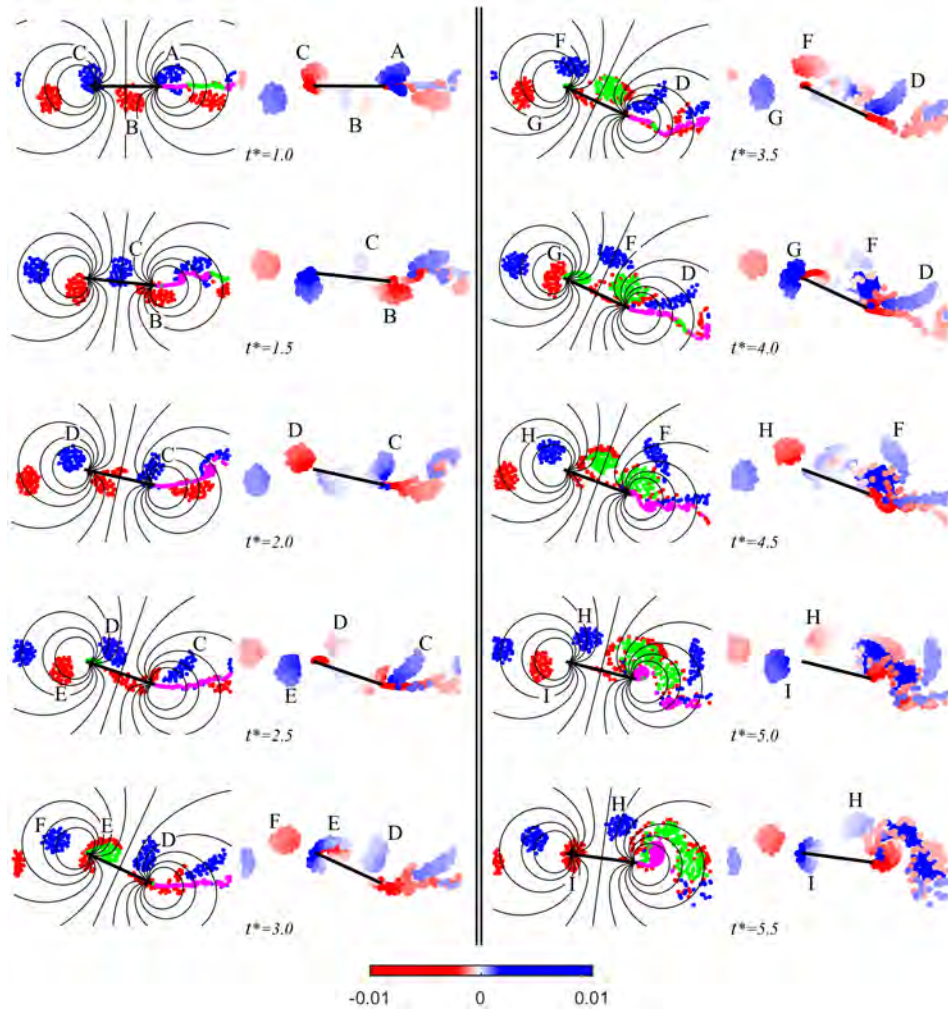


Figure 7.17: LESP maps and colored maps at various time instants highlighting the contribution from individual discrete vortices for  $\phi = 0^\circ$ .

to be opposite. This can indeed be seen in the adjacent colorized map where the two clusters are colored opposite due to their conflicting contributions to the LESP. Meanwhile, a CCW cluster B is seen at the midchord of the airfoil on the bottom surface and, as can be seen, it is positioned over the zero contour line of the LESP map. We can draw two inferences from the colorized map: that the contribution to the LESP from this cluster is negligible due to its overall location, and that the contributions from the individual discrete vortices that form this cluster, ever so small, have opposite signs depending on their respective locations relative to the zero contour line of the LESP map. One can also track the movement of the discrete vortices over different time frames to infer how their contribution to the LESP is affected as their locations in the LESP map change. For example, the CW cluster C has a negative LESP contribution at  $t^* = 1.0$  when it is near the leading edge, and as it moves closer to the midchord at  $t^* = 1.5$ , its contribution becomes negligible, and it regains its ‘LESP strength’ by causing, however, a negative contribution as it moves closer to the trailing edge at  $t^* = 2.0$ .

As seen from figure 7.16, the total  $\mathcal{L}$  (blue curve), initially dominated by the kinematic components, reaches the positive critical value quickly after the start of the pitch-up phase, leading to the release of CW discrete LEVs from the leading edge. The nascent CW LEVs released from the leading edge have a negative contribution to the LESP, as can be seen from the colorized map at  $t^* = 2.5$ . This is also clearly visible in figure 7.15 as a negative  $\mathcal{L}$  contribution from the LEVs (magenta curve) soon after LEV initiation at  $t^* = 2.3$ . This negative contribution from the LEVs help to maintain  $\mathcal{L}$  at  $\mathcal{L}_{crit}$ . Meanwhile,  $\mathcal{L}_D$  due to the disturbance, dominated by the approaching CCW cluster E near the leading edge and the cluster C near the trailing edge between  $t^* = 2.5$  and  $t^* = 3.0$ , tends toward a positive peak. This contribution, along with the increasing influence of  $\mathcal{L}_\theta$ , somewhat compensates for the increasingly negative contribution from the LEVs.

As the LEV structure grows in size, the discrete LEVs that get closer to the midchord lose their LESP strength, making the ones forming the leading-edge shear layer the dominant contributors to  $\mathcal{L}$  among the discrete LEVs, as displayed by the colorized map at  $t^* = 3.0$ . This is also reflected in figure 7.15 where  $\mathcal{L}_{LEV}$  has reached a negative peak at  $t^* = 2.8$  and is moving towards the positive side.

However, also seen at  $t^* = 3.0$  in the LESP-map images is an approaching CW vortex cluster F with a negative  $\mathcal{L}$  contribution. Between  $t^* = 3.0$  and  $t^* = 3.5$ , before  $\mathcal{L}_{LEV}$  could start supporting  $\mathcal{L}$ , the strengthening negative contribution from cluster F causes  $\mathcal{L}$  to drop below the critical value in figure 7.16, causing a disruption in the release of discrete LEVs. The loss of positive contribution from the pitch-rate factor  $\mathcal{L}_{\dot{\theta}}$ , and the leveling off of the pitch-angle factor  $\mathcal{L}_\theta$ , as seen from figure 7.15 and figure 7.16, also contribute to this event.

The LESP map at  $t^* = 3.5$  shows that the detached LEV structure has moved to the midchord region. Meanwhile, cluster D starts to regain its positive LESP strength and cluster F starts losing its negative LESP strength. These effects help  $\mathcal{L}$  to increase and reach  $\mathcal{L}_{crit}$  again, resulting in the resumption of LEV shedding. After this point, the positive contribution from the LEVs continues to increase in figure 7.15, however, counteracted by a stronger negative contribution from the TEVs. Between  $t^* = 3.5$  and  $t^* = 4.0$ , the presence of the approaching CCW cluster G also supports  $\mathcal{L}$  as seen in the LESP-map images at  $t^* = 4.0$ . Under the combined influence,  $\mathcal{L}$  remains at the critical value and the LEV shedding continues. Shortly after  $t^* = 4.0$ , cluster G starts losing its dominance, while the airfoil enters pitch-down phase causing  $\mathcal{L}_\theta$  to decrease and the  $\mathcal{L}_{\dot{\theta}}$  to become negative. These effects result in a strong decrease in  $\mathcal{L}$ , forcing it to drop below  $\mathcal{L}_{crit}$  as seen at  $t^* = 4.5$  in figure 7.16, and thus in the termination of LEV shedding. The detached CW LEVs are subsequently convected to the trailing-edge side of the LESP map, resulting in a strong positive

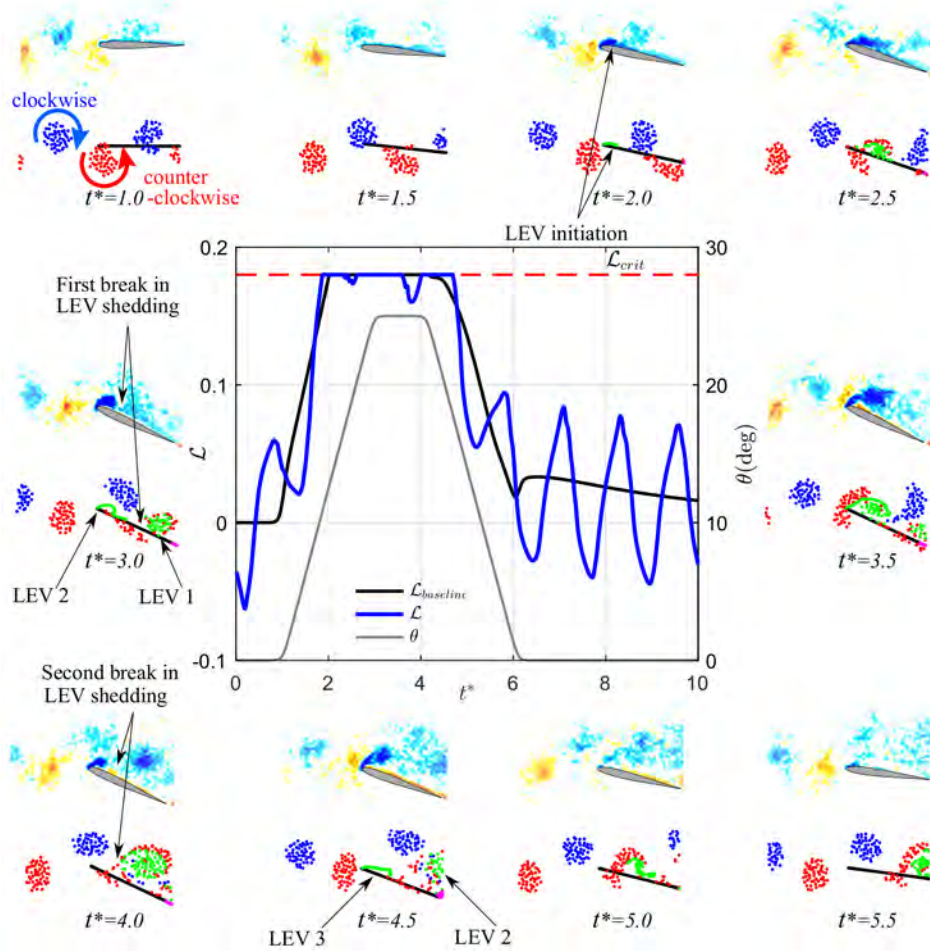


Figure 7.18: Phase-averaged vorticity contours from experiment (top) and discrete-vortex plots from LDVM (bottom) at several time instants showing the flowfield evolution of the pitching airfoil in the presence of the disturbances with  $\phi = 180^\circ$ . The inset shows  $\mathcal{L}$  variation from LDVM for  $\phi = 180^\circ$  compared with that for the baseline case.

contribution from the LEVs to the LESP. These LEVs, along with the approaching CCW cluster I, are seen to create dominant positive regions in the colored maps at  $t^* = 5.0$  and  $t^* = 5.5$  while the oncoming street continues to cause fluctuating contributions. However, the overall  $\mathcal{L}$  in figure 7.16 decreases due to the decline in the dominant kinematic factors  $\mathcal{L}_\theta$  and  $\mathcal{L}_{\dot{\theta}}$ .

### 7.5.3 Pitching airfoil in the presence of disturbance : $\phi = 180^\circ$

The sequence of events in the flowfield development for  $\phi = 180^\circ$  are presented in figure 7.18. A CCW vortex is seen at the leading edge at the commencement of the pitch-up phase at  $t^* = 1.0$ . The LESP history in figure 7.18 shows that  $\mathcal{L}$  reaches the critical value at  $t^* = 1.9$  indicating an early initiation of LEV shedding compared to the baseline case. A developing region of CW vorticity is seen at the leading edge of the airfoil in both experiment and LDVM at  $t^* = 2.0$  in figure 7.18. The most noticeable feature of the LESP history is that it exhibits two dips from the critical value: one

towards the end of the pitch-up phase at  $t^* \approx 2.5$  and another one during the hold phase of motion at  $t^* \approx 3.8$ . Correspondingly, LDVM predicts interruptions in LEV shedding between  $t^* = 2.3$  to  $t^* = 2.6$  and from  $t^* = 3.6$  to  $t^* = 4.0$ . The first interruption is a rather weak one where  $\mathcal{L}$  falls short of its critical value by a small amount for a brief period of time. The outcome of this event is most evident in experimental images at  $t^* = 3.0$  when a new shear-layer rollup is visible near the leading edge. Correspondingly, LDVM results show a second LEV structure developing at the leading edge while the first LEV structure is being convected away after the shear layer is cut off as a result of the interaction with the oncoming vortex street. The new batch of vorticity evolves into a concentrated LEV structure attached to the leading edge through the feeding shear layer which is visible in both the experimental as well as LDVM flow images at  $t^* = 3.5$ . Vortex shedding is interrupted for the second time when this LEV structure interacts with an approaching CCW vortex cluster and gets detached from the leading edge. The flow images at  $t^* = 4.0$  show the second LEV convecting downstream along with the oncoming vortices. LEV shedding resumes again shortly afterwards when  $\mathcal{L}$  reaches the critical value. The third LEV structure stemming from the latest release of vorticity is clearly seen in the PIV image at  $t^* = 4.5$  and is accurately captured in the LDVM results. LDVM predicts the termination of LEV shedding at  $t^* = 4.7$ , soon after the airfoil enters the return phase of kinematics. The discrete-vortex plot at  $t^* = 5.0$  shows that the group of discrete vortices belonging to the third LEV has detached from the leading edge and is getting convected downstream. The PIV image at the same time instant conforms to the LDVM predictions and shows the traces of remnant vorticity detached from the leading edge. The flow snapshots from both the studies at  $t^* = 5.5$  show the airfoil returning to the initial orientation without any further release of vorticity. Finally, a comparison of the LESP history with that of the baseline case reveals that  $\phi = 180^\circ$  results in a delayed termination of LEV shedding. An analysis of the flowfield evolution for the  $\phi = 180^\circ$  case using decomposition of  $\mathcal{L}$  and the LESP map is presented in Appendix A.

#### 7.5.4 Effect of the disturbance on the unsteady lift

Lift-coefficient histories from experimental measurements and LDVM predictions for the pitching airfoil subjected to the disturbance are compared against each other in figure 7.19. The pitch history is plotted in gray line segments. The respective baseline lift coefficients are also superimposed, indicated by the blue lines. The peaks exhibited by the baseline lift profiles are indicated by  $p_1, \dots, p_5$ . Also marked are four valleys  $v_1, \dots, v_4$  associated with the four corners of the motion history. The phase-dependence of the flowfield interactions is reflected in the way these signatures are altered in the presence of the disturbances. The flow images from both the methods for the two values of  $\phi$  are also reproduced in figure 7.19.

The vortex street induces periodic fluctuations in lift when the airfoil is static before and after the execution of the kinematics. Local peaks and valleys associated with this mode of interaction are sometimes distinctly visible even when the airfoil is in motion, for example at  $t^* = 2.0$ . The local peaks and valleys correspond to the proximity of CCW and CW vortex clusters, respectively, to the leading edge. Although not shown in this paper, the lift variation during the motion of the airfoil under the influence of the disturbances may be different from a simple superposition of the lift response due to the disturbances on a static airfoil added to the lift response due to unsteady motion of the airfoil without the disturbances. This lack of superposition is not unexpected because the total lift response is a nonlinear combination of kinematics and disturbance effects, as seen from Eqn. 20.

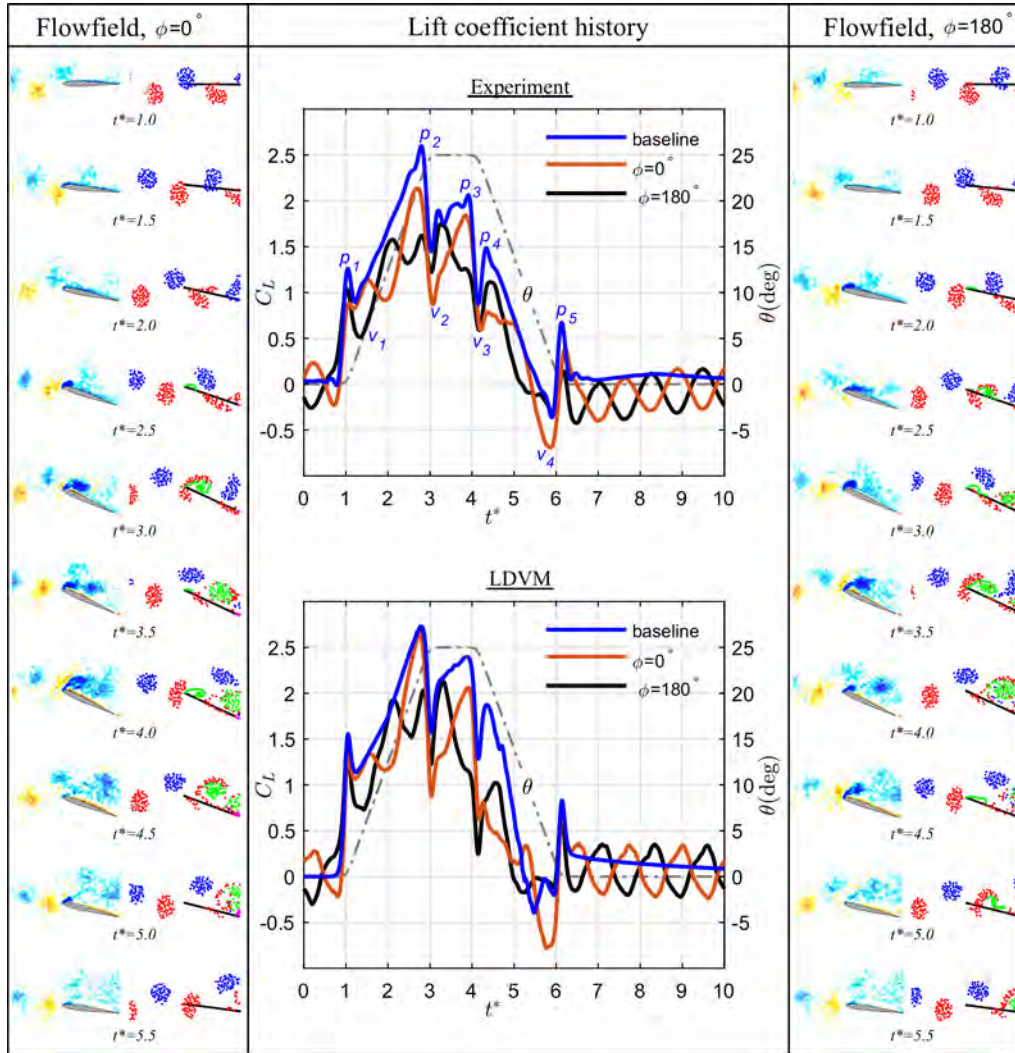


Figure 7.19: Comparison of  $C_L$  history from experiment and LDVM for the two values of  $\phi$ . The flow images from both the methods are also shown for selected time instants.

When the airfoil starts pitching up at  $t^* = 1.0$ , the flow images show a CW vortex coincident with the leading edge for  $\phi = 0^\circ$  while a CCW vortex is located at the same location for  $\phi = 180^\circ$ . The effect of this configuration is evident in the form of a local valley in the lift history for  $\phi = 0^\circ$  at  $t^* \approx 0.9$ . The corresponding local peak for  $\phi = 180^\circ$  is obscured by the dominant apparent mass contributions to lift. Peak  $p_1$ , being predominantly inertia driven, is not affected considerably by the disturbance and hence the nominal magnitude of pure-pitch performance is closely maintained. Shortly after  $p_1$ , a valley  $v_1$  follows in the baseline case. Upon the introduction of the disturbance, the intensity of this valley is increased for  $\phi = 180^\circ$  while it is not considerably affected for  $\phi = 0^\circ$ . The baseline  $C_L$  continues to increase steadily under the influence of the increasing pitch angle and a positive pitch rate until it reaches the peak  $p_2$  at  $t^* = 2.8$ . The  $C_L$  histories for the two cases with flow disturbance, though modulated by fluctuations induced by the disturbances, also show an overall increase during this period of time due to the dominant contributions from the kinematic factors. The flow images from  $t^* = 2.0$  to  $t^* = 3.0$  show that the topology of the LEV structure is different between the two phases. Even though the lift of  $\phi = 180^\circ$  is at an advantageous position compared to that of  $\phi = 0^\circ$  at  $t^* = 2.0$ , the complex flow interactions prove to be destructive for  $\phi = 180^\circ$  between  $t^* = 2.0$  to  $t^* = 3.0$ . As a result, the peak  $p_2$  is disrupted significantly for  $\phi = 180^\circ$ .

At the start of the hold phase,  $\phi = 0^\circ$  experiences a strong disruption in valley  $v_2$  while  $\phi = 180^\circ$  experiences relatively less disruption. Following this, the baseline lift increases and reaches the peak  $p_3$  at  $t^* = 3.9$ . The lift curve for  $\phi = 0^\circ$  exhibits a similar trend during this time period while the lift curve for  $\phi = 180^\circ$  experiences a local peak initially and shows a decreasing trend thereafter. The effect of the flowfield interactions on  $p_3$  is similar to that on  $p_2$ : the intensity of the lift peak for  $\phi = 0^\circ$  is sustained while that for  $\phi = 180^\circ$  is significantly disrupted.

The start of the pitch-down phase is marked by the valley  $v_3$  and the peak  $p_4$  in the baseline lift history. While  $v_3$  is visible as a distinct valley in both cases with the oncoming disturbances, the intensity of  $p_4$  shows a dependence on  $\phi$ . In the presence of the disturbance, the magnitude of  $p_4$  for  $\phi = 0^\circ$  is smaller than that for  $\phi = 180^\circ$ . Thus, the effect of the oncoming vortices on  $p_4$  is the opposite of its effect on  $p_2$  and  $p_3$ . As the airfoil transitions from the pitch-down phase to the terminal hold phase, the baseline case displays a valley  $v_4$  followed by a peak  $p_5$ . The difference in the effect of the disturbance on these two events can also be noticed, more so clearly for  $v_4$  than for  $p_5$ .

The low-order predictions of the effects of the disturbances on the unsteady lift of the airfoil show good agreement with the experimental results. The LDVM accurately captures the trends in the lift fluctuations and overall predicts a lift profile that is in qualitative agreement with experimental observations. The temporal time stamps and phase-dependent modulation of the intensities of the peaks and valleys of the baseline case are correctly reflected in the LDVM results. The fidelity of the LDVM predictions is excellent during the pitch-up and hold phases of motion. The small disagreement during the pitch-down phase for the baseline case is due to the trailing-edge separation induced by the detached LEV structure that closely interacts with the trailing edge shear layer, which is not modeled in LDVM. Interestingly, the agreement between LDVM and experiment during this period is better in the presence of the external disturbance compared to the baseline case. While temporal trends in the lift history are preserved by LDVM, a general over-prediction of lift, consistent with alternative inviscid approaches, can be observed in a direct comparison with experiment.

## 7.6 Interim Conclusions

Water tunnel experiments were performed on an airfoil performing a high-amplitude pitching maneuver in the presence of flow disturbances generated by an upstream circular cylinder undergoing sinusoidal rotation about its axis. Flow visualization using phase-averaged particle-image velocimetry (PIV) and calculations of finite-time Lyapunov exponent (FTLE) ridges revealed that the LEV shedding characteristics of the airfoil were altered by the disturbances. The phase of the oncoming disturbances relative to the kinematic state of the airfoil was varied by adjusting the phase of the sinusoidal rotation of the upstream cylinder. While the airfoil displayed a period of uninterrupted LEV shedding during the baseline maneuver without any external disturbance, phase-dependent interruptions in LEV shedding were observed in the presence of the disturbances. The instants of initiation and termination of LEV shedding were also seen to exhibit a phase-dependent shift. Load measurements were conducted to study the effect of the interactions on the lift of the airfoil. Under static conditions, the airfoil experienced small-amplitude periodic fluctuations in lift. For the pitching airfoil, the inertial and circulatory signatures of the baseline pitch history experienced a phase-dependent modulation due to the disturbances.

A theoretical model based on unsteady thin-airfoil theory was formulated to complement the experimental analysis and to serve as a low-order prediction mechanism. This framework was built upon the LESP-modulated discrete-vortex method (LDVM) that was developed in previous research to predict intermittent LEV shedding from unsteady airfoils in a uniform freestream using the leading-edge suction parameter (LESP). In this work, the LDVM framework was augmented with a low-order model for the oncoming disturbances using discrete-vortex clusters periodically released into the flowfield, superimposed with a uniform flow. Besides accurately replicating the LEV shedding pattern of the airfoil in the nonuniform freestream conditions, the interaction between the LEVs and the oncoming disturbances and the resulting modulation of the unsteady lift of the airfoil were also predicted by the LDVM in good agreement with experimental observations. This good agreement between the theoretical results and the experimental observations even for fairly subtle flow features such as the interruptions of the LEV formation shows that criticality of LESP modulates the LEV formation on rounded leading edges even for external disturbances. While most previous modeling efforts on disturbance effects have focused on airfoil forces and vortex shedding from sharp edges, this work extends the capability to rounded leading edges. Further, because the LESP is connected to a term in standard unsteady airfoil theory, the new insight enables straightforward extension of the LDVM framework—which itself is based on an augmentation of classical airfoil theory—to predict disturbance effects on unsteady airfoil flows.

A decomposition approach was applied to the LESP to understand the contribution to the LEV shedding and dynamics from various sources such as the kinematic states of the airfoil, the vortices shed from it, and the external disturbances. Further, a graphical approach referred to as the LESP map was formulated to take a closer look at the role played by each discrete vortex in the flowfield on the LESP variation, and thus on the LEV shedding pattern. This approach also was used to associate the interruptions in LEV shedding with the spatiotemporal features of the flowfield. For example, the LESP maps showed how a counter-clockwise vortical disturbance approaching the airfoil promotes its LEV shedding tendency while a clockwise disturbance suppresses it. Thus the theoretical modeling not only provides low-order prediction capability but, with the decomposition approach, also provides capability to gain insight on the spatio-temporal effects of the advecting vortical disturbances on the LEV-shedding tendency from the unsteady airfoil.

While the temporal features of the lift history were accurately captured by the LDVM, a small

overall over-prediction of the magnitude, which is typical of potential-flow-based approaches, was observed. Slight disagreement in the lift response was also seen when there was a strong interaction between leading-edge vorticity and trailing edge of the airfoil. These discrepancies can be attributed to the effects like trailing-edge shear-layer separation and viscous dissipation that result from these interactions, and are not accounted for in the aerodynamic model.

## Chapter 8

# Tailored Bluff Body Motion for Generating Desired Wake Structures

This chapter uses numerical simulations to show the range of actuation frequencies that result in locked-on, downstream vortex shedding frequencies from a cylinder-splitter plate bluff body. The numerical simulation performed in ANSYS Fluent is verified with selected published experimental results and extended to higher actuating frequencies. The time histories of the lift coefficient obtained from the simulations are used in conjunction with the vortex shedding snapshots to ascertain the upper and lower bounds of the prescribed frequencies that lead to locked-in vortex generation. Outside the lock-in range, the spectral map of the lift coefficient shows multiple frequency content marked with the onset of distorted vortices signaling a deviation from well behaved von Kármán vortex street. This work relates the prescribed frequency with the wake vortical frequency and motivates the larger effort towards mapping the complete spatiotemporal properties of the von Kármán wake structure with the prescribed motion.

### 8.1 Chapter Introduction

Recent experimental observations from our research group have revealed that vortical wakes generated by upstream bodies can introduce significant changes to the aeroelastic stability, LCO amplitude, and limit cycle phase-space trajectory of downstream aeroelastic structures. Depending on the system and flow parameters, these disturbance structure interactions can range from the destabilization of an otherwise stable equilibrium point [173] to the enhancement of LCO amplitudes, to the introduction of time-periodic LCO amplitude modulation [174], to the annihilation of limit cycles leading to re-stabilization of an otherwise oscillatory system [175]. Understanding, producing, and regulating these system behaviors on-demand would enable us to extend control over the fluid structure interactions. This ability could be useful for applications ranging from enhancing locomotion efficiency in swarms of swimming robots, to increasing power extraction from arrays of flow energy harvesters [176], to protecting aircraft wings, bridge decks, and civil infrastructure from damaging flow-induced oscillations. Most of the published literature focuses on the effect of wake disturbances on wings and airfoils undergoing prescribed motions [177, 178, 179]. However, our work looks to investigate the effect of vortical disturbances on aeroelastic structures that are not fed with any predefined motions. One of the first steps towards achieving on-demand aeroelastic behavior is generating desired vortical wake structures using a disturbance generator. Cylindrical

bluff bodies have received a lot of attention for decades, as they provide a simple geometry to generate and study von Kármán vortices [180]. The von Kármán vortex street is a time periodic series of vortical disturbances typically shed by stationary bluff cylinders over a broad range of Reynolds numbers. Such von Kármán vortices shed from bluff-cylinders are prone to vortex dislocations leading to incoherent vortex structures [181]. Moreover, cylindrical bluff bodies have been experimentally shown to be ineffective in shedding von Kármán vortices at a prescribed oscillation frequency [182]. Hence, such vortices are deemed unsuitable where consistent time-periodic, coherent vortices are required to be generated in a controllable fashion. Recently, Rockwood et. al. [182] have used cylindrical-splitter plate bluff structures to successfully demonstrate controlled and repeatable gust generation for a range of actuated frequencies where coherent von Kármán vortices have been observed to be shed from the generator, locked-on with the actuated frequency. This provides a promising, yet simple technique to generate periodic vortical structures in the wake of the oscillating cylinder-plate arrangement by controlling its rotational frequency. The researchers [182], experimentally investigated the cylinder-plate structures in a water tunnel for Strouhal frequency ratios ranging from 0.3 to 1.1 for two different rotational maximum amplitudes,  $\theta_{max} = \pi/4$  and  $\pi/6$  and observed that the lock-on is predominantly observed above Strouhal frequency ratios of 0.7. Strouhal frequency ratio is defined as  $St/St_n$ , where  $St_n$  is the natural Strouhal frequency of the cylinder alone.

The schematic in Fig. 8.1, shows the cylinder-splitter plate arrangement (henceforth referred to as just the bluff body) being driven by a harmonic excitation to create a von Kármán vortex street. The illustrated vortical parameters are, vortex shedding frequency ( $f_{shed}$ ), the vortex strength ( $\Gamma$ ), and stream-wise and cross stream-wise spatial distances ( $d, w$ ). In this chapter, we have extended the parameter space explored by Rockwood et. al. to numerically simulate cases that extend well beyond the Strouhal frequency ratios explored in their experimental campaign. The geometrical dimensions and test conditions used in their experiments [182] have been adopted for the current investigation as it enables easy comparison with the published experimental data to validate our simulation settings. Additionally, using the same simulation settings, we can extend the investigation to explore higher Strouhal frequency ratios and prescribed oscillation amplitudes. While there are four primary parameters that define a typical von Kármán vortex street as described above, the current scope of the chapter is to investigate the range of prescribed Strouhal number ratios that lead to locked-on vortical shedding from the bluff body.

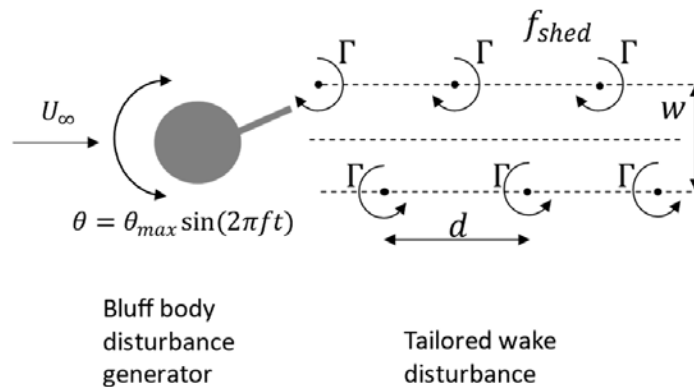


Figure 8.1: The schematic showing tailored vortical disturbances being produced using an actuated cylinder-splitter plate bluff body

## 8.2 Simulation Setup

The geometrical dimensions of the cylinder-splitter plate arrangement used in our simulations are kept the same as the experimental dimensions used by Rockwood et. al. [181]. This allows us to verify our numerical simulation setup by comparing the results directly with the experimental observations by Rockwood et. al. Additionally, it also allows us to expand the parameter space of the prescribed bluff-body motions without the added uncertainty of using a separate simulation parameters and mesh setup. The cylinder diameter is set at  $D = 25.4$  mm and the splitter plate extends  $1D$  downstream of the cylinder with a thickness of 3.2 mm. The fluid domain encapsulating the bluff body extends  $25D$  upstream and  $50D$  downstream of the cylinder center, measured along the streamwise direction. In the cross-streamwise direction, the fluid boundary extends  $25D$  on either side of the cylinder center.

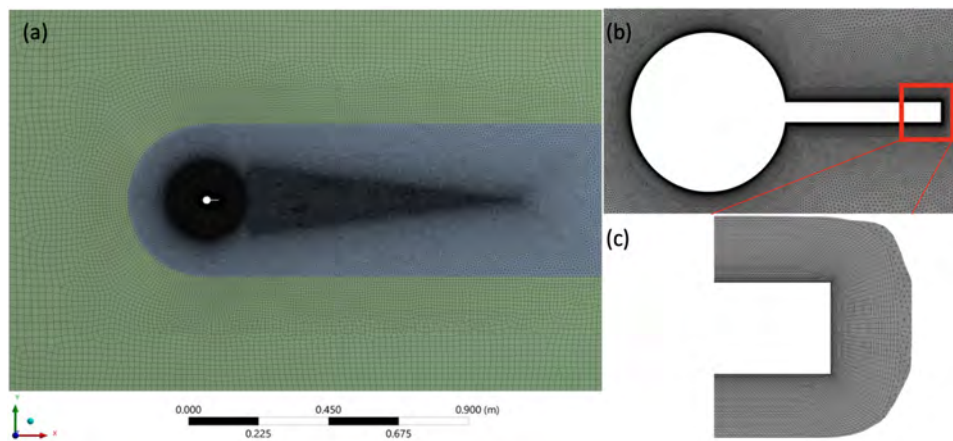


Figure 8.2: The figure shows the mesh used in this numerical analysis (a) shows the computational zone partitioned into 3 domains with increasing mesh refinement (b) shows the zoomed in view of the mesh around the bluff body, and (c) shows the enlarged view of the mesh around the sharp corners of the splitter plate.

As shown in Fig. 8.2(a), the computational zone is subdivided into three domains, the outer rectangular fluidic domain, the inner fluidic domain and the circular domain housing the bluff body geometry. Triangular elements are in the inner fluidic and circular domains, and mixed tri-quad elements in the outermost fluid domain. Medium and fine mesh zones using triangular elements encompasses the wake and the vicinity of the bluff body, respectively. The inner circular domain measures a radius of  $5D$  and is finely meshed to capture the viscous wall-bounded effects of the bluff body. Overall, the hybrid grid consists of a total of 383,000 cells. A circular, sliding interface between the inner circular and middle zones was created to allow the inner zone to rotate with the bluff body geometry. Information from the two zones adjacent to the interface is passed at the cell face at each timestep. This method allows for cells local to the bluff body to remain fixed, while also preventing undesired skewness when the circular domain rotates with a prescribed a harmonic motion.

In the absence of wall-functions, accurate representation of the boundary layer in wall-bounded flows require sufficient refinement near the wall to capture the generation of vorticity and turbulence. Fully resolving the inner most subdivisions of the near-wall region is critical due to the significant contribution of viscosity to wall shear stress. By introducing  $y^+$  as the dimensionless distance to the

wall, the near wall region can be subdivided into three distinct layers, namely the viscous sublayer ( $y^+ < 5$ ), buffer layer ( $5 < y^+ < 30$ ), and the log-law region ( $y^+ > 30$ ). Overall resolution of the boundary layer is influenced by both first cell height and the expansion ratio. For the turbulence model used in the present simulations, it is desired that the first cell centroid height along the wall be at a distance of  $y^+ < 1$ . Being that the  $y^+$  calculation is dependent on Reynolds number, the near-wall first cell height was prescribed as  $1.1 \times 10^{-5}$ , thus satisfying a cell centroid  $y^+ \ll 1$  for the given freestream and rotational velocities. A total of 50 cells in the wall-normal direction were generated using an expansion ratio of 1.05, fulfilling guidelines provided in [183]. A fluid velocity (water) of  $0.3 \text{ m/s}$  was prescribed at the flow inlet corresponding to a Reynolds number of 7600. Due to the relatively transitional Reynolds number effect and the large disturbances caused by the oscillating splitter plate, a  $SSTk - \omega$  turbulence formulation with a one equation Intermittency Transition model was chosen to capture the viscous effects. Freestream turbulence intensity was set at 1%. The simulation was performed using Fluent 16.1.0 with the SIMPLE pressure-velocity coupling method, and second order accurate spatial discretization being used for pressure and momentum. Fixed timesteps varied from  $5 \times 10^{-4}\text{s}$  to  $2.5 \times 10^{-4}\text{s}$ , depending on oscillation frequency of the case being simulated. Temporal step sizes finer than these values did not show appreciable differences in vortex strength or periodic force values. The cell convective Courant number was kept far below 20 for every case, satisfying Fluent recommendations for efficient calculation.

### 8.3 Results and Discussion

The experimental results obtained by Rockwood et. al. is simulated first to verify our simulation settings and the meshing quality. All the comparative cases have a fixed freestream velocity,  $U_\infty$  of  $0.3 \text{ m/s}$  that corresponds to a constant  $D$  based Reynolds number of 7600. Under such conditions, the  $D$  based Strouhal number for a circular cylinder is 0.202 [183].

Case. No	$\theta_{max}[\text{rads}]$	$St/St_n$	$f[\text{Hz}]$
1	$\pi/6$	0.3	0.716
2	$\pi/6$	0.7	1.67
3	$\pi/4$	1	2.39

Table 8.1: The table below shows the three cases that have been selected from the experimental publication of Rockwood et. al. [182] for verifying our numerical model

The actuated frequency,  $f$ , shown in the table above is evaluated as shown below,

$$f = \left( \frac{St}{St_n} \right) \frac{u_\infty}{D} \quad (1)$$

The following choice of cases selected here are representative of the parameter space explored by Rockwood et. al. In Case 1, the bluff body is actuated very slowly, and the vortices form in the separated wake region, as shown in Fig. 8.3(a)-top. This is very similar to a stationary circular cylinder, except that the vortices are highly diffused and lack a prominent vortex core. In Case 2, Figure 8.3(b)-top, at the maximum rotational amplitude of  $\pi/6$ , the generated wake topology approaches that of von Kármán vortex street and is locked-on to the prescribed frequency  $f$ . Coherent vortices with well-defined vortex cores are formed in this operating regime. In Case 3, Fig. 8.3(c)-top, the bluff body is actuated at the natural Strouhal number resulting in formation

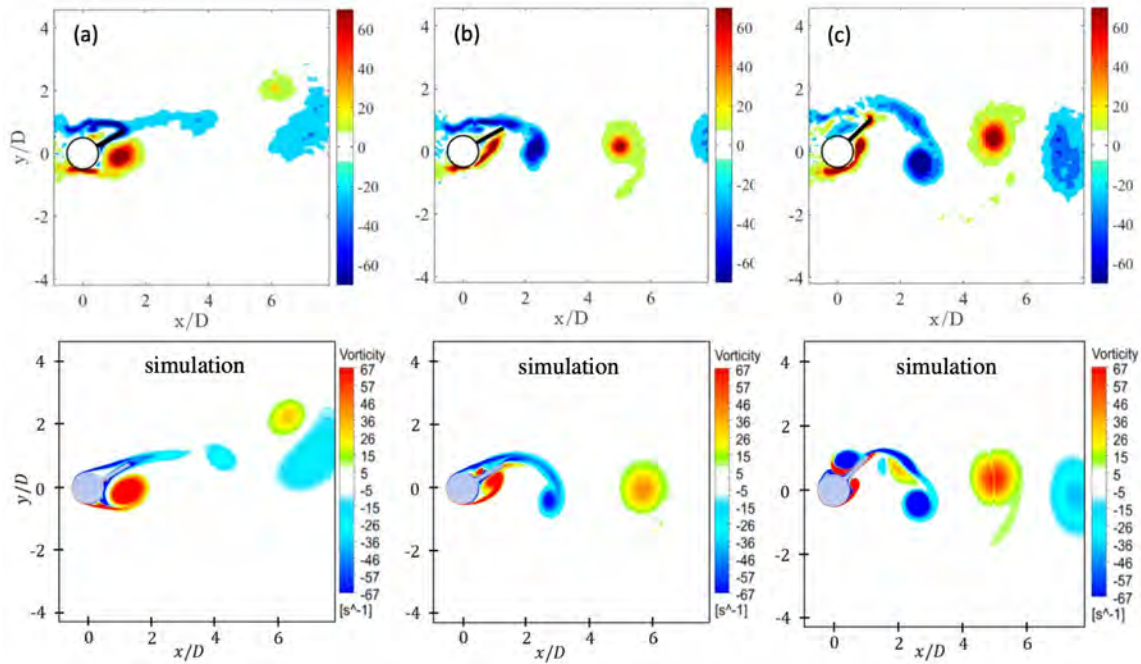


Figure 8.3: The top row of the shows the experimental vorticity plots obtained by Rockwood et. al. [10] for the cases 1, 2 and 3, corresponding to the Strouhal ratios of 0.3, 0.7 and 1 respectively, at their maximum amplitudes of rotation. The bottom row shows the corresponding cases numerically obtained using ANSYS Fluent, showing a very good agreement with the experimental results.

of coherent von Kármán vortices with a well-defined vortex cores and a high vorticity magnitude. In all the three cases, the numerical simulations are able to capture the trends very well, both qualitatively and quantitatively as shown in Fig. 8.3 bottom row. With the numerical simulations comparing very well with the established experimental results, the same simulation parameters and mesh setup are used to explore higher Strouhal frequency ratios at lower oscillation amplitudes of  $\pi/6$ , as shown in Table 8.2. The intention of this exercise is to obtain coherent vortices with alternating vorticity in the wake of the bluff body such that the vortex shedding frequency is locked-on with the bluff body actuation frequency. Hence, the Strouhal frequency ratio is increased for every subsequent simulation until the vorticity degenerates into dislocated vortices and/or the shedding frequency breaks the lock-in.

The simulations for a range of Strouhal frequency ranges from 0.6 to 2.2 are carried out by harmonically oscillating the bluff body with a maximum amplitude of  $\pi/12$ . Fig. 8.3, shown above, illustrates the evolution of the vortex street with increasing actuation frequency. Vortex shedding phenomenon is accompanied by a change in the fluid dynamic forces acting on the bluff body. Hence, the frequency content of the shed vortices could be obtained by analyzing the time history of the fluidic forces acting on the bluff body. In this chapter, the time history of the lift coefficient ( $C_L$ ) obtained from each simulation case is used to supplement the visual, qualitative information of the snapshots with quantifiable information.

For a sample Case 7, the transient effect in  $C_L$  is shown in Fig. 8.5. The numerical simulations are run for ten seconds and the first two seconds are truncated. As described in the previous section, the simulations are run using a fixed time step that varies from  $5 \times 10^{-4}$ s to  $2.5 \times 10^{-4}$ s, case to

Case. No	$St/St_n$	$f$ [Hz]
4	0.6	1.43
5	0.8	1.91
6	1	2.39
7	1.2	2.86
8	1.4	3.4
9	1.6	3.81
10	1.8	4.29
11	2	4.77
12	2.2	5.25

Table 8.2: The additional cases simulated in this chapter are tabulated here where higher Strouhal frequency ratios are explored at lower rotational amplitudes of  $\pi/12$ , keeping the Reynolds number and the simulation settings constant.

case. The time history of  $C_L$  for all the cases are resampled to get a uniform frequency resolution of 0.18 Hz. This processed  $C_L$  data is used to obtain the spectrogram for every simulated case.

The spectrogram allows us to visualize the time evolution of the spectral content of a signal, which in this case is the lift coefficient  $C_L$  of the bluff body. The preprocessed  $C_L$  time history for a given Strouhal frequency ratio is used to obtain the individual spectrograms. The individual spectrograms are stitched together to obtain Fig. 8.6. The strength of each frequency is represented on a color scale as shown in the color bar of Fig. 8.6, where darker tones indicate the stronger presence of that frequency. It is important to note that the  $C_L$  time history is normalized within each Strouhal case. Performing this normalization allows the relative strengths of the spectral content for the respective cases to be identified, while also permitting the global tracking of case to case predominant frequencies. The actuating frequency is superimposed on the spectrogram to easily highlight the frequency range within which the observed shedding frequency from the bluff body locks-in with the actuation frequency.

It is observed that the predominant bluff body shedding frequency matched very well with the actuating frequency. However, at the lower and higher ends of the Strouhal ratios, the predominant frequency is contaminated with multiple frequencies, suggesting that the actuated frequency is not in synchronization with the shedding frequency. It is observed that for  $St/St_n$  of 0.6, the frequency content is dispersed over multiple frequencies. This is consistent with the findings in [182], where the researchers were not able to observe a frequency locking at low Strouhal ratios. In our simulations, we observe a lock-on from  $St/St_n$  of 0.8 to 1.4 characterized by consistent spacing of the shed vortices both in the stream-wise and cross stream-wise directions, as observed in Fig. 4(b)-(e). of 1.6 represents the transitional case beyond which the spectral content is distributed over multiple frequencies as observed from multiple horizontal lines from  $St/St_n$  of 1.8 to 2.2. This is also corroborated from the last row of Fig. 8.4.

## 8.4 Interim Conclusions

In this study, we have successfully replicated the published experimental results obtained by Rockwood et. al. [182] using turbulent CFD simulations at a transitional Reynolds number for a cylinder-splitter plate bluff body actuated with a prescribed harmonic motion. The same simula-

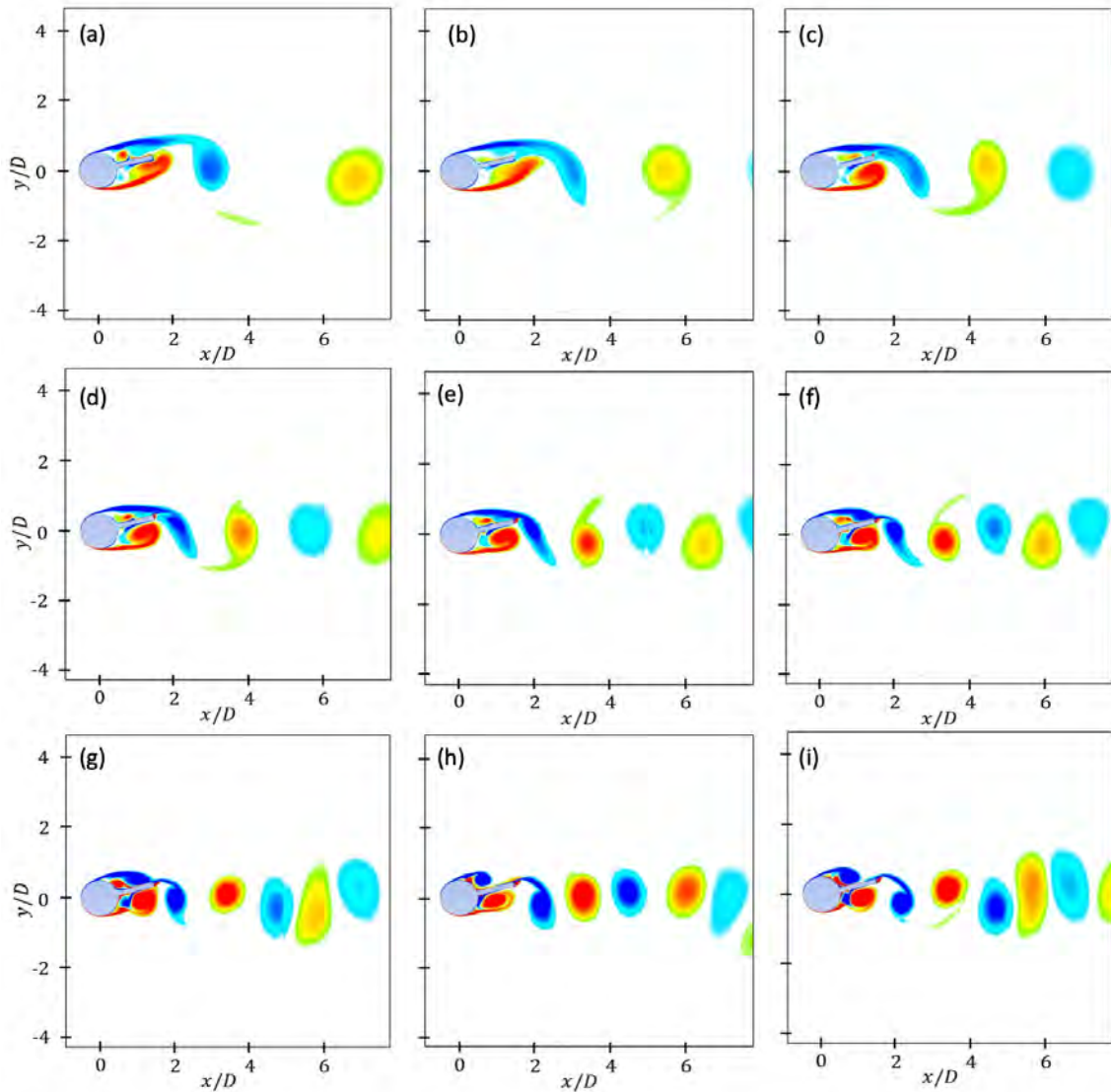


Figure 8.4: The series of simulation snapshots are recorded at the maximum amplitude of the bluff body across a range of Strouhal frequency ratios,  $St/St_n$  and shows the evolution of the vortices as the actuating frequency is increased. The well-defined vortices observed at lower Strouhal frequency ratios slowly become distorted as the actuation frequency is increased. The snapshots labelled (a) – (i) correspond to cases 4 - 12 in Table 8.2.

tion setup has been used to investigate the actuated Strouhal frequency ratio to obtain the actuation frequency range where the shed von Kármán vortices are locked-on with the prescribed frequency. This provides an extension of the work by Rockwood et. al. where their experimental setup limited their investigation from identifying the upper bound of the Strouhal number ratio where the shed vortices were still locked-on with the prescribed frequency. This work lays the groundwork to map the other spatiotemporal vortex parameters with the bluff body actuation parameters.

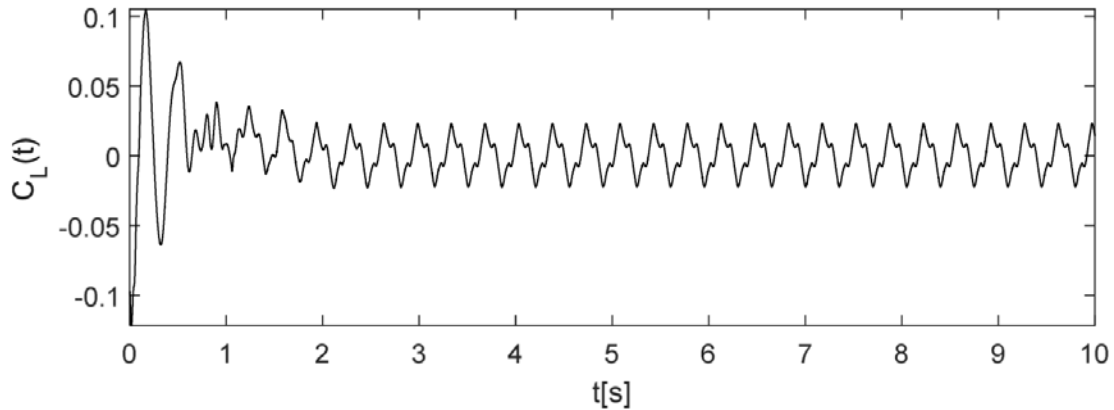


Figure 8.5: A sample  $C_L$  plot for Case 7, shows the variation of the lift coefficient of the bluff body as a function of time. The initial transient effects are observed in the first two seconds of the simulation and are neglected for all analytical purposes

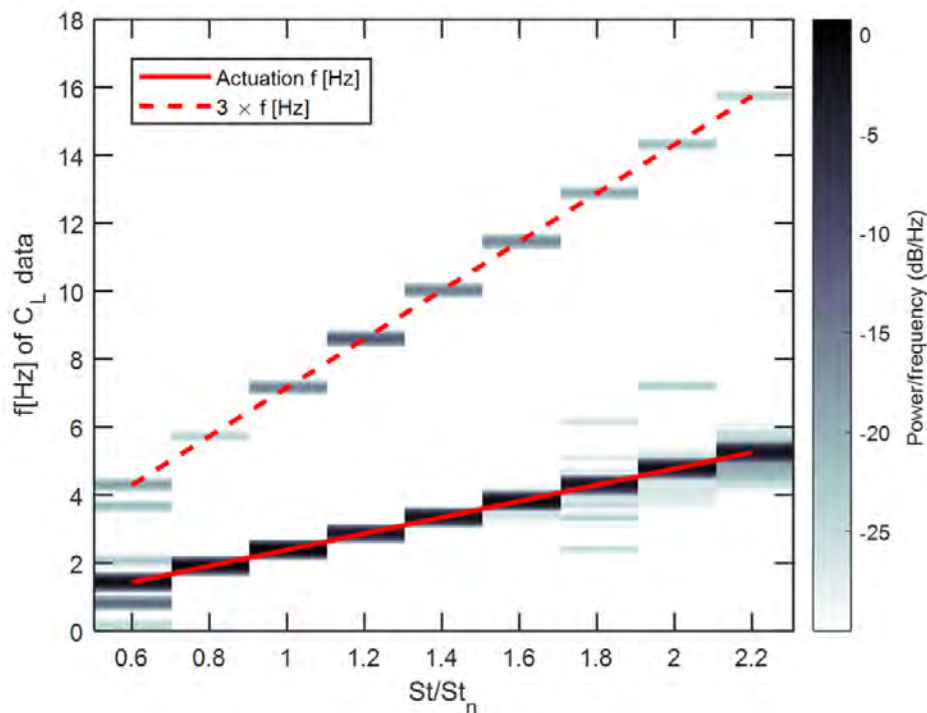


Figure 8.6: The time evolution of the frequency content is plotted for every Strouhal frequency ratio. For each Strouhal ratio, the entire spectrogram is plotted and stitched together to obtain the above figure. The third harmonic of the actuation frequency ( $3f$ ) is co plotted in the above figure to show that a small part of the spectral energy of  $C_L$  is also distributed to the third harmonic frequency.

## Chapter 9

# Design of a Flow Disturbance Generator Based on Oscillating Cylinders With Attached Splitter Plates

This chapter discusses the development and implementation of a dynamic bluff body used to study the response of an aeroelastic wing in a von Kármán wake. Following the success of the static bluff body discussed in Chapter 5 in modulating and annihilating LCOs in a downstream aeroelastic wing with two degrees of freedom, a system which could produce vortices at varying phase and frequency was desired. The chosen design consists of a cylinder with an attached splitter plate due to its ability to produce vortices at the same rate as its oscillation frequency. Validation of this new bluff body disturbance generator was performed using computational and experimental methods. Following this, initial tests in-tandem with a downstream aeroelastic wing were performed to determine if the disturbance generator could excite and annihilate LCOs in the wing.

### 9.1 Chapter Introduction

Recent work by the Aeroelasticity Group at North Carolina State University (NCSU) has demonstrated that aeroelastic stability and limit cycle oscillation (LCO) behavior can be modified by upstream flow disturbances. Aircraft wings, which are practical examples of common aeroelastic systems, have been shown to experience LCOs in both undisturbed and perturbed flows, the latter having been the focus of recent work by the Aeroelasticity Group at NCSU. Initially, the interaction between a pair of in-line, aeroelastic wings was examined by Kirschmeier and Bryant[173]. It was found that the wake produced by the upstream wing experiencing LCOs led to destabilization of the downstream wing, resulting in sustained oscillations at wind speeds below the freestream flutter speed of the downstream wing. Following this work, Gianikos et al.[174] replaced the upstream wing with a static, rectangular, bluff body which produced periodic vortices in its wake. As vortices shed by the bluff body impinged on the aeroelastic wing section, already experiencing LCOs, the LCO amplitude was periodically modulated due to the interaction between the aeroelastic wing section and the vortices. Most recently, Kirschmeier et al.[184] found that the LCOs could be completely

annihilated in the downstream wing when the shedding frequency of the bluff body was equal to three times the oscillation frequency of the LCOs.

Following the completion of these studies and the discovery of the LCO annihilation, the ability to control the frequency and phase of vortices shed by the upstream disturbance generator at constant flow speed was desired. In the process of designing a new upstream disturbance generator, it was decided to pursue cylindrical bluff bodies due to their well-studied ability to produce von Kármán vortices[180]. However, a simple, static cylinder does not allow for variation of the vortex shedding frequency and phase as its vortex shedding frequency is dependent on the freestream velocity and cylinder diameter, as described by the Strouhal number property. Rockwood and Medina[182], found that by inducing prescribed pitch oscillations about the primary axis of the cylinder, the vortex shedding frequency can be altered. Additionally, by adding an attached splitter plate along the trailing edge of the cylinder, Rockwood and Medina[182] found that the shedding frequency can be prescribed at the cylinder's oscillation frequency and produce a well-behaved, locked-in, von Kármán vortex street.

Building on the experimental work done by Rockwood and Medina, Chatterjee et al.[185] performed a CFD analysis to examine the behavior of the vortex wake across a range of Strouhal ratios, that is, the ratio of the Strouhal number due to the forced vortex shedding frequency when compared to the Strouhal number due to the natural shedding frequency of a cylinder of the same diameter without an attached splitter plate. Their results suggested that a cylindrical bluff body with an attached splitter plate produced a well-behaved, locked-in, vortex wake when the Strouhal ratio fell between 0.8 and 1.4. At values above 1.4, the time between each shed vortex was inconsistent, resulting in undesirable variation in control of the system wake when considered for application in conjunction with downstream aeroelastic structures.

Based on the information presented in the brief review above, it was decided to move forward with the cylindrical bluff body design with an attached splitter plate in order to continue investigation of aeroelastic LCO modulation and control. A design requirement for the system was to demonstrate maximum cylinder oscillation frequencies of at least three times the LCO frequency of the existing aeroelastic wing section apparatus under conditions where LCO annihilation has been demonstrated[184]. The work done by Rockwood and Medina[182] and Chatterjee et al.[185] was performed with in a water tunnel apparatus at Reynolds numbers of 7,600 based on the cylinder diameter. This differs from the earlier work done by the Aeroelasticity Group at NCSU which was performed in the NCSU subsonic wind tunnel at airfoil-chord-based Reynolds numbers ranging from 70,000 to 120,000. As a result, the work presented in this chapter was completed with the goal of experimentally validating the Strouhal ratio range described by Chatterjee et al.[185] for applications in future aeroelasticity work in the NCSU subsonic wind tunnel.

## 9.2 Materials and Methods

### 9.2.1 Bluff Body Sizing

The design process used to generate the bluff body for the work outlined in this chapter is focused on a set of design parameters based on previous research done in the Aeroelasticity Group at NCSU. The primary design goal is to produce a bluff body which sheds vortices at a rate which corresponds to the range of Strouhal ratios as discussed in Chatterjee et al[185]. For a standard, static cylinder,

$St/St_n$	$f_{osc}(Hz)$	$u_\infty(m/s)$	$D(cm)$
0.8	12	8	10.67
0.9	12	8	12.00
1.0	12	8	13.33
1.1	12	8	14.67
1.2	12	8	16.00
1.3	12	8	17.33
1.4	12	8	18.67

Table 9.1: Cylinder Sizing Based on Strouhal Ratio

the natural Strouhal number can be found by:

$$St_n = \frac{f_{shed}D}{u_\infty} \quad (1)$$

For cylinders which fall in the Reynolds number range  $1,000 \leq Re \leq 100,000$ , this value is approximately  $St_n = 0.2$ [180]. To calculate the Strouhal ratio,  $St/St_n$ , the Strouhal number for the oscillating cylinder and splitter plate is calculated by setting the frequency of the shed vortices to the oscillation frequency of the body, while the freestream velocity and the cylinder diameter as equivalent to the values used in the natural Strouhal number calculations.

$$St = \frac{f_{osc}D}{u_\infty} \quad (2)$$

From these two equations, the oscillation frequency of the bluff body can be calculated by:

$$f_{osc} = St_n \left( \frac{St}{St_n} \right) \frac{u_\infty}{D} \quad (3)$$

treating the Strouhal ratio,  $St/St_n$ , as a single variable. Sweeping through the range of acceptable Strouhal ratios discussed in Chatterjee et al.[185], a range of oscillation frequencies can be found for any given flow conditions and cylinder diameter. Conversely, the oscillation frequency can be prescribed and a range of acceptable cylinder diameters can be calculated. In order to achieve oscillation frequencies equal to three times the LCO frequency for cases similar to previous work done in the Aeroelasticity Group at NCSU, the parameters shown in Table 9.1 were generated. From this list of possible cylinder diameters, an initial value of  $D = 10.67 \text{ cm}$  was chosen as the design point. However, due to construction constraints and available materials, a final diameter of  $D = 10.48 \text{ cm} = 4.125 \text{ in.}$  was selected. A cross section of the bluff body geometry is shown in Figure 9.1.

## 9.2.2 CFD Simulations

Following the initial design for the new bluff body, a series of CFD simulations were run to validate the ability of the chosen bluff body configuration to generate a well-behaved von Kármán vortex street at the flow conditions of interest. An O-type structured grid was fitted to the bluff body. The velocity-inlet and pressure-outlet boundaries were both located at a distance of 25 cylinder diameters away from the rotational center of the bluff body. The domain was partitioned into an inner and outer region so that sinusoidal rotation of the bluff body did not result in mesh

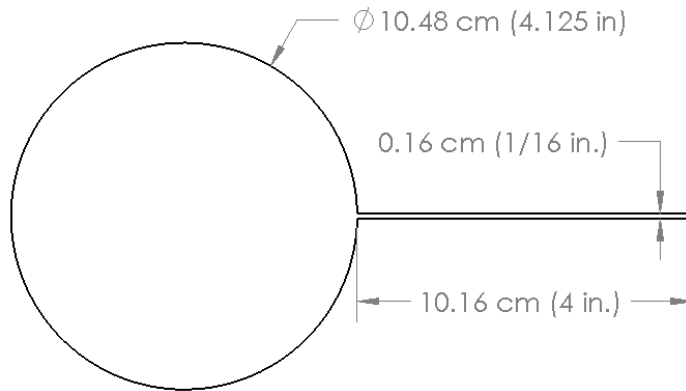


Figure 9.1: Proposed bluff body design cross-section.

deformation. The bluff body contained 660 elements along its surface, resulting in the inner region containing 148,500 elements. A total of 163,500 elements were used in the entire domain. A first layer cell height of  $1.5 \times 10^{-5} m$  ensured a  $y+$  value below 1 over the entirety of the bluff body surface.

Simulations were performed using the commercial package Fluent 20.1. The SST  $k - \omega$  turbulence model was chosen due to the problem involving large extents of separated flow, with the downstream wake being the primary interest. The proposed Reynolds numbers and chosen oscillatory speeds do not allow a laminar flow regime to be assumed, as doing so leads to a highly disorganized and chaotic wake not associated with the results of previous experiments. The decision to use the SST  $k - \omega$  model is further supported by the work performed by Chatterjee et al.[185], in which the SST  $k - \omega$  model was used with an intermittency transition model to successfully replicate the vortex street produced by water tunnel experiments. Later efforts contrasting the inclusion and exclusion of the transition model revealed that its absence did not significantly affect the wake produced by the oscillating bluff body. The removal of the transition model also led to a notable reduction in computational time. For these reasons stated, the authors have decided to implement the SST  $k - \omega$  model in the present CFD simulations. The SIMPLE algorithm was chosen for the pressure-velocity coupling scheme, and a static timestep of  $5 \times 10^{-5} s$  was used for all five cases. Absolute residuals were driven to below  $7 \times 10^{-5}$  at each timestep.

### 9.2.3 Bluff Body Construction

The main body of the cylinder was constructed of braided, carbon fiber tubing produced by DragonPlate™ (Elbridge, NY, USA) with a  $45^\circ$  fiber orientation. A vertical cut was made from one end of the tube to allow the splitter plate sub-assembly to be inserted during construction. The splitter plate, shown in Figure 9.2, was constructed of aluminum in previous design iterations, but added a significant amount of mass and inertia due to its location away from the axis of rotation. To reduce its mass and inertia while maintaining stiffness, a 1/16" thick, carbon fiber and birch laminate produced by DragonPlate™ was selected as a replacement. The laminate is constructed of a solid birch core laminated between two thin sheets of carbon fiber. This allows for a stiff, yet

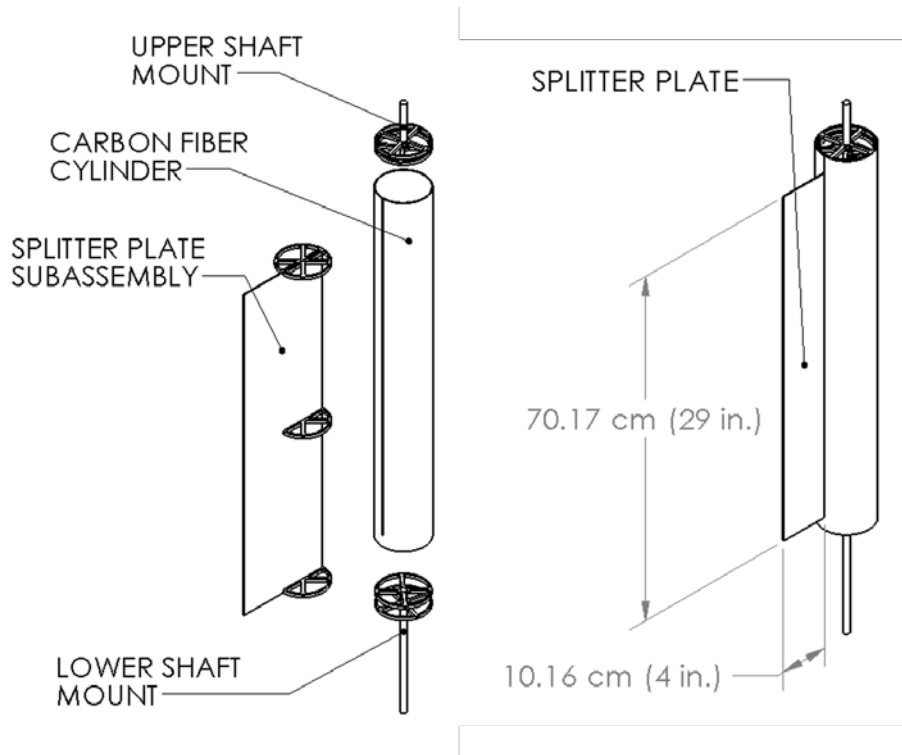


Figure 9.2: Bluff body subassemblies and completed assembly showing splitter plate location and dimensions.

lightweight material, thereby reducing the inertial effects from the splitter plate in the final bluff body configuration. Additionally, the splitter plate was inset into the cylinder and supported using a series of aluminum baffles to further improve stiffness and ensure minimum deformation when the bluff body is oscillating. A series of aluminum baffles of similar design to the splitter plate supports were constructed to support the carbon fiber cylinder and attach mounting shafts. When operated in the wind tunnel, the bluff body is supported at the top with a flexible shaft collar which helps correct for small misalignment errors. The bluff body is then connected to a motor shaft using a rigid shaft collar at the bottom. An exploded view diagram of the bluff body construction can be seen in Figure 9.2.

#### 9.2.4 Testing Apparatus

In addition to computational simulations used to verify the new bluff body geometry, experimental tests were performed in the NCSU closed-return, subsonic wind tunnel, which has a test section measuring  $0.81\text{ m} \times 1.14\text{ m} \times 1.17\text{ m}$ . The motor selected to drive the oscillation of the bluff body was a SureServo SVL-210b from AutomationDirect (Cumming, GA, USA) with a maximum continuous torque of  $3.3\text{ Nm}$  and a maximum instantaneous torque of  $9.9\text{ Nm}$ . This was coupled with a Copley Controls (Canton, MA, USA) Xenus XTL-230-18 digital servo drive to provide motor control. The motor was driven using an external function generator and given a sinusoidal analog input with prescribed amplitude and frequency through the Xenus controller, which then used an internal control loop to ensure correct motion of the bluff body. An example of the oscillatory motion used to drive the bluff body can be seen in Figure 9.3 Sensor data during experimental tests was

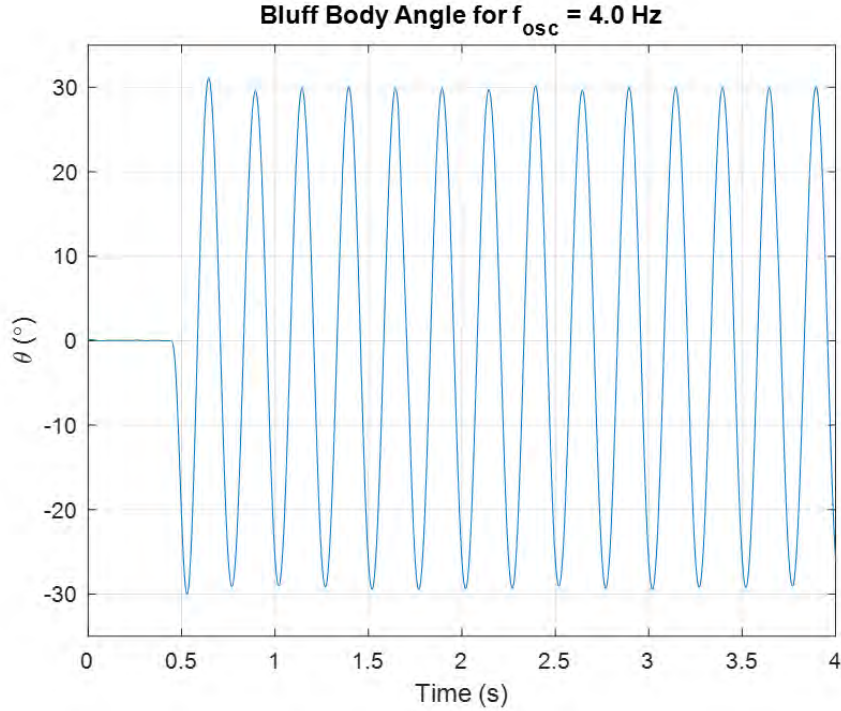


Figure 9.3: Bluff body oscillation for an input frequency and amplitude of 4 Hz and 30° respectively.

$St/St_n$	$f_{osc}(Hz)$	$A(^{\circ})$	$u_{\infty}(m/s)$	$D(cm)$
0.66	4	15	3.25	10.48
0.82	5	15	3.25	10.48
0.98	6	15	3.25	10.48
1.15	7	15	3.25	10.48
1.31	8	15	3.25	10.48

Table 9.2: Test cases for experimental validation of bluff body disturbance generator.

gathered with a National Instruments PXi with LabVIEW in real-time at a sampling frequency of  $f_s = 500 Hz$ . US Digital (Vancouver, WA, USA) E6-10000 optical encoders were used to record pitch amplitude for both the oscillating disturbance generator and the downstream wing, and a Renishaw LM10 (West Dundee, IL, USA) magnetic linear encoder was used to record heave data for the downstream wing. Velocity data was acquired via hotwire anemometry using a MiniCTA 54T30 and a straight, miniature wire probe (55P11) manufactured by Dantec Dynamics (Skovlunde, Denmark).

### 9.2.5 Test Cases

While the design for the cylindrical bluff body was initially optimized for oscillation frequencies near 12 Hz and freestream velocities above 8 m/s, a series of alternative test conditions, shown in Table 9.2, allowed for a full sweep of Strouhal ratios from 0.8 to 1.4, the optimal Strouhal ratio range as given by Chatterjee et al.[185], and one case outside of that range.

$f_{osc}(Hz)$	$A(^{\circ})$	$u_{\infty}(m/s)$	$x_w$
3.5	30	9.25	8D
3.6	30	9.25	8D
3.7	30	9.25	8D
3.8	30	9.25	8D
3.9	30	9.25	8D
4.0	30	9.25	8D
4.1	30	9.25	8D
4.2	30	9.25	8D
4.3	30	9.25	8D
4.4	30	9.25	8D
4.5	30	9.25	8D

Table 9.3: Test cases for initial experiments with downstream aeroelastic wing.

Following initial implementation and validation of the new bluff body disturbance generator, a series of experiments were run to attempt LCO modulation and annihilation with the downstream aeroelastic wing apparatus described by Kirschmeier et al.[184]. This series of tests were run in the NCSU Subsonic Wind Tunnel at a constant freestream velocity ( $u_{\infty}$ ), bluff body oscillation amplitude ( $A_{osc}$ ), and downstream location of the aeroelastic wing measured from cylindrical bluff body center to the wind quarter-chord ( $x_w$ ) while sweeping across a range of bluff body oscillation frequencies ( $f_{osc}$ ), as shown in Table 9.3. While Kirschmeier et al.[184] examined cases wherein the bluff body vortex shedding frequency was approximately three times the wing LCO frequency, this preliminary experiment focused on shedding frequencies near the wing LCO frequency.

## 9.3 Results and Discussion

### 9.3.1 Bluff Body Design Validation

Following the initial CFD simulations and experimental tests, the data were processed in MATLAB 2020a and compared to determine the ability of the new bluff body disturbance generator to produce the desired wake. In the CFD simulations, velocity in the streamwise direction at a location 6D downstream from the bluff body was recorded for the duration of the simulation. In order to remove the transient effects produced when the bluff body initially begins to rotate, the first two seconds of velocity data were excluded for all calculation. The remaining data, shown in Figure 9.4, produced a well-defined, cyclical velocity profile which correlates to the passing of regularly spaced vortex structures. Additionally, flow visualization data, shown in Figure 9.5, displays well-defined, vortex wakes for each of the test cases discussed in Table 9.2. The 4 Hz case, which fell outside the range of acceptable Strouhal ratios at  $Re = 7,600$ , also appears to produce well-organized wake at the higher Reynolds number case simulated here. Fast Fourier Transforms (FFT) were used to quantify the vortex shedding frequency of the bluff body from the simulation results. The downstream velocity data, shown in Figure 9.4, was analyzed with FFT in MATLAB. Since one oscillation of the bluff body constitutes both an upward and downward motion of the bluff body, two vortices are produced with opposite spin direction, which can be seen in the vorticity contours in Figure 9.5. As a result, the FFT, shown in Figure 9.6, displays frequency peaks at a rate of twice the oscillation frequency.

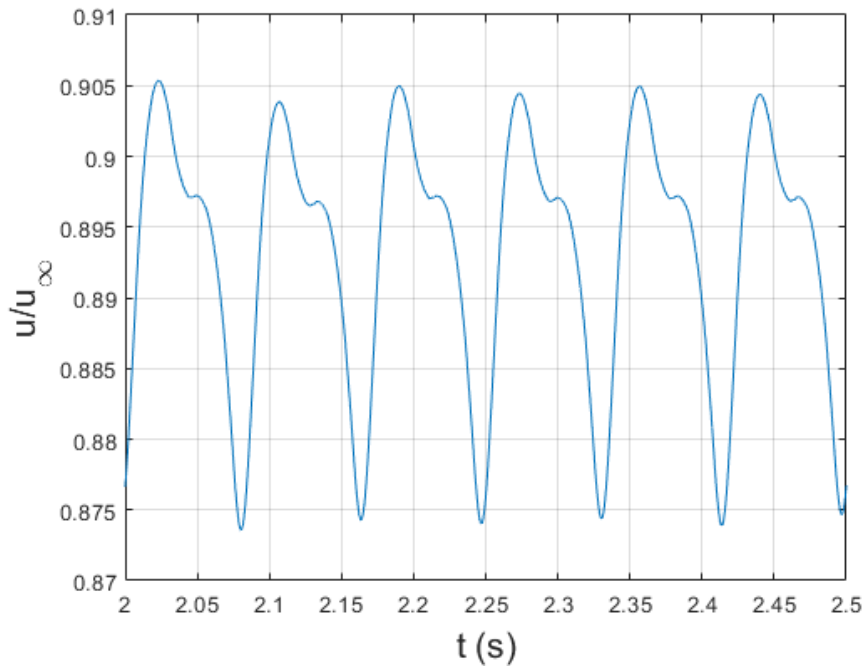


Figure 9.4: Streamwise velocity as a function of time for  $f_{osc} = 6 Hz$  from CFD.

Data gathered via hot wire anemometry during the experimental tests was time-averaged for each of the oscillation frequency cases shown in Table 9.2 and plotted as a function of cross-stream distance from the test section centerline at increments of  $y/D = 1/8$ . All test cases display a clear wake velocity deficit region, as shown in Figure 9.7, but the shape and magnitude of the velocity variation across the flow varied strongly with the oscillation frequency of the bluff body. The results indicate that, for the cases tested here, higher oscillation frequencies produce a larger centerline velocity deficit and also show a sharper variation in velocity across the flow. While data gathered during experimental testing provided velocity profiles extending away from the test section centerline, computational velocities were only computed at the centerline. In order to compare the two methods, the time-averaged velocity at the centerline from each method was plotted as a function of oscillation frequency, as shown in Figure 9.8. In both cases the time-averaged velocities show agreement for the lower oscillation frequencies. However, the experimental data shows a sharp decrease beginning at  $f_{osc} = 7 Hz$ . Explanations for this significant variation from the simulated cases could be due to inconsistencies in the experimental testing apparatus that are only present at these higher oscillation frequencies. Additionally, the SST  $k - \omega$  turbulence model used for the CFD simulations may have failed to capture all of the turbulent effects produced in the physical tests.

### 9.3.2 Aeroelastic Wing LCO Response

Following the validation of the new bluff body disturbance generator to produce the desired wake region. An initial round of tests, outlined in Table 9.3, were performed in tandem with the aeroelastic wing used in Gianikos et al[174] and Kirschmeier et al[184] to determine if this new design could be used to excite and annihilate LCOs in the downstream wing. Although this initial round

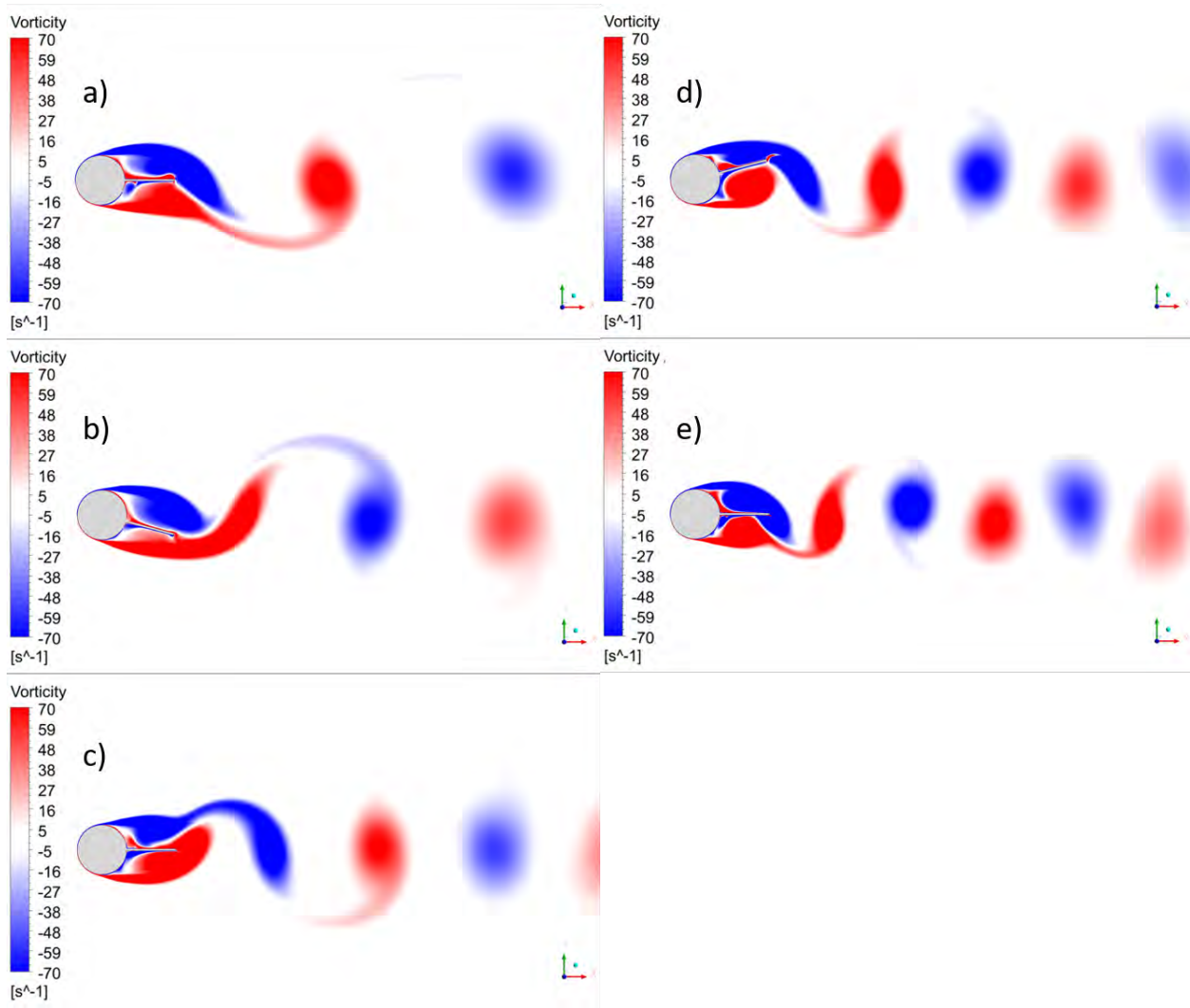


Figure 9.5: Vorticity contours from CFD showing well-defined vortex wakes for oscillation frequencies of (a)  $4\text{ Hz}$ , (b)  $5\text{ Hz}$ , (c)  $6\text{ Hz}$ , (d)  $7\text{ Hz}$  and (e)  $8\text{ Hz}$ .

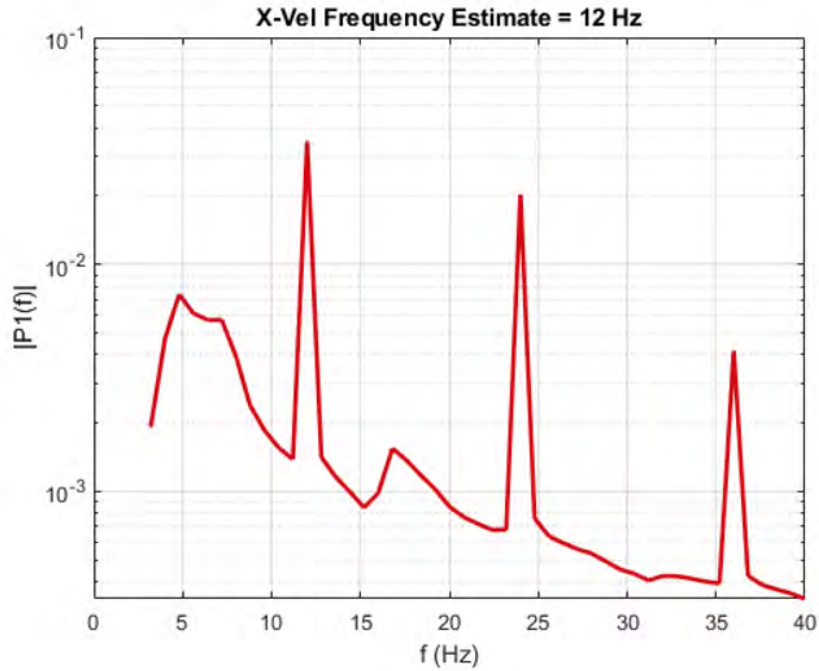


Figure 9.6: Frequency spectrogram for  $f_{osc} = 6 \text{ Hz}$ , showing an initial peak at  $12 \text{ Hz}$  as expected.

of testing focused on a lower shedding frequency compared to previous work, the new disturbance generator was able to excite LCOs in the downstream wing without the need for a manual trigger used in previous experiments. For all cases except the  $f_{osc} = 4.0 \text{ Hz}$  case, vortices produced by the disturbance generator appeared to act as an external forcing function on the wing, but did not excite LCOs, as shown in Figure 9.9. Note that the wing pitch and heave oscillations quickly die down when the bluff body oscillations are stopped at  $t \approx 125 \text{ s}$ . For the case when  $f_{osc} = 4.0 \text{ Hz}$ , which corresponds to  $f_{osc} \approx f_{LCO}$ , the downstream wing was excited to LCO. Initially the pitch amplitude of the wing showed cyclic growth and decay of oscillation amplitude, as shown in Figure 9.10, similar to data reported by Gianikos et al[174]. If the disturbance generator oscillation was stopped as the wing pitch amplitude reached its peak ( $\approx 50^\circ$ ), the wing would remain in LCO without the influence of incoming vortices as shown in Figure 9.11a. Additionally, during initially maintained LCOs by the downstream wing, activation of the disturbance generator oscillation led to annihilation of the LCOs. The effect was not immediate but was marked by a gradual decline in the amplitude of the wing pitch angle. As the amplitude approached zero, the disturbance generator oscillations were stopped, and the wing came to rest with no noticeable oscillations, as shown in Figure 9.11b. Upon further examination, it is likely that the true natural LCO frequency of the downstream wing at this freestream velocity is not  $f_{LCO} = 4.0 \text{ Hz}$ , but rather a value which falls very close to this. The cyclic growth and decay of the wing pitch angle in the presence of incoming vortices at  $4 \text{ Hz}$  appears to demonstrate a “beat-like” phenomenon, similar to the interference between two signals with slightly differing frequencies. Similarly, in the previous study by Kirschmeier et al [184], annihilation was observed when  $f_{shed}/f_{LCO}$  was near 3.

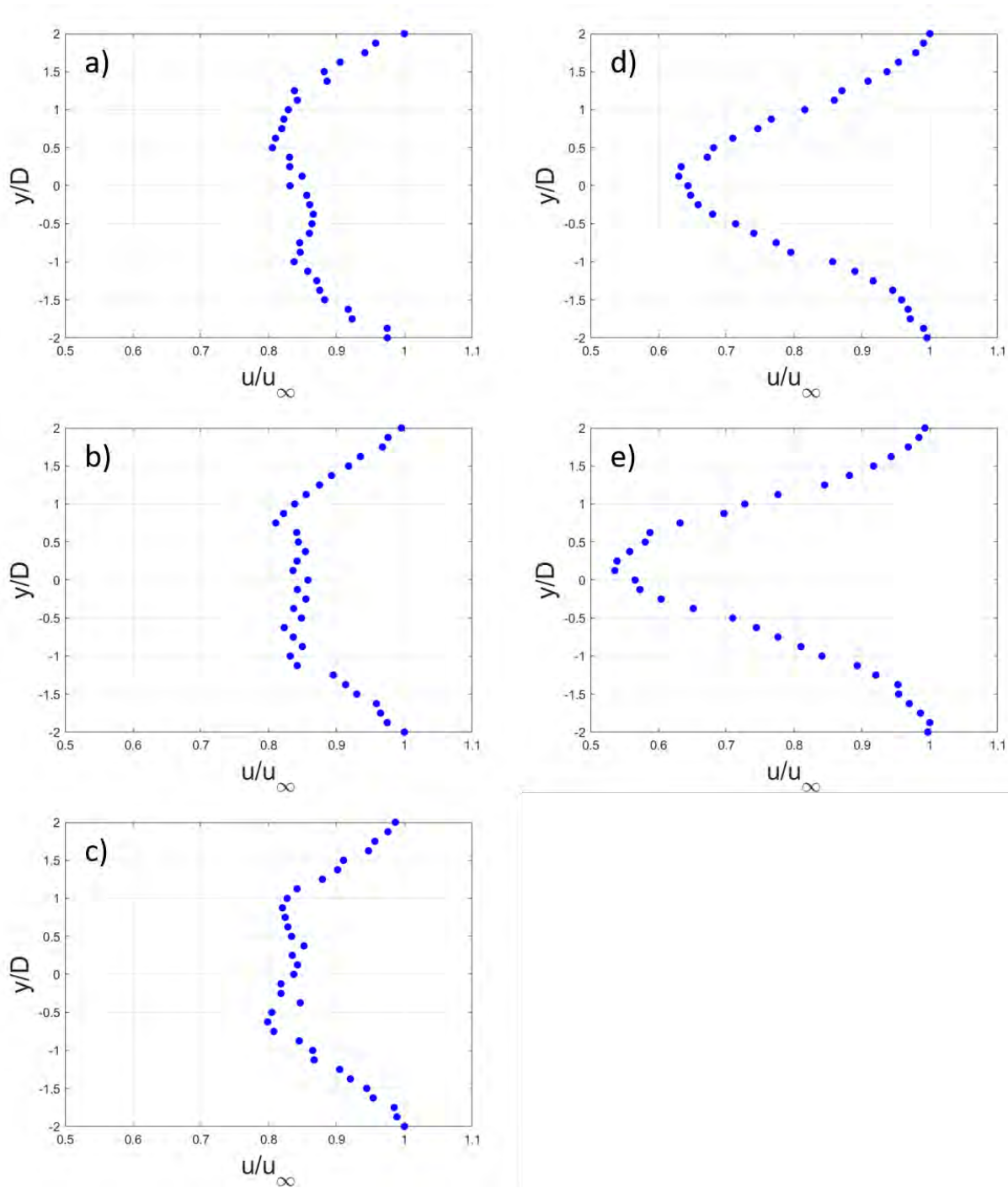


Figure 9.7: Cross-stream, time-averaged velocity profiles for (a) 4 Hz, (b) 5 Hz, (c) 6 Hz, (d) 7 Hz and (e) 8 Hz.

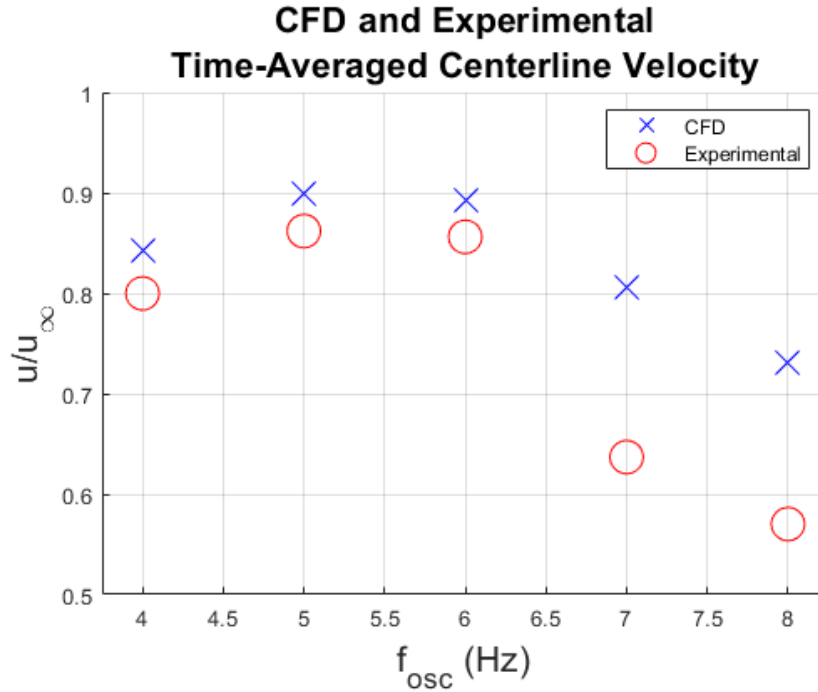


Figure 9.8: Comparison between computational and experimental centerline average velocities.

## 9.4 Interim Conclusions

In this chapter, a newly-designed, cylindrical bluff body with an attached splitter plate was constructed to serve as a disturbance generator to produce a well-defined, von Kármán vortex street with variable frequency at a constant flow speed. Based on preliminary results from both computational and experimental methods, this configuration succeeds in producing the desired wake at frequencies corresponding to 0.8 to 1.4 times the frequency of natural vortex shedding for a plain cylinder at the same speed. Additionally, initial tests which examined the ability of this disturbance generator to modulate, excite, and annihilate LCOs in a downstream aeroelastic wing are discussed. Oscillations of the disturbance generator at a rate nearing the natural LCO frequency of the wing produced increasingly large amplitudes in the downstream wing which were used to force the wing into LCOs, while the same interference from incoming vortices when the wing was already undergoing LCOs resulted in annihilation of the LCO amplitude. Additionally, disturbance generator oscillations at other frequencies did not produce the same result in the downstream wing. This work builds on existing studies which demonstrated LCO modulation and annihilation using a static bluff body which produced vortices at a constant rate ties to the freestream velocity, while the apparatus used in this study is able to produce vortices at a rate which is independent of the freestream velocity.

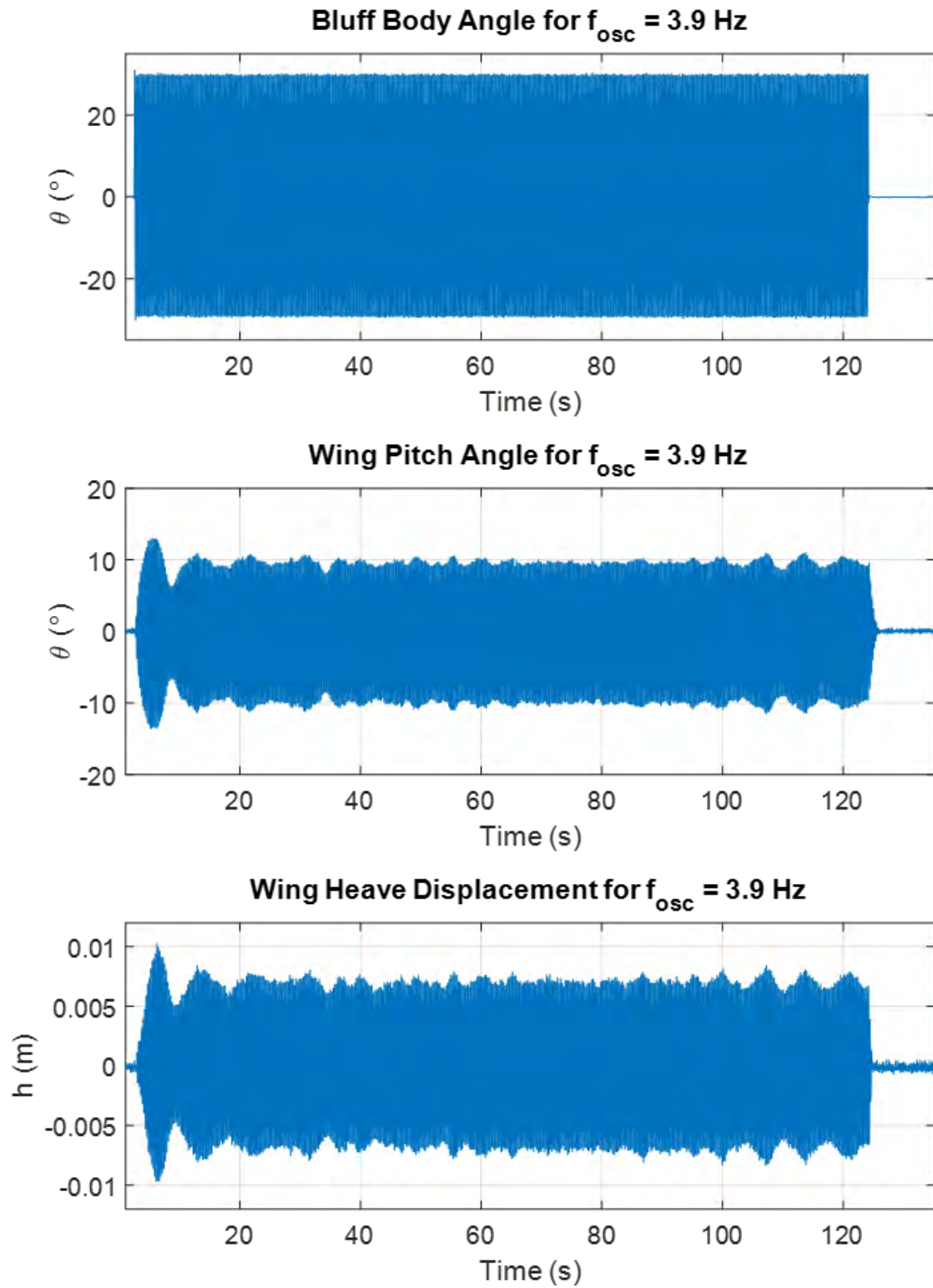


Figure 9.9: Bluff body angle, wing pitch angle, and wing heave displacement during forced oscillations at  $f_{osc} = 3.9$  Hz showing non-LCO response of the wing.

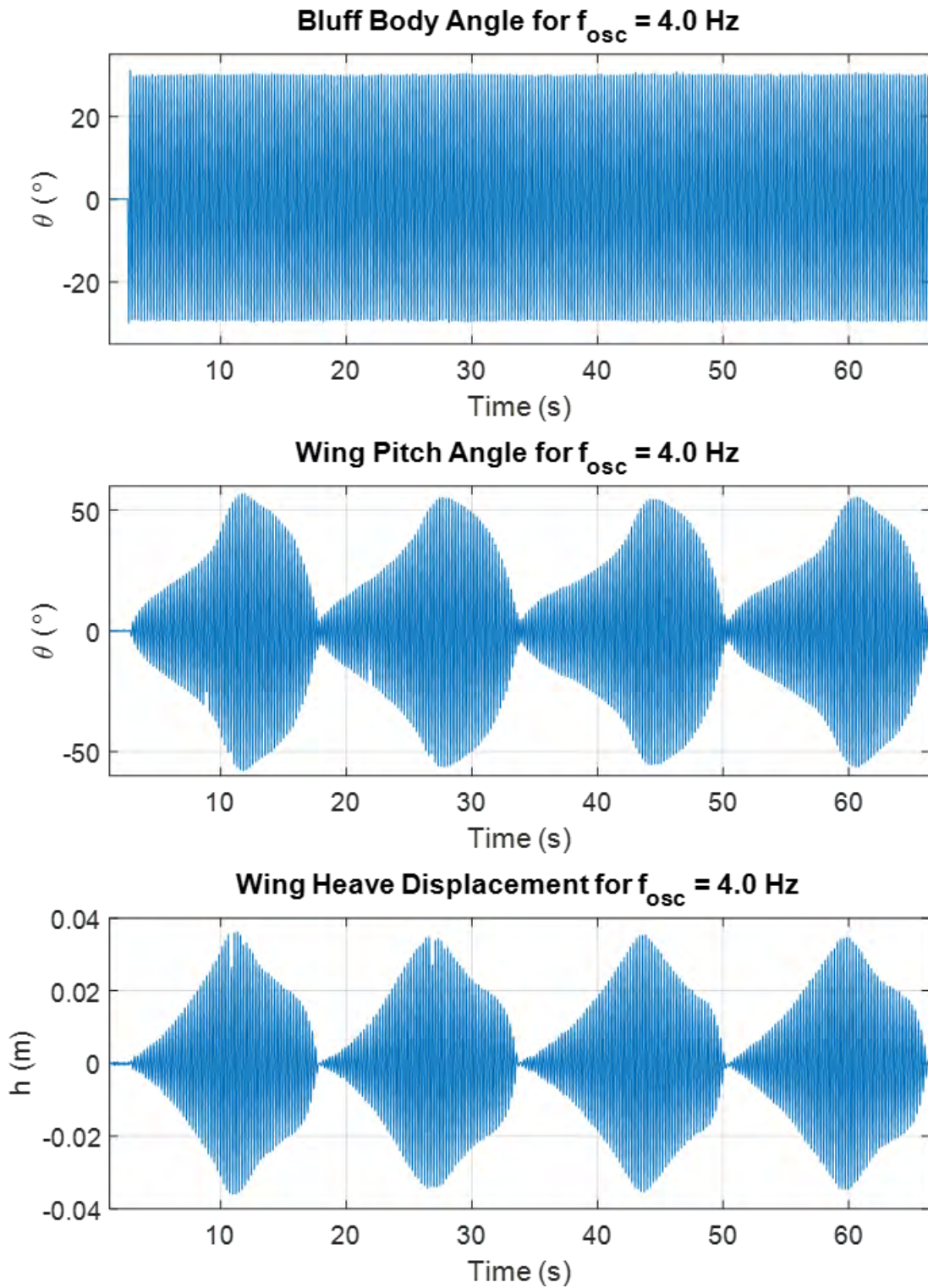


Figure 9.10: Bluff body angle, wing pitch angle, and wing heave displacement during forced oscillations at  $f_{osc} = 4.0$  Hz, showing “beat-like” phenomenon.

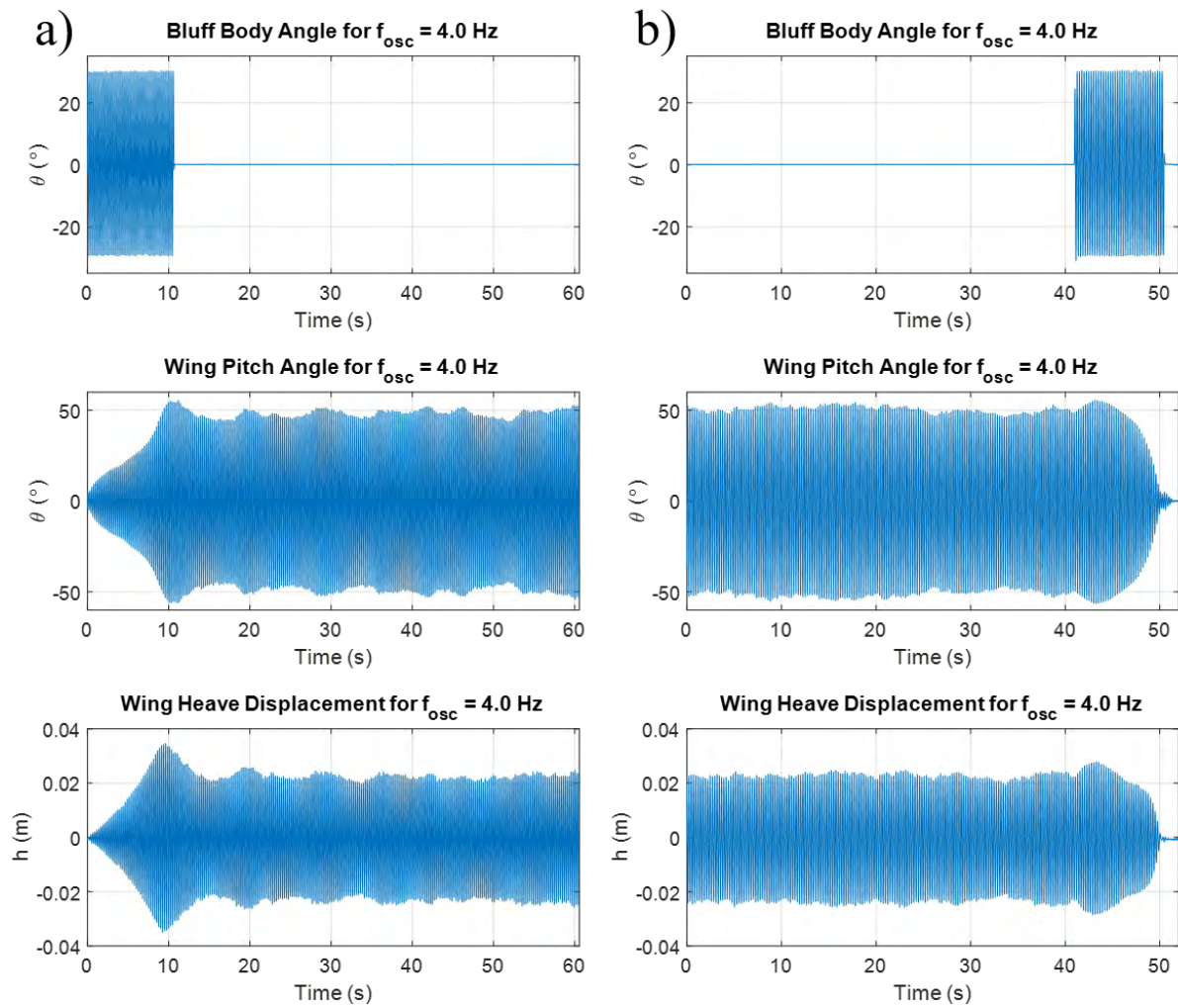


Figure 9.11: Bluff body angle, wing pitch angle, and wing heave displacement after stopping oscillations at  $f_{osc} = 4.0$  Hz, showing: a) excitation of LCOs and b) annihilation of LCOs

## Chapter 10

# Summary and Conclusions

The objective of the research was to study the effect of upstream flow disturbances on the unsteady aerodynamics and aeroelastic behavior of a downstream wing. More specifically, the aeroelastic study was aimed at experimentally exploring if flow disturbances could be used to alter flutter and limit-cycle oscillation (LCO) behavior of an elastically-supported wing. The unsteady aerodynamics portion of the research was aimed at experimentally characterizing the effects of flow disturbances on leading-edge vortex shedding from unsteady airfoils undergoing prescribed motion, modeling these effects using low-order methods, and gaining insight into the flow physics.

To study the aeroelastic behavior, an aeroelastic apparatus was designed and constructed for use in the North Carolina State University subsonic wind tunnel. The apparatus consists of an airfoil supported by springs to allow for pitch and heave motions, with capability to change the pitching axis, center of mass, and pitching moment of inertia. Rotary and linear encoders were used to measure instantaneous pitch and heave deflections. A rectangular-cylinder bluff body was used upstream of the wing to generate flow disturbances in the form of periodic vortex shedding.

The airfoil response in undisturbed flow conditions exhibits a classical constant-amplitude LCO, which gets modified in the presence of flow disturbances to an LCO with more complex dynamics. The complex interaction between the shed vortex wake from the upstream bluff body and the aeroelastic airfoil resulted in modulation of the LCO. The LCO amplitude modulation, which affected both pitch and heave oscillations was, in this case, found to depend on the difference between the LCO third harmonic and the bluff-body shedding frequency. Energy analysis revealed that when the flow disturbances alter the pitch-heave phase difference, the balance of power into and out of the structure over a cycle is disrupted, resulting in either amplitude growth or decay. Further investigation revealed that, when the pitch-heave mass coupling in the system is increased and the shedding frequency is within a certain margin of the third harmonic of the LCO, the wing oscillation is spontaneously and completely annihilated. This LCO annihilation was demonstrated over several repeated trials of the experiment. Although annihilation of LCOs via nonlinear disturbances have previously been reported in the literature in other systems, it is believed that this is the first experimental demonstration of the annihilation of an *aeroelastic* LCO. This result provided the motivation to better understand the factors affecting LCO modulation and control, with an especially important goal of quantifying the effect of the disturbance-to-LCO phase difference. Towards this objective, a three-pronged effort was undertaken: (i) the theoretical/low-order modeling portion of the effort was extended to gain a deeper understanding of vortex effects, (ii) an aeroelastic inverse method was developed to estimate the forces and moments on an aeroelastic airfoil undergoing

LCO with or without flow disturbances, and (iii) a computational study was undertaken, leading to the design of a gust generator for the wind-tunnel study to produce vortical disturbances with controllable phase of the shed wake.

The low-order prediction method, which was developed in parallel with the aeroelastic study, initially focused on extending the capability of a previously-developed LDVM code to handle flow-disturbance effects on an unsteady airfoil. In the LDVM code, the instantaneous leading-edge suction exceeding a pre-determined critical value is used to modulate leading-edge vortex (LEV) shedding from the airfoil. The extension to the code involved modeling the flow disturbances and calculating their effects on the airfoil aerodynamics. This work, undertaken in concert with experiments in a horizontal free-surface water tunnel facility at the Air Force Research Laboratory (AFRL), explored the effects of vortex shedding from an upstream gust generator impinging on an unsteady airfoil undergoing prescribed pitch motion. The results from the modified LDVM code were in excellent agreement with the experimental results. The flow disturbances were seen to modify LEV shedding, the details of which depend on the amplitude and phase of the disturbance relative to the airfoil motion. These results show that criticality of suction at the leading edge governs leading-edge vortex shedding even in the presence of flow disturbances. The new focus on developing an understanding of the effect of vortices led to the development of leading-edge suction parameter (LESP) maps for visualizing the effect of a vortex in the flow on its capability to suppress or enhance LEV shedding from the airfoil. These maps have the potential for use in designing flow disturbances to produce desired LEV shedding from airfoils, which could be used in future work to tailor aeroelastic-airfoil LCO characteristics by appropriate design of flow disturbances.

The aeroelastic inverse method is an algorithm developed in this research to compute the aerodynamic forces and moments of an aeroelastic wing undergoing large amplitude heave and pitch LCOs. The technique is based on inverting the equations of motion to solve for the lift and moment experienced by the wing. The results from the method were validated against prescribed-motion experiments from the AFRL water tunnel with matched Reynolds number and Strouhal-number scaled kinematics. After validation, a study of how mass coupling alters large-amplitude limit-cycle oscillations was conducted by examining the aerodynamic forces and energy transfer mechanisms. It was found that the pitch-heave phase difference, which can be controlled by adjusting the mass coupling, is a mechanism for controlling the amplitude growth in aeroelastic LCOs. This result provides key insight into future efforts for on-demand modulation of LCOs.

Finally, a new gust generator was designed based on the concept developed by AFRL, in which a cylinder with a splitter plate is placed across a uniform flow and oscillated in rotation about its axis. Computational studies of this concept showed that coherent, locked-on von Kármán vortex streets could be generated for cylinder-oscillation Strouhal ratios from 0.7 to 1.1, thus enabling a wider range of vortex shedding frequencies from a single cylinder shape. More importantly, this gust generator allows for control of the shedding phase relative to that of an oscillating downstream wing. A new wind-tunnel gust generator based on this concept was designed and fabricated to replace the rectangular cylinder used in the earlier version of the aeroelastic apparatus. With this new setup, LCO modulation and annihilation have been demonstrated by open-loop control of the cylinder oscillation. This capability now sets the stage for on-demand LCO modulation by appropriate adjustment of the gust-generator phasing.

In summary, the overall research effort under this grant has resulted in four main contributions to the current state of the art: (i) experimental demonstration of aeroelastic LCO annihilation using flow disturbances, which we believe has not been reported before, (ii) a newly developed aeroelastic inverse technique that can be used for estimating forces and moments on a wing undergoing aeroe-

lastic oscillations, (iii) theoretical and low-order prediction of flow-disturbance effects including the development of the novel LESP maps to visualize the effect of vortices on LEV production, and (iv) open-loop control of aeroelastic LCO using a new phase-adjustable gust generator. Taken together, these contributions and the new insights provide substantial improvements in the understanding of flow-disturbance effects on aeroelastic phenomena and unsteady-airfoil aerodynamics. They set the stage for follow-on work including on-demand control of aeroelastic phenomena, which could result in the ability to control/mitigate destructive aeroelastic phenomena like flutter, or harness constructive aeroelastic behaviors for flow-energy harvesting. The new flow-physics insights also have the potential to result in novel mitigation strategies for loads due to gust encounters.

## Appendix A

# Detailed analysis of the LEV shedding phenomena for $\phi = 180^\circ$

The role of various factors governing the LEV shedding phenomena of the pitching airfoil in the presence of disturbances with phase  $\phi = 180^\circ$  is studied here using a decomposition of  $\mathcal{L}$  along with the LESP maps.

Since the motion kinematics of the airfoil remains the same as that of  $\phi = 0^\circ$ ,  $\mathcal{L}_\theta$  and  $\mathcal{L}_{\dot{\theta}}$  histories in figure A.1 (and thus the kinematic component indicated by the green curve in figure A.2) remain exactly the same as their counterparts for  $\phi = 0^\circ$  in figure 7.15. For the flowfield contributions in figures A.1 and A.2, and the total  $\mathcal{L}$  in figure A.2, the corresponding quantities for  $\phi = 0^\circ$  (dashed lines of the respective color) are also included to highlight the differences between the two phases. The total LESP history, and thus the LEV shedding phenomena, in the current scenario are affected by the difference in the phase with which the flowfield elements interact with the kinematic components. Between  $t^* = 1.5$  and  $t^* = 2.0$  during the pitch-up phase, the oncoming disturbance is positioned in figure A.3 such that the CW cluster A loses its negative influence on the LESP while the CCW cluster B approaching the leading edge has a dominant positive contribution, leading to a positive peak in  $\mathcal{L}_D$  in figure A.1. This leads to a faster rise in the LESP and an earlier initiation of LEV shedding compared to the  $\phi = 0^\circ$  case for which the oncoming vortex clusters have a deteriorating effect on the LESP during the same time window in figure 7.17. The strengthening

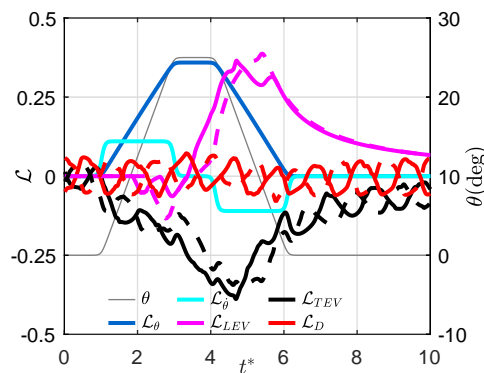


Figure A.1: Contribution to  $\mathcal{L}$  from each factor governing the LEV shedding dynamics for  $\phi = 180^\circ$ .

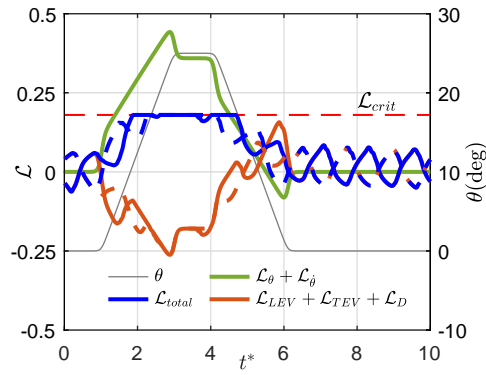


Figure A.2: Total  $\mathcal{L}$  history split into contribution from kinematic factors and that from flowfield elements for  $\phi = 180^\circ$ .

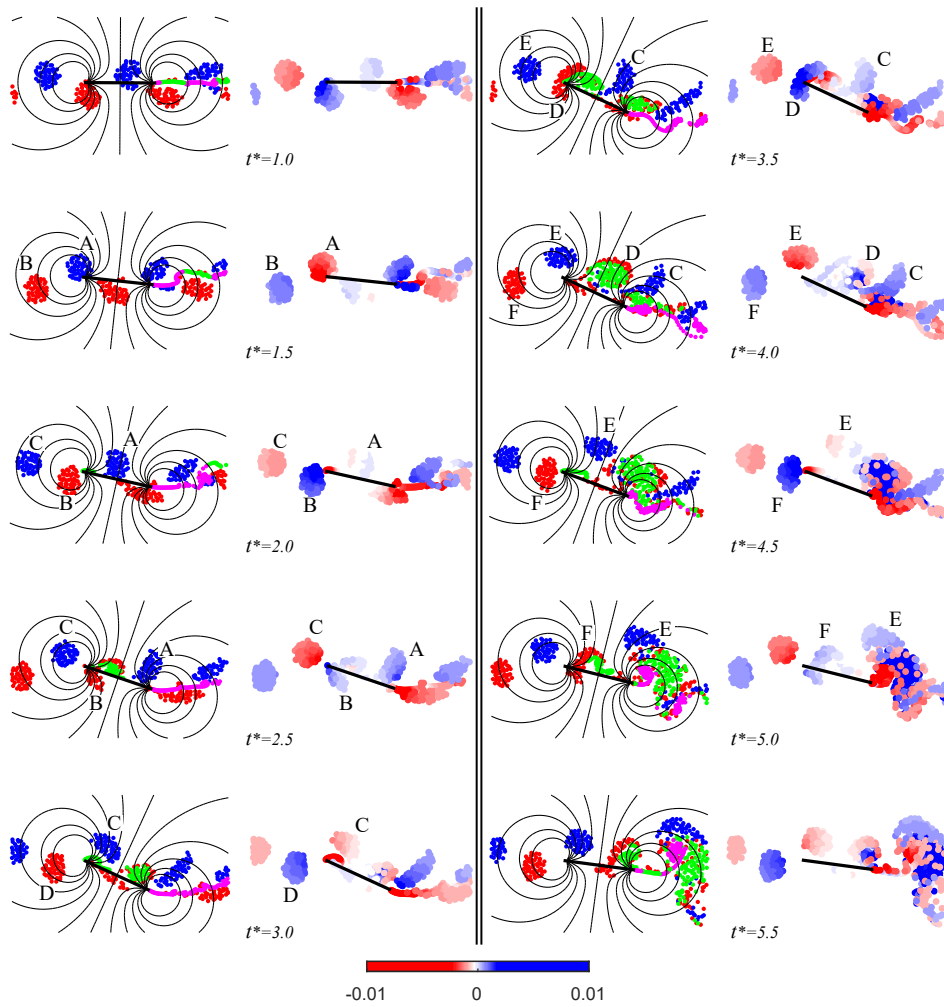


Figure A.3: LESP maps and colored maps at various time instants highlighting the contribution from individual discrete vortices for  $\phi = 180^\circ$ .

negative contribution from the approaching CW cluster C interrupts LEV shedding at  $t^* = 2.5$ . However, the LESP regains its critical value quickly and LEV shedding resumes as soon as cluster C passes the leading-edge region and starts losing its dominance. Aided by the positive contribution of the approaching CCW cluster D, LEV shedding continues until  $t^* = 3.5$  after which the dominant negative contribution of the CW cluster E causes an interruption in LEV shedding as can be seen from the LESP maps at  $t^* = 4.0$ . By this time, the airfoil has entered the pitch-down phase, resulting in a drop in the kinematic contribution to the LESP in figure A.2. However, the timely presence of the CCW cluster F near the leading edge, as seen in the LESP map for  $t^* = 4.5$ , helps  $\mathcal{L}$  to increase to the critical value for a brief stint in figure A.2. Thus, the disturbance phasing helps to prolong the duration of LEV shedding in this case. (This is the opposite of the situation for the  $\phi = 0^\circ$  case where a CW cluster near the leading edge at  $t^* = 4.5$  in figure 7.17 results in an early termination of LEV shedding.) Shortly afterwards, the decline in  $\mathcal{L}_\theta$  and  $\mathcal{L}_{\dot{\theta}}$  overpowers the flowfield contributions, and LEV shedding is terminated as  $\mathcal{L}$  drops below  $\mathcal{L}_{crit}$ .

## Appendix B

# Parametric study of the interaction phenomena using the low-order model

Three case studies are presented here using the low-order model in order to explore the effect of three parameters on the airfoil-disturbance interaction phenomena as well as to demonstrate the effect of the values of some modeling parameters on the low-order predictions.

### 1. Effect of varying $\mathcal{L}_{crit}$

The effect of the modeling parameter  $\mathcal{L}_{crit}$  on the low-order predictions is shown in figure B.1 for the two phases. From figure B.1(a), it can be noticed that the low-order model is successful in accurately predicting the interruption in LEV shedding for  $\phi = 0^\circ$  for a  $\pm 10\%$  difference in  $\mathcal{L}_{crit}$ . For a lower  $\mathcal{L}_{crit}$ , the model still predicts an interruption, however, for a very short amount of time. The same is true for the second interruption for  $\phi = 180^\circ$  around  $t^* = 3.9$  in figure B.1(b). The first interruption for  $\phi = 180^\circ$ , which is a brief one, is captured only while using higher values of  $\mathcal{L}_{crit}$ . For both phases, the initiation of the LEV shedding is delayed for higher values of  $\mathcal{L}_{crit}$ , and is advanced for lower values. As can be seen from figures B.1(c) and B.1(d), the lift predictions are not considerably affected for small variations in  $\mathcal{L}_{crit}$  as considered here. Thus, while qualitative agreement with high-fidelity methods in terms of load predictions can be achieved with small variations in  $\mathcal{L}_{crit}$ , it is important to use the precise value of  $\mathcal{L}_{crit}$  determined using CFD or experimental results (as outlined by, for example, [154]) for the accurate prediction of flow interactions.

### 2. Effect of varying the airfoil position with respect to the centerline of the disturbance

The pivot point of the airfoil is placed at various locations below the centerline so that the oncoming vortices convect over the the upper surface of the pitching airfoil while interacting with the LEV. Figures B.2(a) and B.2(b) show the variations of  $\mathcal{L}$  and  $C_L$ , respectively, for  $\phi = 0^\circ$  for various positions of the airfoil. The centerline results are also included for comparison. The value of uniform-flow speed  $U$  for  $y/d = -1.5$  was obtained as  $0.92U_\infty$  by [155]. The values of  $U$  used in the simulations for the intermediate locations are obtained assuming a linear variation.

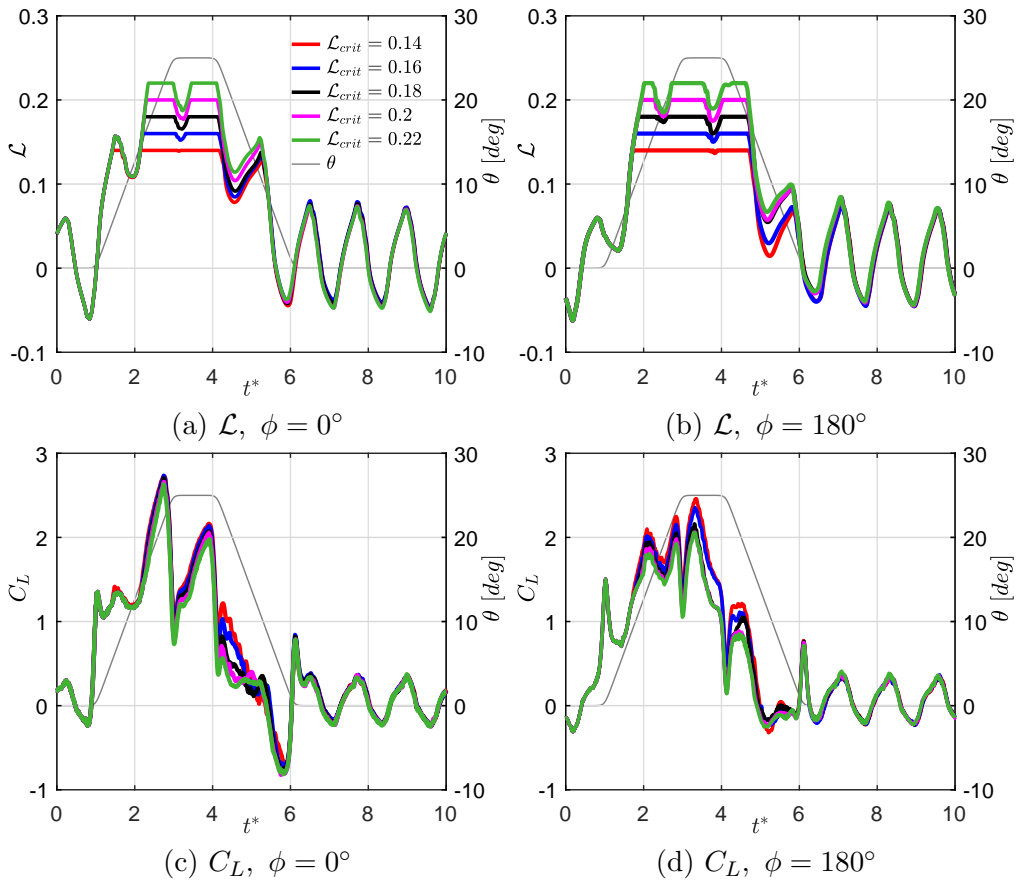


Figure B.1: Effect of the value of  $\mathcal{L}_{crit}$  on  $\mathcal{L}$  and  $C_L$  variations for both phases.

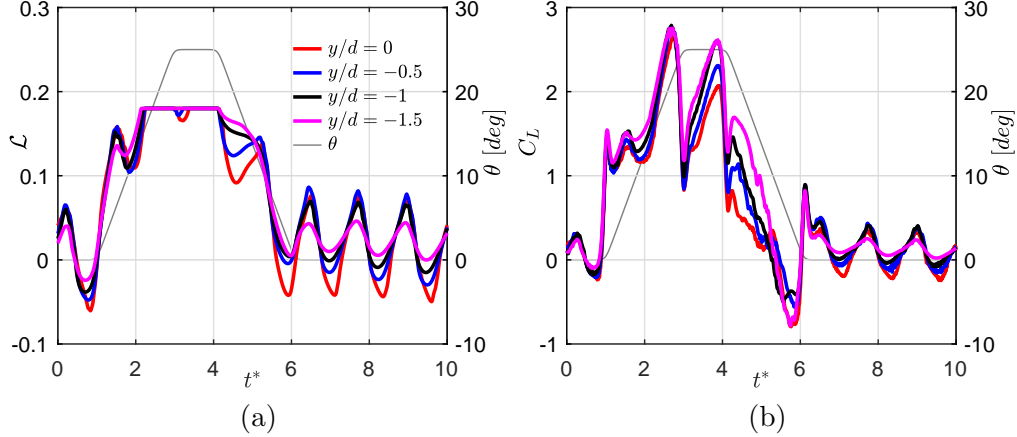


Figure B.2: Effect of centerline distance on (a)  $\mathcal{L}$  and (b)  $C_L$  variations for  $\phi = 0^\circ$ .

The influence of the oncoming disturbance weakens rapidly as the airfoil is moved away from the centerline. The amplitudes of oscillation of both  $\mathcal{L}$  and  $C_L$  can be seen to decrease as the distance of the airfoil from the centerline increases. This results mainly from the decrease in the velocity- and flow-angle fluctuations induced by the vortex clusters. The decrease in the surging effect due to the vortices along with the smaller velocity deficit causes an increase in the mean values of both the quantities for increasing distance from the centerline. A brief interruption of LEV shedding can be observed for  $y/d = -0.5$ . At larger distances, the LEV-interruption phenomenon disappears, and a continuous LEV shedding similar to the no-disturbance case is observed.

### 3. Effect of the strength of the oncoming vortices

The effect of the strength of the oncoming vortical disturbances is examined by varying the nondimensional strength of the vortex clusters in the low-order simulations. Figures B.3(a) and B.3(b) show the variations of  $\mathcal{L}$  and  $C_L$ , respectively, for three values of  $\Gamma/(cU_{ref})$ . Results for  $\Gamma/(cU_{ref}) = 0.3$ , (nominal value used in this work), along with the results for a lower (0.1) and a higher (0.5) value are presented to show the effect of stronger and weaker disturbances. Only  $\phi = 0^\circ$  is considered here since the trends discussed below are independent of the value of  $\phi$ .

The amplitude of fluctuations of both  $\mathcal{L}$  and  $C_L$  are seen to increase with the increase in the strength of the oncoming disturbances. This can be attributed to the larger downwash distributions and flow-angle fluctuations induced by the stronger vortices. Additionally, due to the larger reverse flow induced at the wake center by the stronger vortex street, a reduction in mean is also observed for both the quantities with increasing vortex strength. The LEV shedding characteristics are also seen to be affected by this parameter. For  $\Gamma/(cU_{ref}) = 0.1$ , the vortices are not strong enough to cause an interruption in LEV shedding. On the other hand, for  $\Gamma/(cU_{ref}) = 0.5$ , a larger drop from the critical value is observed in the  $\mathcal{L}$  variation in the presence of stronger vortical disturbances. It is to be noted that in real flows, larger fluctuations may lead to viscous effects such as wake-instability synchronization and associated modification of the lift response under certain conditions ([186]), which cannot be predicted by low-order inviscid models.

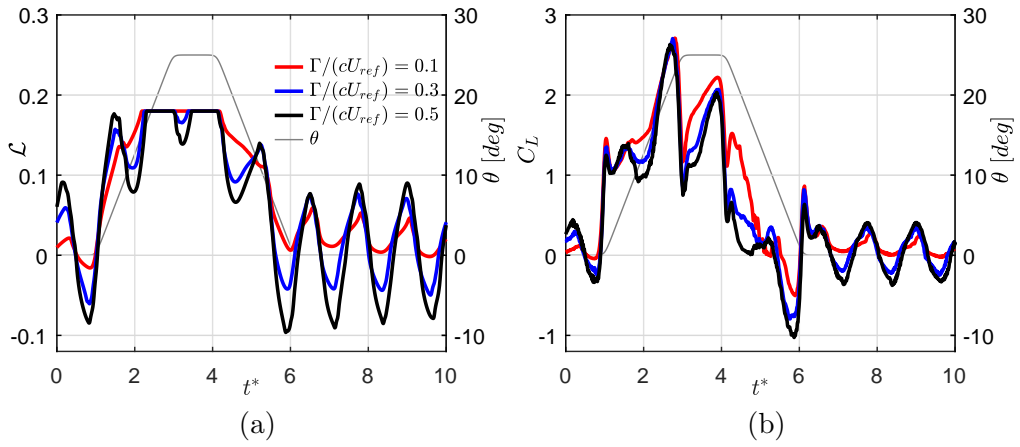


Figure B.3: Effect of oncoming vortex strength on (a)  $\mathcal{L}$  and (b)  $C_L$  variations for  $\phi = 0^\circ$ .

## Appendix C

# List of Publications Resulting from this Effort

### C.1 Journal articles

- A. SureshBabu, K. Ramesh, and A. Gopalarathnam, “Model Reduction in Discrete-Vortex Methods for Unsteady Airfoil Flows,” *AIAA Journal*, Vol. 57, Issue 4, 2019.
- Z. Gianikos, B. Kirschmeier, A. Gopalarathnam and M. Bryant, “Limit cycle characterization of an aeroelastic wing in a bluff body wake,” *Journal of Fluids and Structures*, Vol.95, 2020.
- B. Kirschmeier, G. Pash, Z. Gianikos, A. Medina, A. Gopalarathnam and M. Bryant, “Aeroelastic inverse: Estimation of aerodynamic loads during large amplitude limit cycle oscillations,” *Journal of Fluids and Structures*, Vol. 98, 2020.
- B. Kirschmeier, Z. Gianikos, A. Gopalarathnam and M. Bryant, “Amplitude Annihilation in Wake-Influenced Aeroelastic Limit-Cycle Oscillations,” *AIAA Journal*, Vol. 58, No. 9, 2020.
- A. SureshBabu, A. Medina, M. Rockwood, M. Bryant and A. Gopalarathnam, “Theoretical and experimental investigation of an unsteady airfoil in the presence of external flow disturbances,” *Journal of Fluid Mechanics*, vol. 921,2021.

### C.2 Conference publications/presentations

- Z. Gianikos, B. Kirschmeier and M. Bryant, “Limit Cycle Characterization of an Aeroelastic Airfoil in the Wake of an Upstream Bluff Body,” 2018 AIAA Applied Aerodynamics Conference, AIAA paper 2018-3485.
- A. Medina, A. SureshBabu, M. Rockwood, A. Gopalarathnam, and A. Anwar, “Theoretical and experimental study of wake encounters on unsteady airfoils,” AIAA Scitech 2019 Forum, AIAA paper 2019-0898.
- P. Chatterjee, M. Jenkins, A. SureshBabu, A. Medina, A. Gopalarathnam and M. Bryant, “Tailored Bluff Body Motion for Generating Desired Wake Structures,” AIAA Aviation 2020 Forum, AIAA paper 2020-3007.

- A. Mistele and A. SureshBabu, “Discrete Vortex Method for Modeling Effects of External Flow Disturbances on Airfoils,” AIAA Paper 2021-0002, AIAA Scitech 2021 Forum.
- A. Mistele, A. SureshBabu and A. Gopalarathnam, “Inviscid Model for Unsteady Multi-Airfoil Configurations with Leading-Edge Vortex Shedding,” AIAA 2021-1824, AIAA Scitech 2021 Forum.
- M. Hughes, M. Mook, M. Jenkins, A. SureshBabu, A. Gopalarathnam, and M. Bryant, “Flow Disturbance Generators Based on Oscillating Cylinders with Attached Splitter Plates,” ASME 2021 International Mechanical Engineering Congress and Exposition, Nov. 1-4, 2021 (to be published).
- M. Hughes, A. Gopalarathnam, and M. Bryant, “Toward On-Demand Modulation and Anihilation of Aeroelastic Limit Cycle Oscillations with Dynamic Upstream Disturbance Generator,” Online Symposium on Aeroelasticity, Fluid-Structure Interaction, and Vibrations, Oct. 14-15, 2021 (to be published).

### **C.3 Ph.D. dissertations**

- A. SureshBabu, “Reduced-Order Discrete-Vortex Method for Unsteady Airfoils with Wake Encounter,” Dec. 4, 2018
- B. Kirschmeier, “Wing-Wake Interactions in Aeroelastic Systems,” Aug. 14, 2019

### **C.4 M.S. theses**

- Z. Gianikos, “Limit Cycle Characterization of an Aeroelastic Wing in a Bluff Body Wake,” May 10, 2019

# Bibliography

- <sup>1</sup> Carr, L. W., McAlister, K. W., and McCroskey, W. J., “Analysis of the development of dynamic stall based on oscillating airfoil experiments,” *NASA Technical Note D-8382*, , No. January, 1977, pp. 1–99.
- <sup>2</sup> Zbikowski, R., “On aerodynamic modelling of an insect-like flapping wing in hover for micro air vehicles.” *Philosophical transactions. Series A, Mathematical, physical, and engineering sciences*, Vol. 360, No. 1791, 2002, pp. 273–290.
- <sup>3</sup> Lentink, D., Muijres, F. T., Donker-Duyvis, F. J., and van Leeuwen, J. L., “Vortex-wake interactions of a flapping foil that models animal swimming and flight.” *The Journal of experimental biology*, Vol. 211, No. Pt 2, jan 2008, pp. 267–73.
- <sup>4</sup> Blake, W. and Multhopp, D., “Design, performance and modeling considerations for close formation flight,” Aiaa-98-4343, 1998.
- <sup>5</sup> Derakhshandeh, J. F., Arjomandi, M., Dally, B., and Cazzolato, B., “Flow-induced vibration of an elastically mounted airfoil under the influence of the wake of a circular cylinder,” *Experimental Thermal and Fluid Science*, Vol. 74, No. March, 2016, pp. 58–72.
- <sup>6</sup> Tsui, Y. T., “On Wake-Induced Flutter of a Circular Cylinder in the Wake of Another,” *Journal of Applied Mechanics*, Vol. 44, No. 2, Feb. 1977, pp. 194.
- <sup>7</sup> Kirschmeier, B. and Bryant, M., “Experimental investigation of wake-induced aeroelastic limit cycle oscillations in tandem wings,” *Journal of Fluids and Structures*, Vol. 81, aug 2018, pp. 309–324.
- <sup>8</sup> Lau, Y. L., So, R. M. C., and Leung, R. C. K., “Flow-induced vibration of elastic slender structures in a cylinder wake,” *Journal of Fluids and Structures*, Vol. 19, No. 8, 2004, pp. 1061–1083.
- <sup>9</sup> Bloy, A. W., West, M. G., Lea, K. A., and Joiima’a, M., “Lateral aerodynamic interference between tanker and receiver in air-to-air refueling,” *Journal of Aircraft*, Vol. 30, No. 5, Sep. 1993, pp. 705–710.
- <sup>10</sup> Streitlien, K., Triantafyllou, G. S., and Triantafyllou, M. S., “Efficient foil propulsion through vortex control,” *AIAA Journal*, Vol. 34, No. 11, 1996, pp. 2315–2319.
- <sup>11</sup> Bisplinghoff, R.L., A. H. and Halfman, R., *Aeroelasticity*, Courier Dover Publications, New York, 1996.

- <sup>12</sup> Fung, Y., *An introduction to the theory of aeroelasticity*, Courier Dover Publications, New York, 2008.
- <sup>13</sup> Hamamoto, M., Ohta, Y., Hara, K., and Hisada, T., “Application of fluid–structure interaction analysis to flapping flight of insects with deformable wings,” *Advanced Robotics*, Vol. 21, No. 1-2, 2007, pp. 1–21.
- <sup>14</sup> Nakata, T. and Liu, H., “Aerodynamic performance of a hovering hawkmoth with flexible wings: a computational approach,” *Proceedings of the Royal Society of London B: Biological Sciences*, Vol. 279, No. 1729, 2012, pp. 722–731.
- <sup>15</sup> Taylor, G.K., T. M. T. C., *Animal locomotion*, Springer-Verlag, Heidelberg, 2010.
- <sup>16</sup> Shyy, W., Lian, Y., Tang, J., Liu, H., Trizila, P., Stanford, B., Bernal, L., Cesnik, C., Friedmann, P., and Ifju, P., “Computational aerodynamics of low Reynolds number plunging, pitching and flexible wings for MAV applications,” *Acta Mechanica Sinica*, Vol. 24, No. 4, Aug 2008, pp. 351–373.
- <sup>17</sup> Tang, J., Chimakurthi, S., Palacios, R., Cesnik, C., and Shyy, W., “Computational Fluid-Structure Interaction of a Deformable Flapping Wing for Micro Air Vehicle Applications,” AIAA Paper 2008-0615, June 2008.
- <sup>18</sup> Liani, E., Guo, S., and Allegri, G., chap. Aeroelastic Effect on Flapping Wing Performance, Structures, Structural Dynamics, and Materials and Co-located Conferences, American Institute of Aeronautics and Astronautics, Apr 2007, 0.
- <sup>19</sup> Tang, L., Païdoussis, M. P., and Jiang, J., “Cantilevered flexible plates in axial flow: Energy transfer and the concept of flutter-mill,” *Journal of Sound and Vibration*, Vol. 326, No. 1-2, sep 2009, pp. 263–276.
- <sup>20</sup> Bryant, M. and Garcia, E., “Modeling and testing of a novel aeroelastic flutter energy harvester,” *Journal of Vibration and Acoustics*, Vol. 133, No. 1, 2011.
- <sup>21</sup> Dunnmon, J. A., Stanton, S. C., Mann, B. P., and Dowell, E. H., “Power extraction from aeroelastic limit cycle oscillations,” *Journal of Fluids and Structures*, Vol. 27, No. 8, 2011, pp. 1182–1198.
- <sup>22</sup> Dimitriadis, G. and Li, J., “Bifurcation Behavior of Airfoil Undergoing Stall Flutter Oscillations in Low-Speed Wind Tunnel,” *AIAA Journal*, Vol. 47, No. 11, 2009, pp. 2577–2596.
- <sup>23</sup> Razak, N. A., Andrianne, T., and Dimitriadis, G., “Flutter and Stall Flutter of a Rectangular Wing in a Wind Tunnel,” *AIAA Journal*, Vol. 49, No. 10, 2011, pp. 2258–2271.
- <sup>24</sup> Pigolotti, L., Mannini, C., and Bartoli, G., “Experimental study on the flutter-induced motion of two-degree-of-freedom plates,” *Journal of Fluids and Structures*, Vol. 75, 2017, pp. 77–98.
- <sup>25</sup> Pigolotti, L., Mannini, C., and Bartoli, G., “Destabilizing effect of damping on the post-critical flutter oscillations of flat plates,” *Meccanica*, Vol. 52, No. 13, 2017, pp. 3149–3164.
- <sup>26</sup> Pigolotti, L., Mannini, C., Bartoli, G., and Thiele, K., “Critical and post-critical behaviour of two-degree-of-freedom flutter-based generators,” Vol. 404, 2017, pp. 116–140.

- 27 Boudreau, M., Dumas, G., Rahimpour, M., and Oshkai, P., “Experimental investigation of the energy extraction by a fully-passive flapping-foil hydrokinetic turbine prototype,” *Journal of Fluids and Structures*, Vol. 82, 2018, pp. 446–472.
- 28 Šidlof, P., Vlček, V., and Štěpán, M., “Experimental investigation of flow-induced vibration of a pitch–plunge NACA 0015 airfoil under deep dynamic stall,” *Journal of Fluids and Structures*, Vol. 67, 2016, pp. 48–59.
- 29 Amandolese, X., Michelin, S., and Choquel, M., “Low speed flutter and limit cycle oscillations of a two-degree-of-freedom flat plate in a wind tunnel,” *Journal of Fluids and Structures*, 2013, pp. 1–24.
- 30 Poirel, D., Harris, Y., and Benaissa, a., “Self-sustained aeroelastic oscillations of a NACA0012 airfoil at low-to-moderate Reynolds numbers,” *Journal of Fluids and Structures*, Vol. 24, No. 5, 7 2008, pp. 700–719.
- 31 Strganac, T. W., Ko, J., Thompson, D. E., and Kurdila, A. J., “Identification and Control of Limit Cycle Oscillations in Aeroelastic Systems,” *Journal of Guidance, Control, and Dynamics*, Vol. 23, No. 6, 2000, pp. 1127–1133.
- 32 Shukla, H. and Patil, M. J., “Controlling Limit Cycle Oscillation Amplitudes in Nonlinear Aeroelastic Systems,” *Journal of Aircraft*, Vol. 54, No. 5, 2017, pp. 1921–1932.
- 33 Tsushima, N. and Su, W., “Flutter suppression for highly flexible wings using passive and active piezoelectric effects,” *Aerospace Science and Technology*, Vol. 65, 2017, pp. 78–89.
- 34 Timpe, A., Zhang, Z., Hubner, J., and Ukeiley, L., “Passive flow control by membrane wings for aerodynamic benefit,” *Experiments in Fluids*, Vol. 54, No. 1471, 2013.
- 35 Lissaman, P. B. S. and Shollenberger, C. A., “Formation Flight of Birds,” *Science*, Vol. 168, No. 3934, 1970, pp. 1003–1005.
- 36 Liao, J. C., Beal, D. N., Lauder, G. V., and Triantafyllou, M. S., “Fish Exploiting Vortices Decrease Muscle Activity,” *Science*, Vol. 302, No. 5650, 2003, pp. 1566–1569.
- 37 Fletcher, T. M. and Brown, R. E., “Modelling the interaction of helicopter main rotor and tail rotor wakes,” *The Aeronautical Journal*, Vol. 111, No. 1124, 2007, pp. 637–643.
- 38 Zhao, Q., Sheng, C., and Afjeh, A., “Computational Aerodynamic Analysis of Offshore Upwind and Downwind Turbines,” *Journal of Aerodynamics*, 2014.
- 39 Tadokoro, M., Yokoyama, H., and Iida, A., “Effects of wake-turbine blade interactions on power production of wind turbines,” *AIP Conference Proceedings*, Vol. 1807, No. 1, 2017.
- 40 Choudhry, A., Mo, J., Arjomandi, M., and Kelso, R., “Effects of Wake Interaction on Downstream Wind Turbines,” *Wind Engineering*, Vol. 38, No. 5, 2014, pp. 535–547.
- 41 Binder, A., Forster, W., Mach, K., and Rogge, H., “Unsteady flow interaction caused by stator secondary vortices in a turbine rotor,” *Journal of Turbomachinery*, Vol. 109, No. 2, 04 1987, pp. 251–256.
- 42 Tang, D. and Dowell, E. H., “Experimental and Theoretical Study of Gust Response for High-Aspect-Ratio Wing,” *AIAA Journal*, Vol. 40, No. 3, 2002, pp. 419–429.

- <sup>43</sup> Dowell, E. H., Doherty, J., Joshi, M., Sharma, M., Kielb, R., and Rauseo, M., *Investigation of the Nonlinear Interaction of a Flutter/Limit Cycle Oscillation of a Cantilevered Wing with a Gust Excitation*.
- <sup>44</sup> Wagner, H., “Über die entstehung des dynamischen auftriebes von tragflügeln,” *Zeitschrift für Angewandte Mathematik und Mechanik*, Vol. 5, 1925, pp. 17–35.
- <sup>45</sup> Theodorsen, T., “General theory of aerodynamic instabililty and the mechanism of flutter,” Tech. Rep. NACA-TR-496, National Advisory Committee for Aeronautics, 1935.
- <sup>46</sup> Küssner, H., “Zusammenfassender bericht über den instationären auftrieb von flügeln (summary report on the nonstationary lift of wings),” *Luftfahrtforschung*, Vol. 13, No. 12, 1936, pp. 410–424.
- <sup>47</sup> von Kármán, T. and Sears, W., “Airfoil theory for non-uniform motion,” *Journal of the Aeronautical Sciences*, Vol. 5, 1938, pp. 379–390.
- <sup>48</sup> Sears, W. R., “Some aspects of nonstationary airfoil theory and its practical application,” *Journal of the Aeronautical Sciences*, 1941, pp. 104–108.
- <sup>49</sup> McCune, J. E., Lam, C. G., and Scott, M. T., “Nonlinear aerodynamics of two-dimensional airfoils in severe maneuver,” *AIAA Journal*, Vol. 28, No. 3, 1990, pp. 385–393.
- <sup>50</sup> Wang, C. and Eldredge, J. D., “Low-order phenomenological modeling of leading-edge vortex formation,” *Theoretical and Computational Fluid Dynamics*, Vol. 27, No. 5, 2013, pp. 577–598.
- <sup>51</sup> Ramesh, K., Gopalarathnam, A., Granlund, K., Ol, M. V., and Edwards, J. R., “Discrete-vortex method with novel shedding criterion for unsteady aerofoil flows with intermittent leading-edge vortex shedding,” *Journal of Fluid Mechanics*, Vol. 751, 2014, pp. 500–538.
- <sup>52</sup> Alaminos-Quesada, J. and Fernandez-Feria, R., “Effect of the angle of attack on the transient lift during the interaction of a vortex with a flat plate. Potential theory and experimental results,” *Journal of Fluids and Structures*, Vol. 74, 2017, pp. 130 – 141.
- <sup>53</sup> Wei, Z. A. and Zheng, Z. C., “Energy-Harvesting Mechanism of a Heaving Airfoil in a Vortical Wake,” *AIAA Journal*, Vol. 55, No. 12, Jul 2017, pp. 4061–4073.
- <sup>54</sup> Visbal, M. R. and Garmann, D. J., “Analysis of Dynamic Stall on a Pitching Airfoil Using High-Fidelity Large-Eddy Simulations,” <https://doi.org/10.2514/1.J056108>, 2017, pp. 1–18.
- <sup>55</sup> Okajima, A., “Strouhal numbers of rectangular cylinders,” *Journal of Fluid Mechanics*, Vol. 123, 1982, pp. 379–398.
- <sup>56</sup> Song, J., Kim, T., and Song, S. J., “Experimental determination of unsteady aerodynamic coefficients and flutter behavior of a rigid wing,” *Journal of Fluids and Structures*, Vol. 29, Feb. 2012, pp. 50–61.
- <sup>57</sup> Marsden, C. C. and Price, S. J., “The aeroelastic response of a wing section with a structural freeplay nonlinearity: An experimental investigation,” *Journal of Fluids and Structures*, Vol. 21, No. 3 SPEC. ISS., 2005, pp. 257–276.
- <sup>58</sup> Razak, N. A., Andrianne, T., and Dimitriadis, G., “Flutter and Stall Flutter of a Rectangular Wing in a Wind Tunnel,” *AIAA Journal*, Vol. 49, No. 10, 2011, pp. 2258–2271.

- <sup>59</sup> Šidlof, P., Vlček, V., and Štěpán, M., “Experimental investigation of flow-induced vibration of a pitch–plunge NACA 0015 airfoil under deep dynamic stall,” *Journal of Fluids and Structures*, Vol. 67, 2016, pp. 48–59.
- <sup>60</sup> Strganac, T. W. and Hunter, W. F., “Aniv.) 123,” Vol. 62.
- <sup>61</sup> Poirel, D., Harris, Y., and Benaissa, a., “Self-sustained aeroelastic oscillations of a NACA0012 airfoil at low-to-moderate Reynolds numbers,” *Journal of Fluids and Structures*, Vol. 24, No. 5, jul 2008, pp. 700–719.
- <sup>62</sup> Dowell, E. H. and Tang, D., “Nonlinear Aeroelasticity and Unsteady Aerodynamics,” *AIAA Journal*, Vol. 40, No. 9, Sep. 2002, pp. 1697–1707.
- <sup>63</sup> Poirel, D. C. and Price, S. J., “Structurally nonlinear fluttering airfoil in turbulent flow,” *AIAA Journal*, Vol. 39, No. 10, 2001, pp. 1960–1968.
- <sup>64</sup> Venkatramani, J., Nair, V., Sujith, R. I., Gupta, S., and Sarkar, S., “Multi-fractality in aeroelastic response as a precursor to flutter,” *Journal of Sound and Vibration*, Vol. 386, 2017, pp. 390–406.
- <sup>65</sup> Hammer, P. W., Platt, N., Hammel, S. M., Heagy, J. F., and Lee, B. D., “Experimental Observation of On-Off Intermittency,” *Physical Review Letters*, Vol. 73, No. 8, Aug. 1994, pp. 1095–1098.
- <sup>66</sup> Gammaitoni, L., Marchesoni, F., Menichella-Saetta, E., and Santucci, S., “Intermittency in nonlinear stochastic systems,” *Physics Letters A*, Vol. 156, No. 1-2, Jun. 1991, pp. 37–41.
- <sup>67</sup> Chen, J. M. and Choa, C.-C., “Freestream Disturbance Effects on an Airfoil Pitching at Constant Rate,” *Journal of Aircraft*, Vol. 36, No. 3, May 1999, pp. 507–514.
- <sup>68</sup> Merrill, B. E. and Peet, Y. T., “Effect of Impinging Wake Turbulence on the Dynamic Stall of a Pitching Airfoil,” *AIAA Journal*, Vol. 55, No. 12, 2017, pp. 4094–4112.
- <sup>69</sup> Strogatz, S. H., *Nonlinear Dynamics And Chaos: With Applications To Physics, Biology, Chemistry, And Engineering (Studies in Nonlinearity)*, CRC Press, Dec 2000.
- <sup>70</sup> Schwartz, M., Manzoor, S., Hémon, P., and de Langre, E., “By-pass transition to airfoil flutter by transient growth due to gust impulse,” *Journal of Fluids and Structures*, Vol. 25, No. 8, 2009, pp. 1272–1281.
- <sup>71</sup> Zhang, Y., Tang, B., and Xiao, X., “Time-frequency interpretation of multi-frequency signal from rotating machinery using an improved Hilbert-Huang transform,” *Measurement: Journal of the International Measurement Confederation*, Vol. 82, 2016, pp. 221–239.
- <sup>72</sup> Kirschmeier, B., Pash, G., Gianikos, Z. N., Medina, A., Gopalathnam, A., and Bryant, M., “Aeroelastic Inverse: Estimation of aerodynamic loads during dynamic stall flutter,” *In Review: Journal of Fluids and Structures*, 2020.
- <sup>73</sup> Meirovitch, L., *Fundamentals of Vibrations*, Waveland Pr Inc., Jul. 2010.
- <sup>74</sup> Anderson, J. M., Streitlien, K., Barrett, D. S., and Triantafyllou, M. S., “Oscillating foils of high propulsive efficiency,” *Journal of Fluid Mechanics*, Vol. 360, 1998, pp. 41–72.

- 75 McKinney and Delaurier, “The Wingmill An Oscillating-Wing Windmill,” *Journal of Energy*, 1981.
- 76 Kinsey, T. and Dumas, G., “Parametric Study of an Oscillating Airfoil in a Power-Extraction Regime,” *AIAA Journal*, Vol. 46, No. 6, Jun 2008, pp. 1318–1330.
- 77 Marple, L., “Computing the discrete-time ”analytic” signal via FFT,” *IEEE Transactions on Signal Processing*, Vol. 47, No. 9, 1999, pp. 2600–2603.
- 78 McCroskey, W., McAlister, K., Carr, L., Pucci, S., Lambert, O., and Indergrand, R., “Dynamic stall on advanced airfoil sections,” *Journal of the American Helicopter Society*, , No. May, 1981, pp. 40–50.
- 79 Tang, D. M., Kholodar, D., and Dowell, E. H., “Nonlinear response of airfoil section with control surface freeplay to gust loads,” *Aiaa J.*, Vol. 38, No. 9, 2000, pp. 1543–1557.
- 80 Strganac, T. W., Ko, J., and Thompson, D. E., “Identification and Control of Limit Cycle Oscillations in Aeroelastic Systems,” *Journal of Guidance, Control, and Dynamics*, Vol. 23, No. 6, 2000, pp. 1127–1133.
- 81 Pigolotti, L., Mannini, C., and Bartoli, G., “Destabilizing effect of damping on the post-critical flutter oscillations of flat plates,” *Meccanica*, Vol. 52, No. 13, 2017, pp. 3149–3164.
- 82 Pigolotti, L., Mannini, C., Bartoli, G., and Thiele, K., “Critical and post-critical behaviour of two-degree-of-freedom flutter-based generators,” *Journal of Sound and Vibration*, Vol. 404, 2017, pp. 116–140.
- 83 Dimitriadis, G. and Li, J., “Bifurcation Behavior of Airfoil Undergoing Stall Flutter Oscillations in Low-Speed Wind Tunnel,” *AIAA Journal*, Vol. 47, No. 11, 2009, pp. 2577–2596.
- 84 Poirel, D., Métivier, V., and Dumas, G., “Computational aeroelastic simulations of self-sustained pitch oscillations of a NACA0012 at transitional Reynolds numbers,” *Journal of Fluids and Structures*, Vol. 27, 2011, pp. 1262–1277.
- 85 Sandhu, R., Poirel, D., Pettit, C., Khalil, M., and Sarkar, A., “Bayesian inference of nonlinear unsteady aerodynamics from aeroelastic limit cycle oscillations,” *Journal of Computational Physics*, Vol. 316, 2016, pp. 534–557.
- 86 Khalil, M., Poirel, D., and Sarkar, A., “Probabilistic parameter estimation of a fluttering aeroelastic system in the transitional Reynolds number regime,” *Journal of Sound and Vibration*, Vol. 332, No. 15, 2013, pp. 3670–3691.
- 87 Amandolese, X., Michelin, S., and Choquel, M., “Low speed flutter and limit cycle oscillations of a two-degree-of-freedom flat plate in a wind tunnel,” *Journal of Fluids and Structures*, 2013, pp. 1–24.
- 88 Boudreau, M., Dumas, G., Rahimpour, M., and Oshkai, P., “Experimental investigation of the energy extraction by a fully-passive flapping-foil hydrokinetic turbine prototype,” *Journal of Fluids and Structures*, Vol. 82, 2018, pp. 446–472.
- 89 Lee, Y. S., Kerschen, G., McFarland, D. M., Hill, W. J., Nickkawde, C., Strganac, T. W., Bergman, L. a., and Vakakis, A. F., “Suppressing Aeroelastic Instability Using Broadband Passive Targeted Energy Transfers, Part 2: Experiments,” *AIAA Journal*, Vol. 45, No. 10, 2007, pp. 2391–2400.

- <sup>90</sup> Bichiou, Y., Hajj, M. R., and Nayfeh, A. H., “Effectiveness of a nonlinear energy sink in the control of an aeroelastic system,” *Nonlinear Dynamics*, Vol. 86, No. 4, 2016, pp. 2161–2177.
- <sup>91</sup> Pacheco, D. R., Marques, F. D., and Ferreira, A. J., “Panel flutter suppression with nonlinear energy sinks: Numerical modeling and analysis,” *International Journal of Non-Linear Mechanics*, Vol. 106, 2018, pp. 108–114.
- <sup>92</sup> Koseska, A., Volkov, E., and Kurths, J., “Transition from amplitude to oscillation death via turing bifurcation,” *Physical Review Letters*, Vol. 111, No. 2, 2013, pp. 1–5.
- <sup>93</sup> Strogatz, S. H., “Nonlinear dynamics: Death by delay,” *Nature*, Vol. 394, No. 6691, 1998, pp. 316–317.
- <sup>94</sup> Saxena, G., Prasad, A., and Ramaswamy, R., “Amplitude death: The emergence of stationarity in coupled nonlinear systems,” *Physics Reports*, Vol. 521, No. 5, 2012, pp. 205–228.
- <sup>95</sup> Gianikos, Z. N., Kirschmeier, B. A., Gopalarathnam, A., and Bryant, M., “Limit cycle characterization of an aeroelastic wing in a bluff body wake,” *Journal of Fluids and Structures*, Vol. 95, 2020, pp. 102986.
- <sup>96</sup> Poirel, D. and Yuan, W., “Aerodynamics of laminar separation flutter at a transitional Reynolds number,” *Journal of Fluids and Structures*, Vol. 26, No. 7-8, 2010, pp. 1174–1194.
- <sup>97</sup> Epps, B. P. and Kimball, R. W., “Unified Rotor Lifting Line Theory,” *Journal of Ship Research*, Vol. 57, No. 4, 2013, pp. 181–201.
- <sup>98</sup> Truscott, T. T., Epps, B. P., and Techet, A. H., “Unsteady forces on spheres during free-surface water entry,” *Journal of Fluid Mechanics*, Vol. 704, 2012, pp. 173–210.
- <sup>99</sup> Haario, H., Laine, M., Mira, A., and Saksman, E., “DRAM: efficient adaptive MCMC,” *Statistics and computing*, Vol. 16, No. 4, 2006, pp. 339–354.
- <sup>100</sup> Haario, H., Saksman, E., Tamminen, J., et al., “An adaptive Metropolis algorithm,” *Bernoulli*, Vol. 7, No. 2, 2001, pp. 223–242.
- <sup>101</sup> Smith, R. C., *Uncertainty quantification: theory, implementation, and applications*, Vol. 12, Siam, 2013.
- <sup>102</sup> Bendiksen, O. O., “Energy Approach to Flutter Suppression and Aeroelastic Control,” *Journal of Guidance, Control, and Dynamics*, Vol. 24, No. 1, 2001, pp. 176–184.
- <sup>103</sup> Huang, N. E., Shen, Z., Long, S. R., Wu, M. C., Shih, H. H., Zheng, Q., Yen, N.-C., Tung, C. C., and Liu, H. H., “The Empirical Mode Decomposition and the Hilbert Spectrum for Nonlinear and Non-Stationary Time Series Analysis,” *Mathematical, Physical and Engineering Sciences*, Vol. 454, No. 1971, 1998, pp. 903–995.
- <sup>104</sup> Marwan, N., Carmen Romano, M., Thiel, M., and Kurths, J., “Recurrence plots for the analysis of complex systems,” *Physics Reports*, Vol. 438, No. 5-6, 2007, pp. 237–329.
- <sup>105</sup> Dietz, G., “Experiments on heave/pitch limit-cycle oscillations of a supercritical airfoil close to the transonic dip,” *Journal of Fluids and Structures*, Vol. 19, 2004, pp. 1–16.

- 106 Khalak, A. and Williamson, C., “Motions, Forces and Mode Transitions in Vortex-Induced Vibrations at Low Mass-Damping,” *Journal of Fluids and Structures*, Vol. 13, 1999, pp. 813–851.
- 107 Poirel, D. and Yuan, W., “Aerodynamics of laminar separation flutter at a transitional Reynolds number,” *Journal of Fluids and Structures*, Vol. 26, No. 7-8, 2010, pp. 1174–1194.
- 108 Poirel, D. and Mendes, F., “Experimental Small-Amplitude Self-Sustained Pitch–Heave Oscillations at Transitional Reynolds Numbers,” *AIAA Journal*, Vol. 52, No. 8, 2014, pp. 1581–1590.
- 109 Hedrick, T. L., “Wing inertia and whole-body acceleration: an analysis of instantaneous aerodynamic force production in cockatiels (*Nymphicus hollandicus*) flying across a range of speeds,” *Journal of Experimental Biology*, Vol. 207, No. 10, 2004, pp. 1689–1702.
- 110 Zhang, W., Lv, Z., Diwu, Q., and Zhong, H., “A flutter prediction method with low cost and low risk from test data,” *Aerospace Science and Technology*, Vol. 86, 2019, pp. 542–557.
- 111 Gao, G. and Zhu, L., “Measurement and verification of unsteady galloping force on a rectangular 2:1 cylinder,” *Journal of Wind Engineering and Industrial Aerodynamics*, Vol. 157, 2016, pp. 76–94.
- 112 Kirschmeier, B. and Bryant, M., “Towards efficient aeroelastic energy harvesting through limit cycle shaping,” *SPIE Smart Structures and Nondestructive evaluation*, 2016, p. 12.
- 113 Bendiksen, O. O., “Energy Approach to Flutter Suppression and Aeroelastic Control,” *Journal of Guidance, Control, and Dynamics*, Vol. 24, No. 1, 2001, pp. 176–184.
- 114 Kinsey, T. and Dumas, G., “Parametric Study of an Oscillating Airfoil in a Power-Extraction Regime,” *AIAA Journal*, Vol. 46, No. 6, 6 2008, pp. 1318–1330.
- 115 Bartoli, G., Contri, S., Mannini, C., and Righi, M., “Toward an improvement in the identification of bridge deck flutter derivatives,” *Journal of Engineering Mechanics*, Vol. 135, No. 8, 2009, pp. 771–785.
- 116 Khalil, M., Poirel, D., and Sarkar, A., “Bayesian analysis of the flutter margin method in aeroelasticity,” *Journal of Sound and Vibration*, Vol. 384, 2016, pp. 56–74.
- 117 Goodfellow, I., Bengio, Y., and Courville, A., *Deep Learning*, MIT Press, 2016, <http://www.deeplearningbook.org>.
- 118 Quaiser, T. and Mönnigmann, M., “Systematic identifiability testing for unambiguous mechanistic modeling—application to jak-stat, map kinase, and nf- $\kappa$  b signaling pathway models,” *BMC systems biology*, Vol. 3, No. 1, 2009, pp. 50.
- 119 Leon, L., Smith, R. C., Oates, W. S., and Miles, P., “Analysis of a multi-axial quantum-informed ferroelectric continuum model: Part 2—sensitivity analysis,” *Journal of Intelligent Material Systems and Structures*, Vol. 29, No. 13, 2018, pp. 2840–2860.
- 120 Kaipio, J. and Somersalo, E., *Statistical and computational inverse problems*, Vol. 160, Springer Science & Business Media, 2006.
- 121 Epps, B. P., Truscott, T. T., and Techet, A. H., “Evaluating derivatives of experimental data using smoothing splines,” *Mathematical Methods in Engineering International Symposium*, , No. October, 2010, pp. 29–38.

- 122 Medina, A., Ol, M. V., Mancini, P., and Jones, A., “Revisiting Conventional Flaps at High Deflection Rate,” *AIAA Journal*, Vol. 55, No. 8, 2017, pp. 2676–2685.
- 123 Medina, A., Ol, M. V., Greenblatt, D., Müller-Vahl, H., and Strangfeld, C., “High-Amplitude Surge of a Pitching Airfoil: Complementary Wind- and Water-Tunnel Measurements,” *AIAA Journal*, Vol. 56, No. 4, 2018, pp. 1703–1709.
- 124 Matthew Rockwood, Albert Medina, D. J. G. and Visbal, M. R., “Dynamic Stall of a Swept Finite Wing for a Range of Reduced Frequencies,” *AIAA Aviation 2019 Forum*, 2019.
- 125 Corke, T. C. and Thomas, F. O., “Dynamic Stall in Pitching Airfoils: Aerodynamic Damping and Compressibility Effects,” *Annual Review of Fluid Mechanics*, Vol. 47, No. 1, 2015, pp. 479–505.
- 126 Ramesh, K., Gopalarathnam, A., Granlund, K., Ol, M., and Edwards, J., “Discrete-vortex method with novel shedding criterion for unsteady aerofoil flows with intermittent leading-edge vortex shedding,” *Journal of Fluid Mechanics*, Vol. 751, 6 2014, pp. 500–538.
- 127 Schwartz, M., Manzoor, S., Hémon, P., and de Langre, E., “By-pass transition to airfoil flutter by transient growth due to gust impulse,” *Journal of Fluids and Structures*, Vol. 25, No. 8, 2009, pp. 1272–1281.
- 128 Hémon, P., de Langre, E., and Schmid, P., “Experimental evidence of transient growth of energy before airfoil flutter,” *Journal of Fluids and Structures*, Vol. 22, No. 3, 2006, pp. 391–400.
- 129 McKinney and Delaurier, “The Wingmill An Oscillating-Wing Windmill,” *Journal of Energy*, 1981.
- 130 Liao, Q., Dong, G. J., and Lu, X. Y., “Vortex formation and force characteristics of a foil in the wake of a circular cylinder,” *Journal of Fluids and Structures*, Vol. 19, No. 4, 2004, pp. 491–510.
- 131 Liao, J. C., Beal, D. N., Lauder, G. V., and Triantafyllou, M., “The Kármán gait: novel body kinematics of rainbow trout swimming in a vortex street,” *Journal of Experimental Biology*, Vol. 206, No. 6, 2003, pp. 1059–1073.
- 132 Beal, D. N., Hover, F. S., Triantafyllou, M. S., Liao, J. C., and Lauder, G. V., “Passive propulsion in vortex wakes,” *Journal of Fluid Mechanics*, Vol. 549, 2006, pp. 385–402.
- 133 Toming, G., Chambers, L., and Kruusmaa, M., “Experimental study of hydrodynamic forces acting on artificial fish in a von Kármán vortex street,” *Underwater Technology*, Vol. 32, No. 2, 7 2014, pp. 81–91.
- 134 Li, C., W. Yang, Xu, X., Wang, J., Wang, M., and Xu, L., “Numerical investigation of fish exploiting vortices based on the Kármán gaing model,” *Ocean Engineering*, Vol. 140, 2017, pp. 7 – 18.
- 135 Gopalkrishnan, R., Triantafyllou, M. S., Triantafyllou, G. S., and Barrett, D., “Active vorticity control in a shear flow using a flapping foil,” *Journal of Fluid Mechanics*, Vol. 274, 1994, pp. 1–21.
- 136 Zhang, i., Su, Y., Yang, L., and Wang, Z., “Hydrodynamic performance of flapping-foil propulsion in the influence of vortices,” *Journal of Marine Science and Application*, Vol. 9, No. 2, Jun 2010, pp. 213–219.

- <sup>137</sup> Shao, X. and Pan, D., “Hydrodynamics of a flapping foil in the wake of a D-section cylinder,” *Journal of Hydrodynamics, Ser. B*, Vol. 23, No. 4, 2011, pp. 422 – 430.
- <sup>138</sup> Wei, Z. A. and Zheng, Z. C., “Energy-Harvesting Mechanism of a Heaving Airfoil in a Vortical Wake,” *AIAA Journal*, 2017, pp. 1–13.
- <sup>139</sup> Li, S. and Sun, Z., “Harvesting vortex energy in the cylinder wake with a pivoting vane,” *Energy*, Vol. 88, 2015, pp. 783 – 792.
- <sup>140</sup> Muscutt, L. E., Weymouth, G. D., and Ganapathisubramani, B., “Performance augmentation mechanism of in-line tandem flapping foils,” *Journal of Fluid Mechanics*, Vol. 827, 2017, pp. 484–505.
- <sup>141</sup> Wu, J., Wu, J., Tian, F.-B., Zhao, N., and Li, Y.-D., “How a flexible tail improves the power extraction efficiency of a semi-activated flapping foil system: A numerical study,” *Journal of Fluids and Structures*, Vol. 54, 2015, pp. 886–899.
- <sup>142</sup> Ellington, C. P., Van Den Berg, C., Willmott, A. P., and Thomas, A. L. R., “Leading-edge vortices in insect flight,” *Nature*, Vol. 384, No. 6610, 1996, pp. 626–630.
- <sup>143</sup> Dickinson, M. H., Lehmann, F.-O., and Sane, S. P., “Wing Rotation and the Aerodynamic Basis of Insect Flight,” *Science*, Vol. 284, No. 5422, 1999, pp. 1954–1960.
- <sup>144</sup> Shyy, W., Aono, H., Chimakurthi, S. K., Trizila, P., Kang, C.-K., Cesnik, C. E., and Liu, H., “Recent progress in flapping wing aerodynamics and aeroelasticity,” *Progress in Aerospace Sciences*, Vol. 46, No. 7, 2010, pp. 284–327.
- <sup>145</sup> Pitt Ford, C. W. and Babinsky, H., “Lift and the leading-edge vortex,” *Journal of Fluid Mechanics*, Vol. 720, 2013, pp. 280–313.
- <sup>146</sup> Jefferies, R. W. and Rockwell, D., “Interactions of a vortex with an oscillating leading edge,” *AIAA Journal*, Vol. 34, No. 11, Nov 1996, pp. 2448–2450.
- <sup>147</sup> Rival, D. and Tropea, C., “Characteristics of Pitching and Plunging Airfoils Under Dynamic-Stall Conditions,” *Journal of Aircraft*, Vol. 47, No. 1, Jan 2010, pp. 80–86.
- <sup>148</sup> Perrin, R., Braza, M., Cid, E., Cazin, S., Barthet, A., Sevrain, A., Mockett, C., and Thiele, F., “Obtaining phase averaged turbulence properties in the near wake of a circular cylinder at high Reynolds number using POD,” *Experiments in Fluids*, Vol. 43, 2007, pp. 341–355.
- <sup>149</sup> Okajima, A., Takata, H., and Asanuma, T., “Viscous flow around a rotationally oscillating circular cylinder,” *NASA STI/Recon Technical Report N 76*, 1975.
- <sup>150</sup> Cheng, M., Liu, G., and Lam, K., “Numerical simulation of flow past a rotationally oscillating cylinder,” *Computers and Fluids*, Vol. 30, No. 3, 2001, pp. 365–392.
- <sup>151</sup> Rockwood, M. P. and Medina, A., “Controlled generation of periodic vortical gusts by the rotational oscillation of a circular cylinder and attached plate,” *Experiments in Fluids*, Vol. 61, 2020.
- <sup>152</sup> Katz, J. and Plotkin, A., *Low-Speed Aerodynamics*, Cambridge Aerospace Series, 2000.

- 153 Faure, T. M., Dumas, L., and Montagnier, O., “Numerical study of two-airfoil arrangements by a discrete vortex method,” *Theoretical and Computational Fluid Dynamics*, Vol. 34, No. 1, 2020, pp. 79–103.
- 154 Narsipur, S., Hosangadi, P., Gopalarathnam, A., and Edwards, J. R., “Variation of leading-edge suction during stall for unsteady aerofoil motions,” *Journal of Fluid Mechanics*, Vol. 900, 2020, pp. A25.
- 155 SureshBabu, A., Ramesh, K., and Gopalarathnam, A., “Model Reduction in Discrete-Vortex Methods for Unsteady Airfoil Flows,” *AIAA Journal*, Vol. 57, No. 4, 2019, pp. 1409–1422.
- 156 Graftieaux, L., Michard, M., and Grosjean, N., “Combining PIV, POD and vortex identification algorithms for the study of unsteady turbulent swirling flows,” *Measurement Science and Technology*, Vol. 12, 08 2001, pp. 1422.
- 157 Lefebvre, J. N. and Jones, A. R., “Experimental Investigation of Airfoil Performance in the Wake of a Circular Cylinder,” *AIAA Journal*, Vol. 57, No. 7, 2019, pp. 2808–2818.
- 158 Zhang, Z., Wang, Z., and Gursul, I., “Lift Enhancement of a Stationary Wing in a Wake,” *AIAA Journal*, Vol. 58, No. 11, 2020, pp. 4613–4619.
- 159 Medina, A., SureshBabu, A., Rockwood, M. P., Gopalarathnam, A., and Anwar, A., “Theoretical and Experimental Study of Wake Encounters on Unsteady Airfoils,” AIAA Paper 2019-0898, January 2019.
- 160 Li, J. and Wu, Z.-N., “Unsteady lift for the Wagner problem in the presence of additional leading/trailing edge vortices,” *Journal of Fluid Mechanics*, Vol. 769, 2015, pp. 182–217.
- 161 Vatistas, G. H., Kozel, V., and Mih, W. C., “A simpler model for concentrated vortices,” *Experiments in Fluids*, Vol. 11, No. 1, 1991, pp. 73–76.
- 162 Leonard, A., “Vortex methods for flow simulation,” *Journal of Computational Physics*, Vol. 37, No. 3, 1980, pp. 289–335.
- 163 Li, J., Bai, C.-Y., and Wu, Z.-N., “A Two-Dimensional Multibody Integral Approach for Forces in Inviscid Flow With Free Vortices and Vortex Production,” *Journal of Fluids Engineering*, Vol. 137, No. 2, 10 2014, 021205.
- 164 Li, J. and Wu, Z.-N., “A vortex force study for a flat plate at high angle of attack,” *Journal of Fluid Mechanics*, Vol. 801, 2016, pp. 222–249.
- 165 Li, J. and Wu, Z.-N., “Vortex force map method for viscous flows of general airfoils,” *Journal of Fluid Mechanics*, Vol. 836, 2018, pp. 145–166.
- 166 Li, J., Wang, Y., Graham, M., and Zhao, X., “Vortex moment map for unsteady incompressible viscous flows,” *Journal of Fluid Mechanics*, Vol. 891, 2020, pp. A13.
- 167 Li, J., Zhao, X., and Graham, M., “Vortex force maps for three-dimensional unsteady flows with application to a delta wing,” *Journal of Fluid Mechanics*, Vol. 900, 2020, pp. A36.
- 168 Haller, G., “Distinguished material surfaces and coherent structures in 3D fluid flows,” *Physica D*, Vol. 149, 2001, pp. 248–277.

- 169 Hunt, J. C. R., Wray, A. A., and Moin, P., “Eddies, stream, and convergence zones in turbulent flows,” *NASA Ames/Stanford University Center for Turbulence Research Report*, Vol. CTR-S88, 1988, pp. 193–207.
- 170 Green, M. A., Rowley, C. W., and Smits, A. J., “The unsteady three-dimensional wake produced by a trapezoidal pitching panel,” *Journal of Fluid Mechanics*, Vol. 685, 2011, pp. 117–145.
- 171 Rockwood, M. P., Taira, K., and Green, M. A., “Detecting Vortex Formation and Shedding in Cylinder Wakes Using Lagrangian Coherent Structures,” *AIAA Journal*, Vol. 55, No. 1, 2017, pp. 15–23.
- 172 Huang, Y. and Green, M. A., “Detection and tracking of vortex phenomena using Lagrangian coherent structures,” *Experiments in Fluids*, Vol. 56, No. 7, Jul. 2015, pp. 1–12.
- 173 Kirschmeier, B. and Bryant, M., “Experimental investigation of wake-induced aeroelastic limit cycle oscillations in tandem wings,” *Journal of Fluids and Structures*, Vol. 81, 2018, pp. 309–324.
- 174 Gianikos, Z. N., Kirschmeier, B. A., Gopalarathnam, A., and Bryant, M., “Limit cycle characterization of an aeroelastic wing in a bluff body wake,” *Journal of Fluids and Structures*, Vol. 95, 2020, pp. 102986.
- 175 Kirschmeier, B. A., “Wing-Wake Interactions in Aeroelastic Systems,” *North Carolina State University*, 2019.
- 176 Bryant, M. and Garcia, E., “Modeling and Testing of a Novel Aeroelastic Flutter Energy Harvester,” *Journal of Vibration and Acoustics*, Vol. 133, No. 1, 2011.
- 177 Chen, J. M. and Choa, C.-C., “Freestream Disturbance Effects on an Airfoil Pitching at Constant Rate,” *Journal of Aircraft*, Vol. 36, No. 3, 1999, pp. 507–514.
- 178 Merrill, B. E. and Peet, Y. T., “Effect of Impinging Wake Turbulence on the Dynamic Stall of a Pitching Airfoil,” *AIAA Journal*, Vol. 55, No. 12, 2017, pp. 4094–4112.
- 179 Shi, Z.-W. and Ming, X., “Effects of Unsteady Freestream on Aerodynamic Characteristics of a Pitching Delta Wing,” *Journal of Aircraft*, Vol. 45, No. 6, 2008, pp. 2182–2185.
- 180 Williamson, C. H. K., “Vortex Dynamics in the Cylinder Wake,” *Annual Review of Fluid Mechanics*, Vol. 28, No. 1, 1996, pp. 477–539.
- 181 Williamson, C. H. K., “The natural and forced formation of spot-like ‘vortex dislocations’ in the transition of a wake,” *Journal of Fluid Mechanics*, Vol. 243, No. -1, 1992, pp. 393.
- 182 Rockwood, M. and Medina, A., “Controlled generation of periodic vortical gusts by the rotational oscillation of a circular cylinder and attached plate,” *Experiments in Fluids*, Vol. 61, No. 65, 2020.
- 183 Menter, F. R., Smirnov, P. E., Liu, T., and Avancha, R., “A One-Equation Local Correlation-Based Transition Model,” *Flow, Turbulence and Combustion*, Vol. 95, No. 4, 2015, pp. 583–619.
- 184 Kirschmeier, B. A., Gianikos, Z., Gopalarathnam, A., and Bryant, M., “Amplitude Annihilation in Wake-Influenced Aeroelastic Limit-Cycle Oscillations,” *AIAA Journal*, Vol. 58, No. 9, 2020, pp. 4117–4127.

- <sup>185</sup> Chatterjee, P., Jenkins, M., Babu, A. V. S., Medina, A., Gopalarathnam, A., and Bryant, M., *Tailored Bluff Body Motion for Generating Desired Wake Structures*.
- <sup>186</sup> Choi, J., Colonius, T., and Williams, D. R., "Surging and plunging oscillations of an airfoil at low Reynolds number," *Journal of Fluid Mechanics*, Vol. 763, 2015, pp. 237–253.